RANGE UNCERTAINTY REDUCTION IN PROTON BEAM THERAPY VIA PROMPT GAMMA-RAY DETECTION

A thesis submitted to The University of Manchester for the degree of Doctor of Philosophy in the Faculty of Biology, Medicine and Health

2020

COSTANZA M. V. PANAINO

SCHOOL OF MEDICAL SCIENCE

Division of Cancer Sciences

Contents

Word count: 45225

List of Figures

List of Tables

Abstract

Compared to conventional radiotherapy, proton therapy (PT) offers dosimetric advantages. The full PT exploitation, however, is hindered by the uncertainty in the fall-off position of proton beams, or range uncertainty. A new method, called Prompt Gamma Coincidence (PGC), has been developed to monitor the proton range in tissues through the detection of 2.741/6.128 MeV ^{16}O-induced prompt gamma (PG) rays emitted in coincidence. PG rays are γ-rays naturally emitted from nuclear de-excitations following proton bombardment.

The detection system is comprised of 16 $LaBr_3$ detectors. The information recorded by the system is fed into a reconstruction algorithm. Two versions of the algorithm, Algorithm 1 and 2, have been proposed. They are based on different input data and 3D geometry.
In the first study the system was simulated with a water phantom inside its volume. A 180 MeV proton beam was shot on the phantom, along its central axis. The simulation output was imported into Algorithm 1. To investigate different clinical scenarios the system internal radius was set at 8, 15, and 25 cm. A 5 and 10 mm range undershoot was also modelled.
In a second/third study the emission position reconstruction is reported for an isotropic point ^{60}Co source. The evaluation was both in-silico and experimental. The experimental validation was performed at National Physical Laboratory, with only 8 $LaBr_3$ detectors in place. The internal volume radius was always 9 cm. The output of all evaluations was processed by Algorithm 2. All simulations were performed using the Monte Carlo based Geant4 (10.04) toolkit.

Using Algorithm 1, the peak in the PG profile, for a 180 MeV beam shot on a water phantom, was inferred with a sigma of 4.17, 5.65, and 6.36 mm for an 8, 15, and 25 cm internal radius. For an 8 cm radius, with a 5 and 10 mm undershoot, the sigma was 4.31 and 5.47 mm. These values are comparable to the range uncertainties incorporated in treatment planning. Using Algorithm 2, simulation results show that the emission position of a ^{60}Co source at (0,0,0) is reconstructed within 3 and 1 mm, for 10^5 and 10^6 primary events, respectively. Experimental results show that for sources at (0,0,0) and (0,0,-30) mm, with 10^6 recorded events, the emission position is reconstructed within 5 mm.

Work is being carried out to further optimise the detection system and the algorithms. In light of the positive tests, the first PGC prototype is being constructed. Experimental validation with clinical proton beams are planned.

Declaration

No portion of the work referred to in the thesis has been submitted in support of an application for another degree or qualification of this or any other university or other institute of learning.

Copyright Statement

I The author of this thesis (including any appendices and/or schedules to this thesis) owns certain copyright or related rights in it (the "Copyright") and she has given The University of Manchester certain rights to use such Copyright, including for administrative purposes.

II Copies of this thesis, either in full or in extracts and whether in hard or electronic copy, may be made only in accordance with the Copyright, Designs and Patents Act 1988 (as amended) and regulations issued under it or, where appropriate, in accordance with licensing agreements which the University has from time to time. This page must form part of any such copies made.

III The ownership of certain Copyright, patents, designs, trademarks and other intellectual property (the Intellectual Property) and any reproductions of copyright works in the thesis, for example graphs and tables ("Reproductions"), which may be described in this thesis, may not be owned by the author and may be owned by third parties. Such Intellectual Property and Reproductions cannot and must not be made available for use without the prior written permission of the owner(s) of the relevant Intellectual Property and/or Reproductions.

IV Further information on the conditions under which disclosure, publication and commercialisation of this thesis, the Copyright and any Intellectual Property and/or Reproductions described in it may take place is available in the University IP Policy (see http://documents.manchester.ac.uk/DocuInfo.aspx?DocID=24420), in any relevant Thesis restriction declarations deposited in the University Library, The University Library's regulations (see http://www.library.manchester.ac.uk/about/regulations/) and in The University's policy on Presentation of Theses.

Γιά σένα
Per te

Acknowledgement

Thanks to my supervisor, Dr Michael J. Taylor, and to my co-supervisor, Professor Ranald I. Mackay, for providing guidance, advices and feedback throughout this study. Thanks to all the members of the PRECISE group, and to the group leader Professor Karen J. Kirkby, whose inclusion, support and encouragement has been truly invaluable. Thanks also to the collaborators from the University of Manchester, the University of Birmingham, and the National Physical Laboratory in London, for the advices, the fruitful discussions and the assistance during experimental tests.

Thanks to Tracy, Eliana and Marianne for being extraordinary women, friends, scientists and, most of all, an inspiration. Thanks to Simona for being the sister I never had.

Thanks to Marios, to whom is dedicated this thesis, for making me a better person every day. Thanks also to my cat Fidel, only companion in pandemic time. This thesis was fully written under the solely soundtrack of his purring.

Thanks to my parents for teaching me courage, determination, humbleness and, most of all, love of knowledge.
Grazie ai miei genitori per avermi insegnato il coraggio, la determinazione, l'umiltà e, più di tutto, l'amore per la conoscenza.

The Author

Costanza Panaino was born on January 7^{th}, 1991 in Milan, Italy. She received pre-university education ("Scientific lyceum") at Ravenna, Italy, obtaining her diploma in 2010. In the same year, she started her studies at the University of Milano-Bicocca where she received her B.Sc. degree in Physics in 2013. For her bachelor's thesis, she conducted a research study on Geant4 simulation of X-rays tubes for medical diagnostic. She continued her graduate studies at the University of Milan, receiving a M.Sc. degree in Physics in 2016, with elective courses in medical and nuclear physics. During 2015 and 2016, she spent 13 months within the Department of Medical Physics at the National Cancer Institute of Milan, to research prostate intra-fraction motion during conventional radiotherapy, which was the topic of her master's thesis. From 2016 to 2020, she was enrolled in a PhD project at the University of Manchester based at the Christie NHS Foundation Trust. She pursued an investigation on range uncertainty reduction in proton beam therapy, which is the subject of this thesis. She presented her work in two peer-reviewed publications and at several international conferences. At the 2019 annual conference of the Particle Therapy Co-Operative Network (PTCOG) she was selected as young investigator award finalist.

Chapter 1

Introduction to proton therapy

This Chapter provides an overview on Proton beam Therapy (PT) and the problem of range uncertainty. In the first part, PT history and rationale, the physics behind proton interactions in tissues and the technology needed for PT delivery are described (Sections 1.1, 1.2, and 1.3). The problem of range uncertainty is then introduced, with an insight into range uncertainty sources (Section 1.4) and managing strategies (Section 1.5). The Chapter ends with a brief review on range verification methods (Section 1.6).

1.1 Proton therapy: history and rationale

1.1.1 The history of proton therapy

The idea of repetitively accelerating particles in time-dependent varying potentials dates back to 1936 when Ernest Lawrence invented the cyclotron [1]. Thus, the cyclotron technology was already available when, in 1946, Robert Wilson first envisaged the concept of PT. In *Radiobiological use of fast protons* [2], Wilson described how accelerator-produced proton beams could be used to treat deep-seated tumours within healthy tissues. The study discusses the biophysical rationale for PT as well as the key engineering techniques for beam delivery. Wilson's idea was first picked up at the Lawrence Berkeley Laboratory (LBL) in California. Here, in 1954, the first cancer patient was treated [3]. Between 1954 and 1957 a total of 20 patients received PT at LBL [4]. Shortly after, PT landed in Europe. The Gustav Warner Institute in Uppsala, Sweden, treated its first patient in 1957 [5]. By 1968, in this centre, 69 patients with intracranial lesions received radiosurgical proton irradiation [6]. Wilson's home institution, Harvard University (Harvard Cyclotron Laboratory, HCL), saw its first PT treatment in 1961 [7]. By 1975, in HCL, 732 patients had undergone proton pituitary irradiation [8]. In the same centre, in 1975, the first ocular treatment, for a choroidal melanoma, was performed [9]. A clinical PT program was then started in Russia: in Dubna, 1967 (Joint Institute for Clinical Research, JINR), Moscow, 1969 (Institute for Theoretical and Experimental Physics, ITEP), and St. Petersburg, 1975 (Central Research Institute of Roentgenology and Radiology, CRIRR). By the end of 1981 the facility at ITEP treated 575 patients [10]. In 1979, in Japan, the National Institute of Radiological Science in Chiba (NIRS) treated its first patient [11]. Between 1979 and 1984, at NIRS, a total of

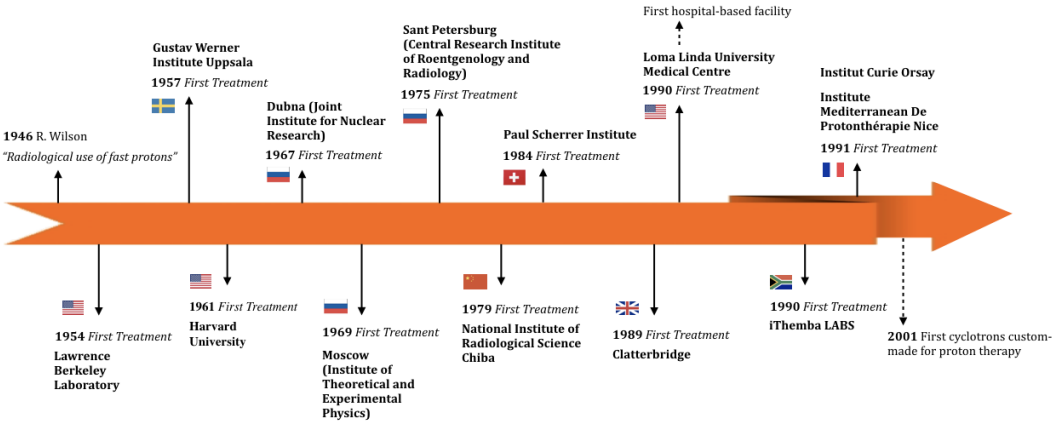

Figure 1.1: The first 50 years of proton radiotherapy

29 patients received PT [12]. In the 80s clinical PT programs started at the Paul Scherrer Institute (PSI), Switzerland (1984) and in Clatterbridge, UK (1989). At this time, however, very few patients were being recruited for PT. Treatments were primarily based in research centres with a reduced beam time availability. In 1990, at the Loma Linda University Medical Centre (LLUMC), California, the first hospital-based PT facility started operation [13]. Hospital-based facilities boosted the spread of PT. In the early 90s, several new clinical PT centres opened, example being the facilities in France, Nice and Orsay, and in South Africa, iThemba LABS, inaugurated, respectively, in 1991 and 1993. Since then, as reported by the up-to-date statistics from the *Particle Therapy Co-Operative Network* (PTCOG), the growth of PT has been exponential. The first 50 years of PT are shown in Figure 1.1.

1.1.2 Proton therapy facilities in the world

Globally, as of May 2020, there are 101 PT facilities in clinical operation [14], 37 under construction [15], and 14 in planning stages [16]. For each category, and for all facilities, a geographical distribution is shown in Figure 1.2. In 2019 only, ∼213,600 patients received PT worldwide as part of their treatment plan [17].

1.1.3 Proton therapy facilities in the UK

The Clatterbridge NHS Foundation Trust Centre, specialised in eye PT, is the oldest UK PT facility. Every year, 40% of all UK ocular melanoma patients are referred to Clatterbridge, where more than 2,830 patients have been treated since 1989 [18].

Since 2008, 1,400 UK patients have undergone PT treatment abroad (mainly Germany, Switzerland, and the USA). In 2010 the UK National Health Service (NHS) invested £250 million in two high energy PT centres, providing a total of six treatment rooms (three per centre). With the first patient being treated in October 2018, The Christie NHS Foundation Trust in Manchester represents the first high energy PT NHS service of the country [19]. The second NHS facility is under construction at the University College London Hospital [20], becoming operational in 2021. When fully up and running the two centres will each treat up to 750 patients per year, corresponding to ∼1% of yearly national radiotherapy

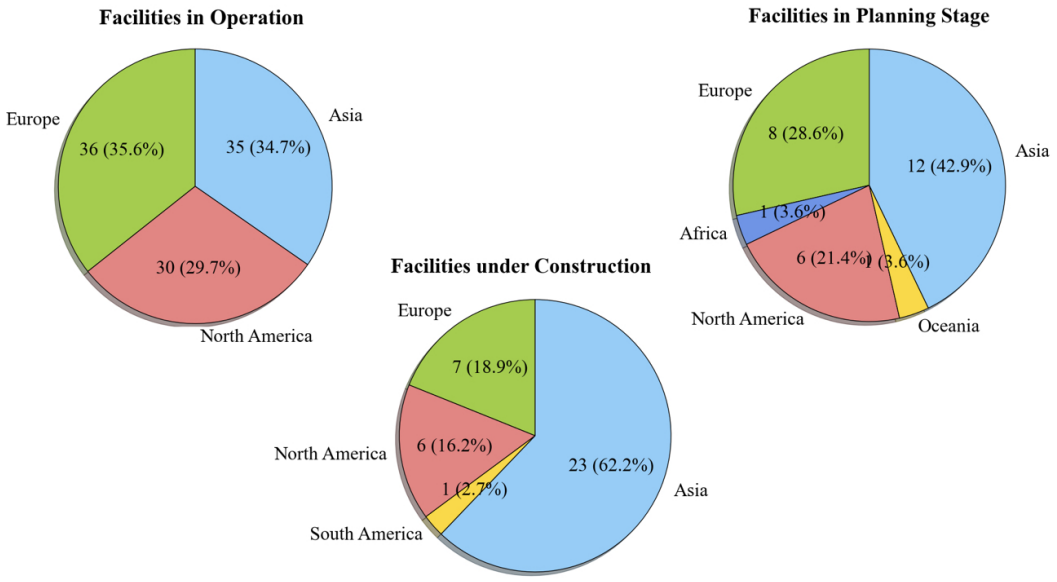

Figure 1.2: Geographical distribution of the PT facilities in clinical operation [14], under construction [15], and in planning stages [16]

episodes ([21], [22]). As of May 2020, in the UK there are four additional high energy PT centres (three operational, one under construction), all belonging to the private sector [23].

1.1.4 Proton therapy cost-effectiveness

In the last decades photon therapy has rapidly evolved. PT, conversely, had improved with a slower pace, mainly due to the technological challenges, the high cost of the facilities and the lack of evidence of cost-competitivness. Initially the cyclotrons in research labs were employed for treatments. Only in 2001, downsized cyclotrons custom made for PT came on the market, significantly reducing the cost of new facilities [24].

Today the costs of PT are still significant, with an up-front investment far greater than that of a photon facility [25]. The most significant useful parameters for cost accounting exercises are: 1) equipment (purchase, maintenance, upgrade, bills), 2) building (purchase, maintenance, upgrade), and 3) personnel (salary and training) [26]. According to Goitein and Jermann [27] the operational cost of a PT facility is dominated by the business cost (42%, primarily repaying the presumed loan for purchase/construction), personnel (28%), and servicing the equipment (21%). The relative costs of proton and photon therapy were evaluated by Goitein and Jermann [27] and Peeters *et al* [28]. Considering a PT facility with three treatment rooms and a photon therapy facility with two linear accelerators, assuming that both facilities have been constantly renewed and have equal image-guided equipment, Peeters *et al* [28] estimated a 3.2 proton-to-photon therapy cost ratio. Cost difference per treatment is relatively small for lung/prostate patients. For lung cancer, for example, cost is £11,160[1] for PT and £7,350 for photon therapy. The highest costs are for head and neck tumours, £35,730 for PT and £10,390 for photon therapy [28].

[1]Prices are provided in euros, conversions are made using euro-to-pound ratio as of May 2020.

Among the constituents of a PT economical evaluation there is the target population, or the proportion of cancer patients eligible for PT. Such proportion is provided by the scientific evidences supporting the added benefit of PT, in terms of tumour control/reduced toxicities. There is an ongoing debate about whether the superior dose coverage achievable with PT is clinically significant for all treatment sites. The majority of PT patients has a follow-up period shorter than 20 years, thus late morbidity data are rare. To prove that the gain in tumour control/reduced toxicities is enough to warrant the cost of PT, large scale collaborative studies [29] and randomised clinical trials are needed. Clinical trails can bring uniformity in clinical parameters, allowing the acquisition of large series of data ([30], [31]).

1.1.5 Proton therapy, the clinical rationale

An enhancement in dose distribution is obtained when a higher dose is delivered to the tumour and/or a reduced dose is delivered to the surrounding healthy tissues. To be accepted by clinicians, every new radiotherapy technology needs to show such an improvement. When it first became available, PT was of interest because its dose conformity seemed far superior than the one offered by photon therapy. With the development, in the "photon world", of Intensity Modulated RadioTherapy (IMRT) [32], the difference in dose conformity between protons and photons has significantly decreased and today, for several treatments sites, the advantages of protons are marginal al best. There are, however, specific circumstances in which PT represents the most valuable tool, this being the case of head and neck cancer.

In head and neck cancer the proximity of critical healthy structures to tumours can result in severe acute and late toxicity. Due to the unique physical properties of protons, the dose coverage obtainable in PT minimises the toxicity to normal structures. This is the reason why, in the past few years, the use of PT in the treatment of head and neck cancer has globally grown tremendously ([33], [34]).

For the paediatric cohort, the overall quality-of-life and the reduction of late toxicities is of paramount importance. One prime example is the treatment of medulloblastoma. With 55 children diagnosed per year in the UK, medulloblastoma is the most common paediatric cancer [35]; it develops in the cerebellum and quickly spreads through cerebrospinal fluid to the other parts of the brain and to the spinal cord [36]. Patients must receive irradiation of the full brain and of the spine. Treatment of the spine with photon therapy invariably exposes anterior structures, such as heart, lungs, and abdominal tissues, to substantial exit doses. Conversely, PT resulted in no cardiac or gastrointestinal side effects [37].

1.2 The physics of proton interactions in matter

Shown in Figure 1.3, the *Bragg curve* is the depth-dose distribution, measured in water, using a monoenergetic proton beam. PT dosimetrical advantages can be summed up by the shape of the *Bragg curve*: low dose is deposited along the entrance channel, with a steep increase and fall-off towards the end of the range, in the *Bragg peak*. The shape of the Bragg curve can be explained by combining the three predominant interaction mechanisms of protons in matter: inelastic Coulomb scattering, elastic Coulomb scattering, and nuclear

reactions. Such interactions are reviewed in the following Sections.

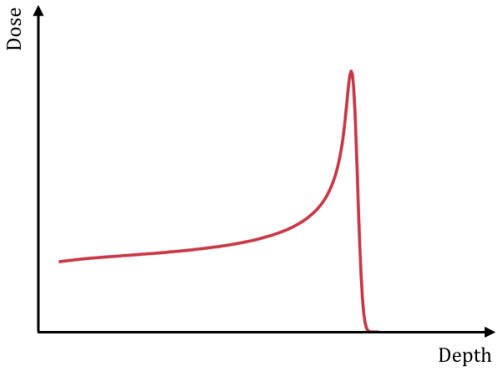

Figure 1.3: The *Bragg curve* shows the dose delivered by a monoenergetic proton beam as a function of the penetration depth. Toward the end of the range ∼1/3 of the total dose is delivered, in the *Bragg peak*.

1.2.1 Inelastic Coulomb scattering

Upon entering any material, a proton interacts with many atomic electrons. In any such interaction, as the proton passes its vicinity, the electron feels the attraction of the Coulomb force. Depending on the proximity of the encounter, this attraction can cause an *ionisation*, the electron is expelled from the atom, or just an *excitation*, the electron jumps to a higher-lying shell within the atom. The energy-gain of the electron comes at the expense of the proton, whose velocity is decreased. In a single collision a proton can only transfer to an electron up to 1/500 of its initial energy. The proton, however, is simultaneously interacting with many electrons, so that the net effect, known as *slowing down approximation*, is a continuous decrease in velocity, until it is stopped. A single interaction does not greatly deflect the proton and interactions occur from all directions at the same time. Thus, except at the very end, protons tracks are quite straight. Assuming a smooth and continuous slowing process, the *linear stopping power*, S, is defined as:

$$S = -\frac{\mathrm{d}E}{\mathrm{d}x} \quad \left[\frac{MeV}{cm}\right] \tag{1.1}$$

where E is the mean energy loss and x is the distance. Dividing S by the density ρ of the absorber medium results in a quantity called *mass stopping power*, S/ρ, defined as:

$$\frac{S}{\rho} = -\frac{\mathrm{d}E}{\rho \mathrm{d}x} \quad \left[\frac{MeV}{g/cm^2}\right] \tag{1.2}$$

The classical formula for S/ρ is attributed to Bethe [38] and Bloch [39] and is written:

$$\begin{aligned} \frac{S}{\rho} = -\frac{dE}{\rho dx} &= \frac{\pi N_A r_e^2 m_e c^2}{\beta^2}\frac{Z}{A}\left[\ln\frac{2m_e c^2\gamma^2\beta^2}{I} - \beta^2 - \frac{\delta}{2} - \frac{C}{Z}\right] \\ &\sim \frac{K}{\beta^2}\frac{Z}{A}\left[\ln\frac{2m_e c^2\gamma^2\beta^2}{I} - \beta^2\right] \end{aligned} \tag{1.3}$$

Where N_A is Avogadro's number, ${r_e}^2$ and m_e are the electron radius and mass, Z and A are the absorber atomic and mass number, $\beta = v/c$, where v is the proton velocity, and $\gamma = (1-\beta^2)^{-1/2}$. The average excitation and ionisation potential I has to be experimentally determined for each material, although it is roughly proportional to Z, with $I/Z \approx 10$ eV. The density (δ) and shell (C) corrections involve quantum mechanics and, for non-relativistic protons, can be neglected. From Eq. 1.3 few key observations can be inferred.

- $S \propto 1/\beta^2 \propto 1/v^2$: the smaller v is, the more energy is transferred.
- $S \propto N_A \rho Z/A$: the higher the absorber electron density $N_A \rho Z/A$ is, the greatest S is.
- There is no dependence between S and the proton mass.

If the absorber material is a mixture/compound it can be assumed that the stopping power per atom is additive. This assumption is know as *Bragg additivity rule* [40]:

$$\frac{S}{\rho} = \sum_i w_i \frac{1}{N_i} \left(\frac{S}{\rho}\right)_i \tag{1.4}$$

where w_i and N_i are the atomic density and the atomic fraction of the i^{th} atom.

Range

Range is the depth in the absorber at which half of protons have come to rest. Consequently, range is, by definition, an average quantity, established for a beam and not for individual particles. The path of protons in a medium is nearly a straight line (lateral scattering is negligible in the clinical regime) and protons loose energy continuously, thus a simplistic one-dimension range calculation can be performed with a numerical approach:

$$R(E) = \int_0^E \left(\frac{\mathrm{d}E'}{\mathrm{d}x}\right)^{-1} \mathrm{d}E' = \int_0^E \left(\frac{1}{S(E)}\right)^{-1} \mathrm{d}E' \approx \sum_0^E \left(\frac{1}{S(E)}\right)^{-1} \Delta E' \tag{1.5}$$

where the continuous transport is approximated by calculating discrete steps.

From Eq. 1.3 we know that $S \propto 1/\beta^2$, while $\beta \propto E$. As a consequence Eq. 1.5 implies that $R \propto E^2$. In fact this exponential is just a bit lower than 2. As proposed by Bragg and Kleeman [41], $R(E)$ can be calculated with a power-law:

$$R(E) = \alpha E^p \tag{1.6}$$

where α is a material-dependent constant and p takes into account v. The power-law validity in Eq. 1.6 can be proved by plotting the range-energy curve in log scales, which results in a straight line. For proton beams in water Bortfeld *et al* [42] estimated the parameters α and p to be 0.0022 and 1.77, respectively. Eq 1.6 then becomes: $R(E) = 0.0022 \cdot E^{1.77}$.

[2] Classical electron radius r_e=$2.817 \cdot 10^{-13}$ cm

Energy and range straggling

Although all protons in a beam have the same initial energy, the microscopic interaction undergone by any specific proton varies randomly, and protons do not all stop at the exact same depth. This phenomenon is known as range/energy straggling. Janni [43] evaluated the standard deviation of straggling as a function of the range. For light material range straggling is 1.2% of the range. This percentage is only slightly higher for heavy materials, suggesting that the shape of the Bragg curve changes very little between different absorbers.

1.2.2 Elastic Coulomb scattering

Other then slowing down, protons scatter by Coulombic interactions with the atomic nuclei. The angular deflection from a single scatter is almost negligible. What counts is the cumulative effect of countless tiny deflections, hence the name Multiple Coulomb Scattering (MCS). For radiotherapy purposes MCS angular distribution can be considered gaussian. In analogy to stopping power, the *scattering power*, T, is defined as:

$$T(x) = \frac{\mathrm{d}\langle\theta^2\rangle}{\mathrm{d}x} \tag{1.7}$$

where $\langle\theta^2\rangle$ is the mean square of the scattering angle θ and x is the absorber thickness. $T(x)$ is defined via $\langle\theta^2\rangle$; scattering is symmetric about the central axis, therefore the mean scattering angle $\langle\theta\rangle$ is zero. The integration of $T(x)$ over x gives the total MCS angle.

1.2.3 Nuclear reactions

Nuclear reactions are much harder to model than stopping and scattering. However, they are by no means rare. Particles emitted from nuclear reactions are called *secondaries*, while protons from the beam are termed *primaries*. Possible secondaries are protons, particles of deuterium (^{2}H), tritium (^{3}H), and helium (^{3}He), and α-particles. Paganetti [44] in-silico calculated the secondaries dose distribution for a 160 MeV proton beam in water. Light secondaries (A<5) were tracked down up to an energy of 100 keV. Results show that the 19.6% of the primaries undergo a nuclear interaction. The average number of secondaries per proton is: 1.8 protons, 0.63 neutrons, 0.38 α-particles, 0.02 ^{2}H, 0.002 ^{3}He, and 0.001 ^{3}H. Secondary neutrons have also a high probability of emitting protons via (n, pn) reactions. With respect to the original beam path, secondaries typically make large angles, whereas primaries, even out of MCS, rarely exceed a few degrees angle.

Figure 1 in Paganetti [44] reports the inelastic nuclear reaction cross section for protons on ^{16}O. The (p, ^{16}O) cross sections from simulation studies, the ICRU 2000 [45], Janni [43], and experimental measurements (Carlson *et al* [46], Renberg *et al* [47], Chapman and Macleod [48]) are compared. In Figures 7, 8, and 9, from Kozlovsky *et al* [49], cross sections for selected (p, ^{16}O) de-excitation lines are constructed from experimental data (Dyer *et al* [50], Lang *et al* [51], Narayanaswamy *et al* [52], Lesko *et al* [53], Tatischeff *et al* [54], Zobel *et al* [55], Kiener *et al* [56], Foley *et al* [57]). The following general features can be inferred:

- The cross section is null when the energy of the primary proton is inferior to an element-dependent threshold value (∼few MeV).
- The cross section is maximum when the energy of the primary proton equals an element-dependent value (∼20 MeV).
- For a high primary proton energy the cross section does not depend on the energy but is comparable with the geometric cross section areas of the absorbers nuclei.

Neutron background

A different background, mainly neutrons, is produced by proton nuclear interactions in the equipments along the beamline. As estimated by Agosteo *et al* [58], the yield of these secondaries depends on the specific facility. Produced in copious quantities, with an energy spectrum spanning 10 orders of magnitude, neutrons can be very penetrating [59]. A major effort must be spent to minimise personnel exposures to neutrons. Additionally, electronic systems need to be hardened/shielded and neutron activation of the beamline components is to be avoided. Neutrons could also increase the risk of late side effects in patients [60].

1.3 Clinical proton beams

1.3.1 Proton beam line

Cyclotrons

New cyclotrons, custom made for PT, accelerate protons up to a fixed energy of 230 or 250 MeV[3]. Compared to classical lab-based cyclotrons, modern cyclotrons are rather compact, with a magnet height of ∼1.5 m and a diameter between 5 (200 tons) and 3.5 m (100 tons), when equipped with room temperature coils or superconducting coils, respectively.

Beam transport system

Once extracted from the cyclotron the beam is effectively continuous and with a fixed energy. From cyclotron to gantry protons travel in vacuum via the Beam Transport System (BTS) [63]. The first element on the BTS is a degrader. The degrader lowers the energy to the value prescribed by the treatment recipe. Along the BTS the beam comes later under the forces of two magnet types. Quadrupole magnets focus the beam into pencil width shapes while dipole magnets deflects the beam into each treatment room.

Fixed and rotating gantries

In the earlier days of PT, treatment rooms were designed with fixed horizontal and vertical beam lines [64]. To target different parts of the body and avoid critical structures, fixed beams rely on the treatment table/chair movement. This solution is now in few centres and for specific treatment sites only. Prostate cancer, for example, is typically treated with

[3]For a detailed description of the cyclotron and its components the reader is referred to the review articles by Amaldi *et al* [61], Flanz [62], and Schippers [63].

two lateral beams and is easily deliverable on a fixed beam line. Today the BTS guides the beam to a treatment head, or nozzle, mounted on a mechanical rotating structure, a rotating gantry. The gantry directs the beam to the patient, who lies on the treatment couch. In conjunction with the beam rotation, the couch can be rotated/shifted, to achieve the maximum possible flexibility for planning and delivering patient treatments [65].

Nozzle

The beam that reaches the treatment room is monoenergetic, with a typical sigma of 4 mm. There are two PT delivery systems, passive scatter and scanning beams, and nozzles components change accordingly.

1.3.2 Beam delivery techniques

Beam delivery: passive scattering

In passive scattering delivery systems [66] a uniform dose in the depth direction is created using a technique called range modulation. Multiple monoenergetic beams, shifted in energy and weighted, are combined to create a flat dose region known as Spread Out Bragg Peak (SOBP). The extent of this region varies with the number of peaks. To achieve a lateral spread, the beam is sent through a scattering system, consisting of one or more high-Z materials. The beam diameter is increased until the maximum lateral tumour cross section is matched. In addition field-specific apertures may conform the beam shape to the target.

Beam delivery: pencil-beam scanning

In scanning delivery systems [67] the beam from the BTS is directly sent to the patient via the gantry and the treatment nozzle. In the nozzle, a pair of quadruple magnets control the beam size, while a pair of magnet dipoles deflect the beam to reach the target. The target is treated in a number of layers, corresponding to different energy levels. For each layer dose is delivered by deflecting the beam. The beam may move discretely, applying dose *spot* by *spot* (*spot scanning*). The beam may also move continuously along lines in the tumour, while its intensity is varied to deliver the correct dose along each line (*continuous scanning*).

With scattering systems some unnecessary dose is usually delivered to the proximal aspects of the beam. Scanning systems offer greater control over the proximal region as well as an improved dose conformability to the target. A superior dose distribution with scanning beams compared to scattering beams has been demonstrated for several tumour sites, such as prostate [68], brain [69], pancreas [70], and lung [71]. A comparison of surface doses from scanning and scattering beams was performed by Arjomandy *et al* [72]. Additionally, due to the proton interactions with the scatterer materials in the nozzle, an extra neutron contamination is produced in scattering systems [73].

1.3.3 Proton treatment planning

The ideal treatment plan, with the target receiving 100% of the prescribed dose and the healthy tissue receiving 0%, is unachievable. Instead, to produce the best clinically acceptable plan, multiple trade-offs are needed. In PT, to combine fields in a treatment plan, there are two main approaches: Single Field Uniform Dose (SFUD) and Intensity Modulated Particle Therapy (IMPT). SFUD plans, associated to both scattering and scanning delivery systems, are constructed by adding together fields that have each been *individually* optimised. Each field delivers a homogeneous dose across the target. In IMPT plans all pencil beams from all fields are *simultaneously* optimised. As such, across the target, the individual fields may be very inhomogeneous while the final dose is homogeneous. Scanning systems are a prerequisite for IMPT. Compared to SFUD approach, IMPT plans allow a higher flexibility in constructing the total dose distribution.

1.4 Range uncertainty in proton therapy

1.4.1 The clinical impact of range uncertainty

Uncertainties in the proton range may have a profound impact on the dose distribution. Indeed, range uncertainty is probably the main factor preventing the full exploitation of PT potential [74]. The sharpest dose fall-off of a proton field usually corresponds to the distal fall-off, thus it may be tempting to aim proton fields directly against Organs At Risk (OARs). In clinical practice, however, this is rarely done as range uncertainties could cause OARs to receive significant radiation. Tumour shrinkage, for example, may lead to an anatomical variation not originally considered in the treatment plan. This is highlighted in Figure 1.4. Figure 1.4a depicts an over-simplified treatment at its start. Sessions after, the tumour may have reduced in volume. As the density along the beam-path has changed, the range is extended and the dose at the Bragg peak is delivered to the OAR (Figure 1.4b).

The clinical case of a target located in close proximity to an OAR, and the impact of range uncertainties, is considered in Figure 1.5. In the first treatment design (Figure 1.5a) the target is irradiated from the right and the left side by two parallel-opposed lateral beams. Such an arrangement is robust against uncertainties. The beam direction does not point towards the OAR, thus the risk of overshooting into the OAR is avoided. There are, however, few disadvantages. First, the radiologic beam path-length to the target is very long, increasing the dose to the normal tissues. Second, the lateral edge of the beams is located on the interface between the target and the OAR. The dose gradient at the beams lateral edge increases with range (from 3 to 12 mm at the 20 to 80% dose level). Therefore a long path-length results in an increased lateral scatter and in a wider dose penumbra. In a more “adventurous” design (Figure 1.5b), the target is irradiated from two oblique angles, with the end-of-range of the beams located on the target-OAR interface. This approach results in a reduced integral dose to the normal tissues. Due to the shorter beam range the distal dose fall-off is sharper, improving the dose conformity to the target. Potentially such

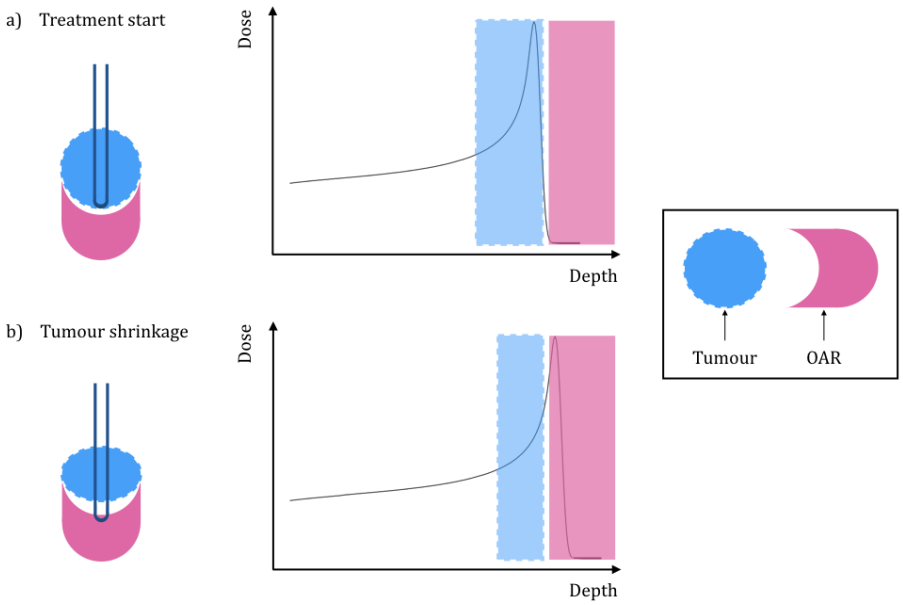

Figure 1.4: Range uncertainty due to tumour shrinkage not considered in the treatment plan. a) Treatment start: the beam is directly aimed against a close OAR and the dose at the Bragg peak is fully delivered to the tumour. b) Few sessions after: the tumour volume has reduced. Because the density along the beam-path has changed, and the plan has not been modified, the dose at the Bragg peak is delivered to the OAR.

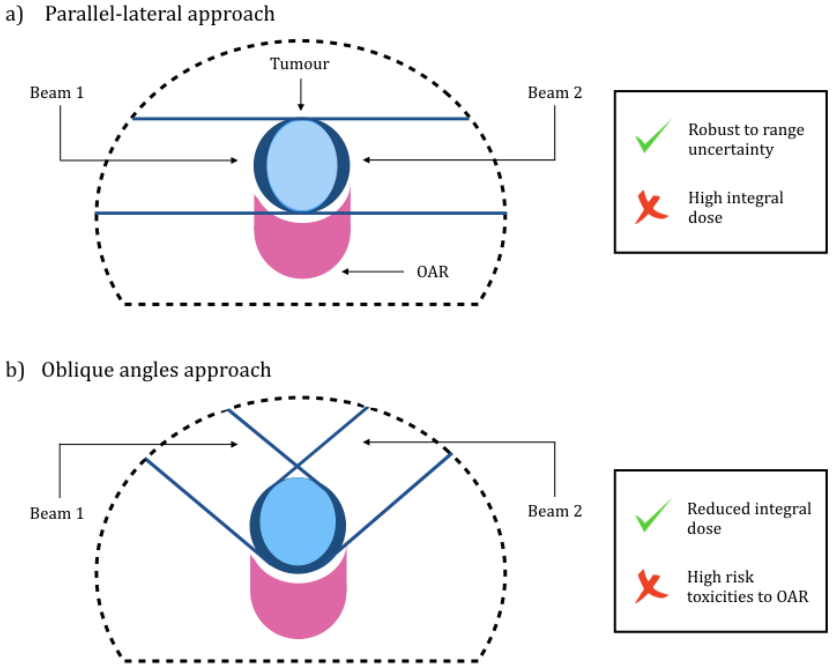

Figure 1.5: Potential treatment designs for a target located in close proximity to an OAR. a) The target is irradiated from the right and left sides by two parallel-opposed lateral beams. b) The target is irradiated from two oblique angles, with the end-of-range of the beams located on the target-OAR interface. The second approach results in a reduced integral dose to the normal tissues and an improved dose conformity to the target, however it is not robust against range uncertainties. Modified from Verburg [76].

design could allow for more dose escalation, whilst maintaining an adequate sparing of the healthy organs. However it is not robust against range uncertainties. A prime example of the clinical case just described is prostate cancer, with the OAR being the rectum [75].

1.4.2 Range uncertainty sources

As summarised in Figure 1.6, range uncertainties sources can be divided into two categories:

- **Dose calculation dependent sources**[4]

  Sources leading to range uncertainties in the Treatment Planning System (TPS).

- **Dose calculation independent sources**

  Sources leading to discrepancies between planning and delivered dose.

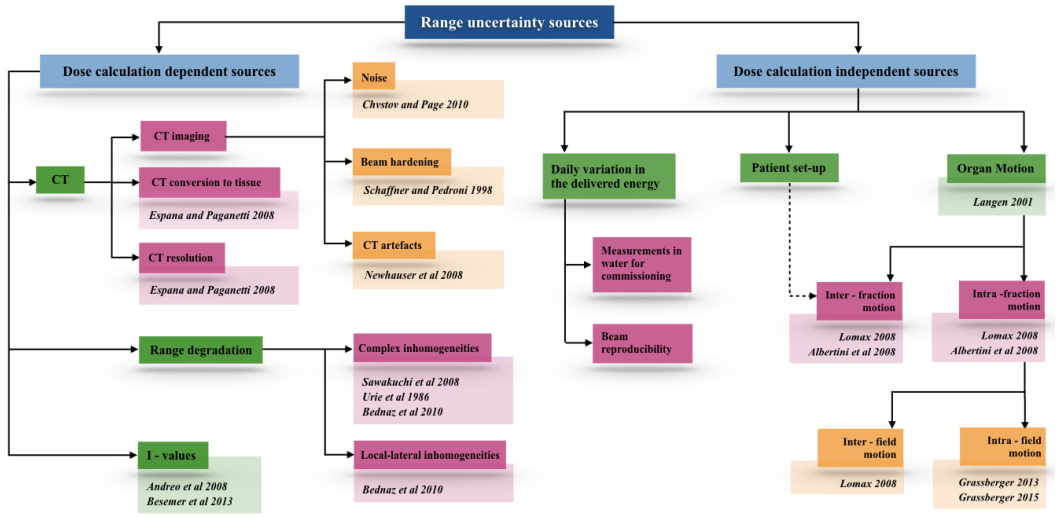

Figure 1.6: Range uncertainty sources and major related studies

1.4.3 Dose calculation dependent sources

Computer Tomography (CT)

TPS and range calculation are based on CT acquisition. CT scans produce a 3D image of patients' body, representing the photon attenuation in tissues relative to water (*Hounsfield Unit* - HU). HUs depend on the X-ray spectrum. Each scanner has its own tube potential and current and generates a different X-ray spectrum. Thus, individual calibrations need to be carried out. CT−related range uncertainty arises from: 1) CT imaging inherent limitation, 2) HUs to proton stopping power conversion, and 3) CT resolution.

Inherent limitations of CT scans, such as image noise and beam hardening, directly affect range calculation. Chvetsov and Paige [79] studied the relationship between HUs noise and range. The associated range uncertainty was estimated between ±0.3% and ±0.7%. Beam hardening depends on the position and density of the tissue and has the greater effect on HUs. According to Schaffner and Pedroni [80] the related uncertainty is ±1.8% and ±1.1% for bone and soft tissue, respectively. CT artefacts can also affect the accuracy of range prediction and are particularly severe in the presence of metal implants [81].

[4]This category includes the uncertainty in the Relative Biological Effectiveness (RBE) value of proton beams. RBE is beyond the scope of this work. The reader is referred to the specialised literature ([77], [78]).

To calculate proton ranges HUs need to be converted to the relative proton stopping powers. Conversion schemes arise from CT scans of phantoms with known density and elemental composition. Although calibration curves are produced using sophisticated algorithms, they still carry inevitable uncertainties. Indeed the actual conversion is not just dependent on the HU value, but also on the material chemical composition. Thus, two materials with the same HUs can have different proton stopping powers and viceversa. Schaffner and Pedroni [80] and Espana and Paganetti [82] estimated as <1% the range uncertainty caused by the HUs to stopping power conversion.

Dual-energy CT, where the patient is scanned with two different X-ray energies, adds information on material composition. It was shown that the use of dual-energy CT reduces range uncertainty due to HUs to stopping powers conversion [83]. HUs conversion range uncertainty could be further decreased by proton−CT [84].

In relatively homogeneous geometries CT voxels size plays a minor role in dose calculation. Problems may arise in highly heterogeneous geometries where densities are small. In the lung, for example, low density materials (i.e. air) and materials with much higher density (i.e. soft tissues), might be averaged to obtain the HU value of a given voxel. Thus, depending on the region in the lung, the standard range uncertainty can raise up to 1 cm [82]. For sites other then the lung, and for the typical clinical CT resolutions, Espana and Paganetti [82] estimated range uncertainty due to CT resolution to be just ∼0.3%.

Mean excitation energy I-values

The mean excitation energy, or I-value, is the main source of uncertainty in the Bethe−Bloch formula (Eq. 1.3). Limited empirical data exist on elemental I-values and most of the I-values of compounds/tissues are determined using the Bragg additivity rule (Eq. 1.4). Accordingly to this rule the I-value of a compound/tissue is the weighted sum of the I-values of all the atomic constituents. As the Bragg additivity rule does not consider the effects of chemical bonds, the calculated I-values have larger uncertainties than the elemental ones. A wide range of water I-values has been reported: 75 ± 3 eV [85], 78.4 ± 1.0 eV [86], 80 ± 2 eV [87], and 81.8 eV [88]. Andreo [89] proved that a difference in water I-value between 75 and 80 eV results in a range uncertainty of 0.8−1.2%. For tissues the I-value uncertainty is ∼10−15%, resulting in a range uncertainty of ∼1.5%. More recently, the impact of I-value variations on range distribution within patients was investigated by Besemer *et al* [90].

Range degradation

Range degradation ([91], [92]) is caused by an increase of MCS through inhomogeneities. Typically TPSs do not predict range degradation. Indeed TPSs engines are based on water equivalent path-lengths in patients, thus they neglect the position of inhomogeneities relative to the distal fall-off of the Bragg curve. Sawakuchi *et al* [92] estimated a range reduction, due to complex inhomogeneities, of ∼0.7%.

Local Lateral Inhomogeneities (LLIs) arise from the scatter disequilibrium caused by MCS at interfaces parallel to the beam direction ([93], [94]). As noticed by Bednarz *et al* [93], for large fields the LLIs might just be local. Conversely, for very small fields, the entire target could be affected. Range effects caused by LLIs have been estimated to be $\sim\pm 2.5\%$.

1.4.4 Dose calculation independent sources

Daily variations in delivered energy

Daily variations in the beam energy are caused by: measurement uncertainty in water for commissioning (± 0.3 mm) and beam reproducibility (± 0.2 mm) [95].

Patient set-up

Range uncertainty is also caused by day-to-day variations in patient positioning respect to the beam, or patient set-up. Range uncertainties from patient set-up can be quite substantial, particularly when areas of large density heterogeneities, or surfaces oblique to the beam direction, are being treated. Accordingly to Paganetti [95], the range uncertainty due to a set-up variation of ~ 1 mm is ± 0.7 mm.

Organ motion

Organ motion and its management has been reviewed by Langen *et al* [96] for many radiotherapy treatment sites. Organ motion is typically divided in inter-fraction and intra-fraction motion. Intra-fraction motion includes both inter-field and intra-field motion.

Inter-fraction motion is the displacement of the patient, or of his/her internal organs, which occurs between different fractions. When fractionation schemes are adopted, the typical course of PT covers 6-8 weeks, for a total of 28-42 sessions. Over such a timescale, patient anatomy may change significantly, mainly because of tumour mass shrinkage and weight loss/gain [97]. The magnitudes of these effects can be substantial, changing slowly and systematically through the whole treatment course. Additionally, patients may present day-to-day variations in physiological parameters (i.e. rectal/bladder filling). Lastly, in this category fall the errors in patients' set-up discussed in the previous section [98]. In PT inter-fraction motion is source of serious concern, as it can lead to severe consequences. Motion-caused geometric changes result in density variations, which affect the beam radiological path-length. This, in turn, may provoke target under-dosage as well as an overdosage of the OARs and the normal tissues distal to the target [99].

Inter-field is the motion of the patient, or of his/her internal organs, in the time in between different fields are being delivered. A possible example is the sudden physiological gas motion in the bowel. For inter-field motion, the effects of field misalignment on treatment IMPT plans have been investigated by Lomax [99].

Intra-field motion is a fast, high frequency motion occurring, to a significant extent, within the delivery time of a single field. Motions due to breathing, cardiac cycles, and

peristalsis fall into this category. For active scanning only, the major effect of intra-field motion is the *interplay* between beam motion (within the same layer or from one layer to the next) and respiratory motion ([100], [101]). The interplay effect does not change the mean target dose but impacts its homogeneity.

1.5 Managing range uncertainty

PT planning is a multi-step process (Figure 1.7). At first the 3D image acquisition of the target[5] is reviewed and the Gross Tumour Volume (GTV) is outlined. Then a margin is drown around the GTV, to generate the Clinical Target Volume (CTV). The CTV includes all areas of risks for microscopical disease non visible on imaging studies. Patients previously treated with chemotherapy/surgery may not have a GTV, in this case the CTV is only based on estimated volumes of residual disease.

Range uncertainty is clinically managed by making plans robust against uncertainties. The way this is achieved depends on the treatment planning approach, SFUD or IMPT.

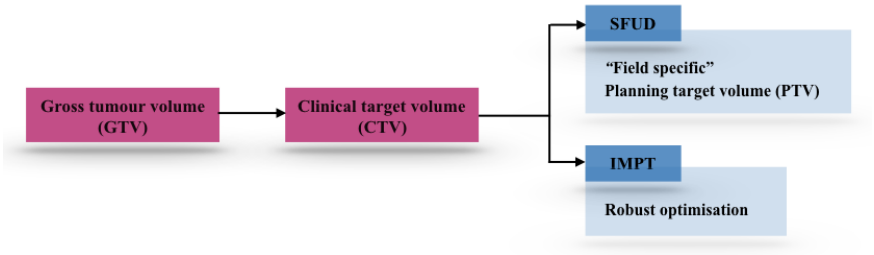

Figure 1.7: Managing range uncertainty in SFUD and IMPT treatment planning

1.5.1 SFUD: CTV expansions

For fields delivering a uniform dose to the target (SFUD), a lateral expansion of the CTV guards against under-dosing of the target due to set-up variations and/or organ motion. A larger expansion, in the distal direction, ensures coverage against range uncertainty. Lateral/range expansions differ for each field in the treatment plan. The final volume, after the expansions, can be regarded as the Planning Target Volume[6] (PTV). If the delivered dose is all within the PTV, the target has received the planned dose. However, the larger the PTV is, the less conformal the dose distribution results.

CTV range expansion: general recipe

Although there is no universally accepted standard, individual beams are typically robust against a 1.5σ end-of-range variation, which corresponds to a range uncertainty of 3.5% of the range. Accordingly, for a normal distribution, a 1.5σ end-of-range variation gives a 94% confidence level that the target will be fully covered. However, a 3.5% range expansion recipe

[5] The default imaging modality for treatment planning is CT. Planning is often enhanced by using other modalities, such as MR and/or PET.

[6] It should be noticed that the concept of PTV is proper of conventional radiotherapy only. Conversely, in PT, "field specific" PTVs are needed [102].

is only generic and adjustments, based on the location of the OARs, should be made for specific targets. For example, if the beam end-of-range is proximal to an OAR, an additional range expansion is added, ensuring that the beam will not overshoot. The beam end-of-range and the edge of the OAR are then separated by a 2σ margin, which gives a 98% confidence level. To take into account random errors, beam delivery and patient setup, an additional margin, usually 1 to 3 mm, is added. The general range expansion recipe is similar in most hospitals [95]: 3.5% (of the range) + 1 mm (Massachusetts General Hospital), 3.5% + 3 mm (MD Anderson Proton Therapy Center, Loma Linda University Medical Center, and Roberts Proton Therapy Center at the University of Pennsylvania), and 2.5% + 1.5 mm (Florida Proton Therapy Institute).

1.5.2 IMPT: robust optimisation

The use of lateral/range expansions is not ideal in IMPT [97]. IMPT plans are achieved by patching together inhomogeneous doses per field. In case of errors, as a result of misalignments of highly in-field dose gradients, degradation in dose conformity is observed not only along the target boundary but also in the middle of the target itself [103]. *Robust optimisation* incorporates range and set-up uncertainties directly into the IMPT plan, thus overcoming the drawbacks of margin-based planning. For a comprehensive review of robust planning in PT the reader is referred to Unkelbach *et al* [104].

1.6 In-vivo range verification

Whatever approach is chosen, margins or robust planning, there will always be the need to test its success by means of *in-vivo* (i.e. in the patient) range verification. Given the perceived importance of in-vivo range verification, several methods have been proposed. As summarised in Figure 1.8, these methods are divided into 1) *direct*, where range is obtained though direct dose measurements and 2) *indirect*, where range is reconstructed from signals resulting from proton irradiation. The main features of all methods are reviewed in Table 1.1 and, with the exception of prompt gamma detection, briefly described here. Prompt gamma detection is the main focus of this thesis and, as such, will be in-deep examined in Chapter 2. For an extensive evaluation of all methods the reader is referred to the review articles from Knopf and Lomax [74] and Parodi and Polf [105].

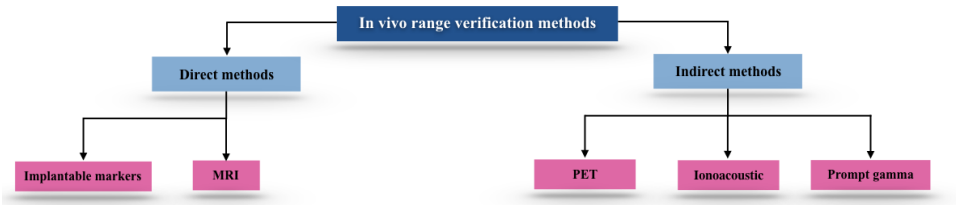

Figure 1.8: Direct/indirect in-vivo range verification methods

Methods	Best dimension	Timing	Best expected accuracy	Technology
Implantable markers	1D	On-line	< 1 mm [106]	• Existing in R&D • Development needed
MRI	3D	Off-line	< 1 mm [107]	• Commercially available
Ionoacustic	3D	On-line	< 1 mm [108]	• Existing in R&D • Development needed
Prompt-gamma	3D	On-line	< 1 mm [109]	• Existing in R&D • Development needed
PET	3D	• On-line • Off-line	> 1 mm [110]	• Commercially available • Development needed • Existing in R&D

Table 1.1: Overview of in-vivo range verification methods; current/potential status

1.6.1 Direct range verification methods

Implantable markers

The use of in-vivo, point-based, time dependent dose rate measurements, performed with implantable makers with a wireless readout, has been first proposed by Lu ([111], [112]). This method does not require any additional time for the patient. The range, however, can only be verified at a limited set of points, while a finer resolution may be required for treatment sites with tissue inhomogeneities along the beam path or in the target. In addition the dosimeters must be inserted in the target, thus only the beam-path from the body surface to the dosimeter, rather than to the distal edge of the target, can be verified. The main limitation is that, in most tumour types, makers implantation is not possible.

MRI

Tissues radiation-induced variations can be detected by MRI imaging. MRI-visible changes have been observed in spine [107] and liver [113]. The main advantages of the MRI method are: the high spatial resolution, the lack of additional ionising radiation exposure, and the MRI scanners availability. It was shown, however, that the proton range can not be verified via the solely inspection of MRI images. Indeed the Signal Intensity (SI) gradient of MRI images does not match exactly with the delivered dose gradient and a dose-SI curve has to be constructed. The temporal evolution of MRI signal is an additional weakness. In the first hours to days after irradiation concurrent anatomical effects interfere with the radiation-induced MRI-changes. Thus, MRI-changes are visible from eight days after irradiation and are completed three months later [114], making impossible any plan adaption. The temporal evolution of the MRI signal is also patient-age dependent and patient specific.

1.6.2 Indirect range verification methods

Ionoacustic

The acoustic signature of proton beams was first studied in 1979 [115]. Recently, the measurement of the acoustic signal as an in-vivo range verification strategy, namely *ionoacustic*

or *protoacustic*, has received renewed attention. Irradiated volumes, heated by incoming beams, release pressure waves. This phenomenon is consistent with the thermal model for the transformation of the energy of moving particles into acoustic energy. When proton pulses are passing through/stopping in a medium two macroscopic waves are generated: a cylindrical α-wave, before the Bragg peak, and a spherical γ-wave, at the Bragg peak. By measuring the γ-wave arrival time τ_γ, the distance l between the Bragg peak and the detector is given by the relation: $l = c \cdot \tau_\gamma$ (c = speed of sound). Waveform have been in-silico analysed in water ([116], [117], [118]) as well as in prostate and liver cancer patients [108].

PET

Dating back to early 90's [119], Positron Emission Tomography (PET) imaging was the first method to be investigated for in-vivo range verification. When protons undergo nuclear reactions in tissues β^+ emitting isotopes, such as ^{11}C ($\tau_{1/2}$ = ~20 min) and ^{15}O ($\tau_{1/2}$ = ~2 min) are released. The positron annihilations with tissue electrons result in the emission of coincident 511 keV γ-rays, detectable with PET scanners. PET range verification is achievable with no additional dose to patients. Also, differently from the use of PET in radiology, radiotracers are not needed, as images are acquired using solely the fragmentation of target nuclei. The PET method is highly dependable on tissues elemental composition. A direct relation linking PET activity to dose distribution is unattainable and a comparison of the measured activity with a modelled activity distribution is required. This is due to several reasons. First, PET activity depends on the tissues composition; different tissues receiving the same dose show different activity patterns. Second, the cross sections for the production of β^+ emitting isotopes are such that the activity pattern drops before the end-of-range. The distal fall-off of the PET signal is therefore shifted upstream to the dose fall-off [120]. Third, due to the different isotopic half-lives, the activity depends on PET imaging time. In perfused tissues, also, activity varies over time due to the wash-out effects [121].
PET imaging can be performed *off-line*, *on-line*, or *in-room* [122].

- ***Off-line PET*** → PET scan some time after the treatment.

  Off-line PET method [110] employs full-ring PET scanners, which offer high detection efficiency and can be matched with CT scanners. PET-CT systems allow an accurate co-registration between treatment and imaging target location and a compensation for patient movements caused by transportation/repositioning. The activity derives from isotopes whose half-life is similar or longer than the patient transportation and set-up time, thus only the activity of ^{11}C is detectable [123]. However, the total yield of ^{11}C is small, as target elements leading its production are scarce. Count-rate is further reduced from the biological wash-out.

- ***On-line PET*** → PET scan during beam delivery.

  When PET range verification is performed *on-line* [124] all isotopes with short half-lives are present and the maximum signal intensity is collectable. Patient repositioning on the PET couch is not needed and wash-out processes are negligible. The main obstacle is the integration of PET scanners in the treatment room. Serious geometric

constraints are implicated in this requirement, mainly because of the need for an opening in the beam portal. Typically a dual-head PET scanner is chosen; this configuration is associated with a reduced spatial resolution and angular coverage [125]. *On-line* systems are further affected by background radiation from dose delivery [126].

- ***In-room PET*** $\rightarrow$ PET scan just after beam delivery.

  In-room PET method [127] is the best compromise between data quality and geometrical efforts. Patients are scanned immediately after treatment, with a stand-alone PET scanner, using the same treatment couch and immobilisation devices. Signals from shorter lived isotopes, such as ^{15}O, are still collectable and wash-out is minimised. Delivery facilities and PET scanners must not interfere. Design studies have been performed on the retro-fitting of delivery facilities, and the use of partial PET ring scanners has been suggested [128]. If the PET scanner can not be installed in the treatment room, it can be mounted on wheels and moved in after the treatment.

The PET method was clinically implemented in several institutes in Japan [129] and the USA ([130], [110]). Still its benefits remain debatable. From a clinical prospective the method is well suited for intracranial/cervical spine patients and, in this cohort, patients with arteriovenous malformations and/or metal implants benefit the most [131]. For head and neck tumours the proton range can be monitored with a 1-2 mm accuracy in well-co-registered bony structures [130]. It not possible, however, to obtain millimetres accurate range verification for all tumour positions or for all tumour sites [110].

Range verification via PET imaging and via prompt gamma rays detection have been a long time in "competition". The clinical adaptation of the two methods was compared by Moteabbed and Paganetti [132], finding the second advantageous.

Chapter 2

Range verification via prompt-gamma detection

This Chapter is focused on range verification via PG detection. The Chapter is divided into three parts. In the first part (Section 2.1) the principal features in PG emission during PT are described. The second part (Section 2.2) is a literature review on PG detection systems. The third part (Section 2.3) is a brief overview on PG reconstruction algorithms.

2.1 Prompt gamma emission in proton therapy

2.1.1 Prompt gamma emission

During proton beam delivery, after an inelastic nuclear interaction between a proton of the beam and a nucleus of the target, the nucleus can be brought into an excited state. Swiftly, by the emission of a γ-ray, the nucleus returns to its ground state (*g.s.*). Being almost instantaneous, within 10^{-9} s [49], such de-exitation is named *prompt gamma* (PG) [133].

2.1.2 Experimental cross sections for prompt gamma emission

PG spectrum is characterised by several discrete lines. The energy of PG rays is in the range 1-10 MeV, with the major decay channels starting above 2 MeV [136]. Typically, just the emission lines from the most abundant isotopes in human tissues, namely carbon ^{12}C, oxygen ^{16}O, and nitrogen ^{14}N, are considered. The most comprehensive literature search, regarding PG rays cross sections after proton irradiation, was presented by Verburg *et al* [137]. It reviewed several experimental studies, which are listed in Tables 9.3, 8.1, and 2.4 for ^{16}C, ^{12}C, and ^{14}N, respectively. All studies had been performed

Study	**Proton energy (MeV)**
Narayanaswamy *et al* [52]	23., 44.6
Lang *et al* [51]	40, 65, 85
Dyer *et al* [50]	5, 23
Lesko *et al* [53]	9 - 50
Kiener *et al* [56]	9 - 19
Benhabiles-Mezhoud *et al* [134]	7 - 26
Belhout *et al* [135]	20, 22.5, 25

Table 2.1: Experimental studies on cross sections for PG rays emission

for γ-spectroscopy in astronomy. In Table 2.1 each study is associated with the energy of the proton beam set in the experiment. Energies up to 85 MeV are reported, this is also the range of interest for PT range verification.

Discrete prompt gamma lines of ^{12}C

Target	Emitter	γ Energy (MeV)	Transition	Study
^{12}C	^{12}C	4.44	2^+ *4.44* $\rightarrow 0^+$ *g.s.*	[50], [51], [53], [135]
	^{11}C	2.00	$\frac{1}{2}^-$ *2.00* $\rightarrow \frac{3}{2}^-$ *g.s.*	[51]

Table 2.2: Discrete PG lines of ^{12}C

The ^{12}C de-excitation scheme is reported in Ajenberg [138]. For the typical energy of clinical proton beams the ^{12}C-induced PG rays are dominated by the 4.44 MeV de-excitation. Such de-excitation is due to the ^{12}C(p, p')^{12}C$\gamma_{4.439}$ reaction, as a major contribution, and to the ^{12}C(p, 2·p)^{11}B $\gamma_{4.445}$ reaction, as a minor contribution. Because of the Doppler broadening kinematic the lines from the two reactions can not be individually resolved. Above the 4.44 MeV state the excited ^{12}C levels mostly decay via α-emission.

Discrete prompt gamma lines of ^{16}O

Target	Emitter	γ Energy (MeV)	Transition	Study
^{16}O	^{16}O	6.13	3^- *6.13* $\rightarrow 0^+$ *g.s.*	[52], [50], [51], [53], [135]
		6.92	2^+ *6.92* $\rightarrow 0^+$ *g.s.*	[56]
		7.12	1^- *7.12* $\rightarrow 0^+$ *g.s.*	[56]
		2.74	2^- *8.87* $\rightarrow 3^-$ *6.13*	[51], [56]
	^{12}C	4.44	2^+ *4.44* $\rightarrow 0^+$ *g.s.*	[50], [51], [53], [135]
	^{15}N	5.27	$\frac{5}{2}^+$ *5.27* $\rightarrow \frac{1}{2}^-$ *g.s.*	[51], [53]

Table 2.3: Discrete PG lines of ^{16}O

The ^{16}O de-excitation scheme is reported in Tilley *et al* [139]. The most important ^{16}O-induced PG rays are: 4.44 MeV (from ^{16}O(p, αp')^{12}C) and 6.13 MeV (from ^{16}O(p, p')^{16}O).

Discrete prompt gamma lines of ^{14}N

Target	Emitter	γ Energy (MeV)	Transition	Study
^{14}N	^{14}N	1.64	1^+ *3.95* $\rightarrow 0^+$ *2.31*	[50], [53], [134]
		2.31	0^+ *2.31* $\rightarrow 1^+$ *g.s.*	[50], [51], [53], [135]
		5.11	2^- *5.11* $\rightarrow 1^+$ *g.s.*	[134]
		0.73	3^- *5.83* $\rightarrow 2^-$ *5.11*	[134]
		3.38	1^- *5.69* $\rightarrow 0^+$ *2.31*	[134]
		2.79	2^- *5.10* $\rightarrow 0^+$ *5.11*	[134]
		3.89	1^+ *6.20* $\rightarrow 0^+$ *2.31*	[134]

Table 2.4: Discrete PG lines of ^{14}N

Compared to $^{12}C/^{16}O$, the amount of ^{14}N atoms in tissues is reduced, thus its relevance for range verification is limited. ^{14}N-induced PG rays play a key role in astrophysics and experimental data have been acquired for many lines. ^{14}N de-excitation scheme is reported in Ajenberg [140], the most important ^{14}N-induced PG rays are: 2.13, 1.64, and 5.11 MeV.

2.1.3 Prompt gamma emission and proton range correlation

PG emissions profiles typically exhibit a peak ∼2-3 mm upstream to the Bragg peak, with the exact shift magnitude dependent upon the specific PG line under consideration. This is consistent with the nuclear reaction cross sections leading to the emission of PG rays (Section 1.2.3): approaching the Bragg peak, the beam decreases its energy, nuclear reaction cross sections drop and less-to-no PG rays are released.

Figure 2.1 shows the profiles of the Bragg curve and of the ^{16}O-induced PG emissions for a 180 MeV proton beam impinging a water phantom. The two strongest ^{16}O-induced PG emissions - the 6.13 MeV line, from the $^{16}O(p, p')^{16}O$ reaction, and the 4.44 MeV line, from the $^{16}O(p, \alpha p')^{12}C$ reaction - are shown. Profiles are acquired using Geant4 10.04 Monte Carlo simulations with 10^8 primary protons. A 2x2x15 cm^3 water phantom was modelled and irradiated along its central axis. The PG profiles correlate well with the Bragg curve, in agreement with the experimental measurements by Verburg *et al* [141].

Figure 2.2a shows the profile of a SOBP proton beam with 180 MeV range and 37 MeV modulation in water. For each pencil beam composing the SOBP the ^{16}O-induced PG profiles are shown in Figures 2.2b (4.44 MeV) and 2.2c (6.13 MeV). In the main plots all profiles are weighted as to compose the SOBP while, in the inserts, profiles are shown with the same intensity. Simulations were performed with 10^7 primary protons per beam.

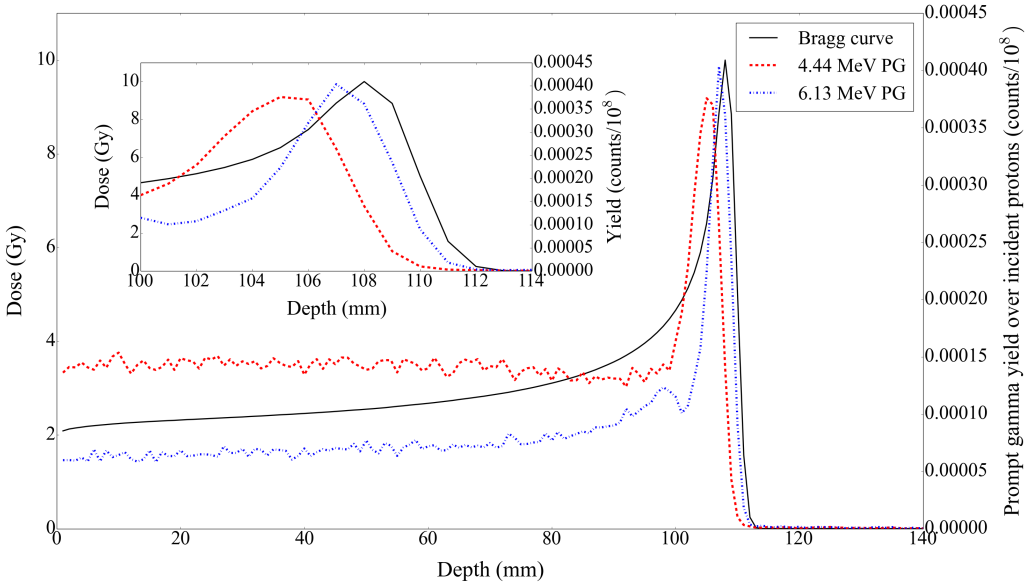

Figure 2.1: Profiles of the Bragg curve (*back* curve), the 4.44 MeV (*red* dashed curve), and the 6.13 MeV (*blue* dot-dashed curve) PG emissions

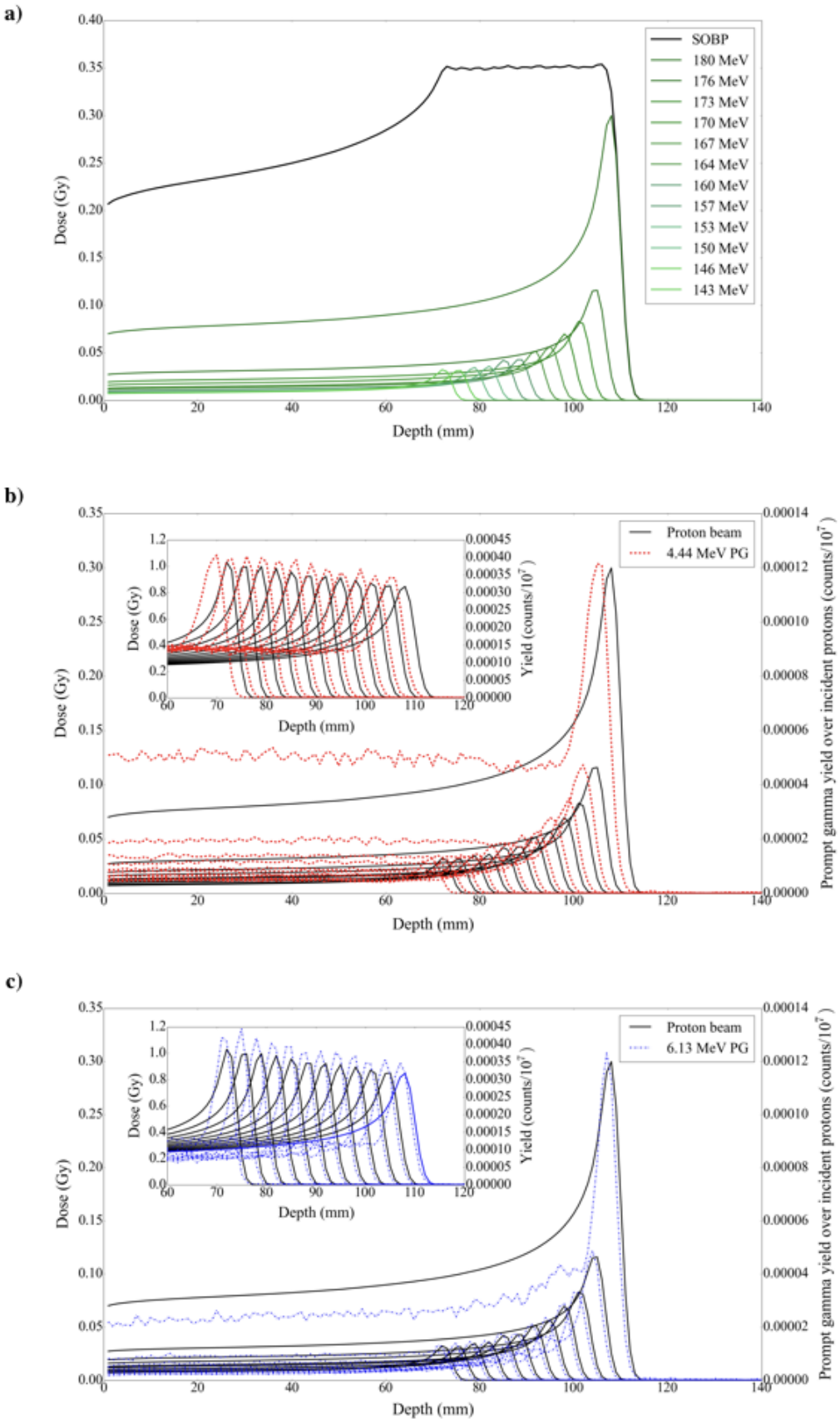

Figure 2.2: Simulation of a SOBP proton beam with 180 MeV range and 37 MeV modulation in water. a) Profiles of the SOBP proton beam (*black* curve) and of the twelve pencil beams composing the SOBP (*green* curves), from 143 to 180 MeV. b) Profiles of the 4.44 MeV (*red* dashed curve) and the c) 6.13 MeV (*blue* dot-dashed curve) PG emissions for each pencil beam composing the SOBP. Main graphs: profiles weighted as to compose the SOBP. Inserts: profiles at the same intensity.

2.1.4 Prompt gamma production yield

One of the most advantageous features of PG imaging is that a sufficiently high production-rate of PG rays is reached with just the application of a therapeutical dose of 2 Gy min^{-1} [132]. The total PG yield per proton is about 10% in water. In other words, if an instantaneous clinical beam current of 2 nA [142], which corresponds to $1.2 \cdot 10^{10}$ protons-per-second, is assumed, $1.2 \cdot 10^{9}$ PG-per-second are generated.

Polf *et al* [143] investigated the possibility of determining the concentration of oxygen, within irradiated tissues, by measuring the amount of emitted 6.13 MeV PG rays. PG yields were evaluated as a function of $^{12}C/^{16}O$ concentration. It was found that the 6.13 MeV PG emission is linearly proportional to the amount of oxygen in the irradiated samples. Further, with a 48 MeV proton beam, it was estimated that $1.64 \cdot 10^{7}$ 6.13 MeV PG rays are released per gram of ^{16}O, per Gy of dose delivered.

Prompt gamma yield and tissues chemical composition

Two simulations are reported, aimed at assessing the PG yield from irradiated targets with heterogeneous chemical composition. In the first simulation, as shown in Figure 2.3a, two 2x2x1 cm^3 slabs of bone ("Bone Compact ICRU", density of 1.92 g/cm^3) and lung material ("Lung ICRP", density changed to 0.26 g/cm^3 to resemble a lung at end-inhalation) were staked together and inserted into a water phantom. The phantom was irradiated along the central axis by a 180 MeV proton beam ($4 \cdot 10^{7}$ primary protons). The slabs are perpendicular to the beam direction, upstream of the Bragg peak. The distance between the centre of the slabs and the front face of the phantom is 4.5 and 5.5 cm for the bone and the lung slab, respectively. Figure 2.3b shows the yield of the 4.44 and 6.13 MeV PG rays emitted along the depth of the phantom. The PG yield was found to be dependent on the material composition and on the density of the medium crossed by the beam.

In the second simulation, as shown in Figure 2.4a, one 1x2x15 cm^3 slab of bone material was inserted into a water phantom parallel to the beam direction. A 180 MeV proton beam ($4 \cdot 10^{7}$ primary protons) impinged the phantom along its central axis, at the water-bone interface. Figure 2.4b shows the yield of the 4.44 and 6.13 MeV PG rays emitted along the depth of the phantom together with the Bragg curve. Figures 2.4c and 2.4d show dose and PG emission (4.44 and 6.13 MeV together) in the ZX plane. As depicted in Figures 2.4c and 2.4d the beam diverges in the two materials, thus two peaks appear in Figure 2.4b, at the depth of 63 and 108 mm, in bone and water, respectively.

Besides the use of PG imaging for range verification, the possibility of determining, through the PG spectrum, the elemental composition of irradiated tissues, is also under study ([144], [145]). By monitoring the changes in elemental composition of tumour and healthy tissues, the response of these tissues to PT could be followed over the full treatment. Changes in tumour composition could be used to determine oxygen concentration, thus tracking variations in the oxygenation levels and in the blood flow (tumour hypoxia). Changes in the composition of healthy tissues, on the other hand, could be linked to treatment side effects.

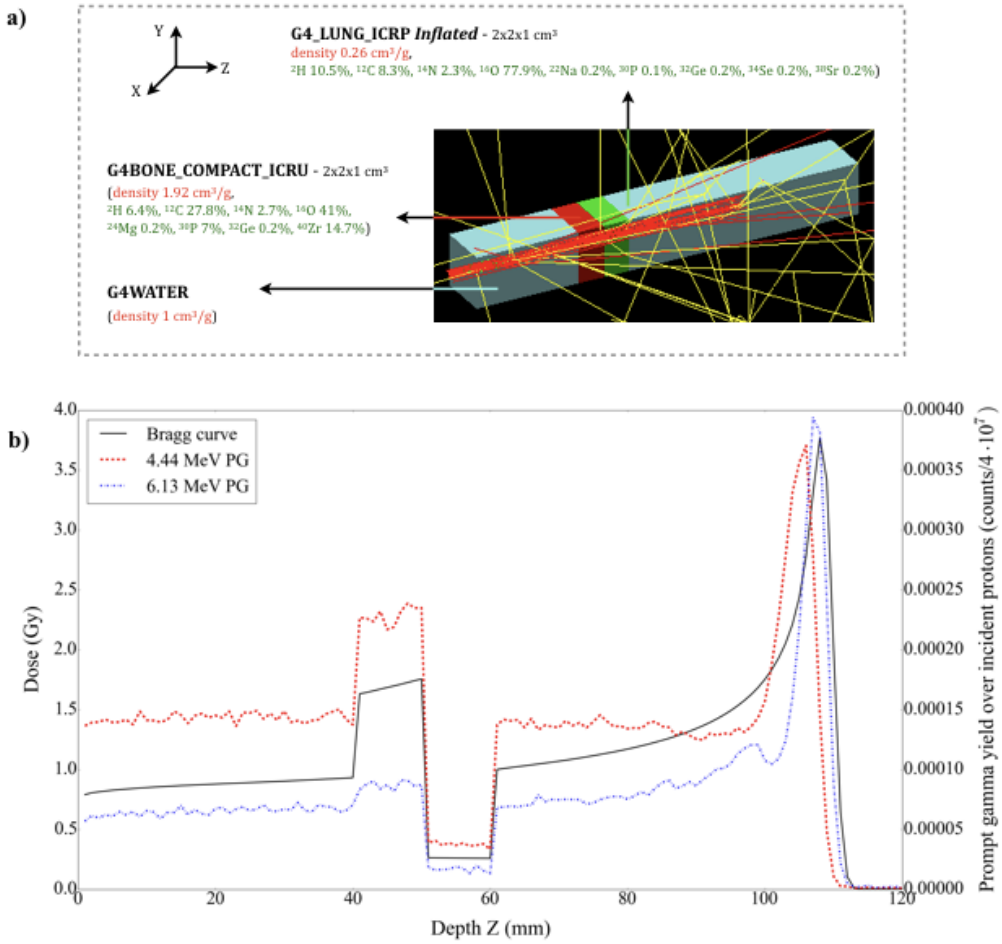

Figure 2.3: Investigation on PG yield dependence from chemical composition - inhomogeneities orthogonal to the beam direction. a) Geometry of the simulation: two slabs of bone and lung material are staked together and inserted into a water phantom, upstream of the Bragg peak. The slabs are perpendicular to the beam direction. b) Profiles of the Bragg curve (*back* curve), the 4.44 MeV (*red* dashed curve), and the 6.13 MeV (*blue* dot-dashed curve) PG emissions.

Prompt gamma yield and beam energy

To treat tumours deep inside the body high energy beams are needed. A longer transit path, however, affects the beam quality. First, the energy distribution at the target is broadened by energy straggling. PG cross sections strongly depend on proton energy, thus the slope of PG profile is related to the width of the beam energy distribution. Second, due to the elimination of protons from the beam by nuclear reactions, the beam intensity at the target is reduced. For all these reasons PG yields increase at low beam energies. The increased energy straggling, in particular, leads to a flattening of the PG profiles in the region of maximum emission, i.e. proximal to the Bragg peak. This effects varies accordingly to the PG line considered and is most pronounced for the ^{12}C-induced PG rays.

Figure 2.5a shows the longitudinal profile of the 6.13 MeV PG emission, from ^{16}O(p, p')^{16}O reaction. PG rays are emitted from a water phantom irradiated, along the central axis, by a proton beam with 80, 100, and 180 MeV energy. Figure 2.5b shows the longitudinal profile of the 4.44 MeV PG emission, from the ^{12}C(p, p')^{12}C and ^{16}O(p, αp')^{12}C reactions. PG are emitted from a bone phantom irradiated by a proton beam with energy as in the

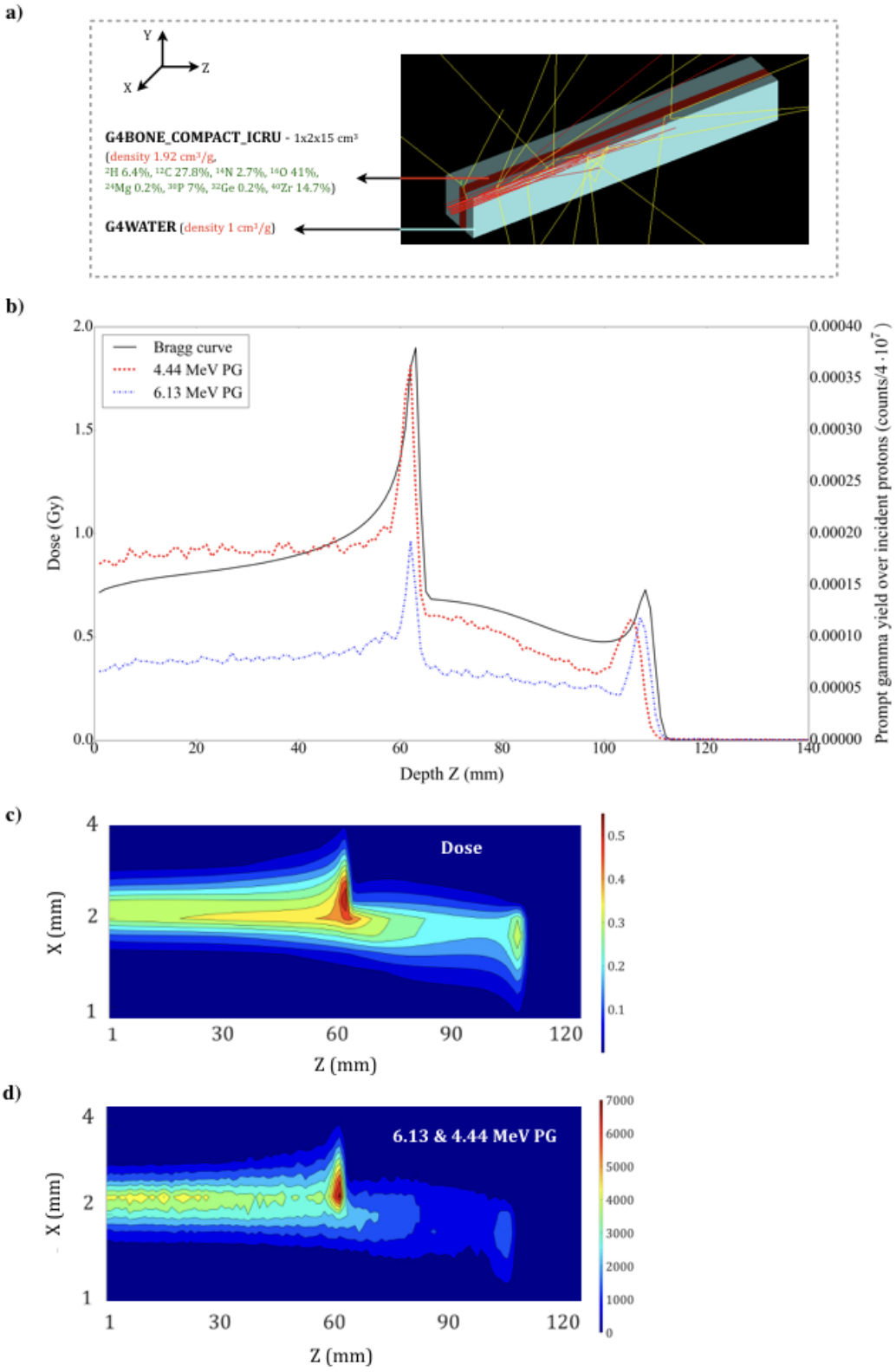

Figure 2.4: Investigation on PG yield dependence from chemical composition - inhomogeneities parallel to the beam direction. a) Geometry of the simulation: one slab of bone inserted into a water phantom parallel to the beam direction. b) Profiles of the Bragg curve (*black* curve), the 4.44 MeV (*red* dashed curve), and the 6.13 MeV (*blue* dot-dashed curve) PG emissions. In addition c) the dose and d) the PG emission (4.44 and 6.13 MeV together) are reported in the ZX plane.

previous case. Distributions, calculated using Geant4 with 10^7 primary protons, were shifted in the main plots to visually display the PG profiles in the Bragg peak region. Results are consistent with the experimental measurements from Keteller *et al* [146].

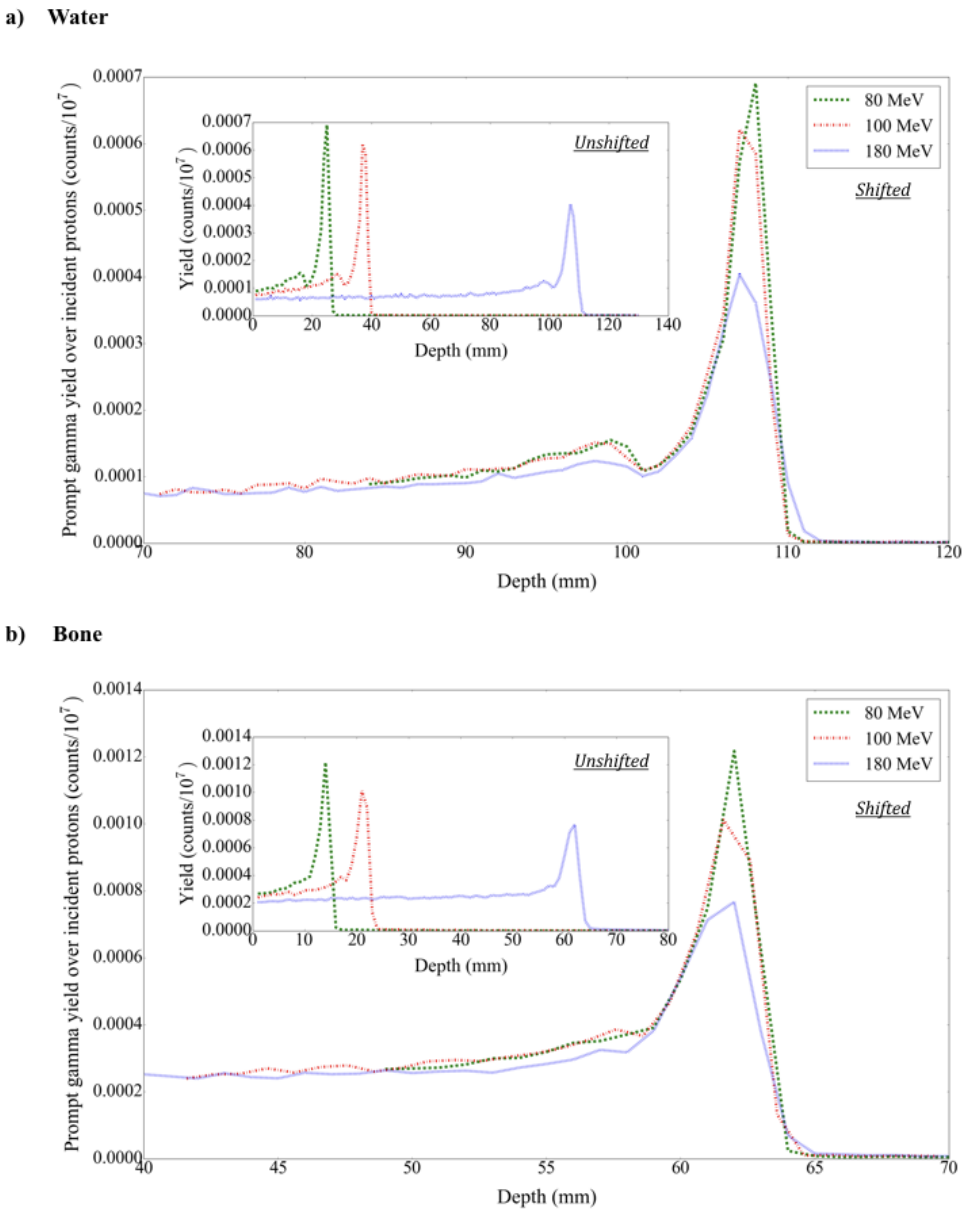

Figure 2.5: Investigation on PG yield dependence from beam energy. Recorded PG emissions are: a) 6.13 MeV (^{16}O(p, p')^{16}O) from a water phantom. b) 4.44 MeV (^{12}C(p, p')^{12}C and ^{16}O(p, αp')^{12}C) from a bone phantom. In both cases the phantom was irradiated, along the central axis, by a proton beam with 80 (*green* dashed line), 100 (*red* dot-dashed line), and 180 MeV (*blue* dotted line) energy.

2.1.5 Angular distribution of detectable prompt gamma

The angular dependence of the total PG detection-rate and of the detection-rate of ^{16}O-induced PG rays was first in-silico investigated by Lee *et al* [147], as a function of proton energy. A water target was shot by a 50 to 200 MeV proton beam. PG emissions were recorded by a detector, whose position was shifted for several polar angles. For both the total PG emission and the ^{16}O-induced PG emission, the detection-rate per incident proton significantly increases as the polar angle decreases, i.e. when the detector is moved backward, closer to the nozzle. This trend increases with beam energy. Indeed, when the detector is in the proximal region, it subtends a larger solid angle covering PG rays produced along the beam-path. Back-scatter cross sections are also larger at higher energies. On the other hand, the ratio between the ^{16}O-induced PG emission and the total PG emission increases linearly

with the polar angle, i.e. when the detector is moved forward, away from the nozzle. This is due to the cross-section for the ^{16}O-induced PG production. The cross-section increases at low proton energies, i.e. when protons are further away from the target entrance.

PG rays detection at backward polar angles was also recommended by Keteller *et al* [146] and Zarifi *et al* [148]. Keteller *et al* [146] observed that the differential cross section of the ^{12}C(p, p')^{12}C reaction increases when the detector is closer to the nozzle. The other process feeding the $^{12}C_{4.44\rightarrow g.s.}$ line (reaction ^{12}C(p, 2·p)^{11}B) is believed to have an isotropic angular distribution. Zarifi *et al* [148] shows that, as the beam energy increases, the position maximising the number of detectable PG rays becomes increasingly backward. Such a preferential position also considerably variates with the PG energy window.

Lee *et al* [147] investigated the total PG detection-rate and the detection-rate of ^{16}O-induced PG emission, as a function of beam energy, for several azimuthal angles. No dependence was found, which implies that, in an homogeneous phantom, the PG detection rate is linearly dependent on the number of detectors around the beam central axis. Therefore, if N detectors are employed around the beam line, it is reasonable to predict a detection rate increase of a factor of N. In patients, however, internal anatomy variations, owing to different attenuations, may impact on the azimuthal detection-rate distribution.

2.1.6 Temporal characteristics of prompt gamma emission

When penetrating tissues with relativistic energies, protons travel fast. Still, from entering the tissues until reaching the target, a measurable time has elapsed. The transit time of protons with a 5-20 cm range, is ∼1-2 ns [149]. The PG Time-Of-Flight spectrum (TOF) is the distribution given by the difference between the time of the proton bunch crossing a reference plane and the arrival time of the PG rays on a detection system. Proton transit time is range dependent. Protons with higher energy travel to a deeper target in a longer time. This implies an extended time-window for PG emission and an average delayed PG detection time. Zarifi *et al* [150] evaluated the dependence of PG TOF data - peak mean, width and integral - as a function of beam energy. As the beam energy increases, TOF peak mean and width raise slightly, while TOF integral exhibits a greater linear increase.

2.2 Prompt gamma detection systems

Since the feasibility of PG detection for in-vivo range verification has been demonstrated [136], the development of a PG detection system, usable in the clinical environment, has progressed at a slow rate. This is mainly due to the energies of the PG rays, too high to be efficiently measured with the standard devices employed in diagnostic imaging. As shown in Figure 2.6, for the realisation of clinical prototypes different approaches have been proposed. Following the classification given by Krimmer *et al* [151], systems can be divided into *imaging* and *non-imaging* systems. Imaging systems require a collimation of some kind, whether the collimation can be mechanical or electronic. Non-imaging systems are integrated yield counting devices, they use additional information such as PG energy or

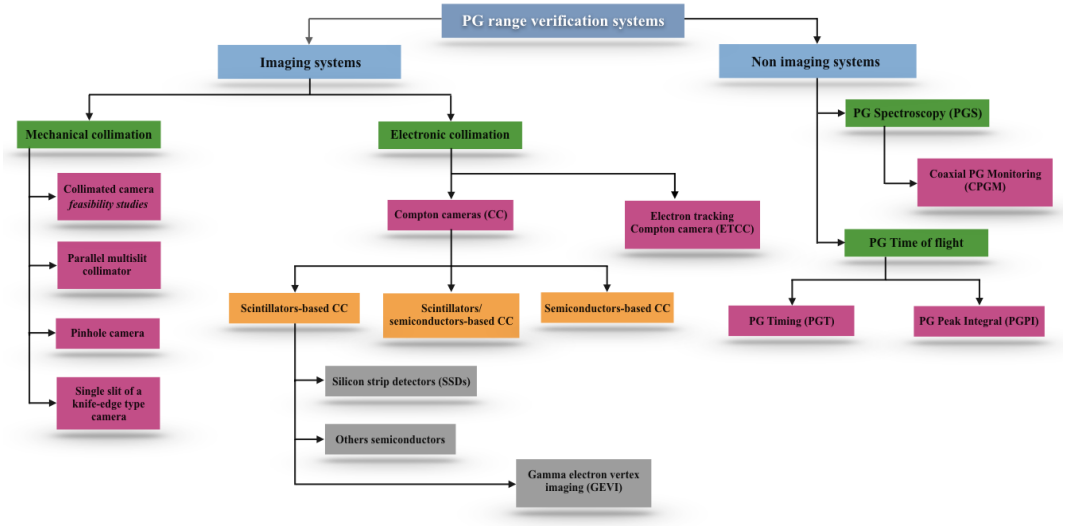

Figure 2.6: PG detection systems for in-vivo proton beam range verification

timing. PG non-imaging systems are the most recent and aimed at minimising the costs and the footprint in the treatment room. The aim of this Section is to review the prototypes worldwide developed as of May 2020. The studies reported here have been further listed in Tables. All Tables are in Appendix 1.

2.2.1 Imaging systems: mechanical collimation

Single detector (feasibility studies)

The first feasibility study has been performed by Min *et al* [136]. Range is detected by counting the PG rays emitted 90° to the beam direction. By comparing the PG and dose profiles in water, at 100, 150, and 200 MeV, a good correlation, within 1-2 mm at 100 MeV, was observed. A 1-2 mm σ has also been observed by Kim *et al* [152] and Min *et al* [153] in retrieving the distal fall-off of a 38 and 70 MeV proton beam, respectively.

The major obstacle of PG imaging is background noise. High-energy neutrons are produced along the beam line and in phantoms, with an increasing yield at higher beam energies. Neutrons are mostly forward oriented, however, if not shielded, they still compete with the PG signal at 90°. The camera design (Figure 2.7) consists of three shielding layers: paraffin to moderate neutrons, borated carbon to capture them, and lead to absorb the γ-rays from (n,γ) reactions. A scintillation detector is typically chosen.

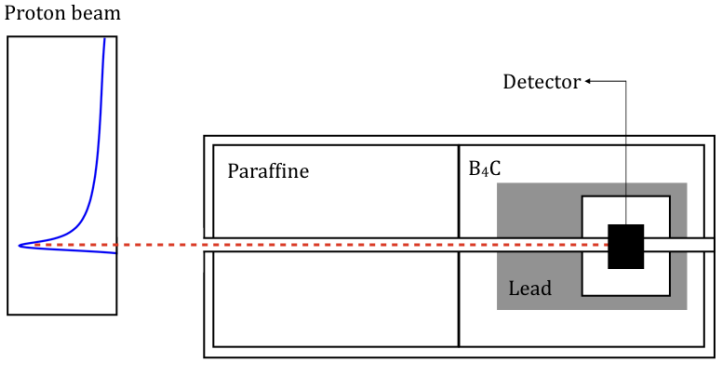

Figure 2.7: Design of a single detector collimated camera for feasibility studies

MultiSlit camera (MS)

Prototypes based on parallel MultiSlit (MS) collimators comprise multiple detectors or position-sensitive detectors behind the collimator. Using a small collimated detector, performance tests, with a 160 MeV beam on a PMMA target, were initially performed by Roellinghoff *et al* [154] and Pinto *et al* [155] (Figure 2.8). PG rays were detected by a $LaBr_3$ and a LYSO scintillator, respectively.

Pinto *et al* [155] further optimised the geometry of a MS camera with a single BGO block (Figure 2.9). Cambraia-Lopez *et al* [156] presented a similar prototype, with a flat-panel detector. A full-body computational phantom, with/without physiologic or setup changes, was employed. Head and pelvis irradiations, at 130 and 200 MeV, respectively, were modelled (10^8 protons) and range shifts as small as 2 mm were reconstructed.

The retrieval precision of the PG distal fall-off position depends on the contrast-to-noise ratio. According to Roellinghoff *et al* [154] such precision can be improved by TOF discrimination, i.e. separating the PG signal from the neutron-induced γ background. Precision is also inversely proportional to the square root of the number of protons delivered per distal spot (typically 10^8).

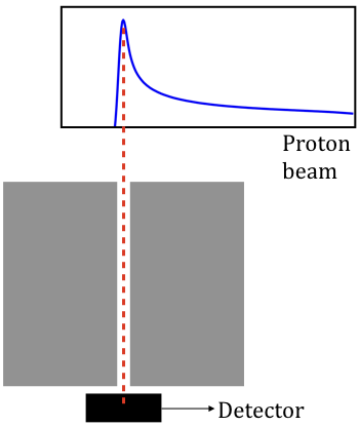

Figure 2.8: Experimental set-up for performance tests: single collimated detector

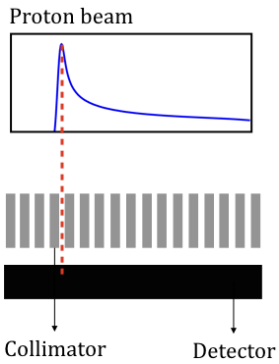

Figure 2.9: Multislit camera with single detector

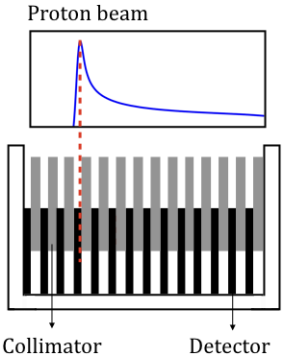

Figure 2.10: Multislit camera with detection array

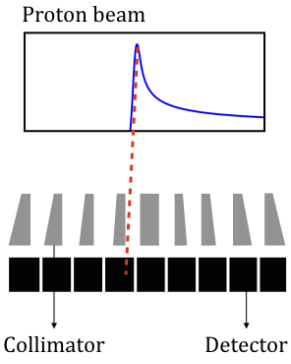

Figure 2.11: Multislit camera, focused collimators

Min *et al* [157] in-silico, optimised an array-type MS camera composed of multiple CsI detectors (Figure 2.10). Each detector counts the PG rays emitted 90° to the beam direction, through its collimation slit. A simplified prototype, with a single detector moving from one location to the next, was built and applied to a 80, 150, and 220 MeV beam on a water phantom. Lee *et al* [158] proposed a system comprised of a multi-hole collimator and a 2D array of CsI detectors (Figure 2.12). The response of the system to a 80, 150, and 200 MeV beam on a water phantom was simulated. The PG profiles, obtained by Min *et al* [157] and Lee *et al* [158], correlates well, within few millimetres, with the relative Bragg curves. It was noticed, however, that, at the highest beam energy of 200 [158] and 220 [157] MeV, the PG profiles only gradually decrease after the distal fall-off. This is due to the increase, with

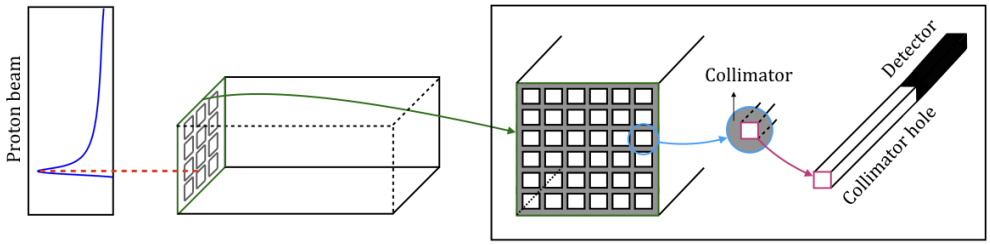

Figure 2.12: Multislit camera with a multi-hole collimator and a 2D detection array

the beam energy, of both γ background and beam lateral dispersion at the end of the range.

Different flavours of the camera proposed by Min *et al* [157] were designed by Park *et al* [159] and Zhang *et al* [160]. Park *et al* [159] built a system composed of two blocks placed in a staggered arrangement, where each block corresponds to the camera from Min *et al* [157]. The system was tested using a 95 to 186 MeV beam impinging a solid plate target. Range shifts were detected within ∼2-3 mm of error for spots of $3.8 \cdot 10^8$ protons. Zhang *et al* [160] presented a prototype with a BGO detection array and a MS focused collimator (Figure 2.11). Experiments were conducted under ^{22}N, ^{88}Y, and ^{232}Th irradiation.

Pinhole camera and Knife-Edge (KE) slit camera

The concept of a pinhole camera has been adapted for PG imaging by Kim *et al* [161] (Figure 2.13). The pinhole aperture is located to view the endpoint of the proton range and a lead shielding enclosure prevents stray γ and neutrons to reach the BGO detector.

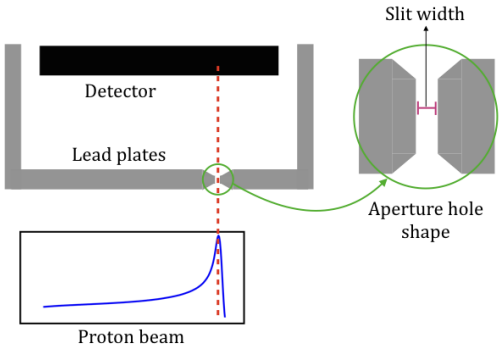

Figure 2.13: Pinhole camera

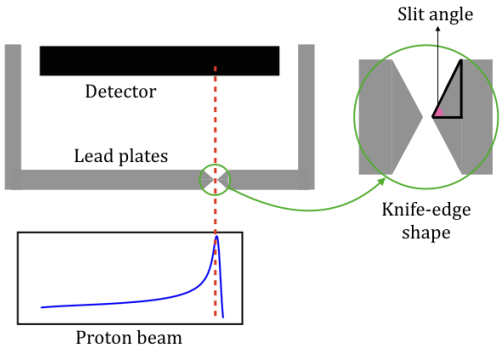

Figure 2.14: Knife-edge slit camera

The pinhole aperture was lately changed to a single slit of the Knife-Edge (KE) type (Figure 2.14). KE slits make an angle with respect to the slit plane. Therefore, compared to the parallel edge slit of a MS camera, the FOV is enlarged.

Bom *et al* [162] in-silico, modelled a KE camera with a CsI detector. For a 50 MeV beam on a head phantom, the PG profile was reconstructed with a 1σ accuracy better than 1 mm. Smeets *et al* [163] built the first prototype of KE camera with a CsI detector. By delivering, on a PMMA phantom, a 100 and 160 MeV beam (dose of 15 and 25 cGy, respectively), a 1-2 mm σ in range estimation was retrieved. A second prototype, compatible with the counts-rates occurring at clinical facilities, was later built by Perali *et al* [164]. PG emissions were acquired with a LYSO detector. Range shifts were reconstructed with a precision of

2σ for $0.5 \cdot 10^8$, $1.4 \cdot 10^8$, and $3.4 \cdot 10^8$ protons at 100, 160, and 230 MeV, respectively.

The camera developed by Smeets *et al* [163] and Perali *et al* [164] was further evaluated by Cambraia-Lopez *et al* [165] and Preignitz *et al* ([166], [167]). In Cambraia-Lopez *et al* a PMMA phantom was irradiated by a 160 MeV beam ($\sim 6.5 \cdot 10^9$ protons). PG rays were measured using either a BGO or LYSO detector. With the LYSO detector in place TOF discrimination was employed to enhance the Signal-to-Background ratio (S/B). With the LYSO, and TOF correction in the 3-7 MeV energy window, the S/B was 1.6. Conversely, with the LYSO, without TOF correction, and with the BGO, the S/B was 3 and 2 times lower, respectively. It was further observed that, with TOF discrimination, for $\sim 6.5 \cdot 10^8$ protons, even a 1 mm range shift translated into a clear variation of the PG profile.

Preignitz *et al* ([166], [167]) investigated the prototype performance with respect to inhomogeneous targets. In a first study [166] targets inhomogeneous along the beam direction were irradiated. When the targets were homogeneous in the field of view of the camera, a range precision of less the 2 mm was estimated. PG imaging, however, failed when the beam stopped near large density gradients, such as in proximity of air cavities or lung tissue. For the reliable detection of a cavity filling, a minimum beam penetration-depth of 7 mm beyond the cavity was required. In a second study [167] laterally inhomogeneous targets were considered. Such targets lead to a range mixing effect when crossed by beams. It was proved that range shifts due to range mixing effects can be revealed by deviations in the PG profiles. Shape and slope of such profiles are also meaningful parameters.

Although the KE slit camera was developed for scanning PT, Preignitz *et al* [168] evaluated its applicability in conjunction with passive scattering delivery, where the neutron-induced γ contamination is rather high. Range shifts of 2-5 mm in magnitude were retrieved. The work by Preignitz *et al* lead Riechter *et al* [169] to perform the first on-patient test of the camera for passive scattering PT. The inter-fraction range variation of the measured PG profiles was $\pm$ 2 mm, which is consistent with the dosimetric variations reported by the control CT. Soon after Xie *et al* [170] reported the first on-patient application of the camera for active scanning PT. In the course of six fractions, the absolute amplitude shifts, aggregated over all spots in 9 energy layers, were in the range 1-2 mm. To evaluate the overall camera capability under clinical condition Nenoff *et al* [171] tested the camera in well defined error scenarios. Different realistic treatment deliveries were employed, shooting on a head phantom. A high shift-detection sensitivity was proved. To record the PG rays Preignitz *et al*, Xie *et al*, and Nenoff *et al* all considered a LYSO detector.

2.2.2 Imaging systems: electronic collimation (Compton camera)

Compton cameras (CCs) are multi-stage devices that determine energy/direction of a PG ray as it Compton-scatters in its stages. To provide interaction positions each stage has a 2D/3D spatial segmentation. The original CC design consists of two detectors (Figure 2.15a): a scatterer and an absorber. γ-rays Compton-scatter in the first detector and are fully absorbed in the second. The three-stage CC design (Figure 2.15b) consists of three detectors. γ-rays Compton-scatter in the first two but just an interaction of any kind is requested in the third. Via the application of the Compton kinematics the probable PG

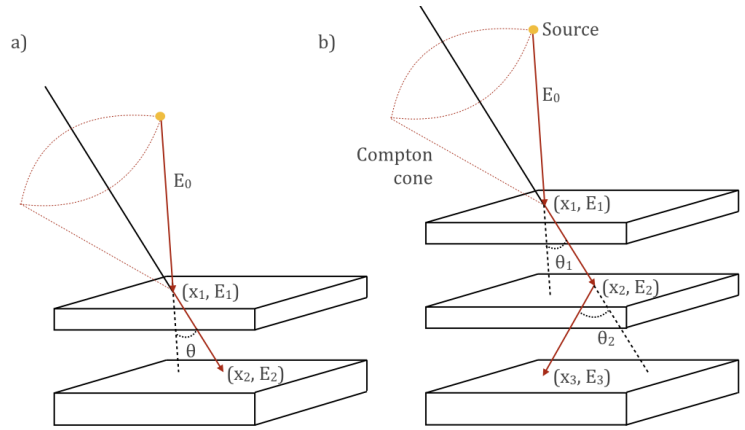

Figure 2.15: a) Two and b) three-stage Compton cameras

rays emission-position is restricted to the surface of a cone, named the *Compton-cone*. From the superposition of multiple Compton-cones the PG rays generation point is obtained.

Three-stage CCs do not require a full absorption, this is advantageous due to the high energy of PG rays. Compared to two-stage CCs, however, the efficiency of three-stage CCs is at least one order of magnitude inferior [172]. With respect to mechanical-collimated systems, CCs offer a higher detection efficiency. CCs also adapt well to PG ray detection, as Compton scattering is the dominant process in the PG ray energy range.

In the following sections different CCs prototypes are classified according to the chosen detectors and their combination.

Compton camera: scintillators

After having characterised a continuous $LaBr_3$ crystal [173], Llosá *et al* [174] built and tested the first two-stage scintillation-based CC. The system, with $LaBr_3$ as scatterer and LYSO as absorber, was then employed by Solevi *et al* [175] to reconstruct the range of a 150 MeV beam on a PMMA phantom. Range shifts were resolved within 10 mm. Secondary neutrons and scattered γ-rays can reach the CC and produce false events. Additionally, with the high intensity beams employed at clinical facilities, PG rays may accumulate in the CC, leading to an increase of random coincidences.

A prototype composed of six $LaBr_3$ detectors was simulated by Gillam *et al* [176] and Ortega *et al* [177]. By irradiating a PMMA phantom with a 140, 160, and 180 MeV beam, Gillam *et al* [176] explored the introduction of a beam hodoscope to improve range reconstruction. Ortega *et al* [177] irradiated a PMMA target with a 100, 140, and 180 MeV beam ($4.12 \cdot 10^8$ protons) evaluating the impact of spurious data and random coincidences. A CC with three $LaBr_3$ crystals, able to work in the two/three-stage modality, was then built. Llosá *et al* [178] reconstructed the emitting-position of a ^{22}Na source with a spatial resolution of 7.8 mm FWHM. Solevi *et al* [175] in-silico reconstructed the image of several point-sources emitting at 2.74, 4.44, 6.13, 5.27, and 7.27 MeV. Spatial resolution ranges from 3 mm FWHM, at 2.74 MeV, to 4.9 mm FWHM, at 7.12 MeV. The performance of the CC presented in Llosá *et al* [178] was further evaluated by Muñoz *et al* ([179], [180], [181]). In Muñoz *et al* [179] ^{22}Na and ^{88}Y sources were reconstructed in both two- and three-stage modality. Source positions were retrieved with a FWHM under 4 and 3.5 mm for 1.275 and 1.836 keV, respectively. The three-stage CC was then tested by Muñoz *et al* [180] in a

4.44 MeV field. Images of the target were successfully reconstructed with the CC in three positions, centred and shifted 10 mm to the left and to the right, with respect to the target.

Compton image reconstruction typically needs a sensitivity correction. A sensitivity matrix quantifies the probability of detecting a PG ray at different positions with respect to the CC, and depends on both the CC geometrical configuration and the energy of the PG rays. Muñoz *et al* [181] presented an analytical model to estimate the sensitivity matrix. Using such a model, point-like sources and extended distribution activities were in-silico reconstructed. The emitting position of a ^{22}Na source was then experimentally retrieved.

$LaBr_3$ has an excellent energy resolution, fast timing response and high Compton probability, however is expensive. $CeBr_3$ comes at a slightly worse resolution but is much less expensive. Barrio *et al* [182] tested the CC from Llosá *et al* with $LaBr_3$, as scatterer, and $CeBr_3$, as absorber. Compared to the $LaBr_3$-only design, the performance of the $LaBr_3$-$CeBr_3$ prototype is slightly inferior. Still the $LaBr_3$-$CeBr_3$ prototype represents a reasonable alternative. Hueso-Gonzalez *et al* [183] built a two-layer BGO CC and tested it with a 70 to 170 MeV beam (10 MeV steps) impinging a PMMA target of variable thickness. Despite its modest energy resolution, results support the use of BGO. Jan *et al* [184] investigated a a two-layer LYSO CC. The system response to the delivery of a 120 MeV beam on a water target was modelled; range shifts were retrieved with an accuracy of less than 1.25 mm.

A compact CC with three Ce:GaGG stages has been developed by Kishimoto *et al* [185]. At the centre of the imaging region, for a 662 keV source, the spacial resolution was 6.81 $\pm$ 0.13 mm (X), 6.52 $\pm$ 0.07 mm (Y), and 6.71 $\pm$ 0.11 mm (Z) FWHM. Taya *et al* [186] further reported on this CC design. Water, $Ca(OH)_2$, and PMMA phantoms were irradiated with a 70 MeV beam. However, due to the low spacial resolution, the range fall-off position could not be clearly reconstructed from the PG profile.

Compton camera: Double Sided Strip Detectors (DSSDs) & scintillators

The combination of Double Sided Strip Detectors (DSSDs) as scatterers, and a scintillator, as absorber, is the subject of several investigations. Seo *et al* [187] studied the capability of a CC, composed of two DSSDs plus a NaI crystal, in resolving a ^{22}Na source. A spacial resolution of 9 and 4.8 mm FWHM was found at 511 and 1.275 keV, respectively. To ease the reconstruction problem a beam tagging device, hodoscope, has been considered. The hodoscope provides the proton trajectory-line. The intersection of the Compton-cone with the beam-line gives two points, one of which is the emission position (Figure 2.16). Roellinghoff *et al* [172] and Richard *et al* [188] consider a camera with a stack of DSSDs, as scatterers, a scintillator, as absorber, and a hodoscope. Only events with energy deposition

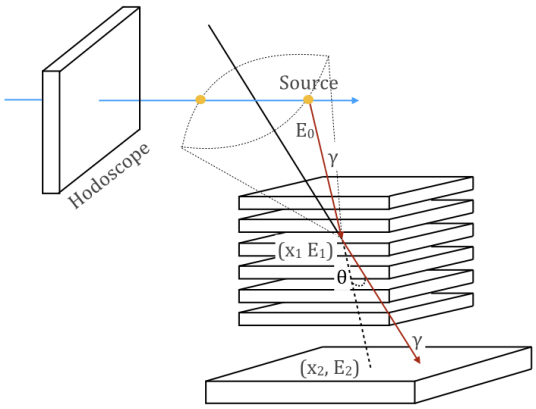

Figure 2.16: Compton camera with hodoscope

in a single DSSD are accepted. Using a LYSO block as absorber, Roellinghoff *et al* [172] simulated the camera response to a polychromatic source. A 8.3 mm FWHM spacial resolution was obtained. The same analysis was performed by Richard *et al* [188]. Four different materials, namely LYSO, NaI, $LaBr_3$ and BGO, were considered as absorber. Due to the high photoelectric cross section, LYSO and BGO were regarded as the most suitable.

A stack of DSSDs may also enable the tracking of Compton-electrons and electrons/positrons from pair production. This confines the original position of the PG-ray to an arc segment of the Compton-cone (Figure 2.17), *Compton-arc*, thus increasing the reconstruction efficiency. In the prototype from Frandes *et al* [189] the initial interaction (either Compton-scattering or pair production) occurs in one of the 36 DSSDs where electron/positrons are tracked. The absorber is a $LaBr_3$ detector. The CC was modelled with a 70, 100, and 140 MeV beam impinging a PMMA target. Although a correlation was found between the dose and the reconstructed PG profiles, to extract the Bragg peak with a millimetric precision further analysis was needed. In the CC from Thirolf *et al* the Compton-scattered electrons are tracked by a stack of six DSSDs coupled with a $LaBr_3$ detector. The CC response to a collimated ^{137}Cs source was modelled [190], and its components were individually characterised in lab [191]. According to Aldawood *et al* [192], for an overall CC spacial resolution of 1.5-2 mm, the position resolution of the absorber should be ∼3 mm.

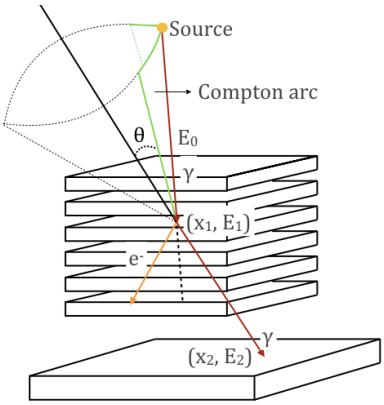

Figure 2.17: Compton camera with electron tracking

Compton camera: CZT & scintillators

A semiconductor-based CC, made of CZT or HPGe, has been in-silico studied by Kormoll *et al* [193], in terms of angular resolution and efficiency. It was found that CZT performs nearly as well as HPGe in the MeV energy range and, due to to the higher energy resolution, its efficiency is even better. This study set the ground for the construction of a prototype comprising two CZT scatterers and one LSO absorber. The prototype was tested by Hueso-Gonzalez *et al* [194] with Bremsstrahlung photons up to 12.5 MeV. A time resolution of 2.6 and 2 ns FWHM was found for CZT and LSO, respectively. The latter improves to 0.6 ns with pixel delay calibration and time walk correction. As potential absorber materials Hueso-Gonzalez *et al* [195] compared BGO and LSO in terms of energy, spacial, and time resolution. Bremsstrahlung photons, as well as a 100 and 150 MeV beam, impinging water and graphite targets, were employed in the study. The cost-factor was considered as well. Despite the overall LSO superiority, BGO offers higher photofraction, which compensates for the low light yield. Additionally BGO has no intrinsic activity and came with lower price. Golnik *et al* [196] tested a CC made of a CZT, as scatterer, and three side-by-side

arranged BGO layers, as absorbers, using a point-like 4.44 MeV source[1]. Source-position reconstruction was successful, even in case of lateral displacements. The efficiency was 2.8 $\cdot 10^{-4}$ and the number of valid events per proton was 1.6 $\cdot 10^{-6}$ mm. Hence, per valid event, more then $5 \cdot 10^9$ protons are needed, per 1 mm target-depth. This number, however, is one oder of magnitude above the number of protons in the strongest spot of a scanning system. Rohling *et al* [197] considered a systems of two CZT-LSO CCs, shifted each other by 90°. The system response to a line source, a cuboid-shaped source with a cavity, and a TPS plan for head and neck irradiation, was in-silico investigated. Simple shapes were successfully 3D reconstructed, but the capability of detecting millimetric range deviations remains debatable. The requirement of larger detectors, or higher detectors number, was stressed in light of the elevated detector loads under clinical conditions. This, together with the need of two or more CCs for 3D reconstruction, significantly increases the costs involved.

Gamma Electron Vertex Imaging (GEVI)

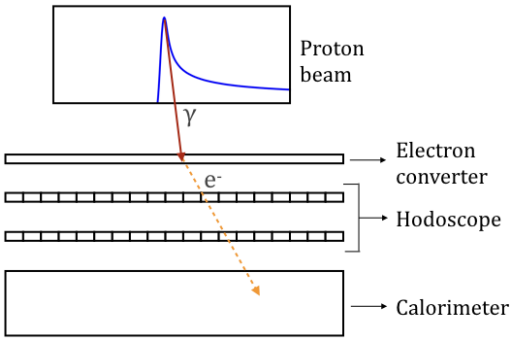

Figure 2.18: Gamma electron vertex imaging

In the Gamma Electron Vertex Imaging (GEVI) method PG rays are first "converted" to electrons, by Compton scattering, then electrons are traced to reconstruct the emission position. A GEVI system, comprised of an electron-converter plate, two DSSDs, and a CsI crystal was first simulated by Kim *et al* [198] (Figure 2.18). The system resolved the range of a 80, 150, and 299 MeV beam in soft tissue with 3-6 mm error. Then Lee *et al* [199] and Kim *et al* [34] built a GEVI system with a Be plate and a plastic scintillator. In Lee *et al* [199] a ^{60}Co (with Be plate) and a ^{90}Sr source (without) were resolved with a position resolution of 16 and 35 mm FWHM, respectively. PG rays from a 45 MeV beam on a PMMA phantom were further imaged. The imaging sensitivity, i.e. the number of good events divided by the number of protons in the beam, was 4 $\cdot 10^{-8}$. Kim *et al* [34] reconstructed the PG profiles of 90 to 180 MeV beams (15 MeV steps) delivered to a water phantom. Imaging sensitivity was 4.8 $\cdot 10^{-7}$ and 1.9 $\cdot 10^{-6}$ for the 90 and the 180 MeV beam, respectively. Sensitivity increases with the beam energy as more PG rays are emitted by high-energy protons. Range was determined with an error of ± 2.7 mm.

Compton camera: semiconductors

Peterson *et al* [200] first simulated a semiconductor-only CC with three HPGe detector stages. By studying the reconstruction of a source, emitting over a range of discrete energies (1-15 MeV), the system was geometrically optimised. The source was then replaced by a 50 to 250 MeV beam (50 MeV steps) impinging a tissue target. The overall efficiency was estimated from 10^{-6} to 10^{-3}. This prototype was further in-silico investigated by Robertson

[1] A ∼0.9 MeV proton beam was shot onto a TiN target inducing the ^{15}N(p,$\alpha\gamma_{4.439}$)^{12}C nuclear reaction

et al [201] and Mackin *et al* [202]. Robertson *et al* [201] compared different detection materials, namely HPGe, BGO, NaI, Xe, Si, and $LaBr_3$. The most suitable detectors for single-material CCs are HPGe and BGO, with an efficiency of $1.15 \cdot 10^{-4}$ and $9.58 \cdot 10^{-5}$, respectively. On the other hand, with an efficiency of $1.26 \cdot 10^{-4}$, the most efficient multi-material CC is comprised of two HPGe and one BGO. Mackin *et al* [202] investigated the influence of Doppler broadening on a full HPGe or CZT design. Several sources, from 0.511 to 7.12 MeV, as well as a 110 MeV beam impinging a tissue phantom, were modelled.

The Polaris J detection system, a CC consisting of with four CZT stages, was designed to work in both two- and three-stage modality. The Polaris J CC was tested by McCleskey *et al* [203], Polf *et al* [204], and Draeger *et al* ([205], [206]) using sealed sources ([203], [205]), a beam irradiating a water target [204], and a beam irradiating a polyethylene target [206]. Accordingly to McCleskey *et al* [203], for a ^{137}Cs source, the CC energy resolution at 662 keV is 9.7 keV FWHM, while, for a ^{60}Co source, the CC position resolution is 2.3 mm FWHM and the efficiency is $2.2 \cdot 10^{-5}$ and $5.8 \cdot 10^{-7}$ for the two- and the three-stage modality, respectively. The emissions of ^{60}Co, ^{137}Cs, and ^{22}Na sources was also measured by Draeger *et al* [205]. Polf *et al* [204] observed that, to acquire the 2D profiles of the PG rays emitted by a 114 and a 150 MeV beam, a maximum dose of 4 cGy is needed. From the extracted 1D profiles the detection of a 3 mm range shift was reported with $\sigma = 1.5$ mm. Draeger *et al* [206] investigated the CC performance under the delivery of a 2 Gy beam from a hypo-fractionated treatment ($\sim 9 \cdot 10^8$ protons for a 180 MeV beam and $\sim 6 \cdot 10^8$ protons for a 120 MeV beam) and a standard delivery beam ($\sim 1 \cdot 10^8$ protons for a 120 MeV beam). To improve the spacial resolution "bad" events, that most likely do not originate from an actual double/triple event in the CC, were removed using different filtering techniques. For the row data, at 2 Gy, the number of valid events per proton was $5.76 \cdot 10^{-6}$ (double modality) and $8.61 \cdot 10^{-6}$ (triple modality). Full 3D images were produced, range shifts up to 2 and 3 mm were detected for 2 Gy and standard delivery, respectively.

Yao *et al* [207] investigated the detection of the PG rays from a 120 MeV beam in water. Range was predicted with an σ inferior to 1.6 mm. Gutierrez *et al* [208] presented the first study toward the development of a new CC with a Si scatterer and two HPGe absorbers.

Electron Tracking Compton Camera (ETCC)

The Electron Tracking Compton Camera (ETCC) (Figure 2.19) consists of a micro-Time Projection Chamber (μ-TPC) and a Pixel Scintillator Array (PSA). The μ-TPC is composed of a gas-filled drift cage, a Gas Electron Multiplier (GAS), and a micro-PIxel Chamber (μ-PIC). The μ-PIC is a 2D gaseous imaging detector, manufactured using printed circuit board technology. The ETCC is based on Compton-scattering. The recoil electron ionises the gas along the track, producing electrons. Under the effect of the electric field in the drift cage, these electrons move towards the μ-PIC, are amplified by the GEM, and, finally, their position is reconstructed by the μ-PIC. Energy and position of the Compton-scattered γ-rays is measured by the PSA, which typically is a GSO crystal pixel array. The μ-TPC was first presented by Tanimori *et al* [209]. The ETCC was then developed by Takada *et al* [210]. Kabuki *et al* [211] 3D reconstructed the position of a ^{131}I source, reporting an angular

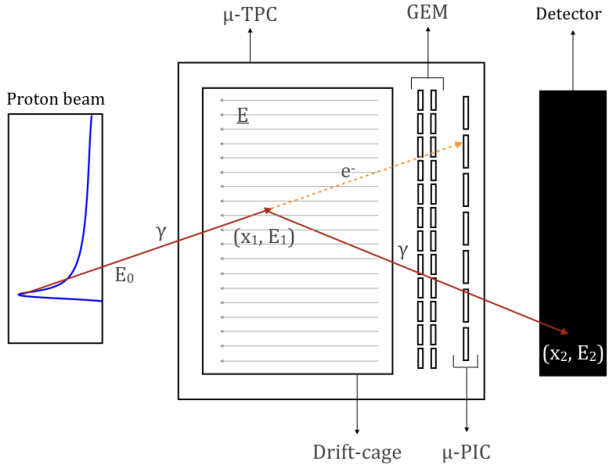

Figure 2.19: Electron tracking Compton camera

resolution of 6.6° FWHM. Kurosawa *et al* [212] tested the ETCC using a 140 MeV beam (2.5 pA) in water. A correlation between the PG and the dose profiles was observed and an efficiency of $3 \cdot 10^{-6}$ was reported. It was also suggested that a gas switch, from Ar to CF_4, and a higher gas pressure could both increase the efficiency. Takahashi *et al* [213] optimised different gas mixtures in terms of gas gain, drift velocity, energy, and position resolution. The efficiency of $Ar/CF_4/isoC_4H_2$ (54:40:6) gas mixture at 1.4 atm was ∼2 times higher than that of Ar/C_2H_2(9:1) at 1 atm.

2.2.3 Non-imaging systems: Time Of Flight (TOF)

As outlined in Section 2.1.6, the transit time of a beam in a medium is range-dependent. In the so-called PG Timing (PGT) technique the mean and the width of the PG TOF distribution are exploited to infer the original beam range. In the more recent PG Peak Integral (PGPI) technique the peak integrals of the PG TOF distributions are utilised.

Prompt Gamma Timing (PGT)

PGT was first introduced by Golnik *et al* [149]. The method was experimentally validated with a 150 MeV irradiating a PMMA phantom of variable thickness and a graphite phantom with variable beam entrance position (with respect to the detector). PGT spectra were acquired with a GAGG:Ce scintillator. Simulations were also performed. In a first campaign, 50 to 230 MeV (10 MeV steps) beams impinged both a PMMA target and a PMMA target with 10% density reduction. In a second campaign, a 150 MeV beam irradiated a PMMA target with a bone insert and a PMMA target with an air-filled cavity. Results proved that PGT mean and width are dependent on proton transit time. Range shifts of ∼2 mm were detected within few seconds. PGT was further experimentally evaluated by Hueso-Gonzalez *et al* [214]. The measurement program consisted of a 100, 160, and 230 MeV beam on a PMMA target with: variable thickness, air cavities of variable thickness at various depths, and bone filling at various depths. Out of comparison, the PGT spectra were acquired with BaF_2 and $LaBr_3$ detectors. Results showed that, in heterogeneous targets, range shifts of 2 and 5 mm are retrievable for 10^{10} (230 MeV) and 10^8 protons (100 MeV), respectively.

The relation between a range over/under shooting and a shift in the TOF mean value is ∼50 ps/cm [214]. The RF signal phase, used as time reference, is not stable over a time-scale

of hours, therefore the TOF mean value can shift up to ∼100 ps. To monitor and correct the RF signal phase, Petzoldt *et al* [215] introduced a Proton Bunch Monitor (PBM) composed of a plastic scintillator on the top of a BGO crystal (phoswich detector concept). The beam impinges a thin PMMA or polypropylene layer. Elastic *pp*-scattering at the hydrogen content of the layer is used to produce two protons exiting the target off the beam direction. Two PBMs, 45° relative to the beam axis, detect both protons in coincidence. The PGT spectra is acquired with a $CeBr_3$ detector. With this set-up a PMMA target, with two air cavities and a bone insert, was shot with a 225 MeV beam. Although very high statistics were employed (over $7.5 \cdot 10^{11}$ protons), the potential benefits of the PGT method with the PBM were illustrated. In a further step, the bunch time spread was investigated by impinging a PMMA layer with a 69 to 225 MeV beam. The bunch time spread strongly depends on the beamline length. For a 69 MeV beam, with ∼2 ns bunch time spread, range shifts of ∼5 mm were resolvable with at least 10^4 PG rays. Werner *et al* [216] reports on the next step towards the clinical application of PGT. A treatment plan, containing 100 equally-weighted spots with fixed energy (162, 226.7 MeV), was delivered to a PMMA target with air cavities of variable thickness introduced at different depths. The dependency of PGT mean and width from the air cavities was quantified.

PGT & in-beam PET combined systems

The in-beam PET innovative imaging, I3PET, is the first prototype to combine together PG and PET methods for in-vivo range verification. In-beam PET (Section 1.6.2) and PGT approaches, in particular, are merged together. I3PET consists of six segmented LFS scintillators, three on the left and three on the right side of the phantom, respectively. Ultra-fast silicon detectors are placed along the beam line as bunch monitor for PGT. The system has been in-silico evaluated by Ferrero *et al* [124] by delivering a 62 - 129 MeV (45 energy layers) treatment plan on a PMMA phantom. Air cavities of various thickness have been included in the phantom. The PGT profiles well predicted the range shifts caused by the cavities, indicating the feasibility to assess PG range verification with a PET detector.

Prompt Gamma Peak Integral (PGPI)

PGPI was first investigated by Krimmer *et al* [217]. The PGPI spectra was recorded with three detectors, one $LaBr_3$ and two BaF_2 facing a PMMA target. Detectors were placed 90° (BaF_2) and 45° ($LaBr_3$) to the beamline while the TOF reference signal came from the accelerator RF. Tests were performed experimentally, using a 65 MeV SOBP at a rate of $3 \cdot 10^9$ p/s, and in-silico, for a 130, 200 MeV beam. Simulation results showed that deviations of a few per cent could be detected. The necessary statistics is reached with $\sim 10^8$ incident protons. For the 65 MeV beam, shifts up to 3 mm were detected.

In a further simulation study, eight $LaBr_3$ detectors, placed homogeneously around a spherical PMMA target, have been modelled with a 160 MeV beam. The combination of signals from different scintillators may be used to detect a target misplacement, while, from their ratios, the target position can be inferred.

2.2.4 Non-imaging systems: Prompt Gamma Spectroscopy (PGS)

As described in Section 2.1.4, the PG yield increases as the beam energy decreases. This property has been exploited by Verburg *et al* [141] as a tool to retrieve the beam range and to identify the chemical composition of the irradiated materials. The method is called PG Spectroscopy (PGS). The first small-scale PGS prototype ([141], [218]) consists of a collimated $LaBr_3$ detector with BGO Compton suppression shield. In Verburg *et al* [141] beams with ranges of 9, 16, and 23 gcm^{-2} were stopped in a water phantom. Measurements were performed from 50 mm before to 30 mm beyond (in 3 mm steps) the beams fall off position. The PG rays, emitted near the Bragg peak, result in discrete γ-energies. These γ-lines have been identified and each of them has been uniquely correlated with the beam energy. In other words cross sections are used as prior knowledge to asses range verification.

In Verburg *et al* [218] cross section measurements, for ^{16}O- and ^{12}C-induced PG emissions, were first acquired with the detector facing 90 different depths of the target. A 165 MeV beam was shot on either a water or a CH_2 target, delivering $2 \cdot 10^{11}$ and $5 \cdot 10^{11}$ protons per target-depth, respectively. On the base of the cross section measurements, the range-reconstruction method was developed. The method was then tested with five beams, from 15.54 to 17.59 gcm^{-2}, at two dose-levels, $5 \cdot 10^8$ and $1 \cdot 10^8$ protons per beam. Each beam impinged a target either in water or solid water. Range shifts were introduced by placing plastic slabs with variable thickness along the beam path. At the higher dose level of $5 \cdot 10^8$, a 1σ precision of $\sim$1 mm was achieved. With a reduced dose level of $1 \cdot 10^8$, precision was 2 to 4 mm. Range shifts were accurately detected and the ^{16}O and ^{12}C concentration, determined by the method, well agreed with the actual values.

A full-scale clinical PGS prototype has been presented by Hueso-Gonzalez *et al* [109]. The system is comprised by eight $LaBr_3$ detectors of which four are stacked with the center aligned to the edge of a collimator and four are distal to these, in a closely packed set-up. The system sustains up to 10^7 events per second. ^{16}O and ^{12}C cross section measurements were first performed during the delivery of 116 to 145 MeV beam (19 layers), with $3 \cdot 10^{10}$ protons per beam, on either a water or a CH_2 target. Range verification was then tested. A treatment plan was design to deliver a 0.9 Gy dose to a cubic target in water. The dose was delivered with 1,410 beams in eight layers, between 15 and 20.3 cm in depth. The system performance was further assessed by introducing: a solid water slab in half the phantom volume, a range shifter in front of it, and a bone insert inside. For each beam the range was determined with a mean precision of 1.1 mm at a 95% confidence level. Martins-Magalhães *et al* [219] presented results obtained with a PGS system composed of a $CeBr_3$ detector. First, water and PMMA targets were irradiated with a 130 MeV beam, while a graphite brick was shot with a 90 MeV beam. Then, using the PMMA phantom, tests were repeated with a slit-collimator (130 MeV) and a semi-collimator (224 MeV). The set-up with the semi-collimator seemed promising for PGS.

A PGS technique for passive scattering PT, where SOBP fields are produced with rotating range modulator wheels, has been evaluated in-silico by Testa *et al* [220] and ex-

perimentally by Verburg *et al* [221]. To detect range differences in phantoms, the relation between the beam range and the number of detected PG rays is exploited. PG rays are binned according to the angle of the modulation wheel. Each bin corresponds to a wheel segment (15° angle), for which the range is estimated by subtracting from the initial range the water equivalent thickness of the wheel and the scatterers. Events within each bin are sorted and histograms, of the time of the events relative to the RF period, are created. The relation between the range and the PG counts is then obtained. Such relationship can be exploited, for instance, to estimate the magnitude of a range shift between two measurements. The difference in the beam range that is required to match the PG counts between different measurements, corresponds to the water equivalent range shift. With this approach the range is verified with a single point of measurement and a simple detector configuration.

Testa *et al* [220] first simulated a SOBP, 16 cm range and 10 cm modulation ($5 \cdot 10^8$ protons), on a water target. Then two prostate plans were generated: a parallel lateral ($\sim$12 cGy) and an anterior-posterior ($\sim$15 cGy) field. PG rays were detected with a collimated $LaBr_3$ crystal. In the water phantom range was determined with 2 mm accuracy. For the prostate treatment a 4 mm range accuracy was achieved for both fields. Verburg *et al* [221] performed experiments with two phantoms. First a water target was irradiated with a SOBP (30 cGy), 16 gcm^{-2} range and 6 gcm^{-2} modulation. Then a SOBP (50 cGy), 12.5 gcm^{-2} range and 7.5 gcm^{-2} modulation, was delivered on a head phantom. In both cases range shifts were introduced by placing plastic slabs in the beam path between the nozzle and the phantoms. The dose rate was always $\sim$10 cGy min^{-1} and the PG detector was a $LaBr_3$ crystal with BGO active shielding. Range shifts were detected with a σ of 0.1 to 0.2 mm at dose levels of 30 to 50 cGy, respectively. The major limitation of the method is that the detected range shifts can not be attributed to a specific location within the field.

Coaxial PG-ray Monitoring (CPGM)

A compact range verification method, called Coaxial PG-ray Monitoring (CPGM), was proposed by Hueso-Gonzalez *et al* [222]. The novelty lies in the placement of a single $LaBr_3$ detector coaxial to the beam axis and behind the treated area. In this position the solid angle subtended by the detector to the treated area is maximum and decreases with the inverse of the square distance. Range shifts can be monitored using solely the number of measured PG rays. Indeed, a range under/overshoot leads to an increased/decreased number of PG rays. The system performance was simulated with a 1 to 150 MeV (1 MeV steps) beam in water. Results predicted a change of $\sim$3% in the number of measured PG rays for a 1 mm shift. Assuming a cluster of 10^8 protons, a 1 mm range error could be detected within 1σ.

2.2.5 Comparison studies

Several studies were performed, aimed at comparing different PG range verification methods.

Comparison of knife-edge and multislit camera

The performances of the KE and MS camera were compared experimentally, by Smeets *et al* [223], and in-silico, by Lin *et al* [224] and Park *et al* [225]. Smeets *et al* [224] considered the PG camera from Perali *et al* [164], the KE slit collimator from Smeets *et al* [163], and the MS collimator from Roellinghoff *et al* [154]. Acquisitions were recorded by irradiating a PMMA phantom with a 100 (1nA), 160 (2nA), and 230 (4nA) MeV beam. Range profiles were reconstructed at the Bragg peak and at the beam entrance in the phantom. Lin *et al* [224] modelled a LYSO crystal as detector, the KE slit collimator from Smeets *et al* [163], and the MS collimator from Min *et al* [157]. A 160 MeV beam was shot on a PMMA phantom. Park *et al* [225] compared a KE camera [164], comprised of a KE collimator and LYSO detectors, with a MS camera, comprised of a MS collimator and CsI detectors. The performances of the two systems were initially tested for point sources, modelled in different locations with respect to the systems, and for an imaginary line source. All sources emit 10^9 PG rays, in the 3-6 MeV range. Lately simulations were performed for a 150 MeV beam delivered on a PMMA target for 10^9, 10^8, and 10^7 protons.

Results confirmed that both collimators are suitable for PG detection. In general the KE camera showed a higher counting efficiency, assessing range retrieval even for 10^7 protons. To correctly estimate the range, however, the KE camera has to be aligned, at least approximately, to the beam fall-off position. This is the major drawback of KE cameras, especially as the beam energy, in scanning systems, changes rapidly and continuously. The MS camera, on the other hand, needs at least 10^8 protons to predict the beam range, but, for such a number, can estimate the range within 1.2 mm, regardless of its location with respect to the fall-off position. The MS camera FOV can be expanded simply by using more detectors and the low statistics can be addressed by merging neighbouring spots [225].

The efficiency dependance from the beam position has also been studied [223]. At the Bragg peak the KE collimator is superior, with half dose needed to reach the same precision. Conversely, at the beam entrance, the MS collimator is more efficient. Whatever the collimator, beam energy and neutron background have a significant impact ([223], [224]). By increasing the beam energy, the performance always worsens, more so with the KE collimator. Neutron contamination, on the other hand, especially affects MS cameras.

Comparison of Compton camera and prompt gamma timing

Hueso-Gonzalez *et al* [226] reviewed progresses and challenges towards the clinical application of CC and PGT methods. CCs require position-sensitive detectors, high in efficiency and resolution. Technical complexity, low coincident efficiency, high detector load, neutron and γ background, and random coincidences are all factors casting doubts on a future clinical implementation. PGT is a low footprint set-up with reduced cost. Being relatively recent, more investigations are required. Large detectors are needed and, on a long time scale, the bunch phase drift poses a challenge on the robustness of the method.

2.3 Reconstruction algorithms

To reconstruct the PG rays distribution an algorithm is typically needed. The complexity of such an algorithm strongly depends on the prototype under consideration.

2.3.1 Mechanical collimated cameras

In general, for imaging systems based on mechanical collimation (Section 2.2.1), the reconstruction algorithm is trivial. Mechanical collimated prototypes already provide the coordinates of the PG emission positions along the beam path. Such prototypes can easily be coupled with a beam monitor or a beam tagging device, i.e. a hodoscope.

2.3.2 Electronic collimated cameras

For imaging systems based on electronic collimation, mainly CCs, (Section 2.2.2) the need for more advanced reconstruction algorithms is clear. In CCs, the probable PG rays emission-position is restricted to the surface of a cone, named the *Compton-cone* (Figure 2.15). The angle of the *Compton-cone* is uniquely provided by the Compton kinematics when the PG-ray is Compton-scattered in the first detector and fully absorbed in the second (two-stage CC) or when the PG-ray is Compton-scattered in the first two detectors and undergoes an interaction of any kind in the third (three-stage CC). If the recoil Compton-electron is tracked, the emission position of the PG-ray is restricted to an arc-segment of the *Compton-cone* (Figure 2.17) [191], *Compton-arc*. In this case the PG-ray full absorption is not required. As a matter of fact, uncertainties - the cone apex location, the scattering angle and the scattering plane - affect the *Compton-cone*. Thus the cone is typically thickened, so that the emission position does not lie on the cone surface but belongs to a small volume around it. Finally, the PG rays distribution is retrieved, by means of reconstructing algorithms, from a large set of overlapping *Compton-cones* or *Compton-arcs*. Reconstruction algorithms can either be analytical or iterative.

Analytical algorithms

A broad choice of analytic reconstruction algorithms have been proposed in literature. Analytical methods gather techniques such as cone-beam projection ([227], [228], [229]), Radon projection [230]), and direct inversion of the Compton transform ([231], [232], [233], [234]). A central-slice theorem for the inversion of the Compton transform was proposed by Maxim *et al* [232]. Subsequently Maxim *et al* [234] showed that the inversion of the Compton transform translates to an analytic Filtered BackProjection (FBP) algorithm, very similar to the standard FBP employed in cone-beam CT. Analytical methods are exact for ideal imaging devices. They are typically very fast but sensitive to the lack of data [233].

Iterative algorithms

At the time of writing, the most widely used image reconstruction algorithms for CCs are iterative. The *List-Mode Maximum Likelihood Expectation Maximisation* (LM-MLEM), the most common iterative algorithm, makes successive approximations to the most probable

source distribution that would have led to the observed data. Adapted for CC by Widerman *et al* [235], the LM-MLEM algorithm application on PG range verification was further exploited by Torngа *et al* [236], Maxim *et al* [237], and Schoene *et al* [238]. Two MLEM variations, the *Ordered-Subset Expectation Maximisation* (OS-EM) and the *Row-Action Maximum Likelihood Algorithm* (RAMLA) were formalised for CC by Kim *et al* [239] and Lee *et al* [240], respectively.

In two-stage CCs the energy of the incident radiation must be known (monochromatic source) or estimated (by assuming, for example, that the second interaction is photoelectric). In three-stage CCs, conversely, the energy can be measured. Compared to two-stage CCs, however, the efficiency of three-stage CCs is at least one order of magnitude inferior [172]. Gillam *et al* [241] developed an MLEM algorithm for two-stage CCs which reconstructs the energy of the incoming radiation, along with the spatial variation in emission density. The algorithm was further employed by Ortega *et al* [177].

The use of MLEM algorithms in the clinical environment is limited by the long computational time. To reduce the computational burden, fast Bayesian CCs reconstruction methods, using GPU, have been developed [242]. The GPU-based approach dramatically improves the computational speed, with only minor losses in reconstruction accuracy.

Based on the Metropolis−Hastings algorithm ([243], [244]), the *Stochastic Origin Ensemble* (SOE) algorithm was originally introduced for PET/SPECT image reconstruction studies [245] and then adapted to CCs by Andreyev *et al* [246]. In terms of computational costs the SOE algorithm outperforms both LM-MLEM and OSEM algorithms [246]. The SOE algorithm was further evaluated by Mackin *et al* [247] and employed in the fields of PG range verification ([202], [204]) and homeland security [248].

A new, substantially modified version of the SOE algorithm, the *Recovery Option Stochastic Origin Ensemble* (RR-SOE), was recently presented by Andreyev *et al* [249] and utilised, for PG range monitoring, by Yao *et al* [207].

Chapter 3

Monte Carlo simulations of prompt gamma rays

In-silico evaluations, using Monte Carlo Geant4 toolkit, are a major component of this work. The present Chapter provides a brief insight on Monte Carlo methods and their rule in PT research (Section 3.1). The focus is then moved on the Geant4 toolkit (Section 3.3). The Chapter ends with a literature review on modelling PG emissions in Geant4. Emphasis is placed on the selection of the most appropriate physics list (Section 3.4).

3.1 The Monte Carlo method

The Monte Carlo (MC) technique is the most accurate tool to simulate particle interactions in matter. MC simulations are widely used in research, as they allow to precisely simulate scenarios difficult to create experimentally. Simulation of particles history begins by sampling a number of events from a source. Then the passage of particles is followed through a user-defined geometry, on a step-by-step basis. For each particle, one step at time, the interaction is chosen by randomly sampling from probability distributions. Interaction probabilities are mathematically defined by means of models, parameterisations, experimental data, or a combination of those. Once primaries have finished, secondaries are saved. The step size, user-defined, should be short, so that the difference in cross section between the beginning and the end of each step is small. A short step size, however, results in a long computing time. To shorten the time the user can decide not to track specific particles. The energy of such particles is then deposited locally, for energy conservation. The successful use of MC simulations depends on physics models, accurately describing particle interactions.

3.2 The role of Monte Carlo in proton therapy

The role of MC in medical physics is ubiquitous ([250], [251]) and the range of MC applications in radiotherapy is extremely broad [252].

The principal usages of MC in PT are listed in Figure 3.1. The main obstacle in the

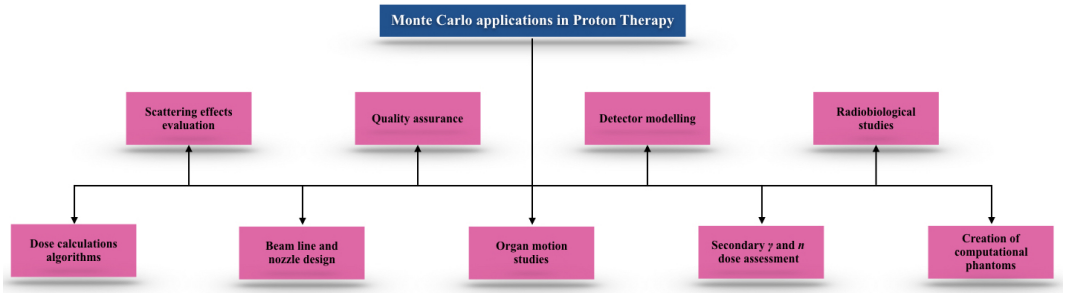

Figure 3.1: The role of Monte Carlo in PT

use of MC in PT is that basic physics libraries are not specifically tailored for PT. Electromagnetic interactions can be accurately simulated. Nuclear interaction cross sections, conversely, are associated to large uncertainties. This is mainly caused by a lack in nuclear physics experiments. Experiments dated back to the 60-70s and were focused on thin targets, whereas thick targets, yielding broad energy distributions, would have been more relevant for PT ([253], [254]). Nuclear interaction cross sections are based on look-up tables such as Evaluated Nuclear Data File (ENDF) ([255], [256], [257]) or EXchange FORmat (EXFOR) [258] databases. ENDF and EXFOR are generated using nuclear reaction models benchmarked to experimental measurements.

3.3 The Geant4 Monte Carlo toolkit

Geant4 (G4) [259], is an open source design platform, aimed at describing, via MC methods, the passage of elementary particles through matter. G4 provides a C++ assembly of object-oriented design with the capability of simulating different process organised in different functions, within a class structure. G4 is flexible and allows the user to create his own "physics list"; a combination of "processes" and "models" defining the interaction probabilities and final state generation. Other than G4, several general purpose MC toolkits, such as MCNPX [260] and FLUKA [261], are also used in PT.

3.4 Geant4 modelling of prompt gamma emission

MC methods are a prime resource for the study of range verification via PG emissions. In this regards G4 is the most employed toolkit. G4 provides several pre-built physics models. Aim of this Section is to review the most suitable models for PG simulations.

For the simulation of electromagnetic processes the standard electromagnetic model is broadly regarded as the most advisable [262]. For the low-energy nuclear inelastic interactions G4 provides the following options: the BERTini intranuclear cascade model (BERT), the BInary Cascade model (BIC), the INCL++ Liege intranuclear cascade model (INCLXX), and the PRECOmpound model (PRECO) [263]. BERT model is typically not used, as it provides a simple model for PG emission that does not consider the discrete nuclear energy levels [137]. Jarlskog and Paganetti [262] validated the G4 toolkit by means of measured

depth-dose distributions in water for a 86 and 209 MeV beam. For a 160 MeV beam longitudinal charge profiles were measured in a Faraday cup. The most accurate results were obtained using the BIC model. Jeyasugiththan *et al* [264] studied the PG spectra produced in a water target irradiated by a 200 MeV beam. The BIC, INCLXX, and PRECO models were compared. The BIC model was found to not accurately reflect the data, producing a low 6.13 MeV line. The PRECO, with an initial nuclear exciton state of 2, was found to be the most suitable. Dedes *et al* [265] and Pinto *et al* [266] focused on the proton-induced PG yields by comparing experimental data with the outcomes of G4 simulations, using all applicable nuclear models. It was observed that all models tend to overestimate the PG yield. The PG spatial prediction, however, is not affected. With the BIC model, PG yields are overestimated by a factor of 1.7 [265], or by the 40.2 $\pm$ 0.3% [266].

Several inter-code comparisons, concerning PG emissions, have been reported. Robert *et al* [254] investigated the nuclear inelastic models in GATE/G4 and FLUKA by comparing the PG angular and energy distributions. Results were restricted to the ^{16}O- and ^{12}C-induced PG rays emitted by a 35 MeV beam on a PMMA target. Substantial discrepancies were observed between the two codes. For instance, the PG yield is twice as large with GATE/G4 than with FLUKA. Verburg *et al* [137] simulated proton-induced nuclear reactions, in the 1-200 MeV incident energy range, on ^{16}O, ^{12}C, and ^{14}N. MC codes, G4 and MCNP6, and dedicated nuclear codes, TALYS and EMPIRE, were employed. In G4 the BIC model was selected. MC results were compared to the available experimental data on PG cross sections. Considerable discrepancies, in MC codes, were found for several PG lines. A variation of the total PG yield by a factor of 2 was noticed near the range fall-off position. Results clearly stressed the need for additional experimental studies of PG emissions in human tissues.

Chapter 4

Publication 1

4.1 Introduction to Publication 1

In this publication are reported the first results of a new method, called PG Coincidence (PGC), to reconstruct the proton range in 3D, through the detection of PG rays. The novelty of the PGC method relies on the simultaneous detection of the ^{16}O-induced 2.741 and 6.128 MeV PG rays, emitted in cascade. The spectrometer is described and its detection capability is investigated with Monte Carlo Geant4 simulations. The development of a mathematical reconstruction algorithm, to determine the PG rays emittance position, is also illustrated.

In the context of range verification via PG detection, with respect to all the approaches previously considered (Figure 2.6), the PGC method does not fit in any of the existing categories. Ideally, as shown in Figure 4.1, it could be regarded as an imaging system with electronic collimation, with the collimation being the 2.741-6.128 MeV energy selection.

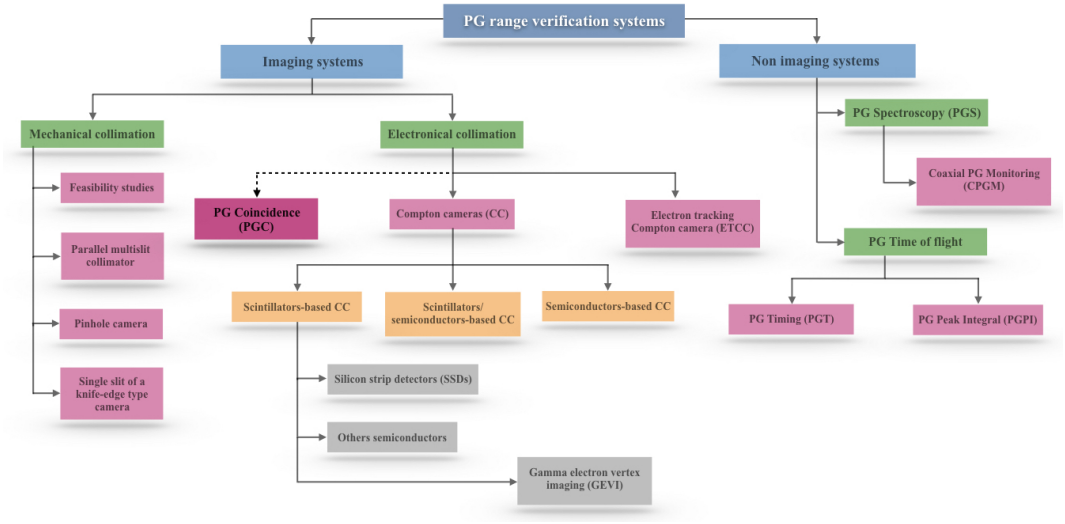

Figure 4.1: The PG coincidence (PGC) method in the context of all previously developed systems for in-vivo range verification via PG detection

The full MATLAB code of the reconstruction algorithm is reported in Appendix 2. The work is published in: *Panaino, C.M., Mackay, R.I., Kirkby, K.J. and Taylor, M.J., 2019. A New Method to Reconstruct in 3D the Emission Position of the Prompt Gamma Rays following Proton Beam Irradiation. Scientific Reports, 9(1), pp.1-12.*

A new method to reconstruct in 3D the emission position of the prompt gamma rays following proton beam irradiation[1]

Costanza M. V. Panaino[1,*], Ranald I. Mackay[1,2], Karen J. Kirkby[1,2] and Michael J. Taylor[1,2]

[1] Division of Cancer Sciences, University of Manchester, M13 9PL, Manchester, UK;

[2] The Christie NHS Foundation Trust, M20 4BX, Manchester, UK;

[*] Corresponding author

A new technique for range verification in proton beam therapy has been developed. It is based on the detection of the prompt γ rays that are emitted naturally during the delivery of the treatment. A spectrometer comprising 16 $LaBr_3$(Ce) detectors in a symmetrical configuration is employed to record the prompt γ rays emitted along the proton path. An algorithm has been developed that takes as inputs the $LaBr_3$(Ce) detector signals and reconstructs the maximum γ-ray intensity peak position, in full 3 dimensions. For a spectrometer radius of 8 cm, which could accommodate a paediatric head and neck case, the prompt γ-ray origin can be determined from the width of the detected peak with a σ of 4.17 mm for a 180 MeV proton beam impinging a water phantom. For spectrometer radii of 15 and 25 cm to accommodate larger volumes this value increases to 5.65 and 6.36 mm. For a 8 cm radius, with a 5 and 10 mm undershoot, the σ is 4.31 and 5.47 mm. These uncertainties are comparable to the range uncertainties incorporated in treatment planning. This work represents the first step towards a new accurate, real-time, 3D range verification device for spot-scanning proton beam therapy.

Keywords: proton therapy, prompt gamma, range verification, reconstruction algorithm.

[1]The layout of the publication has undergone visual changes to improve readability in the thesis format.

4.2 Introduction

When compared to conventional x-ray therapy, proton beam therapy (PT) offers substantial dosimetrical improvements. The depth-dose distribution of proton beams is characterised by a sharp distal fall-off, with the highest amount of energy deposited at the end of the track, in the Bragg peak. This feature is advantageous for cancer treatment: if the beam stops where the target is located, the tumour receives the maximum dose whilst the surrounding healthy tissues are spared [SR1]. At the moment of writing, many new PT facilities are in the planning [SR2] or construction [SR3] stage. One problem that hinders the full exploitation of PT is the uncertainty in the beam range. Range uncertainty is the uncertainty in the exact position of the distal fall-off of proton beams in biological tissues. Range uncertainty can cause a substantial underdosage of the target, failing the curative intent of the therapy, as well as an overdosage of the adjacent organs-at-risk, leading to unwanted toxicities [SR4]. In PT, for non-moving targets, there are several sources of range uncertainty [SR5]. The most important are: Computed Tomography (CT) parameters [SR6], [SR7], [SR8], mean ionisation and excitation values [SR9] and patient set-up [SR10]. Most of these uncertainties are initially taken into account in the treatment planning stage, by adding specific margins to the Clinical Target Volume (CTV) or through incorporating uncertainty in the treatment planning optimisation, robust optimisation [SR11]. During fractionated treatments, anatomical changes could also impact the desired dose distribution [SR12], [SR13], [SR14]. The most typical anatomical changes are: body weight loss/gain or daily variations in the filling of internal cavities. These changes will be found by imaging during the course of the treatment and may require a plan adaptation. If the dose distribution is not modified in light of severe anatomical changes, the total treatment outcome can be compromised [SR15]. For this reason, the introduction of range verification during PT delivery has potential to improve clinical outcomes. Anatomical changes could be detected through daily cone beam CT (CBCT) imaging, however the use of CBCT in the adaptive process for protons is difficult, mainly for the high uncertainty in dose calculation [SR16]. In contrast, a number of techniques unique to PT have been proposed in the last decade for real-time range verification. They are based on the detection of the secondary radiation naturally produced during PT through proton-nuclear inelastic reactions. These techniques provide in-situ range verification without any additional burden to the patient.

One proposed method relies on the detection of Prompt Gamma (PG) rays emitted following proton-nuclear inelastic reactions during therapy. After an inelastic interaction with an incoming proton, the target nucleus can be left in an excited state which can then swiftly return to its ground state via the emission of γ rays [SR4]. These emissions are almost instantaneous, within 10^{-9} s [SR17], hence the use of the adjective *prompt* to describe the de-excitation radiation. The PG-ray spectrum is characterised by several discrete γ-lines, usually with energies between 2 and 15 MeV. In PT, only the PG rays emitted by the most abundant isotopes in human tissues, namely carbon (^{12}C), oxygen (^{16}O) and nitrogen (^{15}N), are usually considered [SR4]. A good correlation between the intensity of the emitted PG

rays and the beams end-of-range has been experimentally proven [SR18]. PG-ray emission occurs along the entire proton track with the maximum intensity located 2-3 millimetres before the Bragg peak; here the cross section for PG-ray production drops as the proton energy decreases [SR19]. One relevant aspect of PG-ray emission is the production rate: it has been estimated by Verburg *et al* [SR18] that $1.64 \cdot 10^7$ PG rays are emitted per gram of ^{16}O per Gray (Gy) of dose delivered in tissue. The delivery of a therapeutic 2 Gy fraction generates a sufficiently high PG-ray yield to allow detection in a clinical environment [SR20]. An alternative approach is range verification through positron emission tomography (PET) imaging [SR21]. The clinical adaptation of PG-rays versus PET imaging range verification methods has been compared by Moteabbed *et al* [SR20], finding the former method advantageous.

Since PG imaging was first proposed, several prototypes have been investigated. These prototypes can be divided in collimated, mechanically or electronically, and uncollimated [SR22]. Mechanical collimated systems are based on a single scintillator, collimated and neutrons-shielded to collect the PG-rays emitted 90° to the beam path [SR23], [SR24]; they have been initially employed to demonstrate the feasibility of PG-rays detection for range verification. Prototypes with parallel slit collimators, requiring multiple or position-sensitive detectors behind the collimation system, have been suggested [SR25], [SR26] afterwards. The concept of a pinhole camera has then been adapted to PG-rays imaging [SR27]. Subsequently the pinhole opening has been substituted with a single slit of the knife-edge type [SR28], [SR29]. Knife-edge camera offers an improved spatial resolution and detection efficiency, but allows a one dimensional projection only of the PG-rays along the beam axis [SR29]. The first two clinical tests of PG-rays imaging for range verification have been performed with knife-edge cameras at Oncoray [SR30] and UPenn [SR31]. Electronically collimated system are emerging as suitable devices for PG rays as they offer a higher detection efficiency. A Compton camera is a device that determines the energy and the direction of a PG ray as it Compton scatters in the camera's components. Compton cameras designs comprise different detectors types such as scintillators [SR32], [SR33], semiconductors [SR34], [SR35] or a combination of them [SR36], [SR37], [SR38]. The Electron Tracking Compton Camera (ETCC) is a Compton camera composed of a gaseous time projection chamber, for electron tracking, and a scintillator, for the registration of the scattered photons [SR39]. Electronically collimation, as opposed to mechanical collimation, allows a three dimensional imaging but suffers from poor geometrical efficiency and low spatial resolution [SR40]. Uncollimated systems are based on PG timing, PG peak integral and PG spectroscopy. In PG timing [SR41] and PG peak integral [SR36] prototypes the width and the peak integral of PG-rays time of flight (TOF) distributions, respectively, are exploited to estimate the proton range. PG Spectroscopy [SR42] is based on the identification of the major PG-lines and their intensity. The energy spectra analysis at a single position proximal to the beam range allows an estimation of the target composition and, via the energy dependence on the cross sections, the residual beam range.

The algorithm used to reconstruct the PG-rays distribution is strictly dependent on the prototype. The need to develop complex reconstruction methods has become urgent in

Compton cameras. In this context a geometrical line-cone reconstruction has been initially presented by Lojacono *et al* [SR43]. Subsequently Maxim *et al* [SR44] showed that the inversion of the Compton transform translates to an analytic filtered backprojection algorithm and developed a reconstruction algorithm that was fast although was unable to deal with complex acquisition designs. Iterative methods, such as the Maximum Likelihood Expectation Maximisation (MLEM) [SR45], [SR46] or the origin ensemble algorithm [SR47], [SR48], have been subsequently regarded as a more versatile alternative. Reconstructive tools are rapidly evolving; the future of several prototypes for PG-ray detection is based on the algorithms development [SR22].

In this article we report the development of a new mathematical reconstruction algorithm to determine the emittance position of ^{16}O γ-rays naturally produced during PT. We additionally demonstrate the potential application of this algorithm for range verification.

4.3 Methods

4.3.1 3D position reconstruction method

^{16}O is one of the most abundant PG-ray emitters in human tissues. The technique developed in this work utilises the 2.741 MeV γ emission from the $I^{\pi} = 2^{-}$ state to the $I^{\pi} = 3^{-}$ state in ^{16}O followed by the emission of a 6.128 MeV γ-ray to the ground state (g.s). A complete de-excitation decay scheme of ^{16}O can be found in Tilley *et al* [SR49]. The time difference between the two decays is ∼25 ps [SR49], which is short compared to the nominal time resolution of scintillator type γ-ray spectroscopy detectors (∼400-500 ps [SR50]). Within the limitation of current spectroscopy detector and electronic systems, these two γ de-excitations are effectively emitted simultaneously in time and position. The cross section peaks for the reactions ^{16}O(p,p'$_{\gamma_{2.742}}$), $2^{-}\rightarrow3^{-}$, and ^{16}O(p,p'$_{\gamma_{6.129}}$), $3^{-}\rightarrow$g.s., have been evaluated (Figure 7 in Kozlovsky *et al* [SR17]). Reaction ^{16}O(p,p'$_{\gamma_{2.742}}$) has a maximum cross section, ∼38 mb, for a proton energy of ∼14 MeV while reaction ^{16}O(p,p'$_{\gamma_{6.129}}$) has a maximum cross section, ∼158 mb, for an energy of ∼13 MeV. The average energy, 13.5 MeV, corresponds to a residual proton range of ∼2.2 mm in water. Due to the coincidence requirement of the algorithm, the population of the state 2^{-}, or above, is essential. For a proton energy of 14 MeV the ^{16}O(p,p'$_{\gamma_{2.742}}$)/^{16}O(p,p'$_{\gamma_{6.129}}$) cross sections have been compared, with the first being the ∼29% of the second. During the proton bombardment of human tissues several 2.741 & 6.128 MeV γ-ray *couples* are produced due to ^{16}O de-excitation following inelastic nuclear reactions. The simultaneous detection, within the timing resolution of the detection system, coupled with a reconstruction algorithm, allows the identification of the common emission point. The identification uncertainty is proportional to the uncertainties in the position and timing resolutions of the system. The PG-ray distribution has a maximum intensity located a few millimeters proximal to the Bragg peak. For a beam passing through homogeneous tissues with constant oxygen concentration [SR51], the beam range can then be determined from the emission points of the detected ^{16}O-induced γ-ray *couples*.

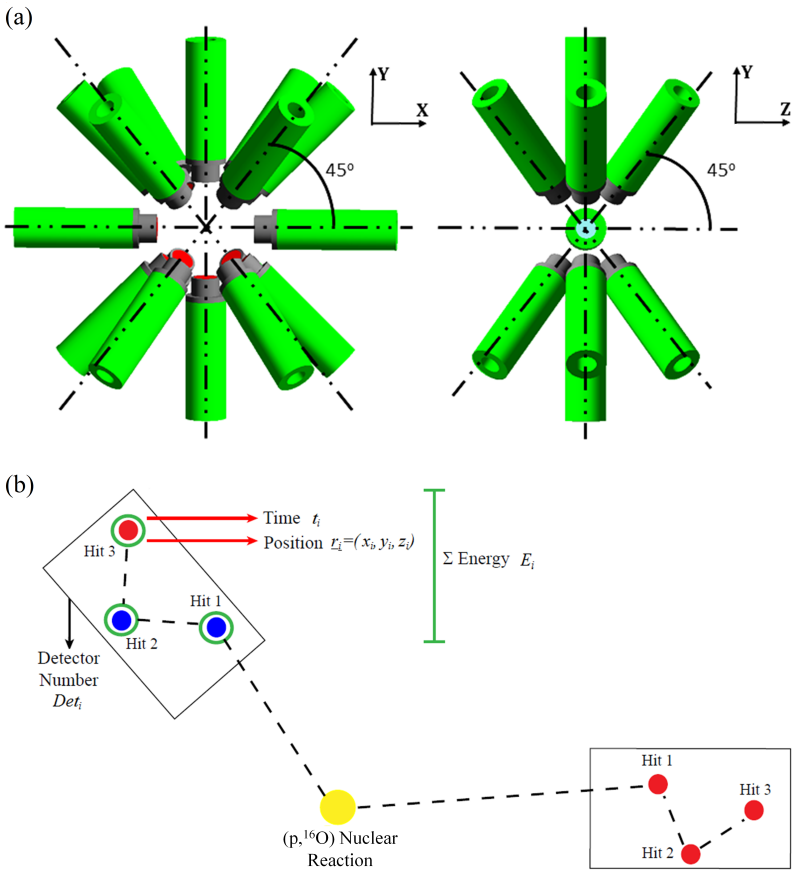

Figure 4.2: (a) The spectrometer under investigation for range verification via PG-ray detection is composed of 16 $LaBr_3$(Ce) scintillation detectors arranged in a symmetrical set-up. (b) During a simulation, for every PG-ray γ_i recorded in a scintillation module of the spectrometer, several pieces of information are saved: the detector number Det_i, the total energy released E_i, the time t_i and the coordinates (x_i, y_i, z_i) of the last hit.

4.3.2 Prompt gamma spectrometer

To maximise the PG-ray signal, a spectrometer without any mechanical collimation has been designed. As depicted in Figure 4.2a, the spectrometer is composed of 16 $LaBr_3$(Ce) cylindrical detectors with dimensions 2" length and 1.5" diameter. The detectors are arranged as follows: a ring of eight symmetrically-spaced detectors in the vertical plane plus one ring of four detectors at backward angles (45°) and one ring of four detectors at forward angles (45°), with respect to the beam axis. For an isotropic source at the centre of the spectrometer, when the distance between the source and the front face of all detectors is 8 cm, this geometry covers 30% of the total solid angle [SR52], [SR53]. The energy resolution of $LaBr_3$(Ce) (∼40 keV FWHM at 1.33 MeV) makes it a suitable detector for high energy PG-ray spectroscopy. In addition, the $LaBr_3$(Ce) intrinsic timing resolution is sub-nanosecond from ∼keV up to more than 4 MeV, allowing an excellent Time-Of-Flight (TOF) discrimination [SR54]. Discussions are being held with clinical scientist colleagues for a small design adaptation to enable clinical implementation.

The spectrometer has been modelled using the Geant4 Monte Carlo (MC) toolkit (version 10.04) [SR55]. When a γ-ray enters the sensitive area of a detector, as shown in Figure

4.2b, it interacts a number of times, termed *hits*, before being totally absorbed. For every γ_i detected, several pieces of information are saved:

1. Det_i = the detector number in which γ_i has been registered;
2. E_i = the total energy by γ_i in Det_i deposited (sum of the energy deposited in all hits in Det_i);
3. t_i = the emission and arrival time difference of γ_i in Det_i;
4. x_i, y_i, z_i = the coordinates of the last hit of γ_i in Det_i.

For all registered γ-rays, this information is available at the end of every simulation.

4.3.3 MATLAB 3D position reconstruction algorithm

In this work, an algorithm has been developed within the MATLAB environment (version R2018b). This algorithm takes as input the detector signals from two coincident γ rays and determines their common emission position. In order to reconstruct the emission position, the data goes through three main functions: 1) γ-Ray *Couple* Selection, 2) γ-Ray *Couple* Analysis, and 3) γ-Ray *Couple* Emission-Position Reconstruction. A flowchart detailing the algorithm is shown in Figure 4.3 and described in the following sections.

Function 1: γ-ray couple selection

The algorithm selects *couples* of γ-rays γ_i and γ_{i+1} which satisfy the following criteria:

1. The two events, γ_i and γ_{i+1}, were recorded in coincidence in two different detectors, i.e. $\mathrm{Det}_i \neq \mathrm{Det}_{i+1}$.
2. The energies, E_i and E_{i+1}, of the two events are 2.741 and 6.128 MeV, irrespective of order.

The energy resolution of a 2"×2"×8" $LaBr_3$(Ce) crystal has been measured by Dhibar *et al* [SR56] at several photon energies up to 4.433 MeV. Above ∼2 MeV the energy resolution is around 3% FWHM (Full Width Half Maximum). The algorithm requires that the energy of one of the two events is in the range 2.659/2.823 MeV while the energy of the other is in the range 5.946/6.321 MeV. These ranges are centred on the two decay energies, namely 2.741 and 6.128 MeV, with the extent reflecting a 3% detector energy resolution. At the end of this function only those events which belong to a γ-ray *couple* are saved. Those events which do not fulfil the criteria above are rejected.

Function 2: γ-ray couple analysis

For each *couple* two spheres are constructed, one for each event in the *couple*. An example of this is illustrated in Figure 4.4, for a (p,^{16}O) nuclear reaction at (0, 0, 0), the centre of the spectrometer. As shown in Figure 4.4a the centre of each sphere corresponds to the hit coordinates of the associated event while the radius of each sphere is the arrival time of that event multiplied by the speed of light (c). The events γ_i and γ_{i+1}, detected in (x_i, y_i, z_i) and

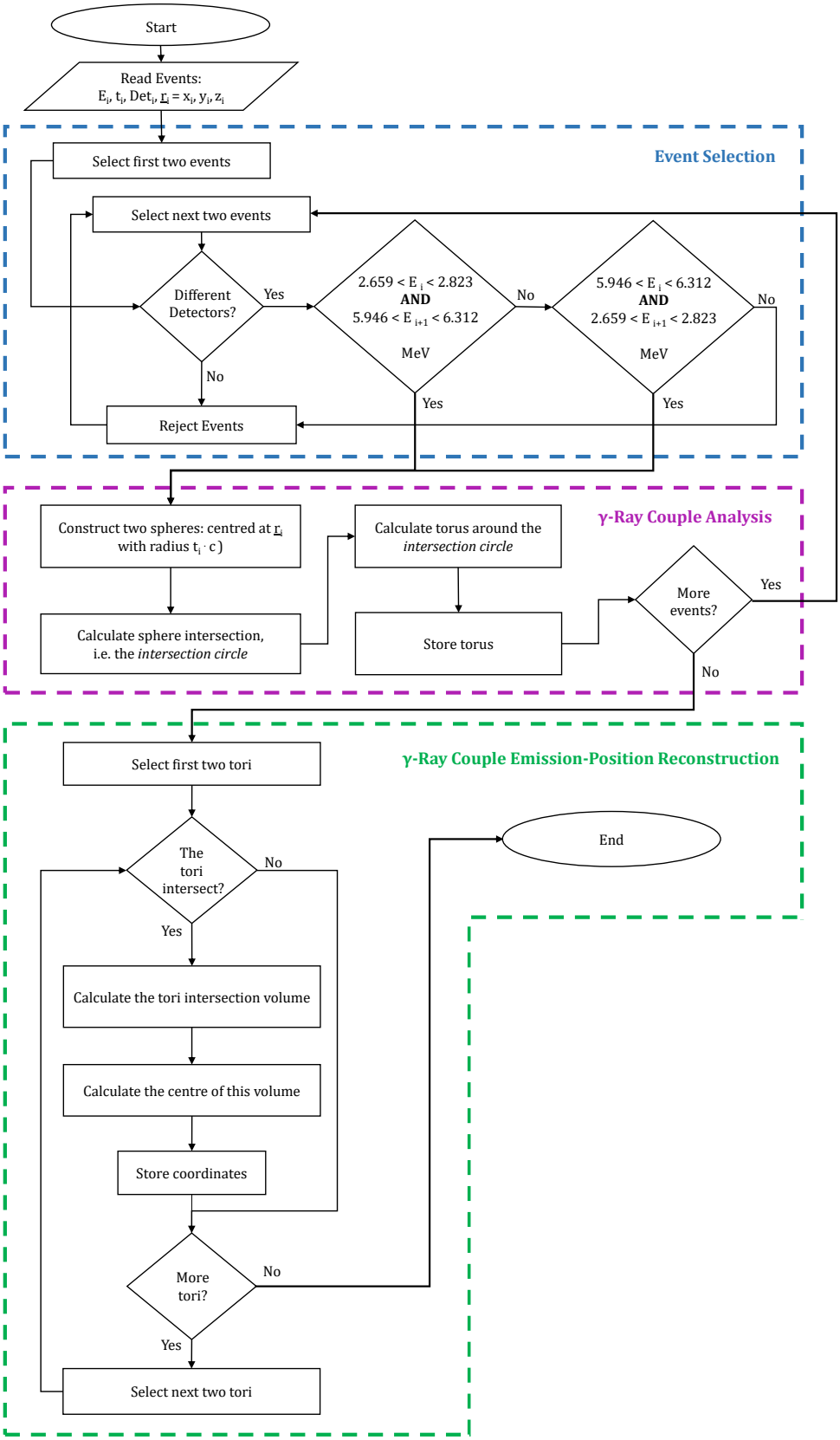

Figure 4.3: Flowchart of the 3D reconstruction algorithm developed in the MATLAB framework. To reconstruct the PG rays emission-positions, a sequence of steps is undertaken. These steps are represented by three main functions: 1) γ-Ray *Couple* Selection, 2) γ-Ray *Couple* Analysis, and 3) γ-Ray *Couple* Emission-Position Reconstruction. For each PG ray γ_i recorded in the spectrometer, the algorithm requires from the Geant4 simulation the following input data: Det_i, E_i, t_i, and (x_i, y_i, z_i).

(x_{i+1}, y_{i+1}, z_{i+1}), at time t_i and t_{i+1} respectively, are represented by two spheres centred in (x_i, y_i, z_i) and (x_{i+1}, y_{i+1}, z_{i+1}) with radius $r_i = t_i \cdot c$ and $r_{i+1} = t_{i+1} \cdot c$. As shown in Figure 4.4b, the intersection between the two spheres, i.e. an *intersection* circle, is calculated. A torus is constructed around the circle and is stored by the algorithm, Figure 4.4c. This calculation is repeated, resulting in one stored torus per *couple*, Figure 4.4d. The rationale behind the construction of a torus around each *intersection* circle is explained. For every *couple*, the original emission position should lie somewhere on its *intersection* circle. Several small uncertainties, such as the scattering in the detector, affect the spheres parameters. These uncertainties are reflected in the parameters of the circles which, consequently, may not cross each other. In light of this, around every circle, a torus is calculated. For each torus the major radius, i.e. the distance between the centre of the tube and the centre of the torus, corresponds to the radius of the *intersection* circle. For the minor radius, i.e. the radius of the tube, a value of 3 mm was determined from MC simulations.

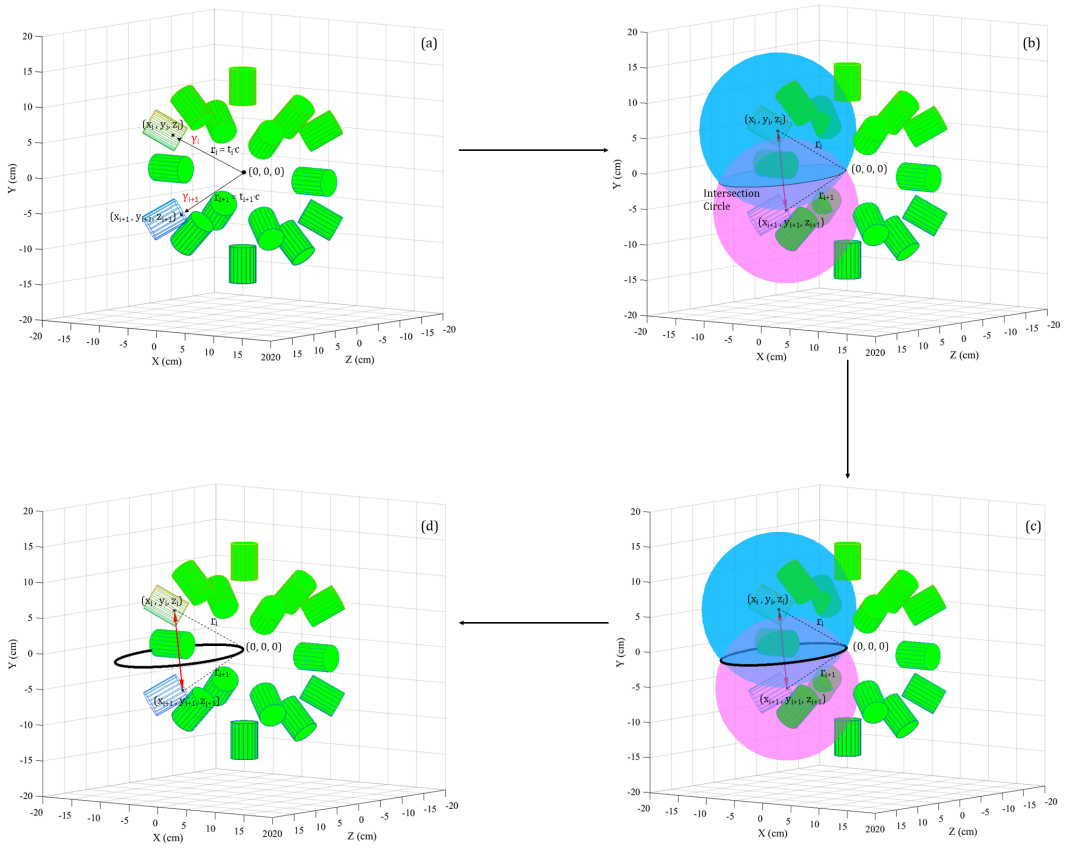

Figure 4.4: (a) In the first function of the algorithm, Event Selection, the input data from Geant4 simulations of those γ rays which belong to *couples* are saved. For each event the saved data are: Det_i, E_i, t_i and (x_i, y_i, z_i). (b) In the second function, γ-Ray *Couple* Analysis, for each *couple* of γ rays γ_i and γ_{i+1} two spheres are constructed. The hit coordinates (x_i, y_i, z_i) and (x_{i+1}, y_{i+1}, z_{i+1}) represent the centres while the hit times t_i and t_{i+1} are employed to estimate the radii ($r_i = t_i \cdot c$ and $r_{i+1} = t_{i+1} \cdot c$). The circle which represents the intersection of the two spheres is calculated. (c) A torus is constructed around the intersection circle. (d) At the end of the second function each previously constructed tours is stored.
All the drawings refer to a (p,^{16}O) nuclear reaction in (0, 0, 0).

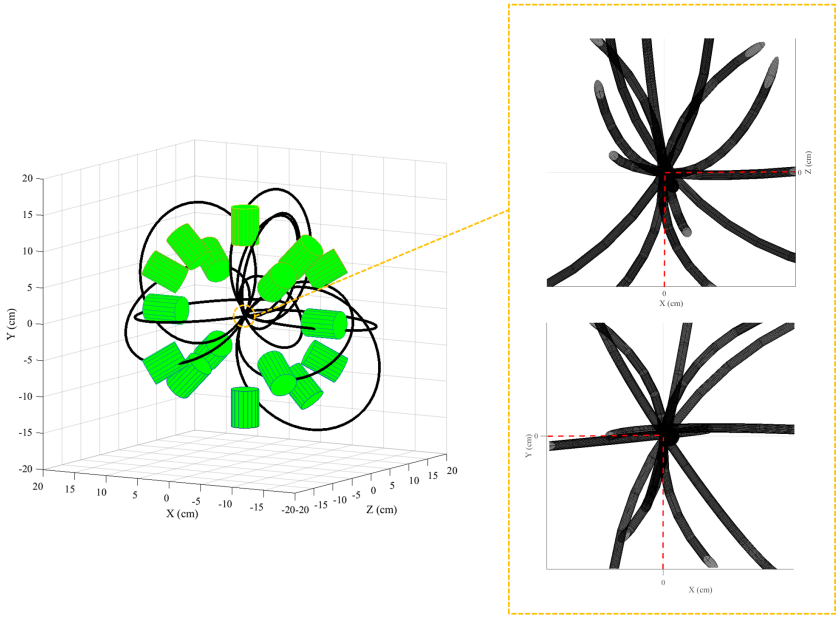

Figure 4.5: At the end of the second function of the algorithm, γ-Ray *Couple* Analysis, n tori are stored, where n is also the number of all the γ rays *couples* originally selected (here reported 11 for display clarity purpose only). A pattern is noticeable: the tori converge to the original position of the (p,^{16}O) nuclear reaction, which, in the present case, is (0, 0, 0).

Function 3: γ-ray *couple* emission-position reconstruction

For clarity, only 11 tori are shown in Figure 4.5. As highlighted by the inset on the right side of this Figure, the tori converge to the emission position. Each couple of tori is retrieved and, if a non-null volumetric intersection between them exists, the intersection volume is calculated (see Figure 4.6). The section of each torus which does not belong to the spectrometer central volume is eliminated before the intersection calculation. This procedure fasten the computational process but allows only the reconstruction of the emitted coordinates

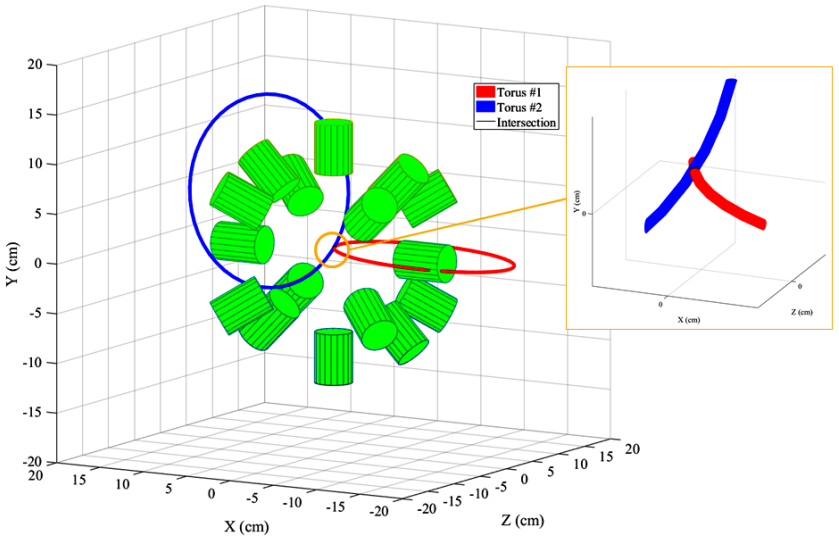

Figure 4.6: In the third function of the algorithm, γ-Ray *Couple* Emission-Position Reconstruction, the intersection between each torus with all the others is calculated. The intersection volume between each chosen *couple* of tori is estimated by triangulating the two tori surfaces and applying a triangle/triangle intersection test routine by Tomas Möller [SR57]. The centre of each non-null intersection volume is stored as an hypothetical position of the (p,^{16}O) nuclear reaction.

located inside the spectrometer. The intersection volume is determined by triangulating the surfaces of the two tori and by applying the triangle/triangle intersection test routine by Tomas Möller [SR57]. The central point of each intersection volume is calculated and stored as a virtual emission position. The intersection each torus with all the others (torus n°1 and torus n°2, ..., torus n°1 and torus n°n, torus n°2 and torus n°3, ..., torus n°2 and torus n°n, ..., torus n°n-*1* and torus n° n) is calculated. If n is the number of tori and N_{NaN} is the number of null intersections between tori, the total number of virtual *e*mission *p*ositions N_{ep} is: $N_{ep} = 2 \cdot n - N_{NaN}$. To obtain the origin of the maximum intensity of the 2.741 & 6.128 MeV ^{16}O-induced PG-ray distribution the N_{ep} x, y, z coordinates of the virtual emission positions are histogrammed.

4.3.4 Geant4 simulations

The Geant4 toolkit has been employed to simulate the spectrometer and a clinical 180 MeV proton pencil beam impinging a homogeneous 4x4x30 cm^3 water (*G4Water*) phantom. For the $LaBr_3$(Ce) detectors, an energy resolution of 3% FWHM [SR58] and a time resolution of 280 ps [SR59] have been chosen. For the spectrometer, to subtend a high solid angle with respect to the PG-ray emitted in proximity of the Bragg peak and to obtain meaningful results within a reasonable computational time, the internal radius was set to 8 cm. As shown in Figure 4.7, both the beam and the phantom have been modelled in the central area of the spectrometer. The beam direction coincides with the phantom central axis (Z axis). The water phantom has been modelled so that the Bragg peak depth for the 180 MeV beam corresponds to the centre of the spectrometer. This is to ensure that the PG rays emitted close to the Bragg peak are detected by the spectrometer with the maximum solid angle. The proton energy distribution was set as Gaussian with a sigma of 1 MeV. The sigma value for the lateral spread was set as 4 mm. These parameters were chosen as they represent typical values determined on our system. The number of initial protons simulated was 10^8.

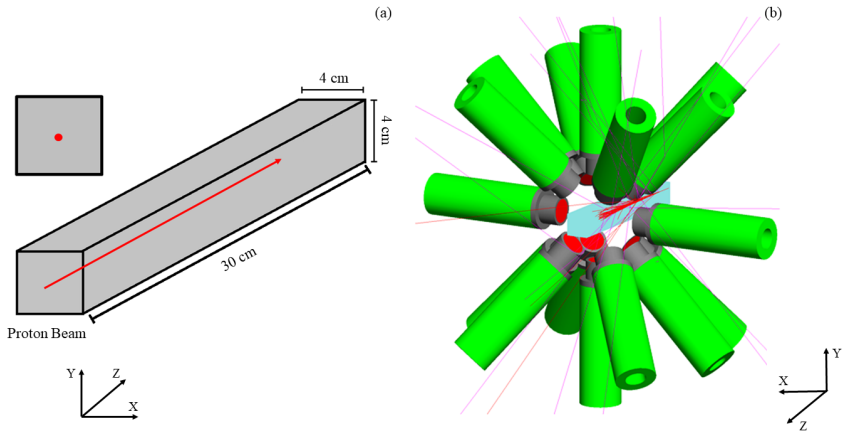

Figure 4.7: Geometry of the Geant4 simulation. (a) A 4x4x30 cm^3 water phantom is irradiated by a 180 MeV clinical proton pencil beam. The beam direction coincides with the phantom central axis (Z axis). (b) Both the phantom and the beam are modelled in the centre of the spectrometer. The water phantom has been modelled so that the Bragg peak depth for the 180 MeV beam corresponds to the centre of the spectrometer, i.e. the point (0, 0, 0). This as to ensure that the ^{16}O-induced PG rays emitted close to the Bragg peak are detected by the spectrometer with the maximum solid angle (Ω = 30%).

The PG rays, emitted in the (p,^{16}O) nuclear reactions, have been recorded by the spectrometer. The simulation outputs have been processed with the algorithm to reconstruct, in full 3 dimensions, the beam end-of-range value in the phantom. In addition, a scoring mesh (20x20x150 bins), with the same size and position of the phantom was created. The quantities scored by this mesh were: 1) the energy deposition per voxel and 2) the 2.741 & 6.128 MeV ^{16}O-induced PG-ray distribution. These quantities are used as a benchmark for the reconstruction algorithm results. To model the interactions in the Geant4 simulation the electromagnetic (*EmStandardPhysics-Option4*, *EmExtraPhysics*) and hadronic (*Hadron Elastic Physics*, *Hadron Physics QGS-BIC*, *IonBinary Cascade Physics*, *Neutron Tracking Cut* and *Stopping Physics*) physics lists have been combined. The *IonBinaryCascadePhysics* was selected as it has been proved [SR60], [SR61] that this is the most suitable to model the PG-ray emission. For all particles, the cut has been set to 0.5 mm.

4.4 Results

In Figure 4.8a, the result of a simulation with a 180 MeV proton pencil beam impinging a water phantom is illustrated. This Figure shows the profiles, along the Z axis, of the following normalised distributions: the proton energy deposition as scored by the mesh (*black* dot-dashed curve), the 2.741 & 6.128 MeV ^{16}O-induced PG-ray distribution also scored by the mesh (*red* dashed curve) and the origin of the maximum intensity of the 2.741 & 6.128 MeV ^{16}O-induced PG rays as determined by the algorithm (*blue* curve). The total number of 2.741 & 6.128 MeV ^{16}O-induced PG-rays *couples*, selected by the algorithm in Function 1, is 826. The two mesh-based distributions refer to a phantom with 2x2x2 mm^3 voxels. Conversely, for the algorithm-reconstructed distribution, the phantom has been divided in 1x1x1 mm^3 voxels. As the mesh scored quantities are used solely for benchmarking a larger voxel size was chosen to reduce computation time. In the mesh scored distributions the Bragg peak position and the maximum intensity position of the 2.741 & 6.128 MeV ^{16}O-induced PG rays are located at a depth of 21.60 and 21.40 cm, respectively. By applying a Gaussian fit on the algorithm reconstructed data the maximum intensity position of the 2.741 & 6.128 MeV ^{16}O-induced PG rays is at a depth of 21.37 $\pm$ 0.42 cm. No smoothing is applied prior to the fit, however the histogram binning may have an effect.

For a clinical implementation of the system, a spectrometer internal radius of 8 cm appears to be only suitable for a very small treatment volume. The most likely clinical scenario for this radius could be a paediatric head and neck case. Additional simulations have been performed to investigate the performance of the spectrometer in different clinical scenarios. In all simulations, the beam and the water phantom have been modelled in the central area of the spectrometer as described in Section 8.3.5. The number of initial protons simulated has been kept fixed at 10^8. The spectrometer internal radius has been set to 15 and 25 cm to represent, respectively, an adult head and neck (Figure 4.9) and a thoracic treatment (Figure 4.10). With respect to the configuration previously described, the solid angle subtended by the spectrometer with respect to the origin (0, 0, 0) decreases from 30% for 8 cm radius to 9% for a 15 cm radius and to 3% for a 25 cm radius. The total

Spectrometer internal radius variation			
Spectrometer radius (cm)	***Treatment site***	***Centroid μ (cm)***	***St. Dev. σ (mm)***
8	head&neck (paediatric)	21.37	4.17
15	head&neck (adult)	21.41	5.65
25	thorax (adult)	21.45	6.36
Proton beam energy variation			
Proton beam energy (MeV)	***|Shift| (mm)***	***Centroid μ (cm)***	***St. Dev. σ (mm)***
180	0	21.37	4.17
177.5	5	20.84	4.31
175	10	20.31	5.47

Table 4.1: Evaluation of the system performance, in reconstructing the end-of-range position of a proton pencil beam, by varying the spectrometer internal radius and the beam energy. The lateral spread (standard deviation), σ, and the centroid, μ, of the algorithm-reconstructed ^{16}O PG-ray distribution, as obtained through the application of a Gaussian fit, are reported. As a reference, the results of a simulation with 8 cm spectrometer internal radius and 180 MeV beam energy are shown when both variations are performed. When different spectrometer internal radii (8, 15, and 25 cm), representing different hypothetical treatment sites, are modelled, the beam energy has been always kept at 180 MeV. Conversely, when the Bragg peak is shifted, with respect to the centre of the spectrometer, by 5 and 10 mm, the spectrometer internal radius has always been set to 8 cm.

number of 2.741 & 6.128 MeV ^{16}O-induced PG-ray *couples*, selected by the algorithm in Function 1, is 387 and 191 when the radius is 15 and 25 cm, respectively. The variation of the spectrometer performance with the internal radius is shown in Table 4.1. Both the lateral spread (standard deviation), σ, and the centroid, μ, of the algorithm-reconstructed maximum intensity ^{16}O PG-ray distribution are reported for each chosen radius. These values have been obtained by applying a Gaussian fit to the reconstruction data.

Simulations have been performed to test the spectrometer ability to estimate range deviations from a peak position expected at (0, 0, 0). With respect to the previous analysis the beam energy has been decreased to 177.5 and 175 MeV, which corresponds, to a peak depth, in water, of 21.06 and 20.54 cm and to a range shift of $\sim$5 and $\sim$10 mm relative to the origin (0, 0, 0). In both simulations the number of initial protons was 10^8 and the spectrometer internal radius was 8 cm. The total number of *couples* is 806 and 766, when the shift is 5 and 10 mm, respectively. Figure 4.8b depicts, along the Z axis, the maximum intensity emission origin of the 2.741 & 6.128 MeV ^{16}O-induced PG ray, detected by the spectrometer and reconstructed by the algorithm, when the beam energy is 180 (*blue* curve), 177.5 (*green* dashed curve), and 175 MeV (*purple* dot-dashed curve). For the three energies, a Gaussian fit is applied to the algorithm reconstructed data. The lateral spread, σ, and the centroid, μ, obtained through the fit, are reported in Table 4.1.

4.5 Discussion

An excellent correlation is observed in Figure 4.8a between the two mesh-scored distributions: the 2.741 & 6.128 ^{16}O-induced PG rays (*red* dashed curve) and the energy deposition due to the electronic stopping of the proton beam (*black* dot-dashed curve). This is consistent with the results of previous in-silico studies [SR23], [SR62] and with the outcomes

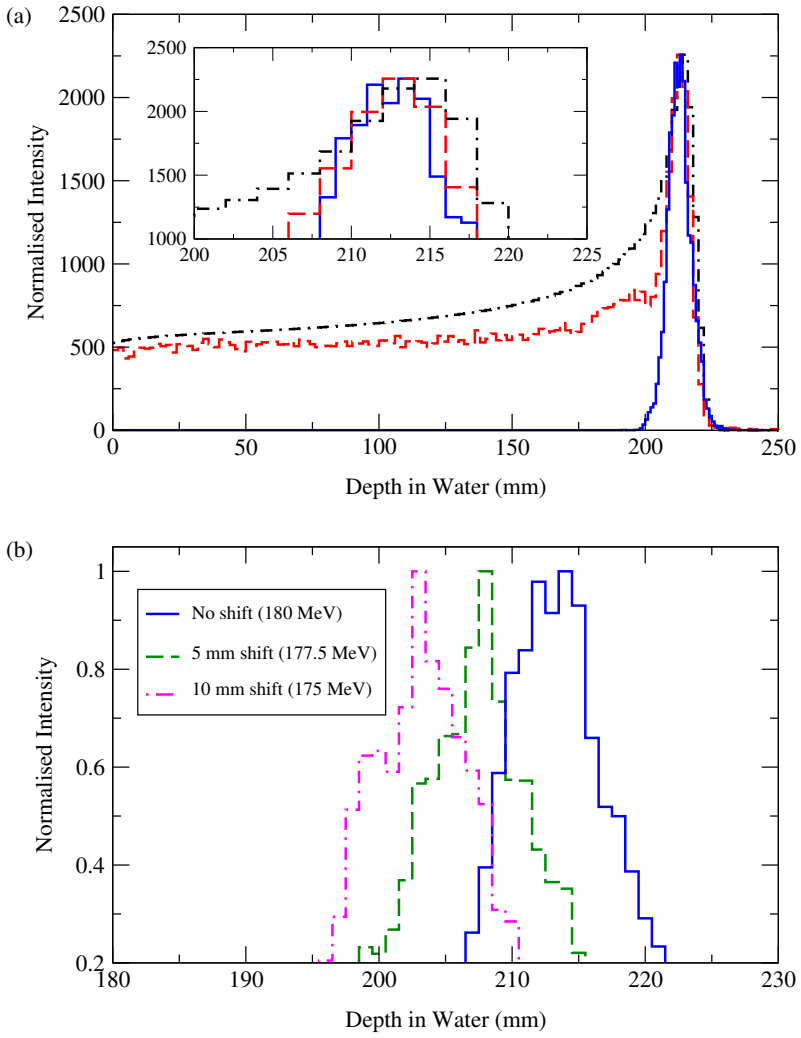

Figure 4.8: (a) A clinical 180 MeV proton pencil beam impinges a 4×4×30 cm^3 water phantom. Two quantities are scored by the phantom: the proton energy deposition (*black* dot-dashed curve) and the 2.741 & 6.128 MeV ^{16}O-induced PG rays (*red* dashed curve). In addition the maximum intensity emission origin of the 2.741 & 6.128 MeV ^{16}O-induced PG rays, detected with the spectrometer and reconstructed with the algorithm, is plotted (*blue* curve). (b) Two clinical proton pencil beams, with energy 175 and 177.5 MeV, impinge the same water phantom. The phantom is modelled so that the spectrometer centre coincides with the Bragg peak for a 180 MeV beam. This translates into a range undershoot of 5 and 10 mm, respectively. The maximum intensity emission origin of the 2.741 & 6.128 MeV ^{16}O-induced PG rays, detected with the spectrometer and reconstructed with the algorithm, is plotted for the 175 (*purple* dot-dashed curve) and 177.5 MeV (*green* dashed curve). For comparison the same plot is shown (*blue* curve) for a 180 MeV beam. All distributions are along the Z axis.

of measurements by Verburg *et al* [SR18]. The 2 mm shift between the depth of the Bragg peak and the depth at which the PG rays are emitted with maximum intensity, highlighted in the inset in the same Figure, is due to the cross-section for ^{16}O PG-ray emission. As shown is Section 4.3.1 the total PG cross section for ^{16}O maximises for incident protons of ∼14 MeV. The distribution (*blue* curve) of γ-ray emittance positions, reconstructed by the algorithm along the Z axis (beam direction), is in agreement with the maximum intensity of the ^{16}O PG-ray distribution.

Table 4.1 shows the results of an investigation into the spectrometer and algorithm performance for increasing treatment volume. To use the device for adult head and neck or adult thoracic based tumours the spectrometer internal radius would have to be set to a

value greater than 8 cm. The reconstruction algorithm takes as one of its inputs the γ-ray detection time, therefore the relative accuracy of the time-of-flight determination increases with flight path, i.e. source to detector distance, up to a limit fixed by the timing resolution of the system. Conversely, for a fixed number of protons/γ-rays, the geometrical efficiency of the spectrometer decreases with increasing radius. For a spectrometer radius of 8, 15, and 25 cm, assuming a proton beam current of 2 nA [SR63], the estimated count rate per detector is 21, 7.8, and 3 Mcps, respectively. At the rate for a realistic treatment radius of 25 cm, using 250 MHz digital electronics, pulse pile up should not be a significant problem. For smaller radii and increased count rate the use of digital electronics would allow logic pile-up rejection or pile-up recovery through pulse shape analysis. The results of an investigation into the spectrometer and algorithm performance for a range undershoot of 5 and 10 mm are presented in Table 4.1 and in Figure 4.8b. Due to the symmetry of the spectrometer these results reflects shifts caused by a range overshoot of the same magnitude.

This work uses a computationally reasonable number of initial protons (10^8), which is comparable to the number of protons delivered in a pencil beam spot. At 68% confidence level, the reconstruction uncertainty is below 7 and 6 mm, for the 25 cm radius case and the 8 cm radius case with a range undershoot of 10 mm, respectively. These uncertainties are comparable to the ones typically fed in to robust planning or the usual margins imposed in PT planning. Following the recipe of Massachusetts General Hospital (MGH), 3.5% of the range plus 1 mm [SR5], for a 180 MeV clinical beam the usual margin is 5.7 mm at 68% confidence level. Currently, the reconstruction obtained in the present work is comparable with the performances of the prototypes based on the Compton camera technique [SR64]. In a second test on patients, Xie *et al* [SR31], using the IBA knife-edge prototype, estimated the shift of the Bragg peak position relative to the plan, with a ± 2 mm precision. Hueso-Gonzalez *et al* [SR42] claims that, with the PG spectroscopy system developed in MGH perfectly aligned on the couch, the absolute range can be reconstructed, in ideal experimental phantoms, with a mean precision of 1.1 mm at 95% confidence level.

For a 180 MeV proton beam, when the internal spectrometer radius is 8 cm, the total number of γ-rays detected is 5,591,199. Amongst these events the 1.34% of them have energies in the two ranges discussed in Section 4.3.3. The number of events accepted by the algorithm in Function 1 is 1,652 (826 *couples*). The authors are additionally investigating the possibility of including, as acceptance criteria, those events whose energy belongs to the single/double escape peaks. With this variation, for the 8 cm radius case, the number of couples rises to 3,884, a $\sim$5 fold increase.

The spectrometer has been modelled with realistic energy and temporal resolution. The detectors of choice for this work are large crystal $LaBr_3$(Ce) scintillators. These crystals possess internal activity, predominantly due to the decay of ^{138}La. The energy of the ^{138}La γ-rays does not overlap with the ^{16}O PG rays of interest. In addition, the coincidence requirement of the algorithm rejects the activity of these γ-rays. The rate of the $LaBr_3$(Ce) internal activity was measured to be 0.85 cts/(s/cm^3) in the energy interval 70-5000 keV [SR54], slow compared to the (p,^{16}O) reaction rate [SR49]. For all these reasons the $LaBr_3$(Ce) internal activity has not been modelled. Additionally, due to the coincidence requirement in the

algorithm, the neutrons-induced γ rays are rejected from the reconstruction process.

The accuracy of this technique is influenced by two main factors, the γ-ray interaction position (x_i, y_i, z_i) in the detector medium and its flight time (t_i). MC simulations can produce detector data with exact final γ-ray interaction positions, however, in reality this hit position is not known to the same precision. Running the simulations many times generates a mean distribution of hits for each detector. A probability density function is then derived from this distribution and sampled to generate interaction co-ordinates needed by the algorithm for non position sensitive detectors. The employment of segmented detector modules, with improved position resolution, is under evaluation. Similarly the exact time difference between γ-ray emission and detection, in reality, is also not available. A common start time provided by a suitable timing device could be employed. If this is achieved, the hit times t_i and t_{i+1} of the two events i and $i+1$ can be individually inferred. In this case the developed algorithm would not need any modification to determine the beam range. An alternative algorithm is under development; it can reconstruct the γ-ray origin without the need for a start time and only needs the γ ray detector arrival times as input.

All the reconstruction results presented in this study were obtained within 30 minutes (Windows 10 64-bit with Intel Core i7-6700 @ 3.41 GHz CPU and 16 GB RAM). The reconstruction algorithm currently runs in a MATLAB environment and a significant decrease in this computational time could be achieved by porting this to a pre-compile binary via a high-level language such as C or C++. Further improvements could be made by porting the algorithm to hardware and both of these options are currently being explored.

4.6 Conclusions

A new technique for range verification in PT has been developed. It is based on the detection of the prompt γ rays that are emitted naturally during delivery. A spectrometer comprising 16 $LaBr_3$(Ce) detectors in a symmetrical configuration is employed to record the prompt γ rays emitted along the proton path. An algorithm has been also developed that takes as inputs the $LaBr_3$(Ce) detector signals and reconstructs the maximum intensity peak position, in full 3 dimensions. The ability to determine proton range in 3D is well suited for spot-scanning systems and for detecting non-uniform anatomical changes such as tumour shrinkage. The spectrometer-algorithm performance has been first investigated for a mono-energetic 180 MeV clinical beam with varying spectrometer radii. The results show that accommodating an adult patient (25 cm spectrometer radius) the proton range could be determined with an uncertainty below 7 mm at 68% confidence level. Additional simulations have been performed with a shift between the beam range and the system origin. In case of a 10 mm range undershoot the PG-ray emission position is reconstructed with an uncertainty below 6 mm at 68% confidence level. Further developments are ongoing to reach the ultimate goal of a clinically compliant system for on-line, real-time range verification.

4.7 Author contributions

In this publication C.M.V.P. developed the Monte Carlo simulation application and the 3D reconstruction algorithm. M.J.T. provided the original concept behind this work, the day-to-day supervision and guided the in-silico developments. R.I.M. provided clinical physics guidance and supervision. K.J.K. provided technical guidance and funding. C.M.V.P. and M.J.T drafted the manuscript. All authors reviewed and approved the manuscript.

4.8 Acknowledgments

C.M.V.P. would like to acknowledge support form CRUK via the funding to Cancer Research UK Manchester Centre: [C147/A18083] and [C147/A25254]. This work was co-founded by the NIHR Manchester Biomedical Research centre.

4.9 Supplementary information

Two simulations have been performed in Geant4; a water phantom ($4\times4\times30$ cm^3) is hit by a clinical 180 MeV proton pencil beam. Both the phantom and the beam are in the central area of the spectrometer and the beam direction coincides with the phantom central axis (Z axis). The phantom has been modelled so that the Bragg peak depth for the 180 MeV beam corresponds to the centre of the spectrometer. This is to ensure that the PG rays emitted close to the Bragg peak are detected by the spectrometer with the maximum solid angle. The number of initial protons simulated has been kept fixed at 10^8. The spectrometer internal radius has been set at 15 and 25 cm. The radius has been varied to represent different clinical scenarios: a head and neck treatment (Figure 4.9) and a thoracic treatment (Figure 4.10). In other words the solid angle subtended by the spectrometer with respect to the origin (0, 0, 0) decreases to 9% (radius 15 cm) and to 3% (radius 25 cm).

The PG rays, emitted in the (p, ^{16}O) nuclear reactions, have been recorded by the spectrometer. The simulations outputs have been processed with the algorithm to reconstruct, in full 3 dimensions, the beam end-of-range value in the phantom. In addition, a scoring mesh ($20\times20\times150$ bins), with the same size and position of the phantom, has been implemented. The quantities scored in the mesh were: 1) the energy deposition per voxel and 2) the 2.741 & 6.128 MeV ^{16}O-induced PG-ray distribution. These quantities are used as a benchmark for the reconstruction algorithm results. The two mesh-based distribution refer to a phantom with $2\times2\times2$ cm^3 voxels. Conversely, for the algorithm-reconstructed distribution, the phantom has been divided in $1\times1\times1$ cm^3 voxels. As the mesh scored quantities are used solely for benchmarking, a larger voxel size was chosen to reduce computation time.

The total number of 2.741 & 6.128 MeV PG-ray *couples*, selected by the algorithm in Function 1, is 387 and 191, when the radius is 15 and 25 cm, respectively. If the *couples* detection rate is Poissonian then the signal-to-noise ratio, SNR, at 191 *couples*, is $\sim$14.

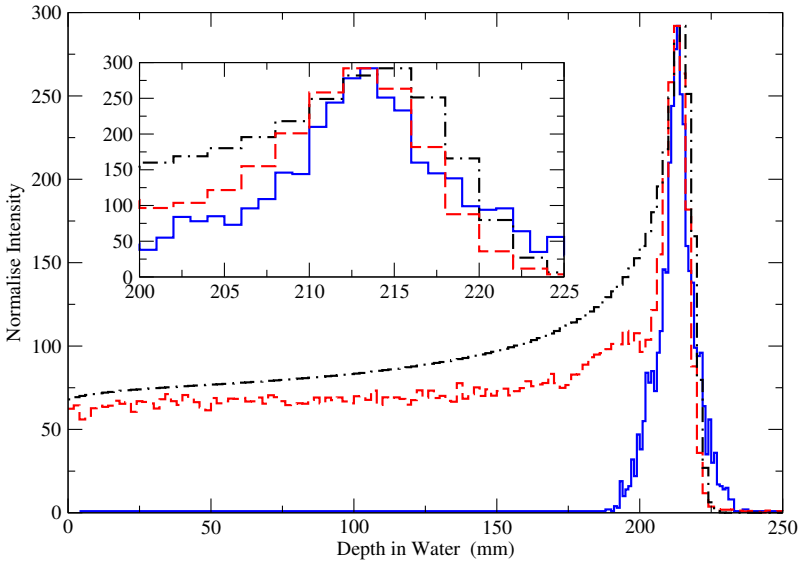

Figure 4.9: A clinical 180 MeV proton pencil beam impinges a water phantom. Two quantities are scored by the phantom: the proton energy deposition (*black* curve) and the 2.741 & 6.128 MeV ^{16}O-induced PG-ray (*red* curve). In addition addition the maximum intensity emission origin of the 2.741 & 6.128 MeV ^{16}O-induced PG-ray, detected with the spectrometer and reconstructed with the algorithm, is plotted (*blue* curve). Distributions are shown along the Z axis. The internal radius of the spectrometer is 15 cm (solid angle $\Omega = 9\%$ subtended by the spectrometer at the central point (0, 0, 0)).

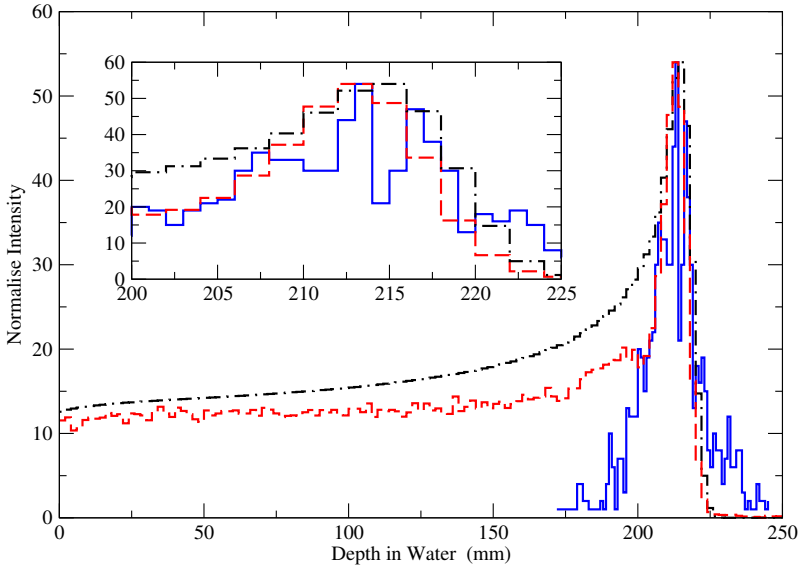

Figure 4.10: A clinical 180 MeV proton pencil beam impinges a water phantom. Two quantities are scored by the phantom: the proton energy deposition (*black* curve) and the 2.741 & 6.128 MeV ^{16}O-induced PG-ray (*red* curve). In addition addition the maximum intensity emission origin of the 2.741 & 6.128 MeV ^{16}O-induced PG-ray, detected with the spectrometer and reconstructed with the algorithm, is plotted (*blue* curve). Distributions are shown along the Z axis. The internal radius of the spectrometer is: 25 cm (solid angle $\Omega = 3\%$ subtended by the spectrometer at the central point (0, 0, 0)).

Bibliography

[SR1] M. Durante and H. Paganetti, "Nuclear physics in particle therapy: a review," *Rep Prog Phys*, vol. 79, p. 096702, 2016.

[SR2] PTCOG, "Particle therapy facilities in a planning stage (update February 2019)," 2020.

[SR3] PTCOG, "Particle therapy facilities under construction (update February 2019)," 2020.

[SR4] A. Knopf and A. Lomax, "In vivo proton range verification: a review," *Phys Med Biol*, vol. 58, p. R131, 2013.

[SR5] H. Paganetti, "Range uncertainties in proton therapy and the role of Monte Carlo simulations," *Phys Med Biol*, vol. 57, p. R99, 2012.

[SR6] B. Schaffner and E. Pedroni, "The precision of proton range calculations in proton radiotherapy treatment planning: experimental verification of the relation between CT-HU and proton stopping power," *Phys Med Biol*, vol. 43, p. 1579, 1998.

[SR7] A. V. Chvetsov and S. L. Paige, "The influence of CT image noise on proton range calculation in radiotherapy planning," *Phys Med Biol*, vol. 55, p. N141, 2010.

[SR8] S. España and H. Paganetti, "The impact of uncertainties in the ct conversion algorithm when predicting proton beam ranges in patients from dose and PET-activity distributions," *Phys Med Biol*, vol. 55, p. 7557, 2010.

[SR9] Y. Kumazaki *et al.*, "Determination of the mean excitation energy of water from proton beam ranges," *Radiat Meas*, vol. 42, pp. 1683–1691, 2007.

[SR10] J. Liebl, H. Paganetti, M. Zhu, and B. A. Winey, "The influence of patient positioning uncertainties in proton radiotherapy on proton range and dose distributions," *Med Phys*, vol. 41, p. 091711, 2014.

[SR11] J. Unkelbach *et al.*, "Robust radiotherapy planning," *Phys Med Bio*, vol. 63, p. 22TR02, 2018.

[SR12] M. Van Herk *et al.*, "Quantification of organ motion during conformal radiotherapy of the prostate by three dimensional image registration," *Int J Radiat Oncol Biol Phys*, vol. 33, pp. 1311–1320, 1995.

[SR13] H. Z. Hui *et al.*, "Effects of interfractional motion and anatomic changes on proton therapy dose distribution in lung cancer," *Int J Radiat Oncol Biol Phys*, vol. 72, pp. 1385–1395, 2008.

[SR14] C. Han, Y. Chen, A. Liu, T. E. Schultheiss, and J. Y. Wong, "Actual dose variation of parotid glands and spinal cord for nasopharyngeal cancer patients during radiotherapy," *Int J Radiat Oncol Biol Phys*, vol. 70, pp. 1256–1262, 2008.

[SR15] Y. Z. Szeto and othersl, "Effects of anatomical changes on pencil beam scanning proton plans in locally advanced NSCLC patients," *Radiother Oncol*, vol. 120, pp. 286–292, 2016.

[SR16] C. Kurz *et al.*, "Comparing cone-beam CT intensity correction methods for dose recalculation in adaptive intensity-modulated photon and proton therapy for head and neck cancer," *Acta Oncol*.

[SR17] B. Kozlovsky, R. J. Murphy, and R. Ramaty, "Nuclear deexcitation gamma-ray lines from accelerated particle interactions," *Astrophys J Suppl S*, vol. 141, p. 523, 2002.

[SR18] J. M. Verburg, K. Riley, T. Bortfeld, and J. Seco, "Energy- and time-resolved detection of prompt gamma-rays for proton range verification," *Phys Med Biol*, vol. 58, p. L37, 2013.

[SR19] J. M. Verburg, H. A. Shih, and J. Seco, "Simulation of prompt gamma-ray emission during proton radiotherapy," *Phys Med Biol*, vol. 57, p. 5459, 2012.

[SR20] M. Moteabbed, S. España, and H. Paganetti, "Monte Carlo patient study on the comparison of prompt gamma and PET imaging for range verification in proton therapy," *Phys Med Biol*, vol. 56, p. 1063, 2011.

[SR21] K. Parodi and W. Enghardt, "Potential application of PET in quality assurance of proton therapy," *Phys Med Biol*, vol. 45, p. N151, 2000.

[SR22] J. Krimmer, D. Dauvergne, J. Létang, and É. Testa, "Prompt-gamma monitoring in hadrontherapy: A review," *Nucl Instr Meth Phys Res A*, vol. 878, pp. 58–73, 2018.

[SR23] C. Min, C. H. Kim, M. Youn, and J. Kim, "Prompt gamma measurements for locating the dose falloff region in the proton therapy," *Appl Phys Lett*, vol. 89, p. 183517, 2006.

[SR24] C. H. Kim, C. H. Min, K. S. Seo, and J. Kim, "Simulation studies on the correlation of distal dose falloff of a 70-MeV proton beam with a prompt gamma distribution," *J Korean Phys Soc*, vol. 50, p. 1510, 2007.

[SR25] C. Min, H. Lee, C. Kim, and S. Lee, "Development of array-type prompt gamma measurement system for in vivo range verification in proton therapy," *Med Phys*, vol. 39, pp. 2100–2107, 2012.

[SR26] M. Pinto *et al.*, "Design optimisation of a TOF-based collimated camera prototype for online hadrontherapy monitoring," *Phys Med Biol*, vol. 59, p. 7653, 2014.

[SR27] J. Kim, "Pinhole camera measurements of prompt gamma-rays for detection of beam range variation in proton therapy," *J Korean Phys Soc*, vol. 55, p. 1673, 2009.

[SR28] J. Smeets *et al.*, "Prompt gamma imaging with a slit camera for real-time range control in proton therapy," *Phys Med Biol*, vol. 57, p. 3371, 2012.

[SR29] I. Perali *et al.*, "Prompt gamma imaging of proton pencil beams at clinical dose rate," *Phys Med Biol*, vol. 59, p. 5849, 2014.

[SR30] C. Richter *et al.*, "First clinical application of a prompt gamma based in vivo proton range verification system," *Radiother Oncol*, vol. 118, pp. 232–237, 2016.

[SR31] Y. Xie *et al.*, "Prompt gamma imaging for in vivo range verification of pencil beam scanning proton therapy," *Int J Radiat Oncol Biol Phys*, vol. 99, pp. 210–218, 2017.

[SR32] G. Llosá *et al.*, "First images of a three-layer Compton telescope prototype for treatment monitoring in hadron therapy," *Front Oncol*, vol. 6, p. 14, 2016.

[SR33] T. Taya *et al.*, "First demonstration of real-time gamma imaging by using a handheld Compton camera for particle therapy," *Nucl Instr Meth Phys Res A*, vol. 831, pp. 355–361, 2016.

[SR34] M. McCleskey *et al.*, "Evaluation of a multistage CdZnTe Compton camera for prompt γ imaging for proton therapy," *Nucl Instr Meth Phys Res A*, vol. 785, pp. 163–169, 2015.

[SR35] E. Draeger *et al.*, "3D prompt gamma imaging for proton beam range verification," *Phys Med Biol*, vol. 63, p. 035019, 2018.

[SR36] J. Krimmer *et al.*, "Development of a Compton camera for medical applications based on silicon strip and scintillation detectors," *Nucl Instr Meth Phys Res A*, pp. 98–101, 2015.

[SR37] S. Aldawood *et al.*, "Development of a Compton camera for prompt-gamma medical imaging," *Radiat Phys Chem*, pp. 190–197, 2017.

[SR38] F. Hueso-González *et al.*, "Test of Compton camera components for prompt gamma imaging at the ELBE bremsstrahlung beam," *J Instrum*, vol. 9, p. P05002, 2014.

[SR39] M. Takahashi *et al.*, "Development of an electron-tracking Compton camera using CF4 gas at high pressure for improved detection efficiency," *Nucl Instr Meth Phys Res A*, vol. 628, pp. 150–153, 2011.

[SR40] H. Rohling *et al.*, "Requirements for a Compton camera for in vivo range verification of proton therapy," *Phys Med Biol*, vol. 62, p. 2795, 2017.

[SR41] C. Golnik *et al.*, "Range assessment in particle therapy based on prompt γ-ray timing measurements," *Phys Med Biol*, vol. 59, p. 5399, 2014.

[SR42] Hueso-González *et al.*, "A full-scale clinical prototype for proton range verification using prompt gamma-ray spectroscopy," *Phys Med Biol*, vol. 63, p. 185019, 2018.

[SR43] X. Lojacono *et al.*, "Low statistics reconstruction of the Compton camera point spread function in 3D prompt-gamma imaging of ion beam therapy," *IEEE Trans Nucl Sci*, vol. 60, pp. 3355–3363, 2013.

[SR44] V. Maxim, "Filtered backprojection reconstruction and redundancy in Compton camera imaging," *IEEE Trans Image Process*, vol. 23, pp. 332–341, 2013.

[SR45] V. Maxim *et al.*, "Probabilistic models and numerical calculation of system matrix and sensitivity in list-mode MLEM 3D reconstruction of Compton camera images," *Phys Med Biol*, vol. 61, p. 243, 2015.

[SR46] S. Schoene *et al.*, "An image reconstruction framework and camera prototype aimed for Compton imaging for in-vivo dosimetry of therapeutic ion beams," *IEEE Trans Radiat Plasma Med Sci*, vol. 1, pp. 96–107, 2016.

[SR47] D. Mackin, S. Peterson, S. Beddar, and J. Polf, "Evaluation of a stochastic reconstruction algorithm for use in Compton camera imaging and beam range verification from secondary gamma emission during proton therapy," *Phys Med Biol*, vol. 57, p. 3537, 2012.

[SR48] A. Andreyev, A. Celler, I. Ozsahin, and A. Sitek, "Resolution recovery for Compton camera using origin ensemble algorithm," *Med Phys*, vol. 43, pp. 4866–4876, 2016.

[SR49] W. H. R. Tilley D R and C. C. M, "Energy levels of light nuclei A = 16-17," *Nucl Phys A*, vol. 564, no. 1, pp. 1–183, 1993.

[SR50] M. Nikl, "Scintillation detectors for X-rays," *Meas Sci Technol*, vol. 17, p. R37, 2006.

[SR51] J. C. Polf *et al.*, "Measurement of characteristic prompt gamma rays emitted from oxygen and carbon in tissue-equivalent samples during proton beam irradiation," *Phys Med Biol*, vol. 58, p. 5821, 2013.

[SR52] A. Drescher *et al.*, "Gamma-gamma coincidence performance of $LaBr_3$:Ce scintillation detectors vs HPGe detectors in high count-rate scenarios," *Appl Radiat Isot*, vol. 122, pp. 116–120, 2017.

[SR53] B. Löher *et al.*, "High count rate γ-ray spectroscopy with $LaBr_3$:Ce scintillation detectors," *Nucl Instrum Methods Phys Res A*, vol. 686, pp. 1–6, 2012.

[SR54] R. Nicolini *et al.*, "Investigation of the properties of a 1" $\times$ 1" $LaBr_3$:Ce scintillator," *Nucl Instr Meth Phys Res A*, vol. 582, pp. 554–561, 2007.

[SR55] S. Agostinelli *et al.*, "GEANT4 - A simulation toolkit," *Nucl Instrum Methods Phys Res A*, vol. 506, pp. 250–303, 2003.

[SR56] M. Dhibar, I. Mazumdar, P. Chavan, S. Patel, and G. A. Kumar, "Characterization of a 2" $\times$ 2" array of large square bars of $LaBr_3$:Ce detectors with γ-rays up to 22.5 MeV," *Nucl Instr Meth Phys Res A*, vol. 883, pp. 183–190, 2018.

[SR57] T. Möller, "A fast triangle-triangle intersection test," *J Graph Tools*, vol. 2, pp. 25–30, 1997.

[SR58] F. Quarati *et al.*, "X-ray and gamma-ray response of a 2" × 2" $LaBr_3$:Ce scintillation detector," *Nucl Instr Meth Phys Res A*, vol. 574, pp. 115–120, 2007.

[SR59] S. Aldawood *et al.*, "Comparative characterization study of a $LaBr_3$(Ce) scintillation crystal in two surface wrapping scenarios: Absorptive and reflective," *Front Oncol*, vol. 5, p. 270, 2015.

[SR60] C. Z. Jarlskog and H. Paganetti, "Physics settings for using the Geant4 toolkit in proton therapy," *IEEE Trans Nucl Sci*, vol. 55, pp. 1018–1025, 2008.

[SR61] M. Pinto *et al.*, "Assessment of GEANT4 prompt-gamma emission yields in the context of proton therapy monitoring," *Front Oncol*, vol. 6, p. 10, 2016.

[SR62] M. Zarifi *et al.*, "Characterization of prompt gamma-ray emission with respect to the Bragg peak for proton beam range verification: A Monte Carlo study," *Phys Med*, vol. 33, pp. 197–206, 2017.

[SR63] G. Pausch *et al.*, "Detection systems for range monitoring in proton therapy: Needs and challenges," *Nucl Instrum Methods Phys Res A*, 2018.

[SR64] J. Krimmer *et al.*, "A cost-effective monitoring technique in particle therapy via uncollimated prompt gamma peak integration," *Appl Phys Letts*, vol. 110, p. 154102, 2017.

Chapter 5

Critique of Publication 1

This Chapter presents additional information on the investigation reported in Panaino *et al* [267]. Some features, briefly considered in the publication, are more deeply evaluated. The expected detector load is estimated (Section 5.1) and the final result is discussed in light of the available literature data on $LaBr_3$ performance at high-count scenarios. A key "geometrical" aspect of the algorithm, the minor radius of the tori, is then considered (Section 5.2). Part of the evaluations in this Chapter was stimulated by the discussion with the reviewers during the Scientific Reports peer-review process.

5.1 Spectrometer detection efficiency

Detector efficiencies are typically divided into two classes: absolute ϵ_{abs} and intrinsic ϵ_{int}. ϵ_{abs} is the ratio of the number of counts recorded by the detector to the number of γ-rays isotropically emitted by the source. ϵ_{int} is the ratio of the number of counts recorded by the detector to the number of γ-rays hitting the detector. ϵ_{abs} depends on the detector properties and on the counting set-up geometry, while ϵ_{int} primarily depends on the detection material, the energy of the incoming radiation, and the detector physical thickness in the direction of the radiation. For isotropic sources ϵ_{abs} and ϵ_{int} are related by the formula: $\epsilon_{abs} = \epsilon_{int} \cdot \epsilon_{geom}$, where ϵ_{geom}, the geometrical efficiency, is the ratio of the number of γ-rays hitting the detector to the number of γ-rays isotropically emitted by the source [268].

5.1.1 Estimation of geometrical efficiency

ϵ_{geom} is defined as $\Omega/4\pi$, where Ω is the solid angle subtended by the source to the detector. For a point source along the axis of a cylindrical detector Ω is given by the formula:

$$\Omega = 2\pi \left(1 - \frac{d_{detector-source}}{\sqrt{d^2_{detector-source} + r^2_{detector}}} \right) \tag{5.1}$$

The spectrometer evaluated in Panaino *et al* [267] is composed of 16 $LaBr_3$ cylindrical detectors (2" length/1.5" diameter). Assuming that the source, i.e. the (p,^{16}O) reaction, is at (0, 0, 0), ϵ_{geom} is reported in Table 5.1. Values are listed for all the internal radii considered in the publication, for both a single detector and the full spectrometer.

	ϵ_{geom}	
Internal radius (cm)	**Single detector**	**Spectrometer**
8	1.36%	21.76%
15	0.40%	6.37%
25	0.14%	2.31%

Table 5.1: Geometrical efficiency values ϵ_{geom} for a single detector and the full spectrometer (16 detectors), internal radii from Panaino *et al* [267]

5.1.2 Estimation of intrinsic efficiency

Figure 5.1 shows the γ-spectrum deposited in the spectrometer in the range 0.1-8 MeV. The range 0-0.1 MeV was omitted as it is predominantly dominated by the X-rays generated in the detectors. The spectrum is associated to a simulation with a 180 MeV beam shot on a water phantom, as described in Panaino *et al* [267] (Section 8.3.5). The average energy <E> is 1.67 MeV. Such a "low" value is due to the high rate of detected 511 keV γ-rays.

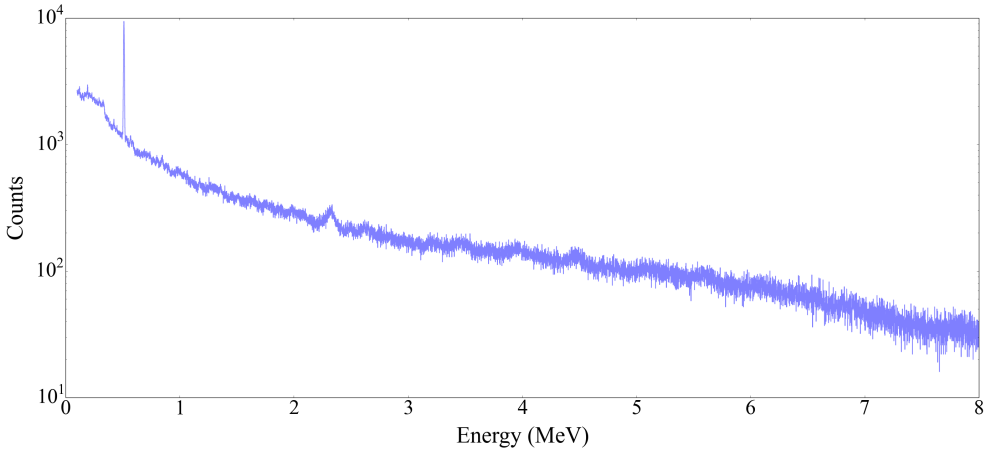

Figure 5.1: Energy spectrum in the range 0.1-8 MeV, deposited in the spectrometer from Panaino *et al* [267], with an 8 cm internal radius. The γ radiation originates from a water phantom impinged by a 180 MeV proton pencil beam with 10^8 initial events (Geant4 simulation).

ϵ_{int} can be estimated using the Beer-Lambert law:

$$\epsilon_{int} \sim 1 - e^{(-\mu \cdot x)} = 1 - e^{\left(-\frac{\mu}{\rho} \cdot \rho \cdot x\right)} \tag{5.2}$$

Where x, μ, and ρ are the thickness, the linear attenuation coefficient and the density of the detector, respectively. The ratio μ/ρ, known as *mass attenuation coefficient*, describes the fraction of incident γ rays attenuated for coherent scatter, Compton scatter, photoelectric effect, and pair production (if applicable) and varies with the energy of the incoming γ radiation. Mass attenuation coefficients are available through the NIST database [269]. For the $LaBr_3$ material (ρ=5.06 cm^2/g), and an incoming γ energy of <E>, μ/ρ is 0.0433 g/cm^3. Thus Eq. 5.2 gives:

$$\epsilon_{int} \sim 1 - e^{(-4.33 \cdot 10^{-2} \frac{cm^2}{g} \cdot 5.06 \frac{g}{cm^3} \cdot 5.08 cm)} = 0.67 = 67\% \tag{5.3}$$

Very small energy depositions do not contribute to triggers and pile-up. If 10% of all events are in this "non detectable" region, ϵ_{int} would be the ~57%.

5.1.3 Estimation of absolute efficiency

For an 8 cm radius, using the single detector ϵ_{geom} value from Table 5.1, and the ϵ_{int} value calculated in Section 5.1.2, $\epsilon_{abs} = \epsilon_{geom} \cdot \epsilon_{int} = 0.78\%$, at any energy producing a trigger. For a 15 and a 25 cm radius the single detector ϵ_{abs} values are listed in Table 5.2.

Internal radius (cm)	ϵ_{abs}
8	0.78%
15	0.23%
25	0.08%

Table 5.2: Single detector absolute efficiency values ϵ_{abs}, internal radii from Panaino *et al* [267]

5.1.4 Estimation of detector load

In case of a clinical delivery with pencil-beam scanning, an instantaneous proton beam current of ∼2 nA, corresponding to $1.2 \cdot 10^{10}$ protons per second (pps), can be estimated [142]. This average takes into account the overall duty cycle of the accelerator during scanning and layer switching. Assuming that a γ de-excitation is emitted from the 10% of the protons, $1.2 \cdot 10^9$ γ per second (γps) are emitted. For an 8 cm internal radius, employing the single detector ϵ_{abs} value from Table 5.2, the expected load per unit time, at any energy producing a trigger, is $\epsilon_{abs} \cdot (1.2 \cdot 10^9)$ γps $= 9.29 \cdot 10^6$ γps. An analogous calculation can be performed for a 15 and a 25 cm radius. Results are reported in Table 5.3.

Internal radius (cm)	**Single detector load (γps)**
8	$9.4 \cdot 10^6$
15	$2.8 \cdot 10^6$
25	$9.6 \cdot 10^5$

Table 5.3: Single detector load per unit time, internal radii from Panaino *et al* [267]

5.1.5 Estimation of detector load, cross-check

The estimation of the detector load, reported in the Section 5.1.4, can be cross-checked using the statistic of the simulations reported in Panaino *et al* [267]. All simulations refer to 10^8 protons. Assuming a proton current of $1.2 \cdot 10^{10}$ pps (∼2nA), 10^8 protons are delivered in 0.008 s. For an 8 cm radius, the spectrometer records 5,591,199 γ-rays. Therefore the total count-rate is 5,591,199 γ/0.008 s $= 6.98 \cdot 10^8$ γps and the count-rate per detector is $6.98 \cdot 10^8$ γps/16 $= 4.3 \cdot 10^7$ γps. The detector load, given by the count-rate multiplied by ϵ_{int}, is $2.4 \cdot 10^7$ γps. For a radius of 15 and 25 cm, the spectrometer measures 2,074,629 and 797,121 γ-rays, respectively. The detector load yields $8.9 \cdot 10^6$ γps (15 cm) and $3.4 \cdot 10^6$ γps (25 cm). With respect to the calculation in Section 5.1.4, this estimate should be more accurate, as it includes neutron-induced γ-rays, also contributing to trigger and pile-up.

5.1.6 $LaBr_3$ performance at high count-rate scenarios

In γ-spectroscopy experiments, to avoid signal distortion, the maximum count-rate capability of a detector must not be exceeded. In our set-up, for a 15 cm spectrometer radius, the

expected detector load per unit time was estimated as $2.8 \cdot 10^6$ γps (Section 5.1.4).

$LaBr_3$ is an excellent detector choice for high count-rate scenarios. Loher *et al* [270] investigated the dependence of energy resolution and photo peak efficiency on the load of a 3"×3" $LaBr_3$ crystal, using radioactive sources. It was observed that, using standard techniques, a good performance can be obtained up to a ∼500 kHz count-rate. At increasing count-rates, the average time difference between two consecutive pulses is shorter than the individual pulse-length. Thus, different pulses overlap in time, resulting in a loss of information. This phenomenon, known as "pile-up", leads to a reduction of the energy resolution and of the photo peak efficiency. To further enhance the $LaBr_3$ capabilities in the region between 500 kHz and 10 MHz a pile-up correction method can be applied [271].

Most existing prototypes for range verification via PG detection (Section 2.2) are affected by the neutron-induced γ background. A γ-γ coincidence set-up, as the one presented in Panaino *et al* [267], has the advantage of discarding background peaks that do not exist in coincidence. Indeed Drescher *et al* [272] proved that a substantial signal-to-noise improvement is gained in γ-γ coincidence over single detector spectroscopy.

The ability to handle high count-rates is of prime relevance in coincidence spectroscopy. In single detector spectroscopy, by moving the source away from the detector, the count-rate is lowered, thus activity levels do not pose a concern. In γ-γ coincidence spectroscopy, the efficiency of coincidence counting drops off as x^{-4}, where x is the source-detector distance, while the count-rate drops only as x^{-2}. As a matter of fact, the two detectors should be as close to each other, and to the source, as possible. According to Drescher *et al* [272], in γ-γ coincidence, $LaBr_3$ detectors can handle counts-rates of ∼400 kHz or greater.

A clinical employment of the spectrometer in Panaino *et al* [267] is envisaged for just an initial fraction of the treatment, instead that for the full beam. The idea is to reduce the beam current for the first spots, and then deliver the rest at normal current. In this way, when range verification in "on", the detector count-rate is acceptable and the internal radius, within the limitation of patient size and treatment location, is minimum.

5.2 Selection of the tori minor radius

In the second function of the algorithm, γ-Ray *Couple* Analysis (Section 4.3.1), for each *couple*, two spheres are generated. The *intersection* circle, representing the intersection of the two spheres, is then calculated. As shown in Figure 5.2, a torus is constructed around the circle. The major radius of each torus corresponds to the radius of the *intersection* circle, thus its value is unique for each *couple*. The minor radius is 3 mm in magnitude, same for all tori. Aim of this Section is to provide a justification for the selection of this value. The tori minor radius was chosen considering an increase of the position-reconstruction σ due to: 1) the inclusion of the $LaBr_3$ time resolution in the simulation and 2) the back-shift effect.

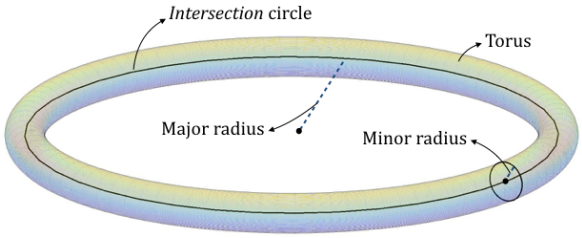

Figure 5.2: In the second function of the algorithm, γ-Ray *Couple* Analysis, for each *couple* two spheres are constructed and the *intersection* circle, which represents the intersection of the two spheres, is calculated. A torus is constructed around each circle. The major radius of each torus is the radius of the *intersection* circle, different for each *couple*. The minor radius is 3 mm in magnitude, same for all tori.

5.2.1 $LaBr_3$ time resolution

In the algorithm, for each γ-ray γ_i, belonging to a *couple*, a sphere is constructed. One essential parameter for this construction is the time difference t_i between the emission and arrival time of γ_i in Det_i. In the simulation, to obtain t_i, a random value is added to the exact emission-to-arrival time difference of γ_i in Det_i. This random value follows a Gaussian distribution with $\sigma_{gaussian} = 280$ ps, where 280 ps is the $LaBr_3$ time resolution [273].

A simulation was performed with no time resolution. The geometry was identical to the one in Panaino *et al* [267]. Indeed it was characterised by a 180 MeV proton beam and a 8 cm spectrometer internal radius. The number of primary events was 10^8. The lateral spread (standard deviation), σ, and the centroid, μ, of the algorithm-reconstructed maximum intensity ^{16}O PG-ray distribution were 21.41 and 0.24 cm, respectively. When the time resolution was included in the simulation, as reported in the manuscript, the σ was 0.42 cm. Thus, by including the $LaBr_3$ time resolution, σ increases by $\sim$2 mm.

5.2.2 Back-shift effect

For each γ-ray, γ_i, belonging to a *couple*, the centre of the sphere is given by the coordinates (x_i, y_i, z_i) of the last hit of γ_i in Det_i. The number and the coordinates of all the previous hits of γ_i in Det_i, before γ_i is fully absorbed in (x_i, y_i, z_i), are not requested in input, although technically available in-silico. By not considering the deviations between all hit positions in Det_i (i.e. assuming a straight path instead than a zig-zig one), the time t_i is not appropriately decreased. Thus, the path length (i.e. the sphere radius) is over-estimated and the source emitting position is back-shifted. This effect, leading to a σ increment of $\sim$1 mm, is shown in Figure 5.3 where the back-shift is exaggerated to aid comprehension.

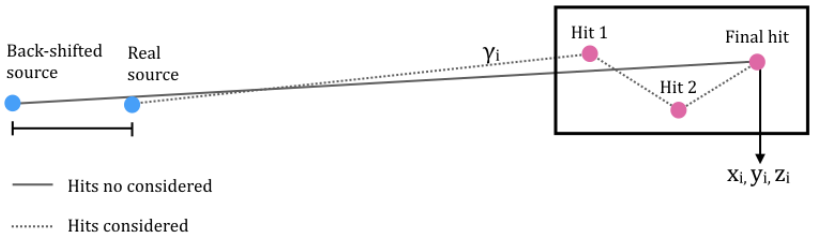

Figure 5.3: Source position back-shift effect: if all hit positions of γ_i in Det_i are not considered, and a straight path (grey line) is chosen with respect to a zig-zig path (grey dotted line), the time t_i is not appropriately decreased, the path length is over-estimated, and the source emitting position is back-shifted.

Chapter 6

Publication 2

6.1 Introduction to Publication 2

In the first publication, Panaino *et al* [267], the development of a new mathematical reconstruction algorithm, Algorithm 1, is reported. Algorithm 1 determines the emittance position of γ-rays in cascade. To assess in-vivo range verification, Algorithm 1 is aimed at reconstructing the emittance position of the ^{16}O-induced PG-rays, naturally produced during PT. In Algorithm 1, when a γ-ray γ_i enters the sensitive area of a detector, the time t_i, difference between the detection time t_{d_i} and the emission time t_{e_i}, is saved (Figure 6.1). If two events γ_i and γ_{i+1} are accepted as a *couple*, the time-values $t_i = t_{d_i}$-t_{e_i} and $t_{i+1} = t_{d_{i+1}}$-$t_{e_{i+1}}$ are both requested in input. In reality, i.e. in the laboratory environment, the emission time t_{e_i} is not easily accessible, unless a suitable timing device is employed. If t_{e_i} is not available, t_i can not be estimated. Conversely T_i, the difference between the detection time t_{d_i} and the start of acquisition t_0, is available. The time-values T_i and T_{i+1}, however, can not be employed in the algorithm from Panaino *et al* [267]. Due to the inclusion of the time frame t_{e_i}-t_0, compared to t_i, T_i is much bigger in magnitude. From a geometrical point of view, this results in a longer radius of the sphere (Section 4.3.1) and an incorrect torus, which does not include anymore the original emittance position.

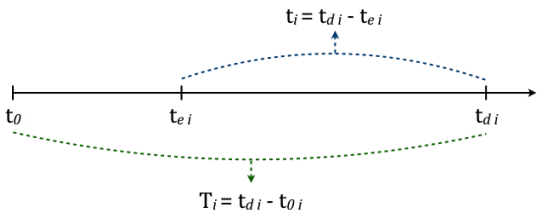

Figure 6.1: For the γ-ray γ_i representation of the detection time t_{d_i}, the emission time t_{e_i}, and the time t_0 at which the acquisition has started.

Assuming that the two events γ_i/γ_{i+1} are emitted together ($t_{e_i} \sim t_{e_{i+1}} = t_e$), it can be proved that the measurable difference T_{i+1}-T_i equals the difference t_{i+1}-t_i.

$$
\begin{aligned}
T_{i+1} - T_i =& (t_{d_{i+1}} - t_0) - (t_{d_i} - t_0) = (t_{d_{i+1}} - t_{e_{i+1}} + t_{e_{i+1}} - t_0) - (t_{d_i} - t_{e_i} + t_{e_i} - t_0) \\
&\sim (t_{d_{i+1}} - t_e + t_e - t_0) - (t_{d_i} - t_e + t_e - t_0) = (t_{d_{i+1}} - t_e) - (t_{d_i} - t_e) \\
&= t_{i+1} - t_i
\end{aligned}
$$

A new version of the algorithm, Algorithm 2, is now presented. Algorithm 2 requests in input, for each *couple* γ_i/γ_{i+1}, only the time-difference t_{i+1}-t_i, instead of the two values t_{i+1}/t_i separately. As a matter of fact, Algorithm 2 is aimed at solving the same reconstruction problem as Algorithm 1, but with one input variable less. The time-related input values, as requested by Algorithm 1 and 2, are depicted in Figure 6.2. Compared to Algorithm 1, Algorithm 2 makes use of a new 3D geometry; still a similar approach is noticeable.

For each γ-ray, γ_i, recorded by the spectrometer, both algorithms are fed the coordinates of the last hit position in the detector (x_i,y_i,z_i). Monte Carlo simulations provide these coordinates exactly, however, as with many large crystal, non position-sensitive detectors, this information is not available in the laboratory environment. The interaction co-ordinates employed in Algorithm 2 are not provided by simulations, instead they are sampled from previously calculated probability density function distributions.

In this publication the reconstruction of the emission position of an isotropic point ^{60}Co source is reported. The source has been modelled at several known locations within the spectrometer central volume. Only realistic detector signals are employed. The full MATLAB code of the reconstruction algorithm is reported in Appendix 3.

The work is published in: *Panaino, C.M., Mackay, R.I., Sotiropoulos, M., Kirkby, K.J. and Taylor, M.J., 2020. Full 3D position reconstruction of a radioactive source based on a novel hyperbolic geometrical algorithm. Computer Physics Communications, 252, p.107131.*

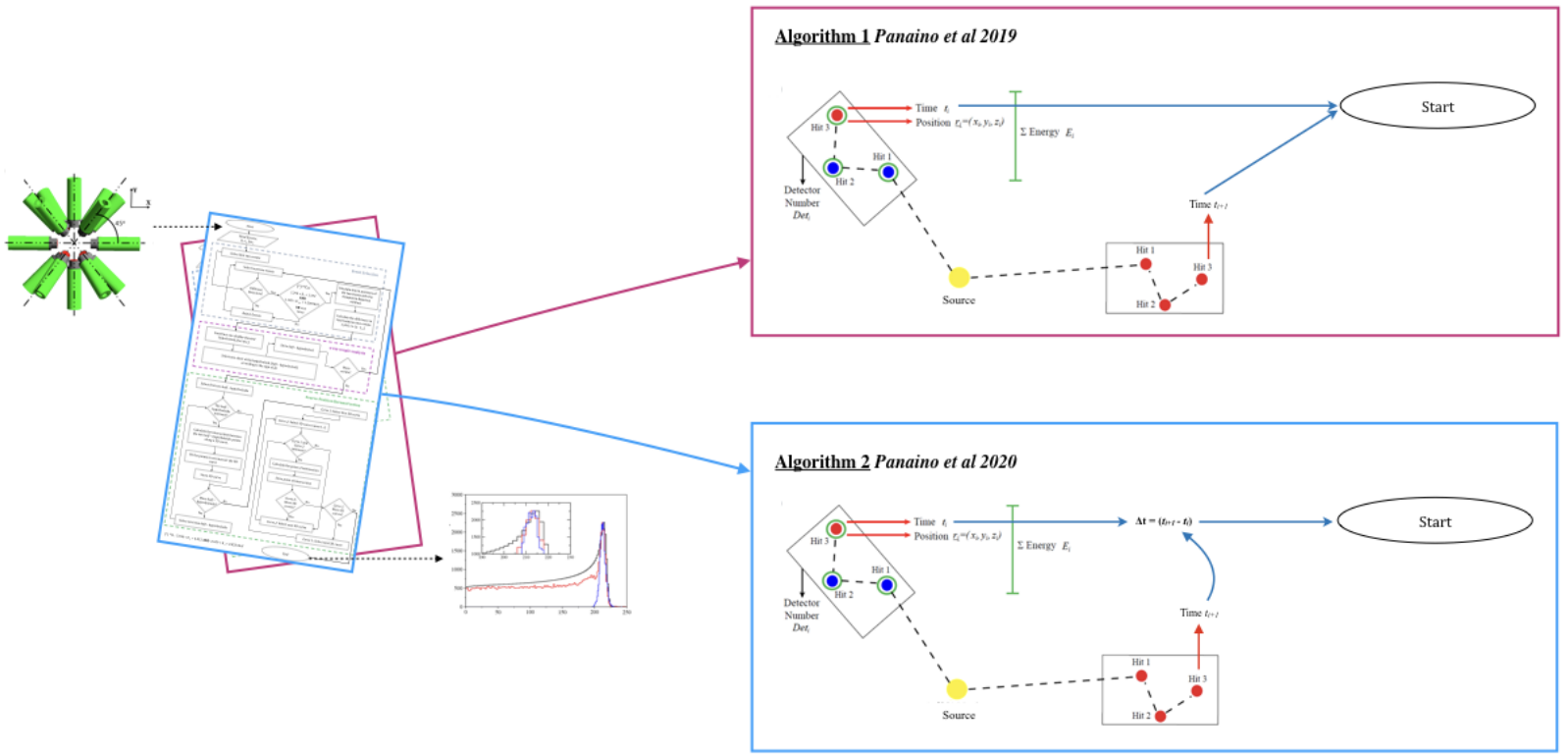

Figure 6.2: Time-related input values, as requested by Algorithm 1 from Panaino *et al* [267] and by Algorithm 2 from Panaino *et al* [274]. For each γ-rays γ_i and γ_{i+1}, belonging to a *couple*, Algorithm 1 requires the two separate values t_{i+1} and t_i, while Algorithm 2 requires only the time-difference t_{i+1}-t_i.

Full 3D position reconstruction of a radioactive source based on a novel hyperbolic geometrical algorithm[1]

Costanza M. V. Panaino[1,*], Ranald I. Mackay[1,2], Marios Sotiropoulos[1], Karen J. Kirkby[1,2] and Michael J. Taylor[1,2]

[1] Division of Cancer Sciences, University of Manchester, M13 9PL, Manchester, UK;

[2] The Christie NHS Foundation Trust, M20 4BX, Manchester, UK;

[*] Corresponding author

A new method to locate, with millimetre uncertainty, in 3D, a γ-ray source emitting multiple γ-rays in a cascade, employing conventional $LaBr_3$(Ce) scintillation detectors, has been developed. Using 16 detectors in a symmetrical configuration the detector energy and time signals, resulting from the γ-ray interactions, are fed into a new source position reconstruction algorithm. The Monte Carlo based Geant4 framework has been used to simulate the detector array and a ^{60}Co source located at two positions within the spectrometer central volume. For a source located at (0,0,0) the algorithm reports X, Y, Z values of -0.3 $\pm$ 2.5, -0.4 $\pm$ 2.4, and -0.6 $\pm$ 2.5 mm, respectively. For a source located at (20,20,20) mm, with respect to the array centre, the algorithm reports X, Y, Z values of 20.2 $\pm$ 1.0, 20.2 $\pm$ 0.9, and 20.1 $\pm$ 1.2 mm. The resulting precision of the reconstruction means that this technique could find application in a number of areas including nuclear medicine, national security, radioactive waste assay and proton beam therapy.

Keywords: reconstruction algorithm, gamma-ray spectroscopy, source emission position reconstruction.

[1]The layout of the publication has undergone visual changes to improve readability in the thesis format.

6.2 Introduction

There are a number of instances where the knowledge of the location of a source of radiation is highly desirable. One example is in cargo scanning where the detection and localisation of illegal radioactive sources could be a major concern for national security. The need to accurately locate radioactive samples is also a crucial requirement in the nuclear energy industry. Radioactive waste measurement instruments, for instance, employ various technologies to locate and quantify the radioactive content in waste samples [CPC1]. In nuclear medicine the position reconstruction of an emitting source represents the core of emission tomographic imaging techniques, such as Single Photon Emission Computed Tomography (SPECT) [CPC2].

The ability to determine the location of a γ-rays source, with high precision using conventional radiation detectors, is a challenge. Some existing techniques utilise the Time Of Flight (TOF) of γ-rays, where both the start (i.e. emission) time and the final (i.e. detection) time of the rays is needed. Usually the final time is provided by the radiation detection instrument but the start time can be extremely difficult to obtain, in particular for radioactive sources. For distributed sources, such as those produced during Proton Beam Therapy (PBT) in cancer treatment, the challenge can be even greater. The precise knowledge of the beam range is essential to guarantee the treatment's efficacy and to avoid toxicities. One proposed method to asses *on-line* proton range verification is given by the detection of the Prompt-Gamma (PG) rays naturally produced during therapy [CPC3]. After an inelastic interaction with an incoming proton the target nucleus is excited to higher energy states and, to return to its ground state, it emits γ-rays [CPC4]. These emissions are almost instantaneous [CPC5] (hence the use of the adjective *prompt*), high in energy (2-15 MeV) [CPC6] and are characterised by a high production rate [CPC7]. A good correlation between the beam range and the intensity of the PG-rays emitted by the most abundant isotopes in human tissues, namely C, O and N, has been experimentally proven [CPC7]. The reconstruction of the PG-rays emitting positions inside the patients' bodies may allow to precisely check the actual location of the proton beams during radiotherapy.

In this work a new method to determine the location of a source of γ-ray radiation with millimetric accuracy for both localised and distributed sources has been developed. The method uses only the signals from conventional, non-position sensitive, fast-timing scintillation detectors. For proof-of-principle $LaBr_3(Ce)$ detectors arranged in a symmetrical configuration have been employed to feed into a novel source position reconstruction algorithm that determines the source origin.

6.3 Methods

6.3.1 Source reconstruction method

The technique developed in this work utilises the coincident detection of the γ-rays emitted in a cascade by a radioactive source or following inelastic nuclear reactions. The emission time difference between these γ rays, if the intermediate state is not isomeric, is on the order of pico or femto seconds, which is short compared to the time resolution of a typical scintillator detector ($\sim$400-500 ps [CPC8]). Within this limitation of current detector and electronic systems, the two γ de-excitations are effectively emitted simultaneously in time and position. The detection of a *couple* of γ-rays in coincidence, together with a reconstruction algorithm, may allow the identification of the common emission point. As a proof-of-principle a ^{60}Co isotropic point source can be employed. The ^{60}Co decay scheme consists of two γ-rays of 1.173 and 1.332 MeV emitted in a cascade. The adopted value for the intermediate state lifetime is 0.713 ps [CPC9].

6.3.2 γ-ray spectrometer

In SPECT, source position determination is only possible through the mechanical collimation of the radiation detector. This minimises the available signal and therefore limits the technique to sources of a particular intensity [CPC10]. The technique developed in this work does not require any collimation of the radiation detectors. Figure 6.3 shows diagrammatically the proof-of-principle spectrometer used which is composed of 16 $LaBr_3$(Ce) cylindrical detectors with dimensions 2" length and 1.5" diameter. The detectors are arranged as follows: a ring of eight symmetrically-spaced detectors in the vertical plane plus one ring of four detectors at backward angles (45°) and one ring of four detectors at forward angles (45°), with respect to the Z axis. For an isotropic source at the centre of the spectrometer, when the distance between the source and the front face of all detectors is 9 cm, this geometry covers 24% of the total solid angle. The energy resolution of $LaBr_3$(Ce), $\sim$40 keV Full Width at Half Maximum (FWHM) at 1.33 MeV, makes it a suitable detector for high energy γ-ray spectroscopy. In addition the intrinsic time resolution of $LaBr_3$(Ce) detectors is sub-nanosecond from a few keV up to 4 MeV, giving excellent time discrimination [CPC11]. $LaBr_3$(Ce) crystals possess internal activity, predominantly due to the decay of ^{138}La. The γ-rays arising from this activity do not interfere with the source γ rays due to the coincidence requirement of the algorithm.

6.3.3 Position reconstruction algorithm

A source position reconstruction algorithm has been developed within the MATLAB environment (version R2018b). For every γ-ray γ_i recorded by the spectrometer several pieces of information are saved and passed to the algorithm; the energy E_i, the time t_i and the detector number Det_i. The algorithm takes as input the detector signals from two correlated γ-rays and determines their emission position. In order to re-construct the emission position, the data goes through three main functions: 1) γ-Ray *Couple* Selection, 2) γ-Ray *Couple*

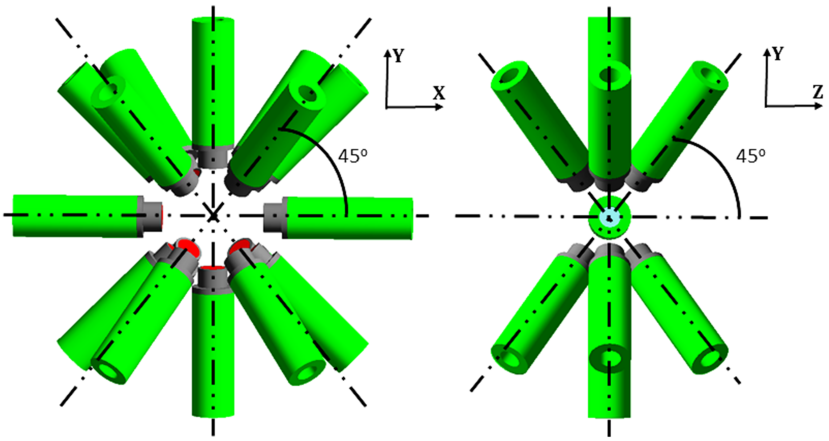

Figure 6.3: The spectrometer utilised in this work for source position reconstruction is composed of sixteen $LaBr_3(Ce)$ scintillation detectors arranged in a symmetrical configuration

Analysis, and 3) γ-Ray *Couple* Emission-Position Reconstruction. A flowchart detailing the algorithm is shown in Figure 6.4 and described in Sections 6.3.3, 6.3.3, 6.3.3, and 6.3.3.

Function 1: γ-ray couple selection

The algorithm selects *couples* of γ-rays, γ_i and γ_{i+1}, which satisfy the following criteria:

1. The two events, γ_i and γ_{i+1}, were recorded in coincidence in two different detectors, i.e. $Det_i \neq Det_{i+1}$.

2. The energies E_i and E_{i+1} of the two events are 1.173 and 1.332 MeV (any order).

At 1.332 MeV the $LaBr_3(Ce)$ energy resolution is 3% FWHM [CPC12] (Full Width Half Maximum). In this case the algorithm accepts γ ray energies of 1.173 and 1.332 MeV $\pm$ 3%. At the end of this function only those events which belong to a γ-ray *couple* are saved. Those events which do not fulfil the criteria above are rejected.

For radioactive sources the γ-ray emission time is not usually measurable, however, using a coincidence technique the time difference ($\Delta t = | t_{i+1} - t_i |$) between two consecutive events (γ_i and γ_{i+1}, with γ_{i+1} being detected after γ_i) can be obtained. The algorithm has been designed to utilise, for each correlated *couple* of γ-rays, the time difference (Δt).

Function 2: γ-ray couple analysis

An hyperbola is a conic section defined as the locus of points P such that the difference of the distance from P to two fixed points, F_1 and F_2, called foci, is a constant value k [CPC13]. A two-sheeted hyperboloid is a quadratic surface obtained by rotating an hyperbola about the line joining the foci [CPC13]. For each *couple* a two-sheeted hyperboloid is constructed. The foci correspond to the hit coordinates of the two events. The constant distance k is the absolute value of the time difference between the two events Δt multiplied by the speed of light c. The source position should lie somewhere on the hyperboloid surface.

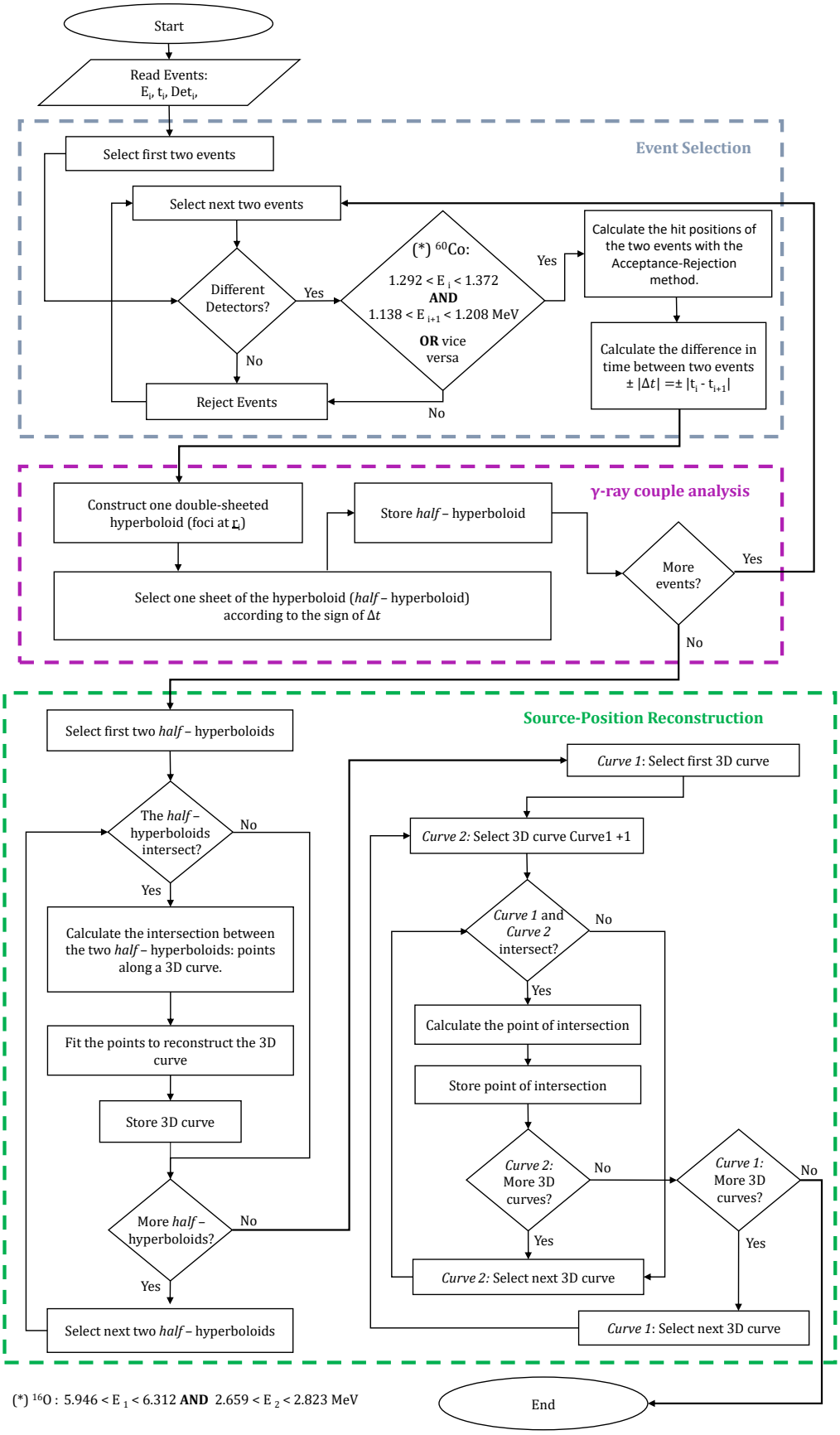

Figure 6.4: Flowchart of the 3D reconstruction algorithm developed in the MATLAB framework. To reconstruct the source position a sequence of steps is undertaken. These steps are represented by three main functions: 1) γ-Ray *Couple* Selection, 2) γ-Ray *Couple* Analysis, and 3) Source-Position Reconstruction. The algorithm has been specifically optimised to utilised those input data, from Geant4 simulations, that are available in real γ-spectroscopy experiments.

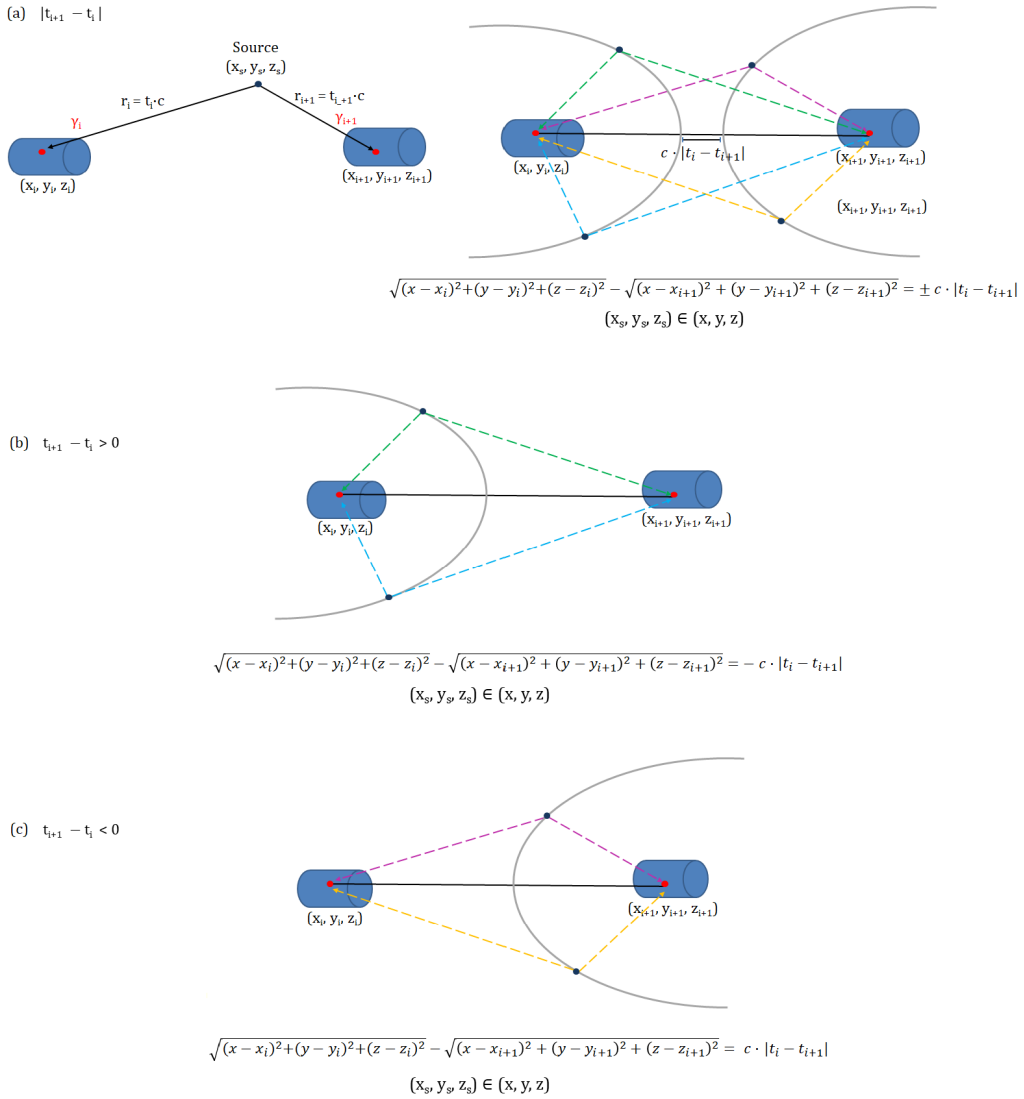

Figure 6.5: (a) Schematic illustration of the second function of the algorithm, γ-Ray *Couple* Analysis: for each *couple* of γ-rays, γ_i and γ_{i+1}, a two-sheeted hyperboloid is constructed. The hit coordinates (x_i, y_i, z_i) and $(x_{i+1}, y_{i+1}, z_{i+1})$ represent the foci. The difference between the distance each point of the hyperboloid has with the two foci is a constant value k. To estimate k the absolute value of the time difference between γ_i and γ_{i+1}, $\Delta t = |t_{i+1} - t_i|$, is employed. (b) - (c) If the sign of Δt is known each *couple* is represented by a sheet only of the two-sheeted hyperboloid (named *half*-hyperboloid).

For example, as shown schematically in Figure 6.5 and in 3D in Figure 6.6, for a source located in (x_s, y_s, z_s), the events γ_i and γ_{i+1}, detected in (x_i, y_i, z_i) and $(x_{i+1}, y_{i+1}, z_{i+1})$, at time t_i and t_{i+1} respectively, are represented by a two-sheeted hyperboloid having foci in (x_i, y_i, z_i) and in $(x_{i+1}, y_{i+1}, z_{i+1})$ and constant k value $\Delta t \cdot c = |t_{i+1} - t_i| \cdot c$. In other words the two-sheeted hyperboloid can be defined as the locus of points that satisfy the following Equation:

$$\begin{aligned} &\sqrt{(x-x_i)^2+(y-y_i)^2+(z-z_i)^2} \quad - \\ &\sqrt{(x-x_{i+1})^2+(y-y_{i+1})^2+(z-z_{i+1})^2} = \quad \pm \quad \Delta t \cdot c \end{aligned} \tag{6.1}$$

Where $(x_s, y_s, z_s) \in (x, y, z)$. The $\pm$ sign on the right hand side of Equation 6.1 defines the two sheets of the hyperboloid.

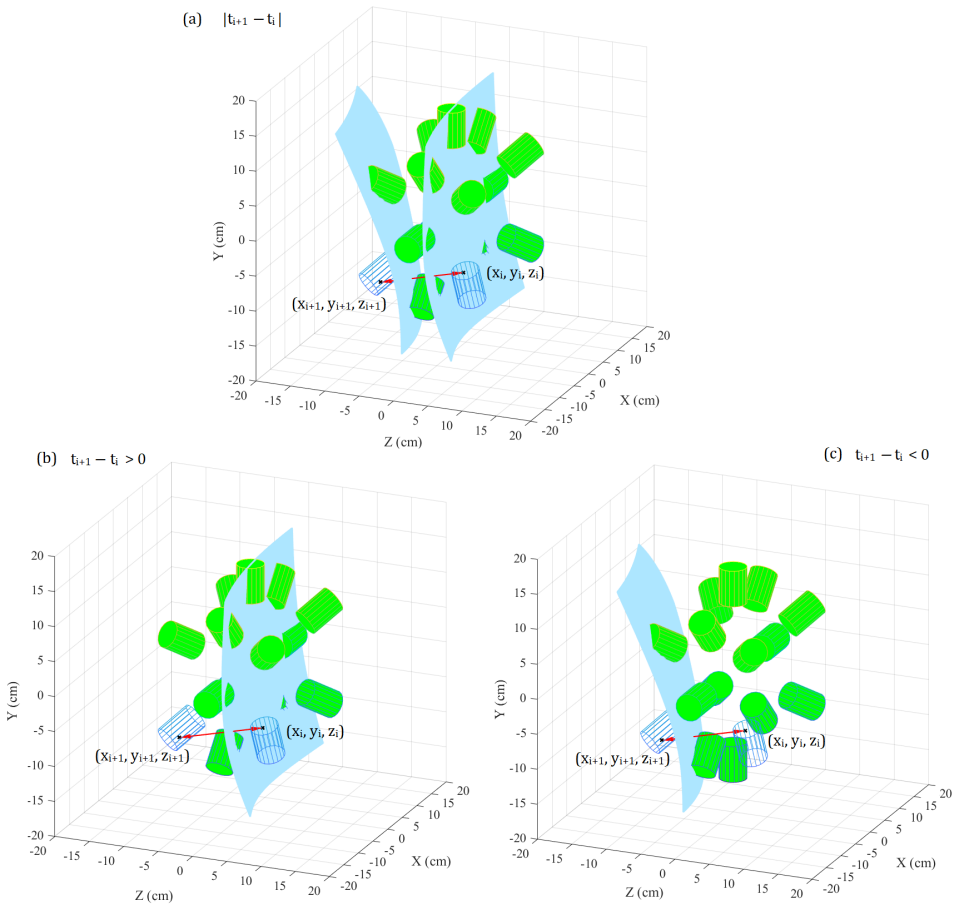

Figure 6.6: (a) 3D illustration of the second function of the algorithm, γ-Ray *Couple* Analysis: for each *couple* of γ-rays γ_i and γ_{i+1} a two-sheeted hyperboloid is constructed where the hit coordinates (x_i, y_i, z_i) and (x_{i+1}, y_{i+1}, z_{i+1}) are the foci. (b) - (c) If the sign of Δt is known each *couple* is represented by a sheet only of the two-sheeted hyperboloid (named *half*-hyperboloid).

- If t_{i+1}-$t_i > 0$:

$$\begin{aligned} &\sqrt{(x-x_i)^2+(y-y_i)^2+(z-z_i)^2} \quad - \\ &\sqrt{(x-x_{i+1})^2+(y-y_{i+1})^2+(z-z_{i+1})^2} = \quad - \quad \Delta t \cdot c \end{aligned} \tag{6.2}$$

- If t_{i+1}-$t_i < 0$:

$$\begin{aligned} &\sqrt{(x-x_i)^2+(y-y_i)^2+(z-z_i)^2} \quad - \\ &\sqrt{(x-x_{i+1})^2+(y-y_{i+1})^2+(z-z_{i+1})^2} = \quad + \quad \Delta t \cdot c \end{aligned} \tag{6.3}$$

If the sign of Δt is known, Equation 6.1 can be reduced to Equation 6.2 or to Equation 6.3. In other words a *couple* is associated with only one side of a two-sheeted hyperboloid (here named *half*-hyperboloid). It is possible to reduce Equation 6.1 to Equations 6.2 or 6.3 even if the sign of Δt is not known. This can be achieved through an analysis of the intensity recorded by each detector unit. A high intensity implies a higher subtended solid angle, relative to the source position and a shorter relative arrival time, both due to a shorter γ-ray path length. Given two events in a *couple* γ_i and γ_{i+1}, detected in Det_i and Det_{i+1}, the following assumptions can be made:

- if $Tot_{events_j}|_{j=Det_i} < Tot_{events_j}|_{j=Det_{i+1}} \rightarrow t_i > t_{i+1}$

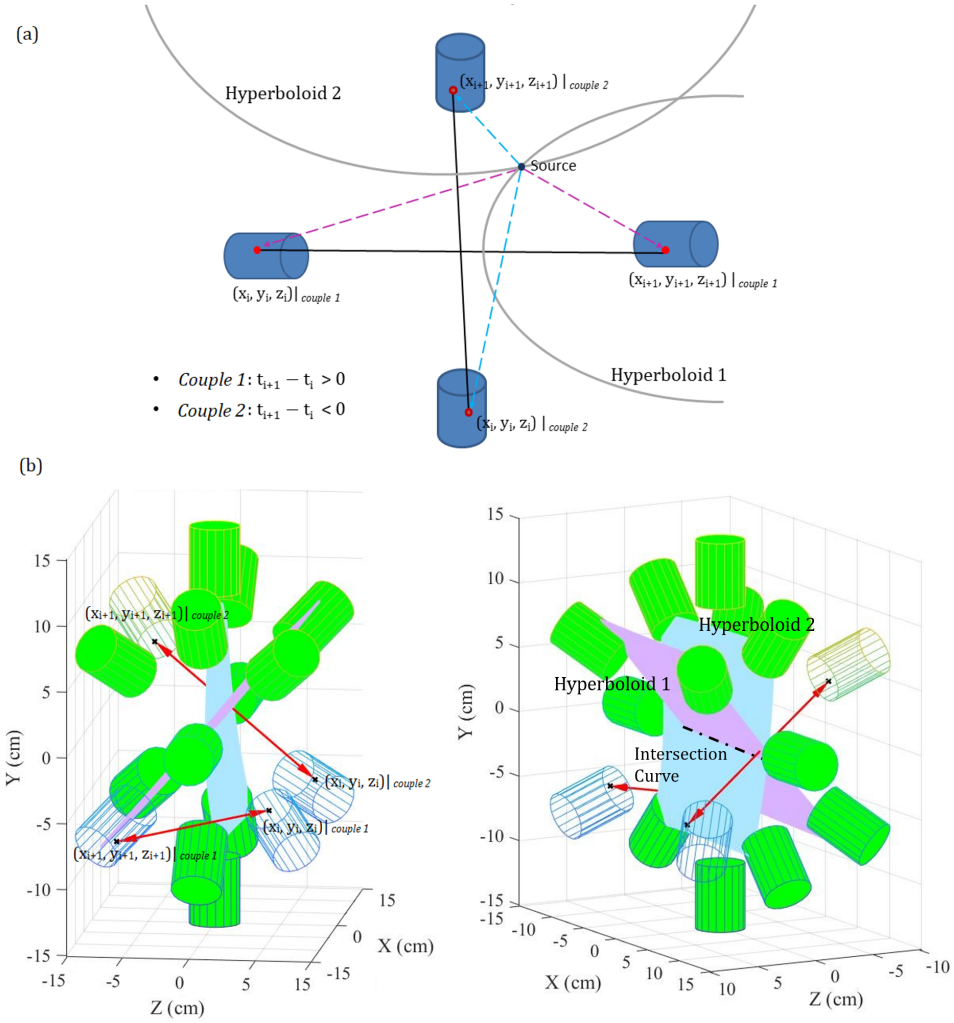

Figure 6.7: (a) Schematic and (b) 3D illustration of the third function of the algorithm, Source-Position Reconstruction: the intersection between two consecutive *half*-hyperboloids is calculated. The original source position should lie somewhere on the intersection curve.

Equation 6.1 can be reduced to Equation 6.2.

- if $\mathrm{Tot}_{events_j}|_{j=Det_i} > \mathrm{Tot}_{events_j}|_{j=Det_{i+1}} \rightarrow t_i < t_{i+1}$
  Equation 6.1 can be reduced to Equation 6.3.

Where $Tot_{events_j}|_{j=Det_i}$ is the number of γ-rays belonging to *couples* recorded in Det_i. It is desirable that every time the condition $\mathrm{Tot}_{events_j}|_{j=Det_i} < \mathrm{Tot}_{events_j}|_{j=Det_{i+1}}$ is satisfied the condition $t_i > t_{i+1}$ is also true, and vice versa.

Function3: source position reconstruction

Intersection between half-hyperboloids

At the end of the previous function n *half*-hyperboloids are stored. In the third function of the algorithm each couple of subsequent *half*-hyperboloids (1/2, 3/4, ..., $n/(n+1)$, ...) is retrieved and, as illustrated in Figure 6.7, their intersection is determined. The maximum number of intersections, $n/2$, is achieved when all of the *half*-hyperboloids couples intersect. The intersections are obtained by triangulating the surfaces of two subsequent *half*-hyperboloids. A triangulated *half*-hyperboloid is a *half*-hyperboloid whose surface has been totally divided into a net of triangles in such a way that every internal point belongs

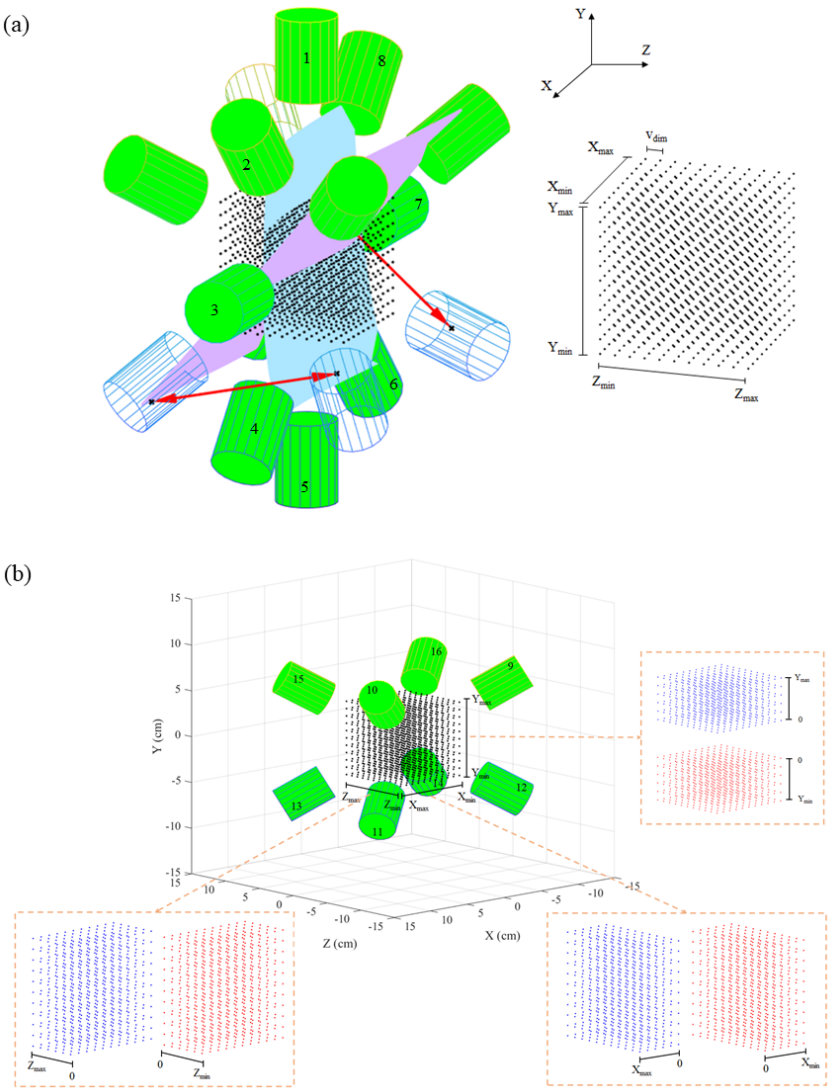

Figure 6.8: (a) In the third function of the algorithm, Source-Position Reconstruction, the intersection between two triangulated *half*-hyperboloids is calculated. Each intersection is estimated inside a virtual voxellated cube located in the central area of the spectrometer. If two *half*-hyperboloids intersect into a specific voxel, the central point of the voxel is saved as an intersection point. Consequently, for each couple of intersecting *half*-hyperboloids, a sequence of points along the intersection 3D curve are produced. The larger the dimensions of the voxelised cube are (X_{neg}/X_{pos}, Y_{neg}/Y_{pos}, Z_{neg}/Z_{pos}) the wider the sampled area is. By increasing the cube dimensions, the algorithm computational time extends. (b) The cube dimensions can be reduced along the three axes independently by employing the intensity of the γ-rays recorded in the detectors at backward/forward angles. The computational time is then shortened.

to a triangle, and the intersection of any two triangles is either void, a common side or a common vertex [CPC14]. Each intersection between two subsequent hyperboloids is then parameterised by a series of points in 3D space following a single trajectory.

As shown in Figure 6.8a each intersection between two *half*-hyperboloids is calculated in a virtual voxelised cube located in the central area of the spectrometer. The larger the dimensions of this cube (X_{neg}/X_{pos}, Y_{neg}/Y_{pos}, Z_{neg}/Z_{pos}) the wider the sampled area. If two *half*-hyperboloids intersect at a specific voxel the central point of that voxel is saved as an intersection point. Consequently the smaller the voxel size v_{dim}, for a constant sample area, the more intersection points may be produced. By both increasing the cube size and/or

decreasing the voxels size the algorithm computational time extends. To reduce the cube size, along the three axes independently, the intensity of the γ-rays recorded in the detectors at backward/forward angles ($\mathrm{Tot}_{events_j}|_{j=Det_9-Det_{16}}$) can be employed. In this regard, with reference to Figure 6.8b, the following analysis is performed:

- To check if the X source coordinate is positive or negative

  1. X = [0, X_{pos}] if:
  $$\sum_{j=Det_{10},Det_{11},Det_{13},Det_{15}} \sum_{i=Det_9,Det_{12},Det_{14},Det_{16}} \left(\mathrm{Tot}_{events_j} \text{-} \sqrt{Tot_{events_j}} \right) > \left(\mathrm{Tot}_{events_i} \text{-} \sqrt{Tot_{events_i}} \right)$$

  2. X = [X_{neg}, 0] if:
  $$\sum_{j=Det_{10},Det_{11},Det_{13},Det_{15}} \sum_{i=Det_9,Det_{12},Det_{14},Det_{16}} \left(\mathrm{Tot}_{events_j} \text{-} \sqrt{Tot_{events_j}} \right) < \left(\mathrm{Tot}_{events_i} \text{-} \sqrt{Tot_{events_i}} \right)$$

- To check if the Y source coordinate is positive or negative

  1. Y = [0, Y_{pos}] if:
  $$\sum_{j=Det_9,Det_{10},Det_{15},Det_{16}} \sum_{i=Det_{11},Det_{12},Det_{13},Det_{14}} \left(\mathrm{Tot}_{events_j} \text{-} \sqrt{Tot_{events_j}} \right) > \left(\mathrm{Tot}_{events_i} \text{-} \sqrt{Tot_{events_i}} \right)$$

  2. Y = [Y_{neg}, 0] if:
  $$\sum_{j=Det_9,Det_{10},Det_{15},Det_{16}} \sum_{i=Det_{11},Det_{12},Det_{13},Det_{14}} \left(\mathrm{Tot}_{events_j} \text{-} \sqrt{Tot_{events_j}} \right) < \left(\mathrm{Tot}_{events_i} \text{-} \sqrt{Tot_{events_i}} \right)$$

- To check if the Z source coordinate is positive or negative

  1. Z = [0, Z_{pos}] if:
  $$\sum_{j=Det_9,Det_{10},Det_{11},Det_{12}} \sum_{i=Det_{13},Det_{14},Det_{15},Det_{16}} \left(\mathrm{Tot}_{events_j} \text{-} \sqrt{Tot_{events_j}} \right) > \left(\mathrm{Tot}_{events_i} \text{-} \sqrt{Tot_{events_i}} \right)$$

  2. Z = [Z_{neg},0] if:
  $$\sum_{j=Det_9,Det_{10},Det_{11},Det_{12}} \sum_{i=Det_{13},Det_{14},Det_{15},Det_{16}} \left(\mathrm{Tot}_{events_j} \text{-} \sqrt{Tot_{events_j}} \right) < \left(\mathrm{Tot}_{events_i} \text{-} \sqrt{Tot_{events_i}} \right)$$

For each co-ordinate axis the choice of detectors used in the above expressions is based on the recorded intensities.

Function3: source position reconstruction - analysis intersection points

Each intersection between two *half*-hyperboloids results in a series of points in the 3D space. The amount of points per intersection depends on both the cube and the voxel sizes. In the third function of the algorithm a curve is obtained by fitting the points with a 3^{rd} order polynomial function. All curves are stored, for a maximum of $n/2$ curves. For each couple of

curves the intersection-point is determined. When all intersections are non-null a maximum number of $2 \cdot (n/2) = n$ intersection points, i.e. possible source positions, are found.

Small uncertainties may affect the parameters of the hyperboloids. These uncertainties are reflected in the intersection calculation. New uncertainties are also introduced by the use of the polynomial fit. As a result the curves may not cross each other. To overcome this, for each couple of curves C_1 and C_2, the following analysis is performed:

1. The points $P_1 = (x_{c_1}, y_{c_1}, z_{c_1})$ and $P_2 = (x_{c_2}, y_{c_2}, z_{c_2})$, belonging to C_1 and C_2 respectively, and characterised by the minimum Euclidean distance $| P_1 - P_2 |$, are selected.

2. The mean value between P_1 and P_2 is saved. It represents a virtual source position $P_{s\_p} = (x_{s\_p}, y_{s\_p}, z_{s\_p})$:

$$x_{s\_p} = \frac{x_{c_1} + x_{c_2}}{2} \quad y_{s\_p} = \frac{y_{c_1} + y_{c_2}}{2} \quad z_{s\_p} = \frac{z_{c_1} + z_{c_2}}{2}.$$

All the virtual source positions are saved. They represent the reconstructed coordinates in which the source was located and, as such, they are the final outcome of the algorithm.

6.3.4 Geant4 evaluation

The Geant4 Monte Carlo Toolkit (version 10.04) [CPC15] has been employed to simulate the spectrometer and an isotropic ^{60}Co source at various known locations within the spectrometer's central area. To facilitate swift simulation and reconstruction time the internal radius of the spectrometer has been set to 9 cm. For the $LaBr_3$(Ce) detectors an energy resolution of 3% FWHM [CPC12] and a time resolution of 280 ps [CPC16] have been used. As mentioned previously the $LaBr_3$(Ce) internal activity does not impact the reconstruction process, therefore, it has not been modelled. Simulations have been performed in air with 10^5 primary events. Both electromagnetic *EmStandardPhysics4* and radioactive decay *G4DecayPhysics* physics lists have been combined together and a secondary particle production "cut" value of 0.5 mm was set to optimise run time without adversely affecting precision. The ^{60}Co γ-rays are detected and recorded by the virtual spectrometer.

When a γ-ray enters the sensitive area of a detector it can Compton scatter multiple times, termed *hits*, prior to absorption via the photoelectric effect. For every γ_i ray detected several pieces of information are registered (see Figure 6.9):

1. Det_i = the detector number in which γ_i has been registered;

2. E_i = the total energy by γ_i in Det_i deposited (sum of the energy deposited in all hits in Det_i);

3. t_i = the emission and arrival time difference of γ_i in Det_i;

The γ-ray emission time is available in the Geant4 simulation and is utilised to calculate the relative arrival times of the detected γ-ray couple. This serves the same purpose as an

electronic event time stamp module used in a real spectroscopy applications. The detector outputs are passed to the algorithm which reconstructs the coordinate of the ^{60}Co source.

6.3.5 Hit positions values identification

For each γ-ray recorded by the spectrometer the algorithm is fed the coordinates of the last hit position within the detector medium. Monte Carlo simulations provide these coordinates exactly, however, as with many large crystal, non position sensitive detectors, this information is not available in reality. In order to obtain an accurate estimate of the final interaction position for a real detector, the Geant4 simulation was used to obtain a 3D probably distribution of photoelectric γ-ray interactions. For this 10^8 ^{60}Co decays were modelled for a source located at (0,0,0). From this data Probability Density Functions (PDFs) for each dimension are derived separately for each detector.

To closer replicate reality, in the algorithm, for each γ_i ray belonging to a *couple*, the exact coordinates of the last hit position are not employed. Conversely, once the detector Det_i in which γ_i has been absorbed is determined, the three PDFs, one for dimension, associated to Det_i, are loaded. These PDFs are sampled using the acceptance-rejection method [CPC17] to obtain a final interaction position, in 3D, for γ_i. The described procedure reflects more accurately what would be observed when using real detectors.

6.4 Results

In Figure 6.10a the reconstructed coordinates for a source modelled at (0,0,0) are reported. For each co-ordinate axis a Gaussian fit has been applied to the algorithm-reconstructed data. The peak centroid position, μ, corresponds to the source location coordinate with the standard deviation, σ, representing the position uncertainty. The reconstructed coordinate values $\mu \pm \sigma$ are: -0.3 $\pm$ 2.5, -0.4 $\pm$ 2.4, and -0.6 $\pm$ 2.5 mm along the X, Y, and Z axis, respectively. The source location has been accurately determined within a 3 mm uncertainty by the algorithm using only realistic detector signals. For this result, the virtual voxelised cube in which the *half*-hyperboloids intersections were calculated, as described in Section

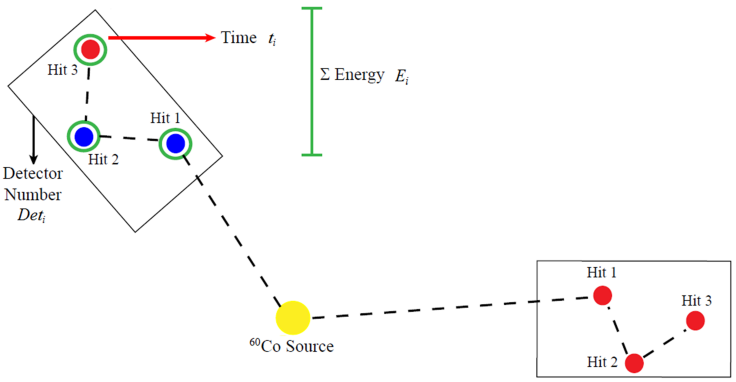

Figure 6.9: During a simulation, for every ^{60}Co-emitted γ-ray γ_i recorded in a detector, several pieces of information are saved: the detector number Det_i, the total energy released E_i, and the last-hit time t_i

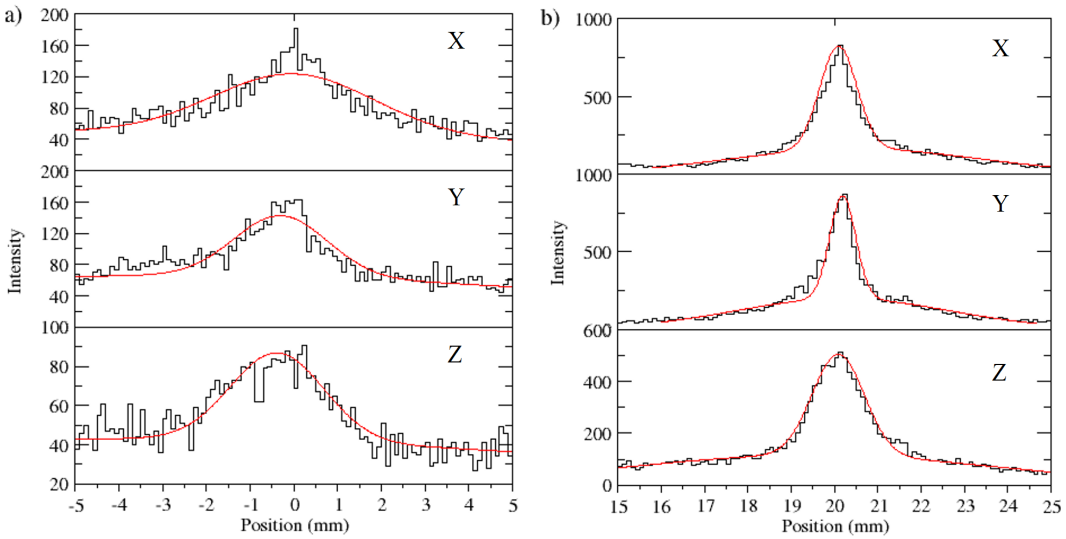

Figure 6.10: Coordinates of a single isotropic ^{60}Co source simulated at a) (0, 0, 0) and at b) (20, 20, 20) mm as reconstructed by the in-house developed algorithm. Along each axis a Gaussian fit has been applied on the algorithm-reconstructed data. The position of the centre of the peak, μ, and the standard deviation of each peak, σ, correspond, respectively, to the reconstructed coordinate and to the uncertainty to within this coordinate is reconstructed. When the source is at (0, 0, 0) the reconstructed coordinates values ($\mu \pm \sigma$) are: -0.3 ± 2.5, -0.4 ± 2.4, and -0.6 ± 2.5 mm along the X, Y, and Z axis, respectively. When the source is at (20, 20, 20) mm the reconstruction values ($\mu \pm \sigma$) are: 20.2 ± 1.0, 20.2 ± 0.9, and 20.1 ± 1.2 mm along the X, Y, and Z axis, respectively.

6.3.3, had a volume of 512 cm^3 (X_{pos} = 4, X_{neg} = -4, Y_{pos} = 4, Y_{neg} = -4, Z_{pos} = 4; Z_{neg} = -4). The total number of recorded γ-rays was 19576. This leads to a geometrical efficiency for the spectrometer, defined as the number of recorded γ-rays divided by the number of initial γ rays emitted by the source, of 20%. In a total computational time of 1 hour and 35 minutes (Windows 64 with Intel Core i7-6700 @ 3.41 GHz CPU and 16 GB RAM) the algorithm selected 566 *couples* and reconstructed 20706 virtual source positions (x_{s_p},y_{s_p},z_{s_p}).

Figure 6.10b shows the reconstructed coordinates for an isotropic source located at (20,20,20) mm. The reconstructed coordinated values, $\mu \pm \sigma$, are: 20.2 ± 1.0, 20.2 ± 0.9, and 20.1 ± 1.2 mm, along the X, Y, and Z axis, respectively. For this source location the uncertainty deduced from the Gaussian fits is less than 1.5 mm. The number of γ-rays recorded was 19345 in agreement with the expected 20% geometrical efficiency. In a total computational time of 2 minutes the algorithm selected 519 *couples* and reconstructed 21945 virtual source coordinates. The cube volume, in this case, was 64 cm^3 (X_{pos} = 4, X_{neg} = 0, Y_{pos} = 4, Y_{neg} = 0 , Z_{pos} = 4, Z_{neg} = 0). For both source locations a voxel size (v_{dim}) of 0.5 mm was chosen to optimise both reconstruction precision and computational time.

6.5 Discussion

It is clear from the Gaussian fit results shown in Figure 6.10 that the reconstructed source locations are in excellent agreement with the known values. The uncertainty associated with the reconstructed position of the source at (20,20,20) mm is better than that of the source at (0,0,0). There are two steps in the algorithm in which the position of the source

plays a crucial role on the reconstruction precision: 1) the selection of only one side of the two-sheeted hyperboloid in Function 2 (Section 6.3.3), 2) the selection of the size of the virtual voxelised cube in which the intersection between two *half*-hyperboloids is estimated in Function 3 (Section 6.3.3).

Every γ-ray *couple* (γ_i and γ_{i+1}) is represented by a two-sheeted hyperboloid, with the source position lying somewhere on the hyperboloid surface. To shorten the computational time and reduce the number of false reconstructed coordinates, only one side of each two-sheeted hyperboloid, a *half*-hyperboloid, can be selected. This selection, as described in Section 6.3.3, is based on the intensity difference of the recorded γ-rays in the two detectors (Det_i and Det_{i+1}) in which the events in the *couple* have been registered. A high intensity difference leads to a correct *half*-hyperboloid selection and, as expected, the intensity difference increases as the source is shifted form the centre of the spectrometer (0,0,0).

The frequency with which the correct *half*-hyperboloid is selected was investigated as a function of the source position. The source position was shifted, along the positive direction of the Z axis, from 1 to 10 cm, in 1 cm steps, and by 15 and 20 cm. The spectrometer radius was fixed at 9 cm. For each source position the γ-ray intensity, as recorded by each detector (Tot_{events_j}), was determined. For all recorded *couples* γ_i/γ_{i+1} the detector numbers $\mathrm{Det}_i/\mathrm{Det}_{i+1}$ and the time values $\mathrm{t}_i/\mathrm{t}_{i+1}$ are employed to evaluate the following condition:

$$\begin{gathered}(Tot_{events_j}|_{j=Det_i} < Tot_{events_j}|_{j=Det_{i+1}} \quad AND \quad t_i > t_{i+1}) \\ OR \\ (Tot_{events_j}|_{j=Det_i} > Tot_{events_j}|_{j=Det_{i+1}} \quad AND \quad t_i < t_{i+1})\end{gathered} \tag{6.4}$$

If the above condition is true the time-intensity correlation holds up. Conversely if

$$\begin{gathered}(Tot_{events_j}|_{j=Det_i} < Tot_{events_j}|_{j=Det_{i+1}} \quad AND \quad t_i < t_{i+1}) \\ OR \\ (Tot_{events_j}|_{j=Det_i} > Tot_{events_j}|_{j=Det_{i+1}} \quad AND \quad t_i > t_{i+1})\end{gathered} \tag{6.5}$$

is upheld, there is no true time-intensity correlation (see Figure 6.11). The larger the source shift from (0,0,0), the larger the fraction of *couples* that fulfil condition 6.4. This is observed for source locations within the spectrometer radius (9 cm). Conversely, locations outside of the array result in a considerably reduced geometrical efficiency. For this technique to work the source has to be located within the central spectrometer volume.

As explained in Section 6.3.3 each intersection between two half-hyperboloids is calculated in a virtual voxelised cube in the spectrometer central volume. The cube size can be reduced, without affecting the reconstruction precision, by using the difference between the intensities of the recorded γ-rays for the detectors at forward and backward angles (Figure 6.8b). When the source is at (0,0,0) it subtends, to within statistical uncertainty, the same solid angle for all detectors. In this special case, where the source is exactly located at

the centre of the spectrometer, the cube size can not be reduced because there is no intensity difference between the forward and backward detectors. When the source is located at (20,20,20) mm the intensity difference is significant and the cube size can be reduced. The cube volume is 512 cm^3 (8x8x8 cm) and 64 cm^3 (4x4x4 cm) when the source is located at (0,0,0) and (20,20,20) mm, respectively. A large cube size, like the one needed for a centrally located source, results in a longer computational time and an increased number of false reconstruction co-ordinates compared to smaller cube sizes. Bearing this in mind a prototype spectrometer should be movable and/or have the ability to adjust the detector angles. One benefit of having a centrally located source with this type of spectrometer is that is can be used to measure absolute source activities [CPC18].

In the current work, for both source locations, a voxel size v_{dim} of 0.5 mm was set to optimise between precision and computational time. For some applications, however, a larger value may be chosen to improve precision. An analysis concerning the dependence of the algorithm accuracy, precision, and computational cost from v_{dim} has been carried out. The simulation output, relative to a source at (0,0,0), has been passed to the algorithm and, in six different runs, v_{dim} was set to: 5, 4, 2, 1, 0.5, and 0.2 mm. It has been noticed that, by increasing v_{dim}, the algorithm computational time significantly increases, passing from $\sim$11 s for v_{dim} = 5 mm to $\sim$5 hrs 58 minutes for v_{dim} = 0.2 mm. The algorithm source reconstruction is achievable, along each axis, to within 2.5 and 4 mm, when v_{dim} is 0.2 and 5 mm, respectively.

To put the results from this work in perspective, a clinical SPECT γ-camera offers a spatial resolution for radioactive source location on the order of 4–6 mm [CPC2]. The spatial resolution with the technique detailed above is superior for non-centrally located sources. It is clear that this technique could be successfully adapted to be used in a number of radioactive source applications including nuclear medicine and national security.

As previously mentioned this technique could also be used for distributed γ-ray sources such as those found in proton beam radiotherapy. One possible usage would be in the reduction of range uncertainty through the detection and position reconstruction of prompt-gamma (PG) rays emitted naturally during therapy. Due to the high energy of the PG-rays and to the huge neutron contamination, PG-rays detection with standard imaging instruments employed in nuclear medicine is inefficient; an optimised device needs to be designed [CPC19]. Although. in the last decade, different detector systems have been proposed, several problems impede their clinical potential [CPC4]. Collimated gamma cameras have been initially used to demonstrate the feasibility of PG-ray detection for range verification [CPC3], [CPC20]. In spite of the collimation used in these systems, the signal is significantly blurred by background neutron radiation [CPC7], [CPC21], [CPC22]. The coincidence requirement of the algorithm described above discriminates between neutron and γ radiation improving the imaging capability of the system. One of the most abundant PG-ray emitters in human tissues is ^{16}O. As opposed to a ^{60}Co source the γ-ray *couples* for the algorithm

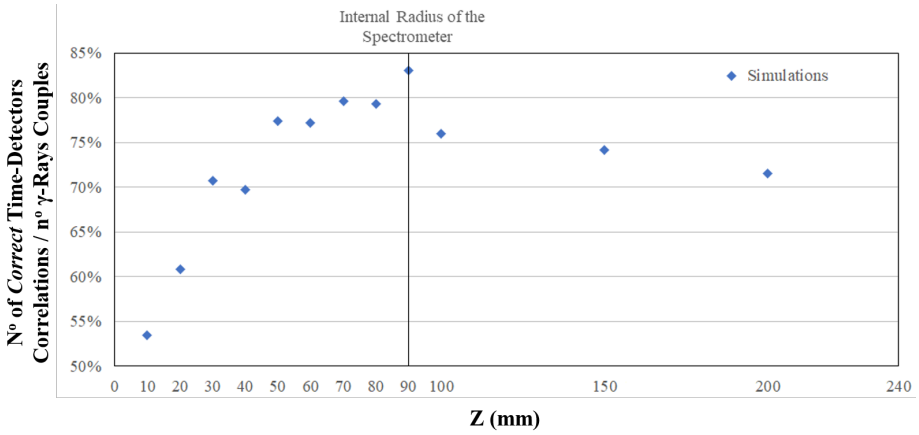

Figure 6.11: Second function of the algorithm, γ-Ray Couples Analysis: the number of *correct* time-detectors correlations divided by the total number of *couples* as a function of the source shift along the positive direction of the Z axis. The internal radius of the spectrometer has always been kept at 9 cm. For a source shift shorter then 9 cm the fraction of *couples* characterised by a *correct* correlation increases with the shift magnitude. On the other hand, for shifts bigger then 9 cm the γ-rays are no more easily geometrically detectable by all the detectors and the number of *correct* correlations decreases.

would be the 2.741 (I^{π}: $2^{-} \rightarrow 3^{-}$) and 6.128 (I^{π}: $3^{-} \rightarrow$ g.s.) MeV (p, ^{16}O)-induced PG-rays [CPC23]. These de-excitations, from a particular ^{16}O nucleus, are effectively, within detection resolution, emitted simultaneously in position and time, almost along the entire proton beam path. The $LaBr_3(Ce)$ spectrometer coupled with the position reconstruction algorithm provides a unique system for tackling the challenge of range uncertainty in proton beam therapy. Discussions are currently being held with clinical scientist colleagues for a small design adaptation of the spectrometer to enable clinical implementation.

The simulation described in this work, with the source at (0,0,0), has been repeated varying the number of primary events: 10^3, 10^4, 10^5, and 10^6. It has been found that both accuracy and precision improve with increasing primary events. With 10^4 primary events, which translates to ∼1900 recoded γ-rays and ∼60 *couples*, the algorithm is able to reconstruct the source position with a 6 mm uncertainty, within ∼10 minutes on the stated system. Conversely, with 10^6 primary events, which implies ∼197,600 recoded γ-rays and ∼5,800 *couples*, the source reconstruction is achieved with a 1 mm uncertainty, but at the price of a long computational time (∼15 hr). In proton beam therapy, PG rays are emitted along the beam path, effectively giving a moving γ-ray source. Initial simulation results for a 180 MeV proton beam on water show that this algorithm can reconstruct the position of the maximum intensity of the PG-rays distribution with an uncertainty of ∼4 mm for 10^8 primary proton events. Verburg *et al* [CPC7] showed that $1.64 \cdot 10^7$ PG-rays are emitted per gram of ^{16}O per Gray of dose delivered.

Conclusions

A new method to determine the location of a radiative source, with millimetric accuracy and without knowing the radiation emission time, has been developed. The method is based on the detection of two γ-rays in coincidence. A spectrometer comprising 16 conventional

$LaBr_3$(Ce) detectors in a symmetrical configuration is employed to detect the source emitted radiation. A source position reconstruction algorithm has been developed; it takes as inputs the $LaBr_3$(Ce) detector signals and reconstructs the position of the γ-ray source, in full three dimensional space. The algorithm only needs the signals available through standard electronics couple to off-the-shelf scintillator detectors. The spectrometer-algorithm performance has been investigated for a ^{60}Co source in two different positions within the central area of the spectrometer. The results show that for sources located at (0,0,0) and (20,20,20) mm the reconstructed location is determined with uncertainties of less than 3 mm and 2 mm, respectively. The developed method has a wide range of possible future research/industrial applications such as source localisation in nuclear medicine, security and radioactive waste assays. The system will also work for distributed sources and could aid in minimising range uncertainty in proton beam therapy. The present article is not intended as documentation for the code mentioned, instead, it describes a general methodology to generate a position reconstruction algorithm. Further developments are ongoing to improve the algorithm and to empirically validate the spectrometer-algorithm performance.

Acknowledgements

C.M.V.P. would like to acknowledge support form CRUK via the funding to Cancer Research UK Manchester Centre: [C147/A18083] and [C147/A25254]. M.S. would like to acknowledge support form Marie Curie Actions Initial Training Networks (ITN) as an Integrating Activity Supporting Postgraduate Research with Internships in Industry and Training Excellence (SPRITE) under EC contract 317169 and the Christie Charitable Fund (registered number 1049751). M.J.T., M.S., K.J.K. and R.I.M. would like to acknowledge funding from the NIHR Manchester Biomedical Research centre.

Author contributions statement

C.M.V.P. developed the Monte Carlo simulation application and the 3D reconstruction algorithm. M.J.T. provided the original concept behind this work, the day-to-day supervision and guided the in-silico developments. R.I.M. provided monthly supervision. K.J.K. provided technical guidance and funding. M.S. contributed to the mathematical conceptualisation of the algorithm. C.M.V.P. and M.J.T. drafted the manuscript. All authors reviewed and approved the manuscript.

Declaration of interest: none.

Bibliography

[CPC1] R. Estep, T. Prettyman, and G. Sheppard, "Tomographic gamma scanning to assay heterogeneous radioactive waste," *Nuclear science and engineering*, vol. 118, pp. 145–152, 1994.

[CPC2] T. Peterson and L. Furenlid, "SPECT detectors: the Anger Camera and beyond," *Phys Med Biol*, vol. 56, p. R145, 2011.

[CPC3] C. Min, C. Kim, M. Youn, and J. Kim, "Prompt gamma measurements for locating the dose falloff region in the proton therapy," *Appl Phys Lett*, vol. 89, p. 183517, 2006.

[CPC4] A. Knopf and A. Lomax, "In vivo proton range verification: a review," *Phys Med Biol*, vol. 58, p. R131, 2013.

[CPC5] B. Kozlovsky, R. J. Murphy, and R. Ramaty, "Nuclear deexcitation gamma-ray lines from accelerated particle interactions," *Astrophys J Suppl S*, vol. 141, p. 523, 2002.

[CPC6] C. Min, H. Lee, C. Kim, and S. Lee, "Development of array-type prompt gamma measurement system for in vivo range verification in proton therapy," *Med Phys*, vol. 39, pp. 2100–2107, 2012.

[CPC7] J. Verburg, K. Riley, T. Bortfeld, and J. Seco, "Energy- and time-resolved detection of prompt gamma-rays for proton range verification," *Phys Med Biol*, vol. 58, p. L37, 2013.

[CPC8] M. Nikl, "Scintillation detectors for X-rays," *Meas. Sci. Technol.*, vol. 17, p. R37, 2006.

[CPC9] M. Bé, V. Chisté, C. Dulieu, E. Browne, V. Chechev, *et al.*, "Table of radionuclides (Vol.1 A= 1 to 150)," *BIPM*, 2004.

[CPC10] N. Schramm, G. Ebel, U. Engeland, T. Schurrat, M. Behe, *et al.*, "High-resolution SPECT using multipinhole collimation," *IEEE Trans Nucl Sci*, vol. 50, pp. 315–320, 2003.

[CPC11] R. Nicolini *et al.*, "Investigation of the properties of a 1" × 1" $LaBr_3$: Ce scintillator," *Nucl Instr Meth Phys Res A*, vol. 582, pp. 554–561, 2007.

[CPC12] F. Quarati *et al.*, "X-ray and gamma-ray response of a 2" × 2" $LaBr_3$:Ce scintillation detector," *Nucl Instr Meth Phys Res A*, vol. 574, pp. 115–120, 2007.

[CPC13] J. Harris and H. Stöcker, *Handbook of mathematics and computational science*. 1998.

[CPC14] N. Amato, M. Goodrich, and E. Ramos, "A randomized algorithm for triangulating a simple polygon in linear time," *Discrete Comput Geom*, vol. 26, pp. 245–265, 2001.

[CPC15] S. Agostinelli *et al.*, "GEANT4 - A simulation toolkit," *Nucl Instrum Methods Phys Res A*, vol. 506, pp. 250–303, 2003.

[CPC16] S. Aldawood *et al.*, "Comparative characterization study of a $LaBr_3$(Ce) scintillation crystal in two surface wrapping scenarios: Absorptive and reflective," *Front Oncol*, vol. 5, p. 270, 2015.

[CPC17] B. Flury, "Acceptance-rejection sampling made easy," *SIAM Review*, vol. 32, pp. 474–476, 1990.

[CPC18] G. Lorusso, R. Shearman, P. Regan, S. Judge, S. Bell, *et al.*, "Development of the NPL gamma-ray spectrometer NANA for traceable nuclear decay and structure studies," *Appl Radiat Isot*, vol. 109, pp. 507–511, 2016.

[CPC19] S. Peterson, D. Robertson, and J. Polf, "Optimizing a three-stage Compton camera for measuring prompt gamma rays emitted during proton radiotherapy," *Phys Med Biol*, vol. 55, p. 6841, 2010.

[CPC20] C. Kim, C. Min, K. Seo, and J. Kim, "Simulation studies on the correlation of distal dose falloff of a 70-MeV proton beam with a prompt gamma distribution," *J Korean Phys Soc*, vol. 50, p. 1510, 2007.

[CPC21] J. Verburg and J. Seco, "Proton range verification through prompt gamma-ray spectroscopy," *Phys Med Biol*, vol. 59, p. 7089, 2014.

[CPC22] F. Roellinghoff *et al.*, "Real-time proton beam range monitoring by means of prompt-gamma detection with a collimated camera," *Phys Med Biol*, vol. 59, p. 1327, 2014.

[CPC23] D. Tilley, H. Weller, and C. Cheves, "Energy levels of light nuclei A= 16–17," *Nucl Phys A*, vol. 564, pp. 1–183, 1993.

Chapter 7

Critique of Publication 2

This Chapter presents additional information on the investigation reported in Panaino *et al* [274]. The algorithm dependance from the initial number of events (Section 7.1) and from the voxel size (Section 7.2) is evaluated, also with respect to the computational time. Two areas of improvement, to further enhance the algorithm precision and accuracy, are then described (Section 7.3). Part of the evaluations in this Chapter was stimulated by the discussion with the reviewers during the peer-review process of Computer Physics Communication.

7.1 Algorithm dependance from the number of simulated events

To investigate how the number of simulated primary events affects the quality of the results presented in Panaino *et al* [274], an analysis was performed as follows. For a ^{60}Co source modelled at (0,0,0), the same simulation as in the publication was carried out. The number of primary events was 10^3, 10^4, 10^5, and 10^6. For each number of primary events ten runs were performed. The initial seed in the random number generator was changed for each run. All simulation outputs were imported in the algorithm. Table 7.1 reports, for every number of primary events, 1) the total number of γ-rays recorded by the spectrometer at all energies and in the ^{60}Co decay energy ranges, 2) the total number of *couples* selected by the algorithm, 3) the total number of reconstructed source positions, and 4) the algorithm computational time. The computational time, in particular, was estimated using the MATLAB Profiler [275] (MATLAB was running on: Windows 64 with Intel Core i7-6700 @ 3.41 GHz CPU and 16 GB RAM). All values were obtained by averaging the results from the different seeds.

For 10^4, 10^5, and 10^6 primary events, considering only one - the same - initial seed, a Gaussian fit was applied, along all axes, to the algorithm-reconstructed data. The peak centroid positions, μ, and the standard deviation, σ, were saved for all fits. Results are displayed in Figure 7.1, as a function of the number of simulated primary events. Both accuracy and precision improve by increasing the number of primary events. However, even in case of 10^4 primary events, which translates into just 1,906 recoded γ-rays and 59

[1] (1.173 ± 3% & 1.332 ± 3%)

Primary events	**Recorded γ-rays**		***Couples***	**Reconstructed source positions**	**Computational time**
	All energies	**^{60}Co decay energies**[1]			
10^3	187	72	7	5	∼1 min 35 sec
10^4	1906	713	59	153	∼9 min 16 sec
10^5	19657	7498	603	20,828	∼1hr 35 min
10^6	197634	75212	5828	1,964,428	∼15 hr 18 min

Table 7.1: Investigation of the algorithm dependance from the number of primary events. A ^{60}Co source was modelled in (0,0,0). The number of primary events was 10^3, 10^4, 10^5, and 10^6. For every number are reported: 1) the total number of γ-rays recorded by the spectrometer at all energies and in the ^{60}Co decay energy ranges, 2) the total number of *couples* selected by the algorithm, 3) the total number of reconstructed source positions, and 4) the algorithm computational time. For each number of primary events, ten runs were performed. The initial seed in the random number generator was changed for each run. Values were averaged from the different seeds.

couples, the algorithm reconstructs the source to within 6 mm along all axes. With very long simulations (10^6 primary events) the source reconstruction is achieved within 1 mm at the price of an excessively long computational cost (∼15 hr).

7.2 Algorithm dependance from the voxel size

To investigate how the voxel size v_{dim} affects the quality of the results presented in Panaino *et al* [274], an analysis was performed as follows. The simulation output, relative to a ^{60}Co source modelled at (0,0,0) with 10^5 primary events, was passed to the algorithm. In six different algorithm-runs the voxel size v_{dim} was changed to: 5, 4, 2, 1, 0.5 (results in the publication), and 0.2 mm. The virtual voxelised solid was always an 8×8×8 cm^3 cube. Figure 7.2 displays a virtual voxelised cube with v_{dim} equal to 5, 1, and 0.5 mm. For each axis a Gaussian fit was applied to the algorithm-reconstructed data. For every selected v_{dim} Table 7.2 reports the algorithm computational time, estimated with the MATLAB Profiler, and the uncertainty σ, with which the source is reconstructed along the three axes. By decreasing v_{dim} the computational time significantly increases. Conversely, by increasing v_{dim}, both the accuracy and the precision of the source reconstruction slightly deteriorate. Even when v_{dim} is 5 mm, however, the source is reconstructed to within 4 mm.

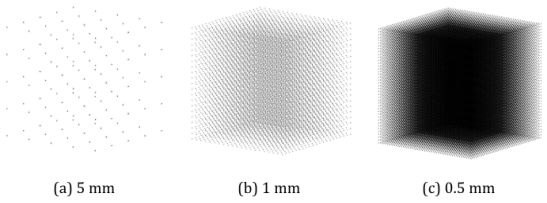

Figure 7.2: Virtual voxelised cube with v_{dim} equals to 5, 1, and 0.5 mm

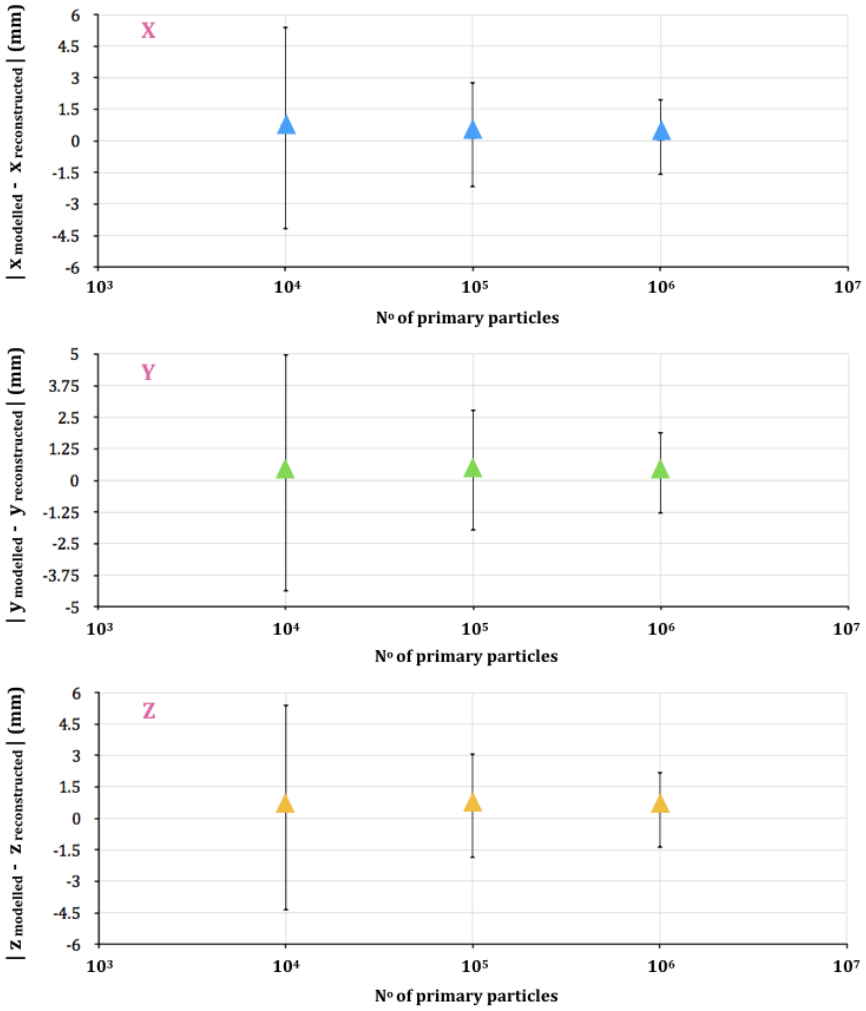

Figure 7.1: Peaks centroid positions and standard deviation values (error bars) of the algorithm-reconstructed data, as a function of the number of simulated primary events. Centroid positions are expressed in terms of euclidean distance between the modelled and the reconstructed source positions.

v_{dim}	Computational time	Sigma σ		
		X (mm)	Y (mm)	Z (mm)
5	11 s	3.8	3.9	3.8
4	17 s	3.5	3.7	3.5
2	76 s	3.4	3.5	3.4
1	13 min	3.3	3.4	3.3
0.5	∼ 1 hr 35 min	2.5	2.4	2.5
0.2	∼ 5 hr 58 min	2.1	2.3	1.9

Table 7.2: Investigation of the algorithm dependance from the voxel size v_{dim}. For every v_{dim} is reported the algorithm computational time and the uncertainty to within the source is reconstructed along all axes.

7.3 Future algorithm improvements

To further enhance the algorithm accuracy and precision a few improvements can be made. With respect to the form presented in Panaino *et al* [274], the authors envisage two immediate areas of development, as described in this Section.

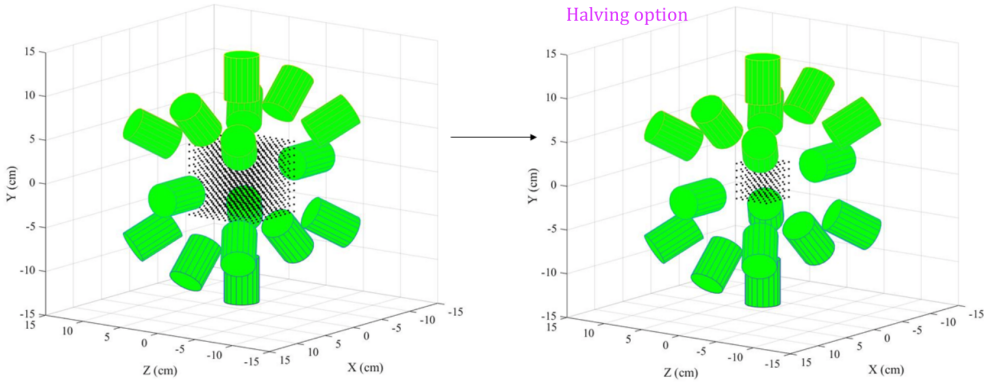

Figure 7.3: In the third function of the algorithm, Source-Position Reconstruction, the intersection between two triangulated *half*-hyperboloids is calculated. Each intersection is estimated inside a virtual voxelated cube located in the central area of the spectrometer. The larger the dimensions of this cube, the wider the sampled area. An increased cube volume also implies a longer algorithm computational time. In the "halving option" the dimensions of the cube are halved along all directions independently. The option is used if the source is at (0,0,0), or close enough to (0,0,0) so that the difference between the intensities of the γ-rays recorded in the detectors at backward/forward angles is not significant. The "halving option" offers a gain in computational time with no worsening of reconstruction precision.

7.3.1 The halving option

In the third function of the algorithm (Section 6.3.3) the intersection between each couple of subsequent *half*-hyperboloids is calculated in a virtual voxelised cube located in the central area of the spectrometer. The larger the dimensions of this cube (X_{neg}/X_{pos}, Y_{neg}/Y_{pos}, Z_{neg}/Z_{pos}), the wider the sampled area. By decreasing the cube size the algorithm computational time can be shortened, without worsening the reconstruction precision. In Panaino *et al* [274] the cube size has been reduced, along the three axes independently, by using the intensity of the γ-rays recorded in the detectors at backward/forward angles. This technique was proved to be successful in the reconstruction of a source at (20,20,20) mm (Section 8.5).

When the source is at (0,0,0), however, it subtends, to within statistical uncertainty, the same solid angle for all detectors. In this case the cube size can not be reduced because there is no intensity difference between the γ-rays recorded in the detectors at backward/forward angles. One solution, in case the source is at (0,0,0), or close enough to (0,0,0) so that the difference between the intensities of the γ-rays recorded in the detectors at backward/forward angles is not significant, consists in halving the dimensions of the cube along all directions independently, with the cube still centred at (0,0,0). In other words:

- if X = [X_{neg}, X_{pos}] $\quad$ [X_{neg}, X_{pos}] $\rightarrow$ [X_{neg}/2, X_{pos}/2]
- if Y = [Y_{neg}, Y_{pos}] $\quad$ [Y_{neg}, Y_{pos}] $\rightarrow$ [Y_{neg}/2, Y_{pos}/2]
- if Z = [Z_{neg}, Z_{pos}] $\quad$ [Z_{neg}, Z_{pos}] $\rightarrow$ [Z_{neg}/2, Z_{pos}/2]

As shown in Figure 7.3, the outcome of this *halving option* is a virtual voxelised cube with a halved volume, which implies a shorter computational time and a lower number of false reconstructed emitting-positions. The same simulation as in the publication - ^{60}Co source at (0,0,0) with 10^5 primary events - was utilised. The simulation was processed by

the algorithm with the halving option "on". As a consequence the virtual voxelised cube (v_{dim} of 0.5 mm) had a reduced volume of 64 cm^3 (X_{pos} = 2, X_{neg} = -2, Y_{pos} = 2, Y_{neg} = -2, Z_{pos} = 2; Z_{neg} = -2). For each co-ordinate axis a Gaussian fit was applied to the algorithm-reconstructed data. The reconstructed coordinate values $\mu \pm \sigma$ were: -0.4 ± 1.7, -0.4 ± 1.6, and -0.5 ± 1.9 mm along the X, Y, and Z axis, respectively. The total algorithm computational time was 3 minutes (Windows 64 with Intel Core i7-6700 @ 3.41 GHz CPU and 16 GB RAM) and 566 *couples* were selected.

The source location has been accurately determined within a 2 mm uncertainty. Compared to the reconstruction of a source at (0,0,0) with the halving option "off" (3 mm uncertainty), the reconstruction precision with the halving option "on" is improved. However, even when the halving option is "on", the reconstruction precision is inferior compared to the reconstruction of a source at (20,20,20) (1.5 mm uncertainty). Indeed, as explained in Section 8.5, the source position affects the reconstruction precision also in the selection of the hyperboloid correct side. This issue is not modified by the halving option.

7.3.2 The polynomial fit

As described in Section 6.3.3, each intersection between two *half*-hyperboloids results in a series of points in the 3D space. Each series of points is then fitted with a 3^{rd} order polynomial function. In Figure 7.4a are reported the points belonging to several 3D curves, while Figure 7.4b shows the same curves after the points were fitted. For clarity, 15 intersections only were depicted. Uncertainties are introduced by the fit, thus it is believed that, in future, the algorithm could benefit from an improvement of this particular step.

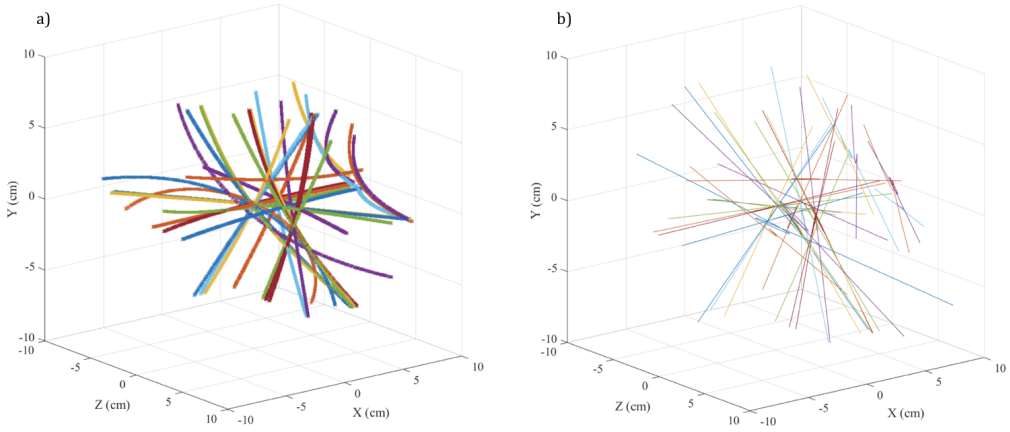

Figure 7.4: In the third function of the algorithm, Source-Position Reconstruction, the intersection between two triangulated *half*-hyperboloids is calculated. a) Each intersection between two *half*-hyperboloids results in a series of points in the 3D space. b) Each series of points is then fitted with a 3^{rd} order polynomial function. The fitting process adds uncertainties to the reconstruction process.

Chapter 8

Publication 3

8.1 Introduction to Publication 3

In the previous publication, Panaino *et al* [274], a new mathematical reconstruction algorithm was illustrated. It determines, in the full 3D space, the emission position of γ-ray sources with a cascade decay. The algorithm is coupled with a multi-detector γ-ray spectrometer; only realistic detector signals are employed. The algorithm capability in reconstructing the emitting position of ^{60}Co sources was investigated in-silico [274].

The authors believe that the algorithm has the potential to be employed in a wide range of industrial and medical applications. In the context of PB therapy, in particular, to assess in-vivo range verification via PG detection, the algorithm is aimed at reconstructing the emission position of the 2.741/6.128 MeV ^{16}O-induced PG rays.

This study reports the experimental validation of the algorithm. Tests have been performed, with a ^{60}Co source, using the NAtional Nuclear Array (NANA) multi-detector spectrometer at National Physical Laboratory (NPL). Further in-silico evaluations are presented. A γ-ray source, emitting at the same energy of the ^{16}O-induced PG rays (2.741 & 6.128 MeV), was modelled. The algorithm performance, in reconstructing the source emission position, was investigated.

The reconstruction algorithm employed in this study is described in Panaino *et al* [274]. The full MATLAB code is reported in Appendix 3. The study is to be submitted in *Applied Radiation and Isotopes*, with authors: *Panaino, C.M., Mackay, R.I., Kirkby, K.J., R. Shearman, S. Collins, B. Phoenix, C. Wheldon, T. Wheldon, P.H. Regan, and Taylor, M.J.*.

Experimental validation of a novel 3D position reconstruction algorithm using a radioactive source and a multi-detector γ-ray spectrometer

Costanza M. V. Panaino[1,*], Ranald I. Mackay[1,2], Karen J. Kirkby[1,2], Robert Shearman[3], Sean Collins[3], Ben Phoenix[4], Carl Wheldon[4], Tzany Wheldon[4], Patrick H. Regan[3], and Michael J. Taylor[1,2]

[1] Division of Cancer Sciences, University of Manchester, M13 9PL, Manchester, UK;

[2] The Christie NHS Foundation Trust, M20 4BX, Manchester, UK;

[3] National Physical Laboratory, TW11 0LW, Teddington, UK;

[4] School of Physics and Astronomy, University of Birmingham, B15 2TT, Birmingham, UK;

[*] Corresponding author

A method has been developed to monitor the proton range in tissues through the detection of ^{16}O-induced prompt gamma (PG) rays emitted in coincidence. PG rays are recorded by a spectrometer and their emission position is reconstructed by an algorithm. The method was experimentally validated using a ^{60}Co source and an array comprised of 8 $LaBr_3$(Ce) detectors. The Monte Carlo based Geant4 toolkit was employed to simulate the experimental set-up and an ideal set-up with 16 detectors. The system/algorithm performance was also assessed by modelling an unrealistic point-like source, emitting at the energy of the ^{16}O-induced PG rays. A ^{60}Co source at (0,0,0) and (0,0,-30) mm was experimentally reconstructed with an uncertainty of less than 5 mm. Simulation results, with the source at the same positions, show a reconstruction precision of $\sim$1 mm in all set-ups. For the unrealistic point-like source, due to the increased scattering in the detectors, the reconstruction sigma rises to 1 cm. Work is being carried out to improve the performance of the method. In light of the positive experimental tests, further evaluations with proton beams are planned.

Keywords: gamma-ray spectroscopy, reconstruction algorithm, source emission position reconstruction.

8.2 Introduction

With respect to conventional radiotherapy with photons, proton therapy (PT) offers substantial dosimetrical advantages. The depth-dose distribution of proton beams is characterised by a low dose along the entrance channel and a sharp distal increase and fall-off towards the end of the range, in the so-called Bragg peak. At the Bragg peak ∼1/3 of the total initial energy is released. The shape of depth-dose distribution is exploited in radiotherapy: if the beam stops at the target, the maximum dose is delivered to the tumour whilst the surrounding healthy tissues are spared [ARI1].

Range uncertainty, the uncertainty in the position of the distal fall-off of proton beams, may have a profound impact on the proton dose distribution. Range uncertainty can cause the target to be substantially under-dosed, failing the curative intent of the therapy, or the adjacent organs-at-risk to be over-dosed, leading to unwanted acute/late side effects. Indeed, range uncertainty is one of the main factors preventing the full exploitation of PT potential [ARI2]. Clinically, range uncertainty is managed by making treatment plans *robust*. The way this is achieved primarily depends on the treatment approach being used. For fields delivering a uniform dose to the target, a lateral expansion of the Clinical Target Volume (CTV) guards against under-dosing of the target due to set-up variations and/or organ motion. In addition, a larger expansion, in the distal direction, ensures coverage against range uncertainty [ARI3]. For Intensity Modulated Proton Therapy (IMPT) *robust optimisation* incorporates range and set-up uncertainties directly into the IMPT plan [ARI4]. Whatever approach is chosen, margins or robust planning, there is always the need to test its success by means of *in-vivo*, i.e. in the patient, range verification.

Several range verification techniques have been proposed. The most advantageous method is based on the detection of prompt gamma (PG) rays emitted after proton-nuclear inelastic reactions [ARI5]. After an interaction between a proton of the beam and a nucleus of the target, the nucleus can be left in an excited state. Swiftly, via the emission of γ-rays, the nucleus returns to its ground state. Being almost instantaneous, within 10^{-9} s [ARI6], such emission is termed *prompt* [ARI7]. The PG spectrum is characterised by several discrete γ-lines, with energy in the range 2 to 15 MeV. Typically, only the PG rays emitted by the most abundant isotopes in human tissues, namely carbon (^{12}C), oxygen (^{16}O) and nitrogen (^{15}N), are considered. A good correlation between the intensity of the emitted PG rays and the fall-off positions of proton beams was experimentally proved by Verburg *et al* [ARI8]. PG-ray emission is also characterised by a favourable production yield. The total PG yield per proton is about 10% in water. Thus, assuming an instantaneous clinical beam current of 2 nA [ARI9], which corresponds to $1.2 \cdot 10^{10}$ protons-per-second, $1.2 \cdot 10^{9}$ PG-per-second are generated. Polf *et al* [ARI10] investigated the possibility of determining the concentration of oxygen, within irradiated tissues, by measuring the amount of emitted ^{16}O-induced PG rays. It was observed that the 6.13 MeV ^{16}O-induced PG emission is linearly proportional to the amount of oxygen in the tissues. It was also estimated that ∼$1.64 \cdot 10^{7}$ 6.13 MeV PG rays are released per gram of ^{16}O, per Gy of dose delivered.

Since PG detection was first proposed for proton range verification [ARI11] the development of a PG detection system, usable in the clinical environment, has progressed at a slow rate. This is mainly due to the energies of the PG rays, too high to be efficiently measured with the standard devices employed in diagnostic imaging. Several different clinical prototypes have been proposed. Following the classification given by Krimmer *et al* [ARI12] systems are divided into imaging and non-imaging systems. Imaging systems require a mechanical or electronic collimation. Non-imaging systems are integrated yield counting devices, they use additional information such as PG energy or timing.

In our first investigation [ARI13], we reported on the development of a new mathematical reconstruction algorithm to determine the emittance position of the 2.741/6.128 MeV ^{16}O-induced PG rays, emitted in cascade decay.

In our subsequent investigation [ARI14], an upgraded version of the reconstruction algorithm was developed. The algorithm determines, with millimetric accuracy, the 3D emitting location of a γ-ray source with a cascade decay. In this version, the algorithm is fed only signals from conventional, non-position sensitive, fast-timing scintillation detectors.

To detect the γ radiation, a spectrometer comprised of 16 $LaBr_3$(Ce) detectors, symmetrically arranged, was considered in both investigations.

In the present study the algorithm from Panaino *et al* [ARI14] is experimentally validated using the NAtional Nuclear Array (NANA) at the National Physical Laboratory (NPL). Additional in-silico evaluations are reported. Simulations were performed with an un-realistic point-like source modelled at various known locations within the spectrometer central volume. The source emits, with equal probability, at the same energetic values of the two ^{16}O-induced PG-lines released in a cascade scheme (2.741/6.128 MeV). The source positions are reconstructed by the algorithm.

A novel range verification method is conceptualised. To the best of our knowledge this is the first method based on the detection of those PG rays which are simultaneously emitted in a cascade decay. The analysis reported here represents the first step toward the implementation of the method in the clinical environment.

8.3 Methods

8.3.1 3D source position reconstruction method

The technique in this work is based on the coincident detection of the γ-rays emitted in cascade by a radioactive source or following inelastic nuclear reactions. If the intermediate state is not isomeric, the time difference between these γ-rays is $\sim 10^{-12}/10^{-15}$ s, which is short compared to the nominal time resolution of scintillator type γ-ray spectroscopy detectors ($\sim$400-500 ps [ARI15]). Within the limitation of current detector and electronic systems, two γ-rays in a cascade are effectively emitted simultaneously in time and position.

The detection of a *couple* of γ-rays in coincidence, coupled with a reconstruction algorithm, allows the identification of the common emission point. The identification uncertainty is proportional to the uncertainties in the position and timing resolution of the system.

The present technique was originally developed to reconstruct the emittance positions of PG rays, following proton irradiation. ^{16}O is among the most abundant PG emitters in biological tissues. Following inelastic nuclear reaction with a proton of the beam, one of the most favourable ^{16}O de-excitation branch is characterised by the 2.741 MeV γ emission, from the $I^{\pi} = 2^{-}$ state to the $I^{\pi} = 3^{-}$ state, followed by the 6.128 MeV γ emission to the ground state (g.s.) [ARI16]. The maximum intensity, relative to the ^{16}O-induced PG distribution, is a few millimetres proximal to the Bragg peak. Thus, the beam range can be inferred from the emission positions of all the detected ^{16}O-induced γ-ray *couples*.

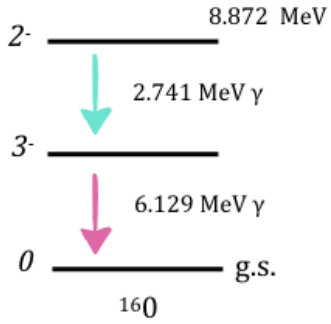

Figure 8.1: De-excitation channel exploited for the proton range verification method. One of the most favourable (p,^{16}O) de-excitation branches is characterised by the 2.741 MeV γ emission, followed by the 6.128 MeV γ emission.

As a proof-of-principle a ^{60}Co isotropic point source can be utilised. ^{60}Co has an ideal decay scheme for coincidence counting, with two γ-rays of 1.173/1.332 MeV emitted in a cascade, following β^{-} decay and negligible internal conversion. The adopted value for the intermediate state lifetime is 0.713 ps [ARI17].

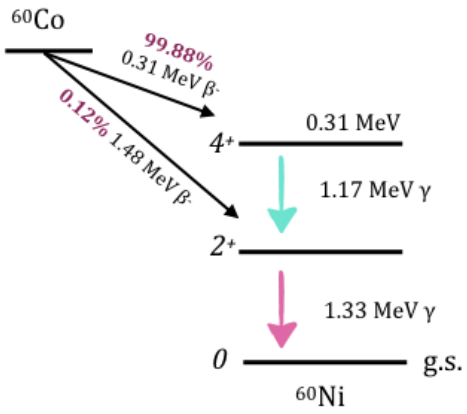

Figure 8.2: ^{60}Co decay scheme. With two γ-rays in cascade, ^{60}Co sources have an ideal decay scheme for coincidence counting and can be used in proof-of-principle evaluations of the range verification method.

8.3.2 γ-ray spectrometer

The technique developed in this work does not require any mechanical collimation of the detectors. The *ideal* spectrometer is composed of 16 $LaBr_3$(Ce) cylindrical detectors (2" length and 1.5" diameter). Detectors are arranged as follows: a ring of eight detectors in the vertical plane, with a 45° mutual angular spacing, plus one ring of four detectors at backward angles (45°), and one ring of four detectors at forward angles (45°), with respect to the Z axis. Such an arrangement is shown diagrammatically in Figure 8.3. For an isotropic source at the centre of the spectrometer, when the distance between the source and the front face of all detectors is 9 cm, this geometry covers 24% of the total solid angle.

$LaBr_3$(Ce) is an appropriate choice for nuclear spectroscopy and metrological investigations of discrete high energy γ-lines. An energy resolution of ∼40 keV Full Width at Half Maximum (FWHM) at 1.33 MeV is achievable. Additionally, $LaBr_3$(Ce) has a relatively high atomic number, leading to a good full-energy peak efficiency per unit volume. The major advantage offered by $LaBr_3$(Ce) is the excellent intrinsic time resolution, from a few keV up to 4 MeV, which allows the coincident coupling of two or more mutually coincident γ-rays from a cascade decay [CPC11]. The timing responses of $LaBr_3$(Ce) detectors in coincidence mode has been extensively studied ([ARI18], [ARI19], [ARI20], [ARI21]). Reǵis *et al* ([ARI20], [ARI21]) demonstrated that discrete nuclear excited states, with lifetimes down to ∼10 ps, are measurable with $LaBr_3$(Ce) detectors.

$LaBr_3$(Ce) crystals exhibit spectral features arising from the internal activity. Such activity, estimated as ∼1 Bq/cm^3 [ARI22], is predominantly associated to the decay of ^{138}La, a primordial radionuclide which makes up ∼0.09% of naturally occurring lanthanum. $LaBr_3$(Ce) crystals also contains internal activity from to the natural decay chain of ^{227}Ac. Due to the coincidence requirement, the spectral emission from the internal activity does not interfere with the γ-rays source. The internal activity, on the other hand, represents an easily measurable background signal, useful for standard internal calibration [ARI23].

8.3.3 3D position reconstruction algorithm

For every γ-ray, γ_i, recorded by the spectrometer, several pieces of information are saved:

- The energy E_i;
- The time t_i, difference between the detection time and the start of acquisition;
- The detector number Det_i, in which γ_i was recorded.

A source position reconstruction algorithm has been developed within the MATLAB environment (version R2018b). The algorithm takes as input the information from each γ-rays *couple* and determines their emission position. Only realistic detector signals are employed, thus the algorithm can be fed with experimental data. Just a brief algorithm overview is given here. The full description is available in Panaino *et al* [ARI14].

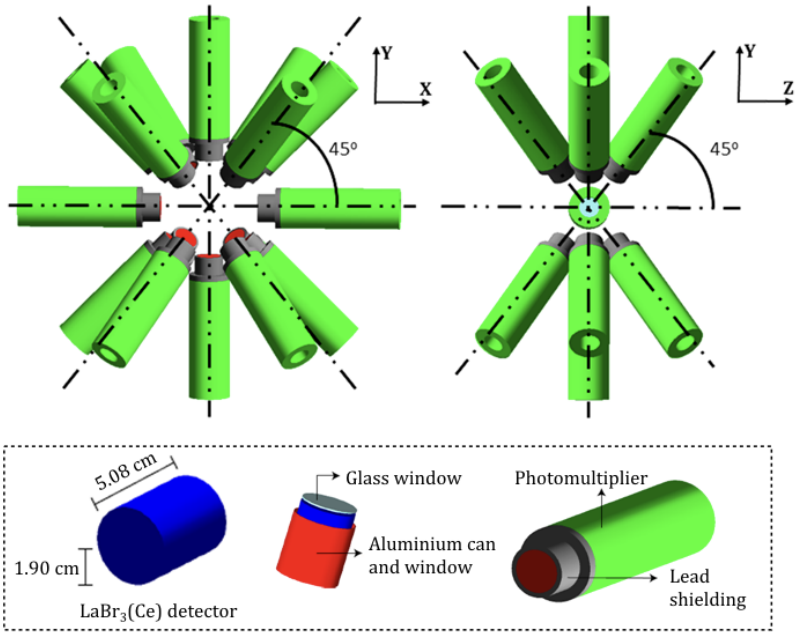

Figure 8.3: Design of the *ideal* spectrometer under investigation for range verification via PG detection. The spectrometer comprises a ring of 8 detectors in the vertical plane, with a 45° mutual angular spacing, plus one ring of 4 detectors at backward angles (45°), and one ring of 4 detectors at forward angles (45°), with respect to the Z axis.

Step 1: γ-ray couple selection

The algorithm selects *couples* of γ-rays, γ_i and γ_{i+1}, which satisfy the following criteria:

1. γ_i/γ_{i+1}, are recorded in coincidence in two different detectors (i.e. $\mathrm{Det}_i \neq \mathrm{Det}_{i+1}$).
2. The energies $\mathrm{E}_i/\mathrm{E}_{i+1}$ of γ_i/γ_{i+1} are:
   - ^{16}O-induced PG rays $\rightarrow$ 2.741/6.128 MeV $\pm$ 3%, any order.
   - ^{60}Co decay $\rightarrow$ 1.173/1.332 MeV $\pm$ 3%, any order.

Step 2: hit positions values identification

For each γ-ray, γ_i, belonging to a *couple* and detected in Det_i, three Probability Density Functions (PDFs_i) for Det_i, are loaded, one per axis. All PDFs_i were previously calculated and stored in the algorithm. The PDFs_i are sampled, using the acceptance-rejection method, to obtain the coordinates (x_i, y_i, z_i) of the last hit position of γ_i in Det_i.

Step 3: γ-ray couple analysis

The *couple* γ_i/γ_{i+1}, detected in (x_i, y_i, z_i)/(x_{i+1}, y_{i+1}, z_{i+1}), at time $\mathrm{t}_i/\mathrm{t}_{i+1}$, is represented by a two-sheeted hyperboloid, having foci in (x_i, y_i, z_i)/(x_{i+1}, y_{i+1}, z_{i+1}) and constant k $= \Delta \cdot \mathrm{c} = |t_{i+1} - t_i| \cdot \mathrm{c}$. One hyperboloid side, a *half*-hyperboloid, is selected. The selection is based on the difference in intensity between the total recorded γ-rays in Det_i and in Det_{i+1}.

Step 4: Intersection between half-hyperboloids

At the end of Step 3 n *half*-hyperboloids are stored, where n is the total number of *couples*. The intersection between each couple of subsequent *half*-hyperboloids is calculated in

a virtual voxelised cube located in the central area of the spectrometer, with voxel size v_{dim}. The larger the dimensions of this cube (X_{neg}/X_{pos}, Y_{neg}/Y_{pos}, Z_{neg}/Z_{pos}), the wider the sampled area. If two *half*-hyperboloids intersect at a specific voxel the central point of that voxel is saved as an intersection point. Thus, for a constant cube volume, the smaller v_{dim} is, the more intersection points may be produced. By both increasing the cube size and/or decreasing the voxels size the algorithm computational time extends. Techniques, based on the intensity of the γ-rays recorded in different detectors, have been developed to reduce the cube size, along the three axes independently. As a compromise between reconstruction precision and computational costs, a voxel size of 0.5 mm was selected.

Each intersection consists in a series of points following a single 3D trajectory. Each series is fitted with a 3^{rd} order polynomial function. Thus, a curve is obtained.

Step 5: Intersection between 3D curves

Each couple of curves is retrieved and their intersection is determined. If such an intersection does not exist, i.e. if the curves do not intersect, the two points, one per curve, with minimum distance, are found. The average coordinates between these points is the intersection.

Algorithm computational cost

When 10^6 ^{60}Co decays are considered, if the spectrometer has 16 detectors and a 9 cm internal radius, up to ∼200000 γ-rays are recorded (all energies) and up to ∼6000 *couples* are accepted by the algorithm in Step 1. The emission position reconstruction is completed in ∼15 hrs (Windows 64 with Intel Core i7-6700 @ 3.41 GHz CPU and 16 GB RAM) [ARI14].

8.3.4 Experimental analysis

Experimental tests have been conducted at the NPL using the NANA ([ARI24], [ARI23], [280], [281]). NANA is a multi-detector γ-ray spectrometer designed to measure relatively low-multiplicity γ-ray coincidences of 2-3 γ-rays in a discrete cascade. Using time-correlated, γ-ray coincidences, NANA allows the traceable characterisation of radionuclides with complex decay schemes.

The original design of NANA, shown in Figure 1 from Lorusso *et al* [ARI23], comprises 12 $LaBr_3$(Ce) detectors. A lead shielding reduces the Compton cross-talk between detectors. Due to unavailability of four detectors, in the current work eight detectors only were in place. Among the eight detectors four were held in the central ring, with a 90° mutual angular spacing, and four were arranged at backward angles (45°) relative to the Z axis. With respect to the ideal spectrometer presented in Panaino *et al* ([ARI13], [ARI14]) and shown in Figure 8.3, in the experimental set-up the total detectors number is halved. The spectrometer in the experimental set-up is shown in Figure 8.4, CAD design, and in the left side of Figure 8.5. Each $LaBr_3$(Ce) detector comprises a cylindrical crystal (2" length and 1.5" diameter) housed in an aluminium holding can and attached to a Hamamatsu R9779 fast-timing photomultiplier tube (PMT). The pulses from the energy output of the PMTs are sent directly to

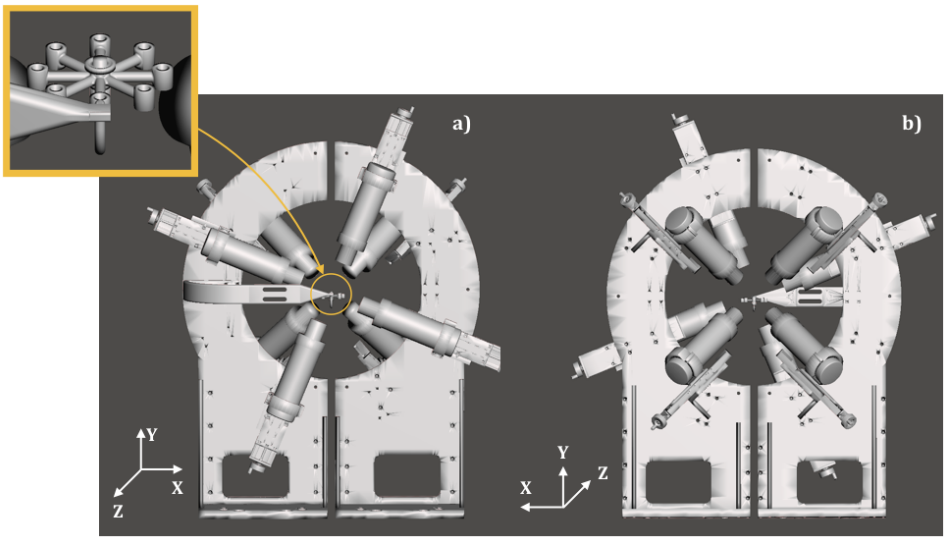

Figure 8.4: CAD design of the NANA at NPL. In the experimental set-up the NANA was comprised of eight $LaBr_3$(Ce) detectors: a) four in the central ring, with a 90° mutual angular spacing and b) four at backward angles (45°) relative to the Z axis (b). A 3D printed source holder allowed the source to be located at 9 different positions within the XZ plane (Y = 0).

a CAEN V1751, 1 GHz 8 channels digitiser, which provides an independent, synchronised time-stamped energy signal for each input channel. The spectrometer internal radius was set at 9 cm. For an isotropic source at the centre of the spectrometer (i.e. at (0,0,0)), this geometry covers 12% of the total solid angle.

A 10 kBq source was employed. The source holder, illustrated in the inset in Figure 8.4, was designed and 3D printed for the experiment; it allowed the source to be located at the spectrometer centre, (0,0,0), as well as at eight additional satellite positions in the XZ plane (Y = 0). The distance between the source holder and the satellite positions is 30 mm.

Measurements were acquired with the source at (0,0,0) and (0,0,-30) mm. Once each measurement was completed the reconstruction algorithm (Section 8.3.3) was fed with the experimental data. Due to the algorithm computational cost, the first 10^6 events, at all energies producing a trigger, were retrieved and imported in the algorithm.

8.3.5 Geant4 simulations

The Geant4 10.04 Monte Carlo toolkit [ARI27] has been employed. In a first in-silico study the spectrometer was modelled with the same detectors number and positions as in the experimental set-up. An isotropic point ^{60}Co source was located within the spectrometer central volume at (0,0,0) and (0,0,-30) mm, i.e. the same locations as in the experimental tests. The source holder and the spectrometer frame were not modelled. Runs have been performed with 10^6 primary events. In Figure 8.5 the Geant4 geometry is shown in comparison with the NANA.

In a second in-silico study the *ideal* spectrometer, with 16 detectors, was modelled. The ^{60}Co source was located at (0,0,0) and (0,0,-30) mm. The present evaluation aims at comparing the source emission position reconstruction with 8 and 16 detectors.

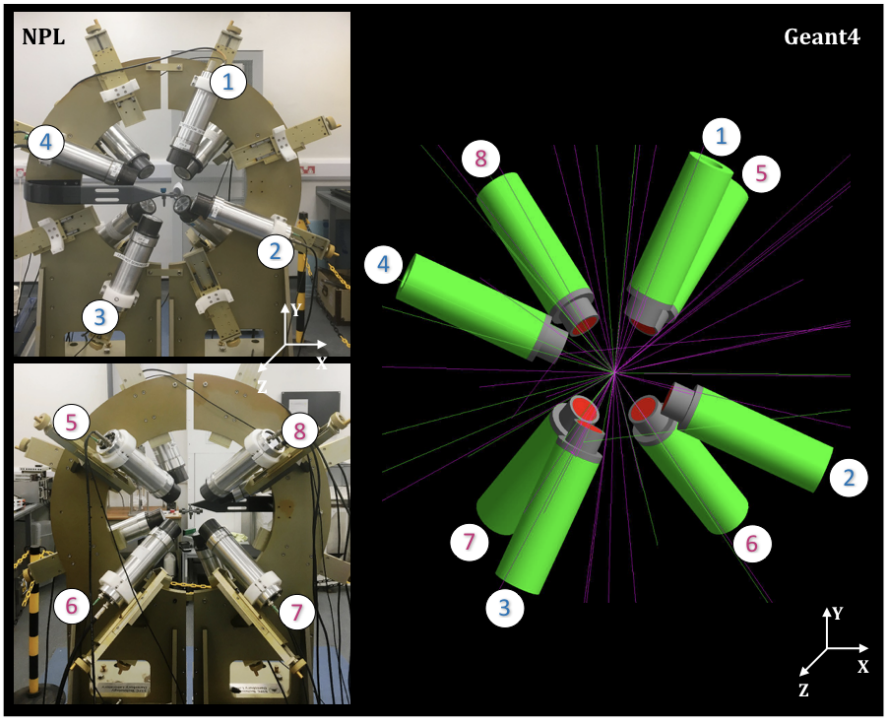

Figure 8.5: Left: the NANA at NPL. Right: the geometry of the experimental set-up in Geant4.

In a third in-silico study the *ideal* spectrometer was modelled. An isotropic point source was located in the central volume of the spectrometer, at (0,0,0) and (20,20,20) mm. The source emits with equal probability at 2.741 and 6.128 MeV, which are the energetic values of the two ^{16}O-induced PG-lines in cascade[1]. With respect to the de-excitation from a ^{60}Co source, the higher energy of the ^{16}O-induced PG rays implies an increased amount of scattering in the detector medium and a reduced number of *couples* accepted by the algorithm. Thus, 10^7 primary events were simulated.

For the $LaBr_3$(Ce) detectors an energy resolution of 3% FWHM [ARI28] and a time resolution of 280 ps [ARI29] have been used. The $LaBr_3$(Ce) internal activity has not been modelled. Both electromagnetic *EmStandardPhysics4* and radioactive decay *G4DecayPhysics* physics lists have been combined together and a secondary particle production "cut" value of 0.5 mm was set to optimise run time without adversely affecting precision. All simulations have been performed in air with a spectrometer internal radius of 9 cm.

8.4 Results

8.4.1 Reconstruction of a ^{60}Co source

^{60}Co source at (0,0,0)

Figure 8.6 shows the experimental ^{60}Co spectrum obtained with detectors 1-4, vertical plane (Figure 8.6a), and detectors 5-8, backward angles (Figure 8.6b), for an isotropic source located at (0,0,0). The algorithm reconstructed coordinates, relative to the same source, are presented in Figure 8.7. This Figure reports the reconstruction, of 1) the experimental data

[1]The Geant4 script for this source is reported in Appendix 4.

acquired at NANA, *black* histogram (Figure 8.7a), 2) the simulation data with 8 detectors, *blue* histogram, and 3) the simulation data with 16 detectors, *red* histogram (Figure 8.7b).

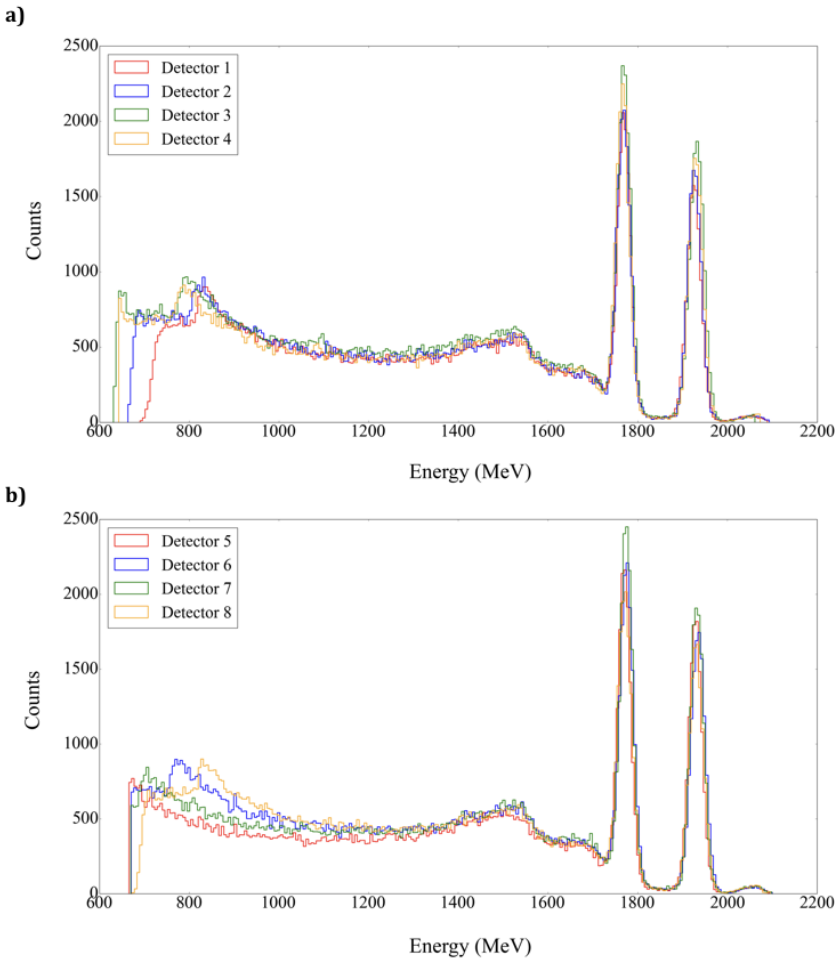

Figure 8.6: Experimental ^{60}Co spectrum obtained for a source at (0,0,0) with a) detectors 1-4 (vertical plane) and b) detectors 5-8 (backward angles, 45°, relative to the Z axis)

For the analysis of the experimental data, the algorithm was fed the first 10^6 recorded γ-rays. 2509 *couples* were selected and $\sim 4.9 \cdot 10^5$ virtual source positions were reconstructed. For each co-ordinate axis a Gaussian fit was applied to the algorithm-reconstructed data. The peak centroid position, μ, corresponds to the source location coordinate, while the standard deviation, σ, represents the position uncertainty. The reconstructed coordinate values $\mu \pm \sigma$ are reported in Table 8.1 along all axes. The source location was determined by the algorithm within a 5 mm uncertainty.

In the simulations, the total number of recorded γ-rays was 108698, in the 8 detectors set-up, and 197685, in the 16 detectors set-up. This leads to a spectrometer geometrical efficiency, defined as the number of recorded γ-rays divided by the number of initial γ-rays emitted by the source (10^6), of $\sim$11% and $\sim$20%. Simulation data were processed by the algorithm. In the 8 and 16 detector set-up, respectively, the algorithm selected 2960 and 5639 *couples* and reconstructed $\sim 4.9 \cdot 10^5$ and $\sim 1.8 \cdot 10^6$ virtual source positions. All reconstructed coordinate values $\mu \pm \sigma$ are reported in Table 8.1. The source location has been determined within 1 mm uncertainty in both set-ups.

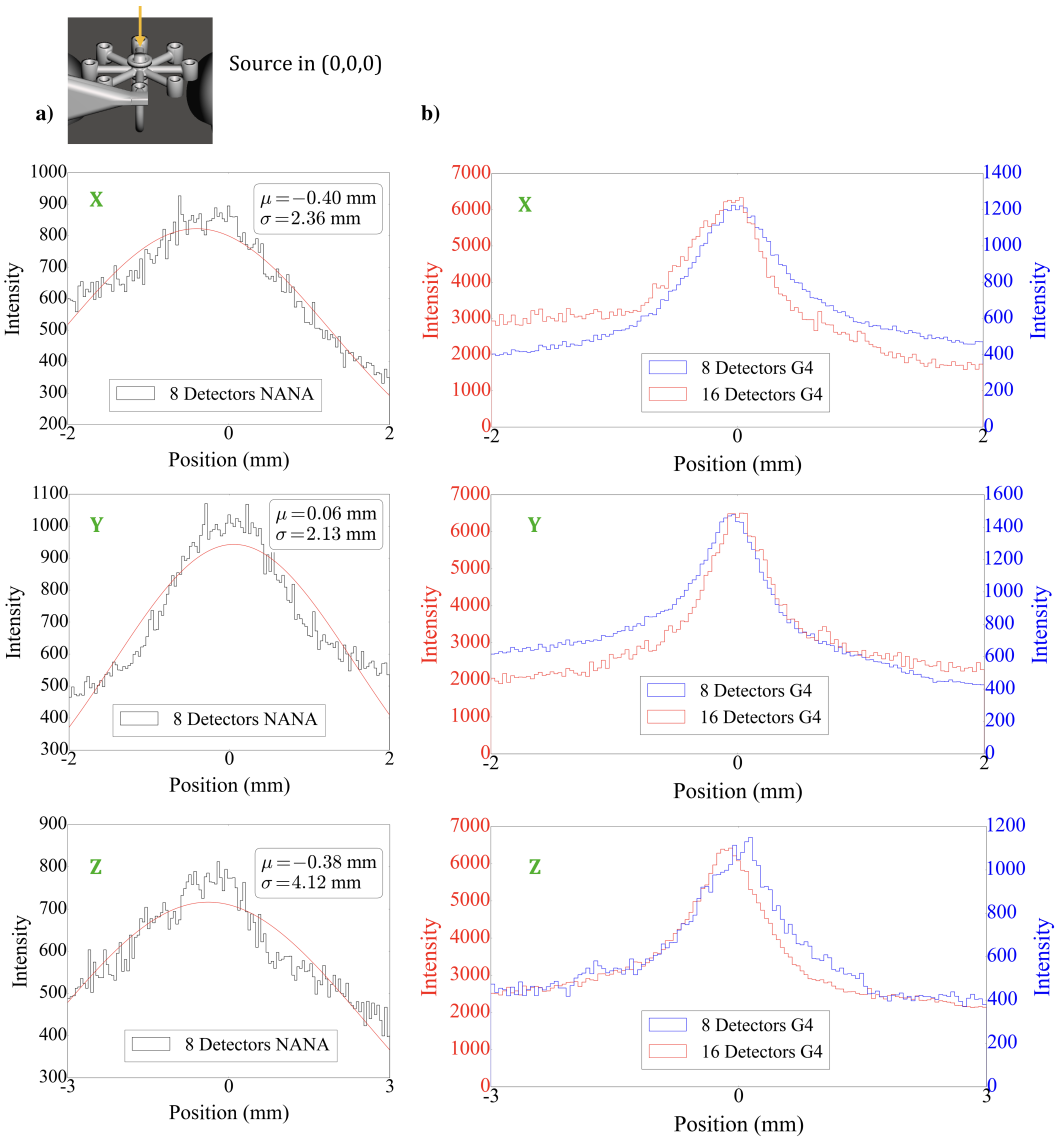

Figure 8.7: Coordinates of a single isotropic ^{60}Co source at (0, 0, 0) reconstructed by the in-house developed algorithm. The algorithm is fed: 1) the experimental data acquired at NANA, *black* histogram, with only 8 $LaBr_3$(Ce) detectors in place, 2) the simulation data with 8 detectors, *blue* histogram, and 3) the simulation data with 16 detectors, *red* histogram (*ideal* detection system).

Source at (0,0,0)						
	X		***Y***		***Z***	
	μ (mm)	σ (mm)	μ (mm)	σ (mm)	μ (mm)	σ (mm)
NANA (8 detectors)	-0.4	2.36	0.06	2.13	-0.38	4.12
G4 (8 detectors)	0.0	1.1	-0.1	1.0	0.1	1.1
G4 (16 detectors)	0.0	0.8	0.0	0.9	-0.2	1.1

Table 8.1: Emission position reconstruction of a ^{60}Co source at (0,0,0). The lateral spread (standard deviation), σ, and the centroid, μ, of the algorithm-reconstructed ^{60}Co emitting position, as obtained through the application of a Gaussian fit, are reported along all axes. The algorithm is fed with: 1) the experimental data acquired at NANA, 2) the simulation data with 8 detectors, and 3) the simulation data with 16 detectors.

^{60}Co source at (0,0,-30) mm

Figure 8.8b reports the algorithm reconstructed coordinates for an isotropic source at (0,0,-30) mm. The algorithm is fed: 1) the experimental data acquired at NANA, *black* histogram

(Figure 8.8a), 2) the simulation data with 8 detectors, *blue* histogram, and 3) the simulation data with 16 detectors, *red* histogram (Figure 8.8b).

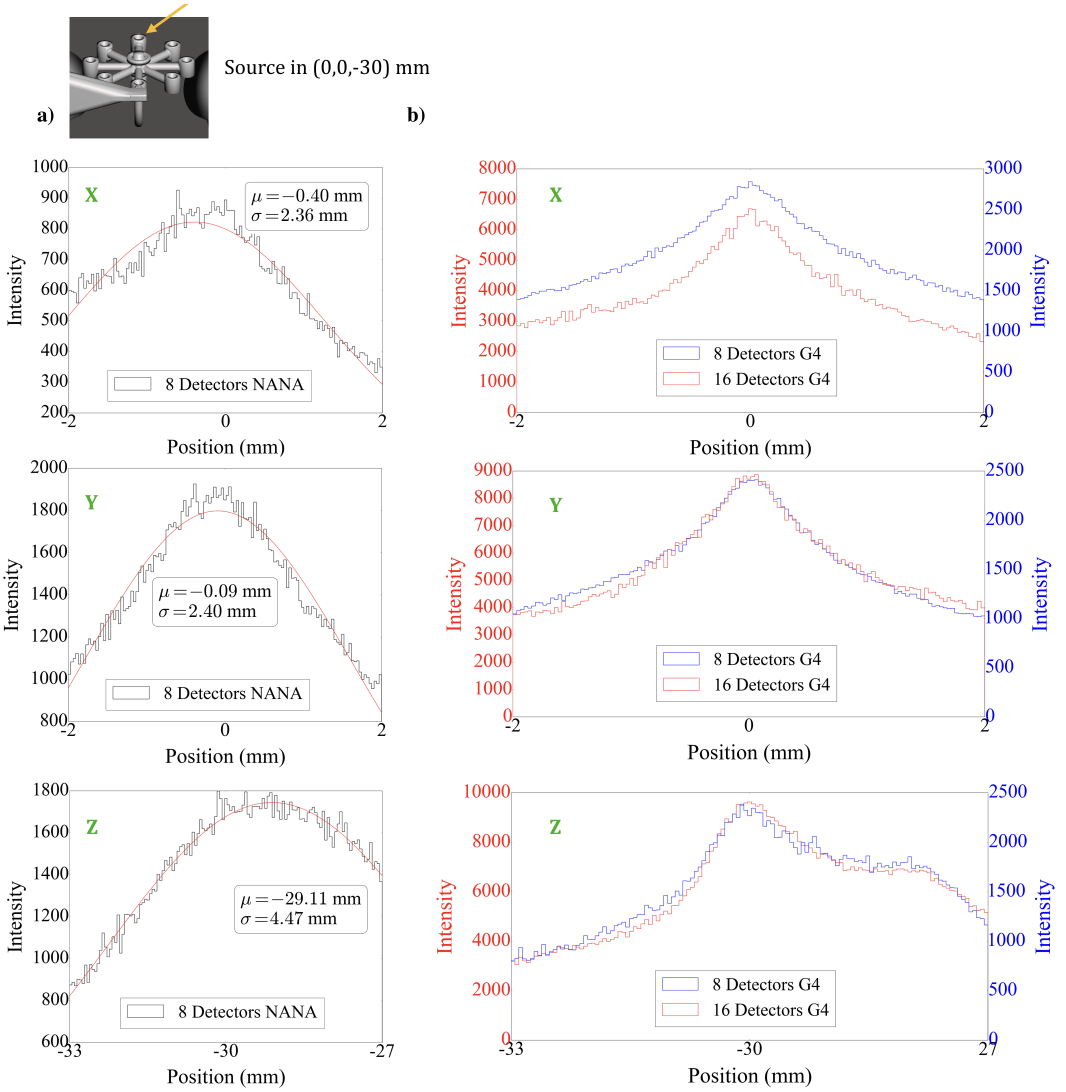

Figure 8.8: Coordinates of a single isotropic ^{60}Co source at (0,0,-30) mm reconstructed by the in-house developed algorithm. The algorithm is fed: 1) the experimental data acquired at NANA, *black* histogram, with only 8 $LaBr_3$(Ce) detectors in place, 2) the simulation data with 8 detectors, *blue* histogram, and 3) the simulation data with 16 detectors, *red* histogram (*ideal* detection system).

For the analysis of the experimental data the first 10^6 recorded γ-rays were considered. The algorithm selected 2354 *couples* and reconstructed $\sim 2.7 \cdot 10^5$ virtual source positions. For each axis a Gaussian fit was applied to the algorithm-reconstructed data. The source location was determined by the algorithm within a 5 mm uncertainty. In the simulations, the total number of recorded γ-rays was 100327, in the 8 detectors set-up, and 189301, in the 16 detectors set-up. This leads to a spectrometer geometrical efficiency of $\sim$11% and $\sim$19%, for the 8 and 16 detectors set-up, respectively. Simulation data were processed by the algorithm. The number of *couples* was 2734, in the 8 detectors set-up, and 5588, in the 16 detectors set-up, while the number of reconstructed virtual source positions was $\sim 2.8 \cdot 10^5$ and $\sim 1.5 \cdot 10^6$, in the 8 and 16 detectors set-up, respectively. The source location has been determined within 1 mm uncertainty in both set-ups. All reconstructed coordinate values are reported in Table 8.2.

Source at (0,0,-30) mm						
	X		***Y***		***Z***	
	μ (mm)	σ (mm)	μ (mm)	σ (mm)	μ (mm)	σ (mm)
NANA (8 detectors)	-0.4	2.36	-0.1	2.4	-29.1	4.5
G4 (8 detectors)	-0.2	1.4	0.0	0.7	-30.2	1.1
G4 (16 detectors)	-0.1	0.6	0.0	0.5	-30.0	1.0

Table 8.2: Emission position reconstruction of a ^{60}Co source at (0,0,-30) mm. The lateral spread (standard deviation), σ, and the centroid, μ, of the algorithm-reconstructed ^{60}Co emitting position, as obtained through the application of a Gaussian fit, are reported along all axes. The algorithm is fed with: 1) the experimental data acquired at NANA, 2) the simulation data with 8 detectors, and 3) the simulation data with 16 detectors.

8.4.2 Reconstruction of a ^{16}O source

^{16}O source at (0,0,0)

Figure 8.9a shows the reconstructed coordinates, for an isotropic source modelled at (0,0,0), along the X, Y, and Z axis. The source emits, with equal probability, at 2.741 and 6.128 MeV. These are the energetic values of the two ^{16}O-induced PG-lines, emitted in cascade, under exploitation for the range verification method in development. The algorithm selected 1333 *couples* and reconstructed 31626 virtual source positions. A Gaussian fit was applied to the reconstructed data. The reconstructed coordinated values, $\mu \pm \sigma$, are: 0.21 $\pm$ 5.25 (X), 0.05 $\pm$ 4.53 (Y), and -1.53 $\pm$ 10.44 mm (Z).

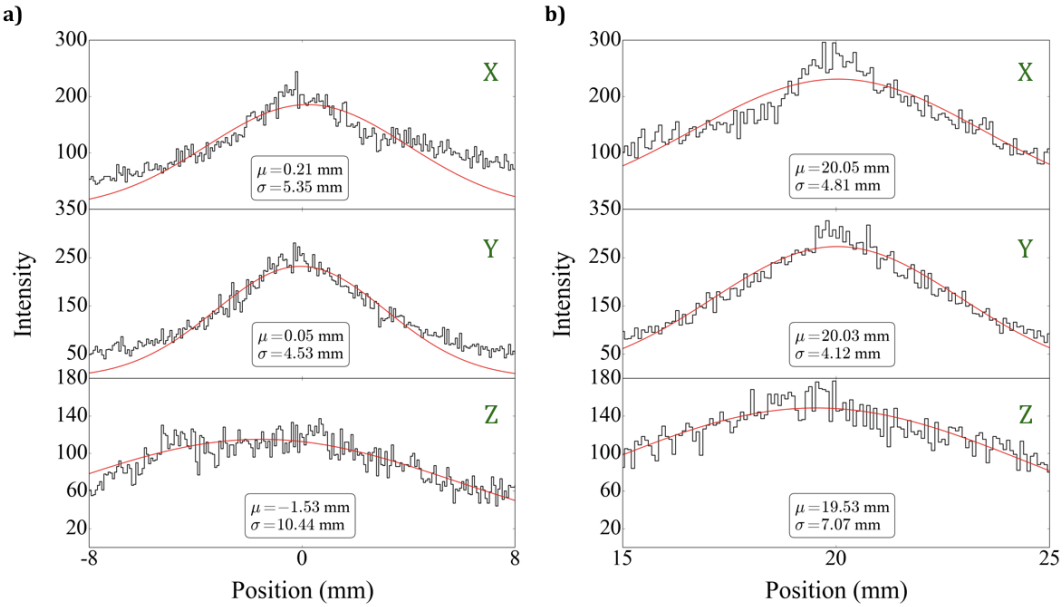

Figure 8.9: Coordinates of a single isotropic source simulated at a) (0, 0, 0) and at b) (20, 20, 20) mm, as reconstructed by the in-house developed algorithm. The source emits with equal probability at 2.741 and 6.128 MeV. Along each axis a Gaussian fit has been applied on the algorithm-reconstructed data. The position of the centre of the peak, μ, and the standard deviation of each peak, σ, corresponds, respectively, to the reconstructed coordinate and to the uncertainty to within this coordinate is reconstructed. When the source is at (0, 0, 0) the reconstructed coordinates values ($\mu \pm \sigma$) are: 0.21 $\pm$ 5.25, 0.05 $\pm$ 4.53, and 1.53 $\pm$ 10.44 mm along the X, Y, and Z axis, respectively. When the source is at (20, 20, 20) mm the reconstruction values ($\mu \pm \sigma$) are: 20.05 $\pm$ 4.81, 20.03 $\pm$ 4.12, and 19.53 $\pm$ 7.07 mm along the X, Y, and Z axis, respectively.

^{16}O source at (20,20,20) mm

Figure 8.9b shows, along the X, Y, and Z axis, the reconstructed coordinates for an isotropic source at (20,20,20) mm. The source emits at 2.741 and 6.128 MeV. The algorithm selected 1273 *couples* and reconstructed 32640 virtual source positions. A Gaussian fit was applied to the reconstructed data. The reconstructed coordinated values, $\mu \pm \sigma$, are: 20.05 ± 4.81 (X), 20.03 ± 4.12 (Y), and 19.53 ± 7.07 mm (Z).

8.5 Discussion

In a previous investigation [ARI14] a γ-ray spectrometer, coupled with a reconstruction algorithm, has been proposed to reconstruct, in 3D, the emission position of γ-rays sources with a cascade decay. The reconstruction is achieved with high precision, using only realistic detector signals. In particular, the radiation emission time is not requested. The spectrometer, in its *ideal* design, comprises 16 $LaBr_3$(Ce) detectors. Due to the coincidence requirement of the algorithm, the $LaBr_3$(Ce) internal activity does not pose a concern.

The present study reports on preliminary experimental tests conducted at NPL using the NANA, a γ-ray spectrometer comprised of 8 $LaBr_3$(Ce) detectors. The position of a 10 kBq ^{60}Co source, located at (0,0,0) and (0,0,-30) mm, was retrieved to within 5 mm.

In-silico evaluations, using the Monte Carlo Geant4 toolkit, have also been reported. The experimental set-up, as well as the *ideal* set-up with 16 $LaBr_3$(Ce) detectors, were both modelled. Sources at (0,0,0) and (0,0,-30) mm were reconstructed to within 1 and 0.5 mm, in the 8 and 16 detectors set-up, respectively. With respect to the experimental set-up, the source holder and the frame have not been modelled, thus the scattering into these components was not accounted for. In addition, unlike the experimental set up, simulations considered point-like sources, not realistic. In other words, the uncertainty due to the finite dimension of the source, ∼3 mm in diameter, is not considered. It is noteworthy that, for each allowed location ((0,0,0) plus the satellite positions), the source holding frame offers an internal diameter of 5 mm. A shift in the initial source placement, with respect to the exact centre, may worsen the reconstruction accuracy. Under these circumstances a very good agreement was observed between experimental and simulation data. This raises the confidence in the use of simulations as a tool to improve the spectrometer design.

For the analysis of the experimental data, the first 10^6 recorded γ-rays were employed. Similarly, 10^6 primary events were considered in the simulations. The excellent source reconstruction was achieved at the price of a long computational time. Indeed, for a ^{60}Co source at (0,0,0), the computational time was ∼15 hours, for the 16 detectors set-up, and ∼7 hours, for the experimental and in-silico set-up with 8 detectors (Windows 64 with Intel Core i7-6700 @ 3.41 GHz CPU and 16 GB RAM). The algorithm is aimed at providing a fast feedback on recorded radiation; thus a reduction of computational complexity is imperative. Options are currently being explored in this direction, such as porting the algorithm to a pre-compiled binary via a high-level language (C/C++) or to hardware (GPU).

The ability to determine the location of a γ-rays source, using conventional detectors, is highly desirable in many instances. Examples are cargo scanning for national security, radioactive waste measurements, and emission tomographic imaging techniques in nuclear medicine. Thus, the method has the potential to be employed in a wide range of applications. Nevertheless, its prime area of development is range verification in PT. Indeed the algorithm was originally aimed at reconstructing the emittance positions of 1.173/1.332 MeV ^{16}O-induced PG rays, emitted in a cascade decay. In this context, simulations have been produced (10^7 primary events) modelling the *ideal* spectrometer and an isotropic point source emitting at 2.741 and 6.128 MeV. The source was located at (0,0,0) and (20,20,20) mm. These positions were chosen to establish a comparison with the simulation results reported in Panaino *et al* [ARI14], relative to a ^{60}Co isotropic point source. Although a source emitting at 1.173/1.332 MeV does not exists in reality, the modelling of unrealistic point-like sources ([ARI30], [ARI31], [ARI32]) and/or extended activity distributions ([ARI33], [ARI34]) is common practice, especially in Compton cameras studies for range verification.

With respect to the ^{60}Co de-excitation, the higher energy of the ^{16}O-induced PG rays implies an increased amount of scattering in the detector medium and a reduced number of *couples* accepted by the algorithm. Thus, for an ^{16}O source at (0,0,0) with 10^7 primary events, 1333 *couples* are selected. In comparison, for a ^{60}Co source at (0,0,0), for 10^6 primary events, the number of *couples* is 3639. The algorithm reconstructs the source position to within 1 cm along all axes.

Results are promising yet preliminary and, as such, further analysis is required. Work is being carried out to optimise both the spectrometer and the algorithm.

8.6 Conclusions

Real-time range monitoring in PT is crucial. A method was proposed to indirectly verify the proton range in biological tissues through the detection of ^{16}O-induced PG rays emitted in a coincidence decay. Such a method is based on a multi-detector spectrometer coupled with an in-house developed reconstruction algorithm. The spectrometer comprises 16 $LaBr_3$(Ce) detectors in a symmetrical design. The algorithm takes as inputs the detector signals and reconstructs the PG rays position, in full 3D space. In the present investigation the method was experimentally validated using the NANA at NPL. The NANA has a similar design to the one envisaged for the spectrometer in our method. Despite, at the time of the experiments, the NANA comprised only 8 detectors, ^{60}Co sources at (0,0,0) and (0,0,-30) mm were reconstructed with an uncertainty of less than 5 mm. The spectrometer/algorithm performance was further in-silico investigated by reconstructing the emission position of a γ-ray source, emitting at (0,0,0) and (20,20,20). The source emits at the same energy of the ^{16}O-induced PG rays. As expected, the higher energy of the PG rays implies an increased amount of scattering, thus the reconstruction sigma rises to 1 cm. Work is being carried out to improve the method. In light of the positive experimental results with ^{60}Co sources the first prototype, with 16 detectors, is being constructed. In-beam test are planned.

Acknowledgement

C.M.V.P. would like to acknowledge support form CRUK via the funding to Cancer Research UK Manchester Centre: [C147/A18083] and [C147/A25254]. M.J.T., K.J.K. and R.I.M. would like to acknowledge funding from the NIHR Manchester Biomedical Research centre.

Author contributions statement

In this publication C.M.V.P. developed the Monte Carlo simulation and the reconstruction algorithm. M.J.T. provided the original concept behind this work, the day-to-day supervision and guided the in-silico developments. C.M.V.P. performed the experimental tests at NPL with the technical support of S.C., R.S., and P.H.R. T.W. and C.W. provided additional support and lab equipments. M.J.T. overviewed the analysis of the experimental data. R.I.M. provided clinical physics guidance and supervision. K.J.K. provided technical guidance and funding. C.M.V.P. drafted the manuscript. All authors reviewed and approved the manuscript.

Bibliography

[ARI1] M. Durante and H. Paganetti, "Nuclear physics in particle therapy: a review," *Rep Prog Phys*, vol. 79, p. 096702, 2016.

[ARI2] A. Knopf and A. Lomax, "In vivo proton range verification: a review," *Phys Med Biol*, vol. 58, p. R131, 2013.

[ARI3] H. Paganetti, "Range uncertainties in proton therapy and the role of Monte Carlo simulations," *Phys Med Biol*, vol. 57, p. R99, 2012.

[ARI4] J. Unkelbach *et al.*, "Robust radiotherapy planning," *Phys Med Biol*, vol. 63, p. 22TR02, 2018.

[ARI5] M. Moteabbed, T. Yock, and H. Paganetti, "The risk of radiation-induced second cancers in the high to medium dose region: a comparison between passive and scanned proton therapy, IMRT and VMAT for pediatric patients with brain tumors," *Phys Med Biol*, vol. 59, p. 2883, 2014.

[ARI6] B. Kozlovsky, R. Murphy, and R. Ramaty, "Nuclear deexcitation gamma-ray lines from accelerated particle interactions," *Astrophys J Suppl S*, vol. 141, p. 523, 2002.

[ARI7] R. Murphy, B. Kozlovsky, J. Kiener, and G. Share, "Nuclear gamma-ray deexcitation lines and continuum from accelerated-particle interactions in solar flares," *Astrophys J Suppl S*, vol. 183, p. 142, 2009.

[ARI8] J. Verburg, K. Riley, T. Bortfeld, and J. Seco, "Energy- and time-resolved detection of prompt gamma-rays for proton range verification," *Phys Med Biol*, vol. 58, p. L37, 2013.

[ARI9] G. Pausch *et al.*, "Detection systems for range monitoring in proton therapy: needs and challenges," *Nucl Instr Meth Phys Res A*, vol. 954, p. 161227, 2020.

[ARI10] J. Polf and other, "Measurement of characteristic prompt gamma rays emitted from oxygen and carbon in tissue-equivalent samples during proton beam irradiation," *Phys Med Biol*, vol. 58, p. 5821, 2013.

[ARI11] C. Min, C. H. Kim, M. Youn, and J. Kim, "Prompt gamma measurements for locating the dose falloff region in the proton therapy," *Appl Phys Lett*, vol. 89, no. 18, p. 183517, 2006.

[ARI12] J. Krimmer, D. Dauvergne, J. Létang, and É. Testa, "Prompt-gamma monitoring in hadrontherapy: A review," *Nucl Instr Meth Phys Res A*, vol. 878, pp. 58–73, 2018.

[ARI13] C. M. Panaino, R. Mackay, K. Kirkby, and M. Taylor, "A new method to reconstruct in 3D the emission position of the prompt gamma rays following proton beam irradiation," *Sci Rep*, vol. 9, pp. 1–12, 2019.

[ARI14] C. Panaino, R. Mackay, M. Sotiropoulos, K. Kirkby, and M. Taylor, "Full 3D position reconstruction of a radioactive source based on a novel hyperbolic geometrical algorithm," *Comput Phys Commun*, vol. 252, p. 107131, 2020.

[ARI15] R. Nicolini *et al.*, "Investigation of the properties of a 1" × 1" $LaBr_3$:Ce scintillator," *Nucl Instr Meth Phys Res A*, vol. 582, pp. 554–561, 2007.

[ARI16] W. H. R. Tilley D R and C. C. M, "Energy levels of light nuclei A = 16-17," *Nucl Phys A*, vol. 564, pp. 1–183, 1993.

[ARI17] M. Bé, V. Chisté, C. Dulieu, E. Browne, V. Chechev, *et al.*, "Table of radionuclides (Vol.1 A= 1 to 150)," *BIPM*, 2004.

[ARI18] J. Régis, G. Pascovici, J. Jolie, and M. Rudigier, "The mirror symmetric centroid difference method for picosecond lifetime measurements via γ–γ coincidences using very fast $LaBr_3$Ce scintillator detectors," *Nucl Instr Meth Phys Res A*, vol. 622, pp. 83–92, 2010.

[ARI19] J. Régis *et al.*, "The time-walk of analog constant fraction discriminators using very fast scintillator detectors with linear and non-linear energy response," *Nucl Instr Meth Phys Res A*, vol. 684, pp. 36–45, 2012.

[ARI20] J. Régis *et al.*, "The generalized centroid difference method for picosecond sensitive determination of lifetimes of nuclear excited states using large fast-timing arrays," *Nucl Instr Meth Phys Res A*, vol. 726, pp. 191–202, 2013.

[ARI21] J. Régis *et al.*, "Germanium-gated γ–γ fast timing of excited states in fission fragments using the EXILL&FATIMA spectrometer," *Nucl Instr Meth Phys Res A*, vol. 763, pp. 210–220, 2014.

[ARI22] F. Crespi *et al.*, "Alpha–gamma discrimination by pulse shape in $LaBr_3$:Ce and $LaCl_3$," *Nucl Instr Meth Phys Res A*, vol. 602, pp. 520–524, 2009.

[ARI23] G. Lorusso *et al.*, "Development of the NPL gamma-ray spectrometer NANA for traceable nuclear decay and structure studies," *Appl Radiat Isot*, vol. 109, pp. 507–511, 2016.

[ARI24] P. Regan *et al.*, "Development of NANA: A fast-scintillator, coincidence gamma-ray array for radioactive source characterisation and absolute activity measurements at the UK National Physical Laboratory," *J Phys Conf Ser*, vol. 620, no. 1, p. 012005.

[ARI25] R. Shearman *et al.*, "Commissioning of the UK NAtional nuclear array," *Radiat Phys Chem*, vol. 140, pp. 475–479, 2017.

[ARI26] S. Collins, R. Shearman, J. Keightley, and P. Regan, "Investigation of γ-γ coincidence counting using the National Nuclear Array (NANA) as a primary standard," *Appl Radiat Isot*, vol. 134, pp. 290–296, 2018.

[ARI27] S. Agostinelli *et al.*, "Geant4 a simulation toolkit," *Nucl Instr Meth Phys Res B*, vol. 506, pp. 250–303, 2003.

[ARI28] F. Quarati *et al.*, "X-ray and gamma-ray response of a 2" $\times$ 2" $LaBr_3$: Ce scintillation detector," *Nucl Instr Meth Phys Res A*, vol. 574, pp. 115–120, 2007.

[ARI29] S. Aldawood *et al.*, "Comparative characterization study of a $LaBr_3$(Ce) scintillation crystal in two surface wrapping scenarios: absorptive and reflective," *Front Oncol*, vol. 5, p. 270, 2015.

[ARI30] S. Peterson, D. Robertson, and J. Polf, "Optimizing a three-stage Compton camera for measuring prompt gamma rays emitted during proton radiotherapy," *Phys Med Biol*, vol. 55, p. 6841, 2010.

[ARI31] D. Robertson, J. Polf, S. Peterson, M. Gillin, and S. Beddar, "Material efficiency studies for a Compton camera designed to measure characteristic prompt gamma rays emitted during proton beam radiotherapy," *Phys Med Biol*, vol. 56, p. 3047, 2011.

[ARI32] P. Solevi *et al.*, "Performance of MACACO Compton telescope for ion-beam therapy monitoring: first test with proton beams,"

[ARI33] H. Rohling *et al.*, "Requirements for a Compton camera for in vivo range verification of proton therapy," *Phys Med Biol*, vol. 62, p. 2795, 2017.

[ARI34] E. Muñoz *et al.*, "Study and comparison of different sensitivity models for a two-plane Compton camera," *Phys Med Biol*, vol. 63, p. 135004, 2018.

Chapter 9

Discussion

9.1 The problem of range uncertainty

Radiotherapy is an essential component of cancer care. Most cancer patients receive, in their treatment, a combination of surgery, chemotherapy and radiotherapy. The ∼2/3 of cancer patients undergone radiotherapy [276]. Among them, the ∼80% receives conventional radiotherapy, the ∼19% receive other radiotherapy treatments - such as brachytherapy - and the ∼1% is referred to PT. The number of PT patients, however, is steadily increasing [276].

The rationale behind the use of proton beams to treat deep-seated tumours comes from the proton depth-dose distribution and was first proposed by Wilson (1946) [2]. In 1991, at Loma Linda University Medical Centre, California, the first hospital-based PT facility started operation [13] while, in 2001, downsized cyclotrons, custom made for PT, came on the market, reducing the cost of facilities [24]. As of May 2020, there are worldwide 101 PT facilities in clinical operation [14], 37 under construction [15], and 14 in planning stage [16].

The depth-dose distribution of proton beams, i.e. the *Bragg Curve*, is characterised by a low dose along the entrance channel and a sharp increase and fall-off toward the end of the track, in the *Bragg peak*. This feature is advantageous in cancer treatments: the beam stops where the target is located, therefore the tumour receives the maximum dose whilst the surrounding healthy tissues are spared. With respect to conventional radiotherapy, PT offers a similar dose to the tumour with reduced healthy tissues toxicities, or an increased dose to the tumour with similar, or reduced, toxicities [276]. With the development of IMRT [32], the most advanced delivery technique for conventional radiotherapy, the difference in dose conformity between protons and photons has decreased. Today, for most treatments sites, PT advantages are marginal at best. There are, however, specific circumstances in which PT represents by far the best approach. A prime example is the paediatric cohort, where the overall quality-of-life and the reduction of late toxicities is paramount [37].

The full PT exploitation is hindered by the uncertainty in the fall-off position of proton beams, or range uncertainty. At the 2012 American Association of Physicists in Medicine (AAPM) [277] meeting, a poll was conducted regarding the main obstacle for protons to replace photons. Among the delegates, 20% asserted that photons can not be replaced, 40% voted for range uncertainty and 40% for the unproven advantage of lower integral dose [276].

The sources of range uncertainty are numerous, even considering only non-moving targets. As reviewed in Section 1.4.2, sources are typically classified into dose calculation *dependant* and *independent* [95]. Dose calculation dependent sources, leading to range uncertainties in the TPS, derive from CT imaging (noise [79], beam hardening [278], and CT artefacts [60]), CT conversion to tissue [82], CT resolution [82], range degradation effects [93], and uncertainties in the I-values [90]. Dose calculation independent sources, leading to discrepancies between planned and delivered dose, are caused by daily variations in the delivered energy and patient set-up [95]. Range uncertainty is clinically managed by making plans robust against uncertainties. The way this is achieved depends on the treatment planning approach. In SFUD plans a distal CTV expansion ensures coverage against range uncertainty [95]. Conversely, in IMPT, where CTV expansions are not ideal [97], *robust optimisation* incorporates range and set-up uncertainties into the treatment plan [104].

Whatever approach is chosen there will always be the need to prove it success by means of in-vivo range verification [74]. In the last twenty years several methods have been proposed [105]. As reviewed in Section 1.6, these methods are divided into 1) *direct*, where range is obtained though direct dose measurements and 2) *indirect*, where range is inferred from signals correlated to PT. Direct methods employ implantable markers [106] or MRI [107], while indirect methods make use of PET [110], ionoacustic [25], or PG detection. The most promising range verification method is via PG detection [69].

The PG spectrum is characterised by several discrete lines (1-10 MeV). Typically, just the lines from the most abundant isotopes in human tissues (^{12}C, ^{12}O, and ^{14}N) are considered. The principal features in PG emission during PT have been described. Attention was posed on: 1) the correlation between PG emission and beam range (Section 2.1.3), 2) the PG yield and its dependance from tissues chemical composition (Section 2.1.4) and beam energy (Section 2.1.4), and 3) the angular distribution of PG emission (Section 2.1.5).

The development of a clinically usable PG detection system has progressed at a slow pace. This is mainly caused by the PG energy, too high to be registered with the standard devices employed in diagnostic imaging (SPECT/PET). Several systems have been proposed. Krimmer *et al* [151] reviewed these systems and categorised them into *imaging* and *non-imaging*. Imaging systems require a mechanical or electronic (Compton camera (CC)) collimation. Non-imaging systems are integrated yield counting devices, which make use of a different source of information, such as PG energy or time. In Section 2.2 the review from Krimmer *et al* [151] is reported expanded and updated. In Appendix 1 all studies are additionally listed in Tables. To the best of our knowledge this is the most comprehensive review on range verification in PT via PG detection.

An essential component of each system is the algorithm employed to reconstruct the PG emittance position. The algorithm complexity depends on the prototype. CCs, in particular, need to be coupled with more advanced algorithms. The main analytical and iterative algorithms developed for CCs have been reviewed in Section 2.2.5.

9.2 The PG Coincidence (PGC) method

In this thesis the investigation of a new method, called PG coincidence (PGC), is reported. The PGC method reconstructs the proton range in 3D via PG detection. The PGC method, in particular, focuses only on the 2.741 and 6.128 MeV ^{16}O-induced PG lines. These γ-lines are emitted in cascade. The time difference between the two lines is negligible ($\sim$25 ps), thus they can be regarded as simultaneously emitted in time and position. During proton beam irradiation, several 2.741 and 6.128 MeV PG *couples* are produced. By detecting these *couples*, the emission positions can be reconstructed. Eventually, from all the emission positions, the range is inferred. Compared to all methods in literature, the PGC method does not fit in any category. Ideally it could be regarded as an imaging system with electronic collimation; where the collimation is the 2.741-6.128 MeV energy selection. Usually PG detection systems are severely affected by neutron-induced background noise. High-energy neutrons are produced along the beam line and in phantoms. In the PGC method, however, the requirement for coincidences rejects the neutron-induced γ background.

The PGC method is based on two components. These components are:

- the *detection system*, to record the ^{16}O-induced PG *couples*;
- the *reconstruction algorithm*, to retrieve the *couples* emission positions.

9.3 PGC method: the detection system

The PGC detection system is composed of 16 symmetrically-spaced cylindrical modules (2" length and 1.5" diameter). The modules, $LaBr_3$ scintillation detectors, are arranged as follows: eight in a vertical ring, four at backward angles (45°), and four at forward angles (45°), with respect to the beam axis. The detection system does not include any mechanical collimation. The lack of collimation translates into an higher registered PG signal. In other words, the beam range can be potentially retrieved with fewer protons. This spectrometer design has been in-silico modelled, by means of Monte Carlo Geant4 simulations, with realistic energy and temporal resolution. Due to the good energy resolution and the excellent timing properties [279], $LaBr_3$ crystal is a common choice in γ-spectroscopy.

It should be noted that $LaBr_3$ crystals possess internal activity, mainly caused by the ^{138}La decay. The energy of the ^{138}La γ-rays does not overlap with the ^{16}O-induced PG rays. More important, the coincidence requirement of the PGC method rejects the ^{138}La γ-rays. For these reasons, the $LaBr_3$ internal activity has not been modelled.

For the PGC detection system, to be introduced in the clinical workflow, two main considerations needs to be given. The first consideration regards the system performance at high count-rate scenarios. In general, to avoid signal distortion, the maximum count-rate capability of a detector should not be exceeded. For this reason, for a single module, the expected load per unit time was calculated, assuming a clinical PT delivery with pencil-beam scanning. The intrinsic efficiency of a 2"$\times$1.5" $LaBr_3$ detector was estimated as $\sim$57%. For

a system internal radius of 8, 15, and 25 cm, considering a (p, ^{16}O) nuclear reaction at (0, 0, 0), a geometric efficiency of 1.36%, 0.4%, and 0.14% and an absolute efficiency of 0.78%, 0.23%, and 0.08%, respectively, were determined per module. Assuming an instantaneous proton beam current of 2 nA [142], which translates into $1.2 \cdot 10^{10}$ protons per second (pps) and $1.2 \cdot 10^{9}$ γ per second (γps), the expected detector load per unit time, at any energy producing a trigger, is $\sim 9.29 \cdot 10^{6}$, $\sim 2.8 \cdot 10^{6}$, and $9.6 \cdot 10^{5}$ γps, for a 8, 15, and 25 cm radius, respectively. For a 25 cm radius, employing 250 MHz digital electronics, a good performance could be obtained from the $LaBr_3$ detectors using standard techniques. For smaller radii and/or increased count-rates, a pile-up correction method, such as pile-up rejection or pile-up recovery through pulse shape analysis [271], could be applied. The system can also be employed with just an initial fraction of the treatment, instead that with the full beam. The idea is to reduce the beam current for the first spots, and then deliver the rest at normal current. By doing this, when range verification in "on", the detector count-rate is acceptable and the radius is minimum.

The second consideration regards the technological challenges arising from the introduction of the spectrometer in the treatment room. Design studies have been performed in conjunction with the clinical scientist colleagues at the Christie. Efforts have been devolved in optimising a design with minimum footprint and no interference with the existing delivery facilities. The first prototype is envisaged to be located in the treatment room. It is mounted on wheels and can be moved around the treatment bed during beam delivery.

The detection system envisaged for the PGC method is very similar to the NANA ([280], [281]) at NPL. NANA is a multi-detector γ-ray spectrometer designed to measure relatively low-multiplicity γ-ray coincidences of 2-3 γ-rays in a discrete cascade. NANA design comprises 12 $LaBr_3$ detectors: eight in a vertical ring and four at backward angles (45°) with respect to the beam axis.

9.4 PGC method: the reconstruction algorithm

9.4.1 Algorithm 1

The initial version of the PGC reconstruction algorithm, Algorithm 1, was presented in Panaino *et al* [267] (Chapters 4-5 and Appendix 2). Algorithm 1 associates to each *couple* a torus. Eventually the emitting positions are retrieved by intersecting each torus with all the others. For each γ-ray, γ_i, belonging to a *couple*, the algorithm takes as input:

1. the detector number Det_i in which γ_i was registered;
2. the total energy E_i released by γ_i in Det_i;
3. the time difference t_i between the emission and detection time of γ_i;
4. the coordinates (x_i, y_i, z_i) of the last hit of γ_i in Det_i.

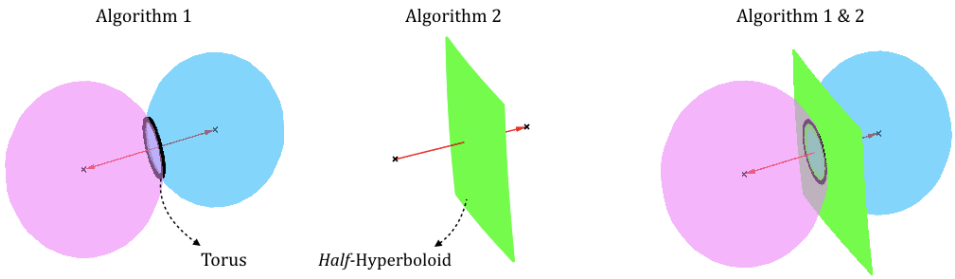

Figure 9.1: Reconstruction algorithms: to every ^{16}O-induced PG *couple* Algorithm 1 assigns a torus while Algorithm 2 assigns a *half*-hyperboloid

9.4.2 Algorithm 2

A second version of the PGC reconstruction algorithm, Algorithm 2, was presented in Panaino *et al* [274] (Chapters 6-7 and Appendix 3). Algorithms 1 & 2 are aimed at solving the same reconstruction problem. Indeed Algorithm 2 is an upgraded version of Algorithm 1 with a different 3D geometry. Algorithm 2 associates to each *couple* the single side of a two-sheeted hyperboloid (named *half*-hyperboloid). Eventually the emitting positions are retrieved by intersecting each *half*-hyperboloid with all the others. For the same *couple*, the torus, assigned in Algorithm 1, and the *half*-hyperboloid, assigned in Algorithm 2, are shown in Figure 9.1. The original emitting position belongs to both the torus and the *half*-hyperboloid. For each γ-ray, γ_i, belonging to a *couple*, Algorithm 2 takes as input:

1. the detector number Det_i;
2. the energy E_i;
3. the time difference T_i between the start of acquisition t_0 and the detection time.

Algorithm 2 still needs the coordinates $(\mathrm{x}_i, \mathrm{y}_i, \mathrm{z}_i)$. With large crystals, non position sensitive detectors, however, this coordinates are not available. Thus, instead of being retrieved by simulations, the coordinates are sampled from probability density functions.

9.4.3 Algorithms 1 & 2: differences

The main difference between Algorithm 1 and 2 is given by time-related input values. For each γ-ray, γ_i, belonging to a *couple*, Algorithm 1 requests the time difference t_i between the detection and the emission time. In reality, however, the emission time can be potentially retrieved only by means of a timing device suitable for TOF measurements. If this is achieved t_i could be inferred. Usually, however, such a device is not available and t_i can not be estimated. On the other hand T_i, the time difference between the detection time and the start of acquisition t_0, is easily obtainable. T_i is much longer then t_i and can not be employed in Algorithm 1. Algorithm 2 requests in input, for each *couple* γ_i and γ_{i+1}, only their difference T_{i+1}-T_i = t_{i+1}-t_i, instead of the two values $\mathrm{t}_{i+1}/\mathrm{t}_i$ separately.

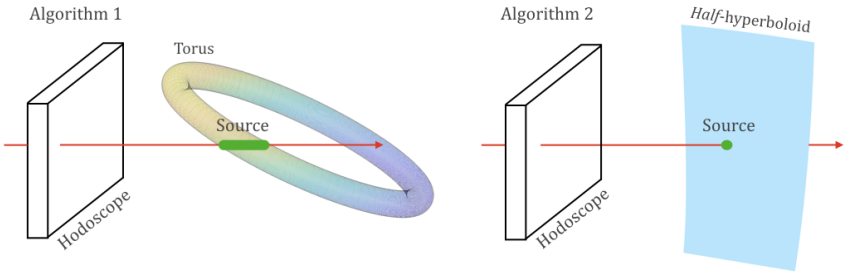

Figure 9.2: Algorithm 1 & 2; inclusion of the proton trajectory-line as input information

9.4.4 Algorithms 1 & 2: potential improvements

Proton trajectory-line

Both algorithms could be improved by adding, as additional input information, the proton trajectory-line. This could be provided with a beam tagging device, hodoscope, as already proposed for CCs ([172], [188]). Figure 9.2 depicts how the trajectory-line could potentially simplifying the algorithms. In Algorithm 1 the emitting position belongs to the trajectory-line and is included in the torus internal volume. In Algorithm 2 the emitting position is given by the intersection between the *half*-hyperboloid and the trajectory-line.

Increasing the statistics

The performance of both algorithms can be improved by increasing the statistics. Two solutions are currently being investigated.

- The first solution consists in enlarging the algorithms acceptance criteria by including those events whose energy belong to the single/double escape peaks. With this variation, for the simulation described in the Publication 1, 180 MeV proton beam impinging a water tank, with a system internal radius of 8 cm, the number of *couples* rises from 826 to 3885, i.e. a 5 fold increase.

- There is no reason why the PGC method should not work for any detectable γ-ray *couple*, where the life of the intermediate state is ∼ps. In light of this, the second solution consists in employing a ^{12}C-induced *couple*, together with the ^{16}O-induced *couple* used so far. As shown in Figure 9.3, a potential ^{12}C cascade would be given by the following de-excitations: 1) ^{12}C(p,p'$_{\gamma_{3.215}}$), $0^+ \rightarrow$ g.s and ^{12}C(p,p'$_{\gamma_{4.439}}$), $3^- \rightarrow$ g.s. Such inclusion would aid range reconstruction in those scenarios where the fall-off position belong to a tissue with high ^{12}C concentration (and low ^{16}O concentration). In addition, a comparison of the detected ^{16}O/^{12}C-induced PG *couples* could provide an insight into the biological composition of the irradiated tissues.

9.5 PGC method: performance

The system/algorithm performance was analysed in all reported publications. In Publication 1 [267] the spectrometer was simulated with a water phantom inside its central volume.

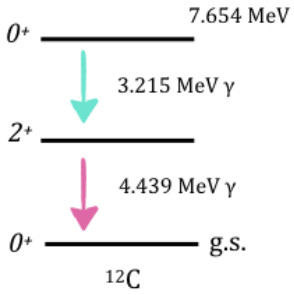

Figure 9.3: Potential ^{12}C-induced cascade for the PGC method

A 180 MeV proton beam (10^8 initial particles) was shot on the phantom, along its central axis. The simulation output was imported into Algorithm 1. To investigate different clinical scenario the radius of the spectrometer central volume was progressively increased. For an 8 cm radius, which could accommodate a paediatric head and neck case, the range was detected with a $\sigma = 4.17$ mm. For a 15 and 25 cm radius, to accommodate an adult head and neck or adult thoracic case, the σ increased to 5.65 and 6.36 mm, respectively. The scenario of a 5 and 10 mm range undershoot, with an 8 cm radius, was also modelled. The range was still reconstructed with $\sigma = 6$ mm. These uncertainties are comparable to the ones typically fed into robust planning or to the usual margins imposed in PT planning. This should be regarded positively. Indeed the authors believe the algorithm has considerable scope for improvement, leading to an inferior σ in range retrieval.

In Publication 2 [274] and 3 the emission position reconstruction is reported for an isotropic point ^{60}Co source. The evaluation was both in-silico (Publication 2 and 3) and experimental (Publication 3). The experimental test, in particular, was performed using the NANA at NPL, with only eight $LaBr_3$ detectors in place. The radius of the spectrometer internal volume was 9 cm in all evaluations. Data were always processed by Algorithm 2.

First simulations results show that for sources at (0,0,0) and (20,20,20) mm, with 10^5 primary events, the emission position is reconstructed within 3 and 2 mm, respectively (Publication 2). For sources modelled at (0,0,0) and (0,0,-30) mm, with the number of primary events increased to 10^6, the reconstructed location is determined with uncertainties of $\sim$1 mm (Publication 3). The improved precision, however, comes at the price of a much longer computational time, from $\sim$1 to $\sim$15 hours.

Even with only eight detectors in place, experimental results show that for sources at (0,0,0) and (0,0,-30) mm, with 10^6 recorded events processed by the algorithm, the emission position is retrieved within 5 mm.

In Publication 3, the in-silico reconstruction of an isotropic point source emitting at 2.741/6.128 MeV, the energy values of the ^{16}O-induced PG lines in cascade, is presented. The output was imported into Algorithm 2. This study was aimed at assessing the system/algorithm performance in the PG range on interest. Due to the increased scattering in the detector medium, the reconstruction precision decreases, with the sigma rising to 1 cm.

9.6 PGC method: alternative application areas

The PGC method has been primarily developed for proton range verification via PG detection. There are, however, a number of different instances where the knowledge of the location of a source of radiation is crucial. Examples are cargo scanning for national security, nuclear energy industry, and radioactive waste measurements. In nuclear medicine the position reconstruction of an emitting source represents the core of emission tomographic imaging techniques, such as SPECT and PET. The author of this thesis strongly believes that the PGC method has the potential to be successfully employed in all these scenarios.

Chapter 10

Future investigations

Several analysis, regarding the PGC method, are envisaged as future investigations. An overview is provided here. This Chapter is divided into two parts; the first (Section 10.1) focuses on in-silico investigations, while the second describes the planned experimental tests, with clinical proton beams (Section 10.2), postponed due to the COVID-19 pandemic.

Algorithm 2, based on an hyperbolic-geometry, was first presented in Panaino *et al* [274]. The algorithm is coupled to a detection system. Due to the capability of processing experimental data, Algorithm 2 represents the prime choice in all future investigations.

10.1 In-silico evaluations

10.1.1 Range reconstruction with Algorithm 2

In Panaino *et al* [274] the emission position reconstruction of several ^{60}Co sources was in-silico demonstrated using Algorithm 2. In a subsequent investigation Algorithm 2 was validated with experimental data acquired using real ^{60}Co sources. Additionally, the system/algorithm performance, in reconstructing the emission position of γ-ray *couples*, with the same energy as the ^{16}O-induced PG rays (2.741/6.128 MeV), was shown. Next step is to in-silico evaluate the system/algorithm performance in reconstructing the proton range.

10.1.2 Inhomogeneous phantoms

So far the PGC method has only been discussed with respect to proton beams impinging water phantoms. The PGC method is essentially based on ^{16}O-induced PG *couples*. Thus, if the phantom is homogeneous, i.e. the amount of oxygen along the beam path is constant, the variation with the beam path of the ^{16}O PG yield is only based on the cross sections behind (p,^{16}O) nuclear reactions. To move forward towards the clinical implementation it is essential to investigate how the PGC method performs in more realistic scenarios. In other words, simulations need to be performed with beams impinging heterogeneous phantoms, i.e. with the amount of oxygen changing along the beam path.

DICOM phantom development and import in Geant4

The existing Geant4 simulation has been expanded with the DICOM extended example [282]. This integration allows to create a voxelised phantom from the information contained in a DICOM file. The phantom is automatically modelled in the central volume of the detection system. So far two DICOM data-sets have been imported in the simulation.

1. The Muscle-Bone-Lung (MBL) DICOM study, in-house generated using MATLAB 2018b, is a 5x5x5 cm^3 voxellised phantom. MBL consists of 100 slices and a 100x100 pixels matrix size; each voxel has dimensions 0.5x0.5x0.5 mm^3. As detailed in Figure 10.1a, MBL is internally divided into five sections, with variable chemical composition. The section interfaces are orthogonal to the Z axis. The employed materials, all homogeneous in density and composition, are: soft tissue (density: 1.055 g/cm^3), 5-year-old compact bone (density: 1.75 g/cm^3), and air.

2. The HIGH_RES_HEAD DICOM study [283] has been created from a high resolution CT scan of a tissue-equivalent paediatric head phantom (ATOM, [284]). As depicted in Figure 10.1b, ATOM provides realistic head and spine anatomical details of a 5-year-old child and is composed by seven homogeneous tissue-equivalent materials (density in g/cm^3): soft tissue (1.05), brain (1.07), paediatric spinal disc (1.10), paediatric trabecular bone (1.13), 5-year-old compact bone (1.75), tooth dentine (1.66), and tooth enamel (2.04).

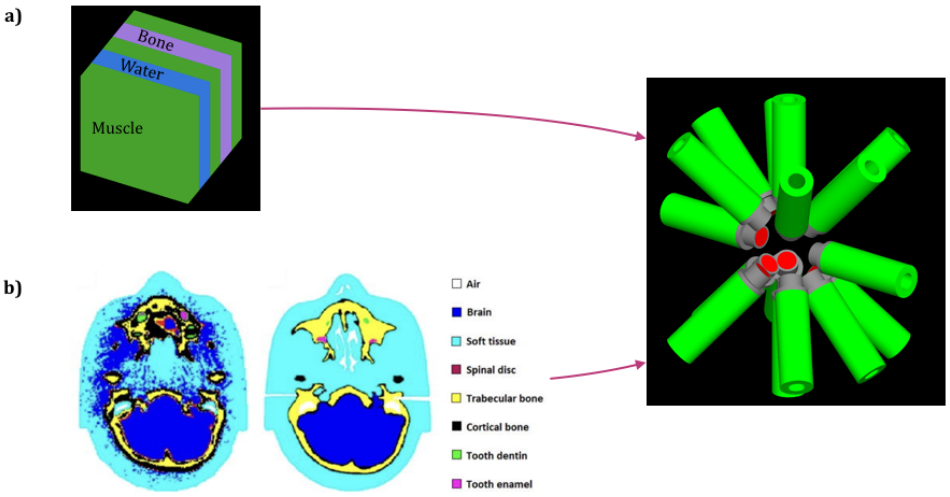

Figure 10.1: Two DICOM data-sets have been imported in the simulation. a) The MBL DICOM study is a 5x5x5 cm^3 voxellised phantom. MBL consists of 100 slices and a 100x100 pixels matrix size; each voxel has dimensions 0.5x0.5x0.5 mm^3. MBL is divided into five sections whose interfaces are orthogonal to the Z axis. The employed materials, all homogeneous, are: soft tissue, compact bone, and air. b) The HIGH_RES_HEAD DICOM study [283] provides realistic head and spine anatomical details of a 5-year-old child and is composed by seven homogeneous materials: soft tissue, brain, paediatric spinal disc, paediatric trabecular bone, 5-year-old compact bone, tooth dentine, and tooth enamel.

Once loaded in the simulation, all DICOM projects are set as multifunctional detectors. By doing this, for each phantom, the simulation provides in output the distribution of an user-selected quantity, scored in all voxels. Being able to accept DICOM files, the

system/algorithm performance can now be tested for scenarios of increased complexity, including, in the long-term future, the imaging 3D data sets of real patients.

10.1.3 Reducing the computational complexity

By increasing the complexity of the phantoms, and by delivering a number of initial protons which is comparable to the number of protons in a pencil beam spot ($\sim 10^8$), the simulation computational cost is expected to rise. Such cost can be shortened by running the simulation on the Condor High Throughput Computing facility at the University of Manchester.

The reconstruction algorithm currently runs in the MATLAB environment. It is believed that a significant decrease in the computational time could be achieved by importing this to a pre-compiled binary via a high-level language. Indeed a full conversion in C++ is currently underway. Further improvements could be made by porting the algorithm to GPU.

10.2 Experimental evaluations

This section briefly reports on the "journey" towards the construction of the first PGC detection system prototype (Section 10.2.2) and the preparation of the first experimental tests with clinical proton beams (Section 10.2.3). The impact of the COVID-19 pandemic is considered as well (Section 10.2.4). The research room at the Christie NHS Foundation Trust (Section 10.2.1) was envisaged as the most suitable location to test the prototype.

10.2.1 The research room

The Christie NHS Foundation Trust in Manchester is the first high energy PT NHS service of the country [19]. The NHS PT service at the Christie is equipped with a 5.6M research room in the fourth gantry space [285]. Founded by charitable donors, through the Christie Charity [286], the research room is envisaged to run as a national facility allowing translational biological and physical experiments. The research room is provided with a single horizontal beam line delivering active scanning, to emulate treatments in the clinical gantry rooms. At the end of the beam line, modular flexible research end-stations, designed for a variety of applications, can be located. The research room does not require a gantry, as it is both easier and cheaper to move the sample in front of the beam, rather than the opposite.

10.2.2 Development of a clinical prototype

Between October 2019 and January 2020 16 $LaBr_3$ scintillators detectors (2" length and 1.5" diameter) have been collected. Due to the high number needed, the detectors have been partially purchased and partially borrowed from the nuclear physics groups at The University of Manchester, The University of Birmingham, and the NPL in London. The electronic apparatus has been purchased as well.

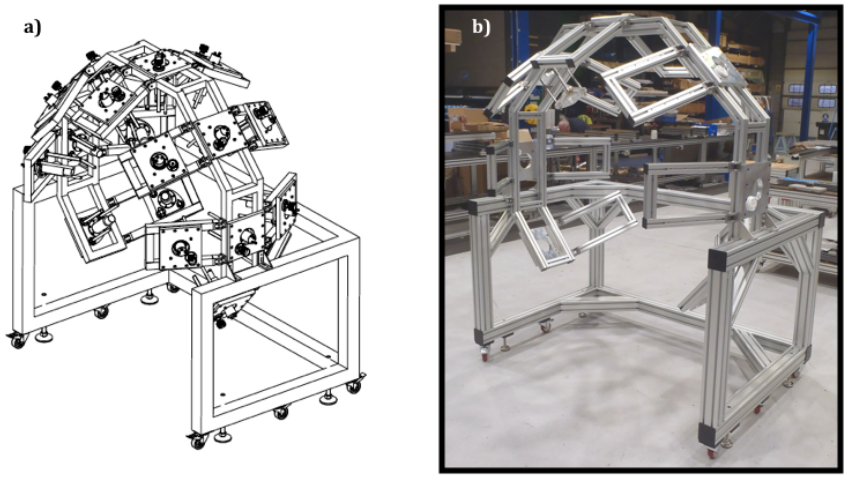

Figure 10.2: Spectrometer holding frame for the first prototype to be tested in the clinical environment. a) Frame design. b) Final structure assembled at the manufacturer.

On the 6-7 June 2019, at the STFC IMPACT Sandpit "Dragon den" style in Manchester, Miss C. Panaino, author of this thesis, and Dr. M. Taylor, main supervisor, were awarded with a £10,000 grant for the project: *A flexible detector array for range verification in proton therapy*. The monetary prize was fully invested in the design and construction of the spectrometer holding frame. The frame design was first optimised by the University of Manchester design engineering team. The frame was then built (Hepco Motion Ltd [287] and Bollin Dale Ltd [288]). In February 2020 the frame was delivered at the Christie NHS Foundation Trust and located in the research room. Figure 10.2 shows the frame design (Figure 10.2a) and the its structure at the manufacturer (Figure 10.2b).

10.2.3 Experimental tests

The planned experimental tests should have been composed of two parts. In a first part the system/algorithm emission-position reconstruction capability would have been assessed with a ^{60}Co source. As in Publication 3 (Chapter 8), the source would have been moved at various known locations within the spectrometer central volume. In a second part, the range-monitoring of clinical pencil beams would have been assessed. Proton beams from 70 to 230 MeV (in steps of 10 MeV) would have been delivered on a water tank (MP3-M water phantom system PTW). Eventually Algorithm 2 would have been employed to reconstruct both the emitting position of the source and the end-of-range depth of beams in the tank.

10.2.4 The impact of COVID-19

At the end of February 2020 all "ingredients" had been collected and experimental tests were ready to start. Due to the COVID-19 outbreak, however, from March 2020 the access to the research room was forbidden, all planned experiments were cancelled, and the author of this thesis, as well as all students and staff members within the University of Manchester, were transferred to full-time home-work. Before the planned end of the PhD project (September 2020), the described situation is not expected to change. Thus, this thesis will not report, as desired, the experimental tests of the prototype with clinical proton beams.

Chapter 11

Conclusions

PG detection is regarded as the most promising approach to asses real-time range monitoring in PT. PG rays are γ-rays naturally emitted from nuclear de-excitations following proton bombardment. As measured by Verburg *et al* [141], the PG profiles correlate well with the Bragg curve. In addition, the PG yield is favourable. Indeed Polf *et al* [143] estimated that $1.64 \cdot 10^7$ 6.13 MeV ^{16}O-induced PG rays are released, per gram of ^{16}O, per Gy of dose delivered. However, despite the clear potential behind PG detection, the development of a clinically usable PG range monitoring system has progressed at a slow rate. This is mainly due to the PG energy (1-10 MeV [136]), too high to be registered with the detector systems typically employed in nuclear imaging.

In this work is presented a new method, named PG Coincidence (PGC), to reconstruct the proton range in biological tissues. The PGC method is based on the detection of 2.741/6.128 MeV ^{16}O-induced PG rays emitted in coincidence. The PGC method consists in a detection system coupled with a reconstruction algorithm. The detection system comprises 16 $LaBr_3$ detectors, in a symmetrical design. No mechanical collimation is requested. The algorithm takes as inputs the signals from the system and reconstructs the PG rays emission position, in the full 3D space. Due to the use of coincidences both the neutron-induced γ-background and the background form the $LaBr_3$ internal activity do not pose a concern. Two versions of the algorithm, Algorithm 1 and 2, were illustrated. Their main difference is based on the requested input data and on the employed 3D geometry.

This thesis reports on the PGC system/algorithm performance. Investigations were both performed in-silico, using Monte Carlo Geant4 (10.04) toolkit, and experimentally, using the NANA at NPL. For what concerns the in-silico analysis, the reconstruction of 1) the PG profile peak, for a 180 MeV beam delivered on a water phantom, (Algorithm 1) and 2) the emission position of a ^{60}Co source and of a point-like ^{16}O source (Algorithm 2) have been reported. The experimental validation of the method was later performed with a real ^{60}Co source using the NANA. Even if, during the tests, only 8 $LaBr_3$ detectors were in place, the position of a source at (0,0,0) and (0,0,-30) was reconstructed to within a 5 mm σ.

The results presented in this thesis are promising, yet preliminary and further investi-

gations are needed. The detection system design, for example, should be optimised to both minimise the interference with delivery facilities and maximise the geometrical efficiency, a key factor in coincidence measurements. On the other hand, the algorithm would benefit from an increase in statistics. The introduction of a beam tagging device, hodoscope, should also be considered as it could provide the proton trajectory-line. This, in turn, would aid the reconstruction process. Lastly, the algorithm computational time needs to be reduced.

The end of the PhD project represents the beginning on a new line of investigations, both in-silico and experimental, whose time-scale has been in broad terms delineated. In light of the positive results obtained at NPL, the first PGC prototype has been constructed. Experimental validation with clinical proton beams, postponed due to the COVID-19 pandemic, are planned for the nearest future.

Chapter 12

Appendix 1

In Section 2.2 a literature review on range verification via PG detection is reported. In this Appendix the in-silico and experimental studies reported in the review are listed in Tables.

PG range verification system	Section	Table
Imaging systems		
Mechanical collimation	2.2.1	
• Single detector (feasibility studies), multislit camera		A1
• Pinhole and knife-edge slit camera		A2
Electronic collimation	2.2.2	
• Compton camera: scintillators		A3
• Compton camera: semiconductors & scintillators		A4
• Gamma electron vertex index, Compton camera: semiconductors		A5
• Electron tracking Compton camera		A6
Non-imaging systems	2.2.4	
• Time of flight		A7
• Spectroscopy and coaxial monitoring		A8
Comparison studies	2.2.5	A9

For each PG range verification system is reported the paragraph (Chapter 2) in which the system is described and the Table (Appendix 1) in which the studies are listed.

Table A1: Imaging prompt gamma detection systems. Mechanical collimation.

Part 1 - Single detector (feasibility studies), multislit camera

Study	**Year**	**Proton energy**	**Calibration Source**	**Detector**	**Phantom**	**Analysis**
	Single detector (feasibility studies)					
Min *et al* [136]	2006	100, 150, 200 MeV	*N/A* [1]	CsI	Water	In silico (MCNPX) & experimental
Min *et al* [153]	2007	38 MeV	*N/A*	CsI	Water	In silico (MCNPX) & experimental
Kim *et al* [152]	2007	70 MeV, SOBP 62−72 MeV width	*N/A*	CsI	Water	In-silico (MCNPX, FLUKA, SRIM)
	MultiSlit (MS) camera					
Min *et al* [157]	2012	80, 150, 220 MeV	*N/A*	CsI	Water	In silico (MCNPX) & experimental
Lee *et al* [158]	2012	80, 150, 200 MeV	*N/A*	CsI	Water	In silico (MCNPX)
Roellinghoff *et al* [154]	2014	160 MeV	*N/A*	LYSO	PMMA	Experimental
Pinto *et al* [155]	2014	160 MeV	*N/A*	1) $LaBr_3$, 2) BGO	PMMA	1) Experimental, 2) in silico (Geant4)
Cambraia-Lopes *et al* [156]	2018	1) 130, 200 MeV, 2) 200 MeV	*N/A*	Ideal-detector	1) full-body, 2) PMMA	In silico (Geant4)
Park *et al* [159]	2019	95.09, 122.6, 146.45, 186.3 MeV	*N/A*	CsI	SP34[2]	Experimental
Zhang *et al* [160]	2020	N/A	^{22}Na, ^{88}Y, ^{232}Th	BGO	*N/A*	In silico (Geant4) & experimental

[1] Not applicable

[2] 98% $(C_8H_8)_n$ + 2% TiO_2

Table A2: Imaging prompt gamma detection systems. Mechanical collimation.
Part 2 - Pinhole and knife-edge slit camera

Study	**Year**	**Proton energy**	**Detector**	**Phantom**	**Analysis**
	Pinhole camera				
Kim [161]	2009	50 MeV	CsI	Water	In silico (MCNPX) & experimental
	Knife-Edge (KE) slit camera				
Bom *et al* [162]	2012	125 MeV	BGO	Head	In silico (Geant4)
Smeets *et al* [163]	2012	100, 160 MeV	CsI	PMMA	In silico (MCNPX) & experimental
Perali *et al* [164]	2014	100, 160, 230 MeV	LYSO	PMMA	Experimental
Cambraia-Lopes *et al* [165]	2015	160 MeV	LYSO	PMMA	Experimental
Preignitz *et al* [166]	2015	1) 137.5, 144 MeV, 2) 100-120 MeV (1 MeV steps)	LYSO	1) Head, 2) lung (with/without rib)	In silico (MCNPX) & experimental
Preignitz *et al* [168]	2016	SOBP with: 1) 12 cm range and 2, 6, 12 cm width, 2) 10 cm range and 5 cm width, 3) 16.5 cm range and 6.8 cm width	LYSO	1) Water, 2) head, 3) PMMA with one/two air cavity, bone & fat insert	Experimental
Preignitz *et al* [167]	2016	100-120 MeV (1 MeV steps)	LYSO	Lung (with/without rib, tumour shrinkage)	Experimental
Riechter *et al* [169]	2016	SOBP with 13.5 cm range and 10.7 width	LYSO	*N/A*	Patient (Head & neck)
Nenoff *et al* [171]	2017	IMPT, SFUD, DS plans with 2 equally-weighted fields (photon-equivalent dose of 60 Gy)	LYSO	Head, brain tumour in the temporal lobe	Experimental
Xie *et al* [170]	2017	SFO plans with 3 equally-weighted fields (right-superior-oblique field, 160-101 MeV & 17 layers, right lateral field, 155-100 MeV & 17 layers, superior-inferior field: 160-101 MeV & 18 layers)	LYSO	*N/A*	Patient (Head & neck)

Table A3: Imaging prompt gamma detection systems. Electronic collimation.

Part 1 - Compton camera: scintillators

Study	**Year**	**Calibration Source**	**Proton energy**	**Detector**	**Phantom**	**Analysis**
	Compton camera: scintillators					
Gillam *et al* [176]	2011	*N/A*	140, 160, 180 MeV	$LaBr_3$	PMMA	In-silico (Geant4)
Llosá *et al* [174]	2013	^{22}Na	*N/A*	$LaBr_3$ & LYSO	*N/A*	Experimental
Kishimoto *et al* [185]	2015	622 keV	*N/A*	Ce:GaGG	*N/A*	In-silico (Geant4) & experimental
Ortega *et al* [177]	2015	*N/A*	160 MeV	$LaBr_3$	PMMA	In-silico (FLUKA)
Taya *et al* [186]	2016	*N/A*	70 MeV	Ce:GaGG	Water, $Ca(OH)_2$, PMMA	In-silico (Geant4) & experimental
Llosá *et al* [178]	2016	^{22}Na, ^{137}Cs, ^{60}Co	*N/A*	$LaBr_3$	*N/A*	Experimental
Solevi *et al* [175]	2016	1) ^{22}Na, Am-Be, PG-like point source	2) 150 MeV	$LaBr_3$	1) *N/A*, 2) PMMA	In silico (MCNPX) & experimental
Hueso-Gonzalez *et al* [183]	2017	1) ^{22}Na	2) 70-170 (10 MeV steps)	BGO	1) *N/A* 2) PMMA	Experimental
Muñoz *et al* [179]	2017	1) ^{22}Na, ^{88}Y, 2) 4.439 MeV	*N/A*	$LaBr_3$	*N/A*	1) In-silico (GATE), 2) experimental
Barrio *et al* [182]	2018	^{22}Na	*N/A*	$LaBr_3$ & $CeBr_3$	*N/A*	Experimental
Muñoz *et al* [180]	2018	4.439 MeV	*N/A*	$LaBr_3$	*N/A*	Experimental
Muñoz *et al* [181]	2018	1) 1275, 4439 keV sources, planar/thick phantom with homogeneous activity, Sheep-Logan phantom emitting at 1275 keV, 2) ^{22}Na	*N/A*	$LaBr_3$	*N/A*	1) In-silico (GATE), 2) experimental
Jan *et al* [184]	2018	*N/A*	120 MeV	LYSO	Water	Experimental

Table A4: Imaging prompt gamma detection systems. Electronic collimation.
Part 2 - Compton camera: semiconductors (DSSDs or CZT) & scintillators

Study	**Year**	**Calibration Source**	**Proton energy**	**Detector**	**Phantom**	**Analysis**
	Compton camera: semiconductors (DSSDs) & scintillators					
Seo *et al* [187]	2010	^{22}Na	*N/A*	DSSDs + NaI	*N/A*	Experimental
Roellinghoff *et al* [172]	2011	Source emitting the prompt gamma distribution for a carbon ion beam at 310 MeV/u in water	*N/A*	DSSDs + LYSO	*N/A*	In-silico (Geant4)
Richard *et al* [188]	2012	Source emitting the prompt gamma distribution for a carbon ion beam at 310 MeV/u in water	*N/A*	DSSDs + LYSO, NaI, $LaBr_3$, BGO	*N/A*	In-silico (Geant4)
	Compton camera: semiconductors (DSSDs) & scintillators with electron tracking					
Frandes *et al* [189]	2010	*N/A*	70, 100, 140 MeV	DSSDs + $LaBr_3$	PMMA	In silico (MCNPX)
Thirolf *et al* [190]	2014	^{137}Cs	*N/A*	DSSDs + $LaBr_3$	*N/A*	In-silico (Geant4)
Aldawood *et al* [192]	2017	^{137}Cs, ^{60}Co	*N/A*	DSSDs + $LaBr_3$	*N/A*	Experimental
	Compton camera: semiconductors (CZT) & scintillators					
Kormoll *et al* [193]	2011	0.5, 1.75, 3 MeV	*N/A*	(CZT, HPGe) + LSO	*N/A*	In-silico (Geant4)
Hueso-Gonzalez *et al* [194]	2014	Bremsstrahlung γ up to 12.5 MeV	*N/A*	CZT + LSO	*N/A*	Experimental
Golnik *et al* [196]	2016	4.439 MeV	*N/A*	CZT + BGO	*N/A*	Experimental
Rohling *et al* [197]	2017	1) line and 2) cuboid source with cavity, both emitting the PG spectra from 3)	3) TPS plan (head & neck), 100.83-121.20 MeV, 0.1 Gy	CZT + LSO	Head & neck (CT)	In-silico (Geant4)

Table A5: Imaging prompt gamma detection systems. Electronic collimation.
Part 3 - Gamma electron vertex index, Compton camera: semiconductors

Study	**Year**	**Calibration Source**	**Proton energy**	**Detector**	**Phantom**	**Analysis**
	Gamma Electron Vertex Index (GEVI)					
Kim *et al* [198]	2012	1) Source emitting the prompt gamma distribution from a 150 MeV proton beam in soft tissue	2) 80, 150, 200 MeV	DSSDs + CsI	1) *N/A* & 2) Soft tissue	In-silico (Geant4)
Lee *et al* [199]	2017	1) ^{90}Sr, 2) ^{60}Co	3) 45 MeV	DSSDs + calorimeter	1-2) *N/A* & 3) PMMA	Experimental
	Compton camera: semiconductors					
Peterson *et al* [200]	2010	1) 0-15 MeV (0.1 MeV steps), 2.31, 4.44, 6.13 MeV source	2) 50-250 MeV (50 MeV steps)	HPGe	1) *N/A* & 2) Soft tissue	In-silico (Geant4)
Robertson *et al* [201]	2011	1) 0-15 MeV (0.1 MeV steps), 2.31, 4.44, 6.13 MeV source	2) 50-250 MeV (50 MeV steps)	HPGe, BGO, NaI, Xe, $LaBr_3$, Si	1) *N/A* & 2) Soft tissue	In-silico (Geant4)
Mackin *et al* [202]	2013	1) 0.511-7.12 MeV	2) 110 MeV	HPGe, CZT	1) *N/A* & 2) Soft tissue	In-silico (Geant4)
McCleskey *et al* [203]	2014	1) ^{137}Cs, ^{60}Co, ^{152}Eu	2) 155, 158 MeV	CZT	Water	1) experimental, 2) in-silico (Geant4)
Polf *et al* [204]	2015	*N/A*	150 MeV, 114 MeV	CZT	Water	Experimental
Draeger *et al* [205]	2017	^{60}Co, ^{137}Cs, ^{22}Na	*N/A*	CZT	*N/A*	Experimental
Draeger *et al* [206]	2018	*N/A*	120, 180 MeV	CZT	HDPE	Experimental
Gutierrez *et al* [208]	2018	^{88}Y, ^{57}Co, ^{139}Co	*N/A*	Si + HPGe	*N/A*	In-silico (Geant4) & experimental
Yao *et al* [207]	2019	*N/A*	120 MeV	CZT	Water	In-silico (Geant4)

Table A6: Imaging prompt gamma detection systems. Electronic collimation.
Part 4 - Electron tracking Compton camera

Study	**Year**	**Calibration Source**	**Proton energy**	**Detector**	**Phantom**	**Analysis**
	Electron Tracking Compton Camera (ETCC)					
Kabuki *et al* [211]	2007	1) ^{133}Ba, ^{137}Cs, 2) ^{131}I	*N/A*	GSO + μ-TPC with Ar-C_2H_6(10%) at 1 atm gas mixture.	1) *N/A*, 2) thyroid	Experimental
Takahashi *et al* [213]	2011	^{133}Ba	*N/A*	GSO + μ-TPC with 1) Ar/C_2H_6(90:10) at 1/2 atm and 2) Ar/CF_4/isoC$_4H_{10}$ (54:40:6) at 1/1.4 atm	*N/A*	Experimental
Kurosawa *et al* [212]	2012	*N/A*	140 MeV	GSO + μ-TPC with Ar-C_2H_6(90:10) at 1 atm	Water	Experimental

Table A7: Non-imaging prompt gamma detection systems. Time of flight

Study	**Year**	**Proton energy**	**Detector**	**Phantom**	**Analysis**
	Prompt Gamma Timing (PGT)				
Golnik *et al* [149]	2014	1) 50-230 MeV (10 MeV steps), 2-3) 150 MeV	Ce:GaGG	1) PMMA with/without density reduced by the 10%, 2) PMMA with variable thickness and graphite with variable beam entrance position, 3) PMMA with bone insert and PMMA with air cavity	1-3) In-silico (Geant4), 2) experimental
Hueso-Gonzalez *et al* [214]	2015	100, 160, 230 MeV	BaF_2, $LaBr_3$	PMMA with variable thickness, PMMA with air cavities of variable thickness at various depths, PMMA with bone filling at various depths	In-silico (Geant4) & Experimental
Petzoldt *et al* [215]	2015	1) 225 MeV, 2) 69, 90, 110, 130, 160, 180, 200, 225 MeV	Phoswich detector (plastic scintillator & BGO) as proton bunch monitor + $CeBr_3$ with energy resolution: 1) 235 and 2) 240 ps FWHM $\gamma > 2$ MeV	1) PMMA with two air cavities and a bone insert, 2) PMMA layer. Scattering foil: 1) polypropylene, 2) PMMA	Experimental
Werner *et al* [216]	2019	162.0, 226.7 MeV	$CeBr_3$	PMMA with air cavities of variable thickness at various depths	Experimental
	Prompt Gamma Peak Integral (PGPI)				
Krimmer *et al* [217]	2017	1) 65 MeV, 2) 130, 200 MeV, 3) 160 MeV	1-2) $LaBr_3$ + BaF_2, 3) $LaBr_3$	PMMA	1) Experimental, 2-3) in-silico (Geant4)

Table A8: Non-imaging prompt gamma detection systems. Spectroscopy and coaxial monitoring

Study	**Year**	**Proton energy**	**Detector**	**Phantom**	**Analysis**
	Prompt Gamma Spectroscopy (PGS)				
Verburg *et al* [141]	2013	Ranges of 9, 16, 23 gcm^{-2} in water	$LaBr_3$ (BGO shielding)	Water	Experimental
Verburg *et al* [218]	2014	1) 165 MeV, 2) 151 MeV, 3) beams with ranges 15.54, 16.07, 16.58, 17.09, 17.59 gcm^{-2}	$LaBr_3$ (BGO shielding)	1) Water and polyethylene, 2) water with/without water equivalent slab, 3) water and solid water with/without a plastic slab of various thickness	In-silico (Geant4) & experimental
Testa *et al* [220]	2015	1) SOBP with 16 cm range and 10 cm width, 2) lateral field (SOBP 25.7 cm range and 8.5 cm width), anterio-posterior field (SOBP 17 cm range and 6.2 cm width)	LYSO	1) Water, 2) prostate (TPS plan)	In-silico (TOPAS)
Verburg *et al* [221]	2015	1) SOBP with range R_{80} of 16 and 6 gcm^{-2} of width, 2) SOBP with range R_{80} of 12.5 and 7.5 gcm^{-2} width	$LaBr_3$ (BGO shielding)	1) Water, 2) head	Experimental
Martins-Magalhães *et al* [219]	2017	1) 130 MeV, 2) 90 MeV, 3) 224 MeV	$CeBr_3$	1) Water, PMMA, graphite, 2) aluminium, 3) water	Experimental
Hueso-Gonzalez *et al* [109]	2019	1) 116, 145 MeV, 2) 1410 pencil beams in 8 layers, dose region 15-30.3 cm depth (in water)	$LaBr_3$	1) Water and polyethylene, 2) water, water + solid water insert, water + water equivalent range shifter, 3) water + bone insert	Experimental
	Coaxial Prompt Gamma Monitoring (CPGM)				
Hueso-Gonzalez *et al* [222]	2019	1-125 MeV (1 MeV steps)	$LaBr_3$	Water	In silico (Geant4)

Table A9: PG detection systems. Comparison studies

Study	**Year**	**System 1**	**System 2**
Smeets *et al* [223]	2016	Parallel multislit (Roellinghoff *et al* [154])	Knife-edge (Smeets *et al* [163])
Lin *et al* [224]	2017	Parallel multislit (Min *et al* [157])	Knife-edge (Smeets *et al* ([163])
Park *et al* [225]	2019	Parallel multislit (Min *et al* [157])	Knife-edge (Smeets *et al* ([163])
Hueso-Gonzalez *et al* [226]	2016	Compton camera (Hueso-Gonzalez *et al* [195])	PG timing (Hueso-Gonzalez *et al* [214])

Chapter 13

Appendix 2

In this Section is reported the full MATLAB 2018b code for Algorithm 1. Algorithm 1 is the position reconstruction algorithm illustrated in Panaino *et al* [267].

Algorithm 1 - Tori

Panaino, C.M., *et al*, 2019. *Scientific Report*, 9(1), pp.1-12.

```
cd('/Users/…/InputFile');
```

Folder where the .txt file from Geant4 is saved

```
fileName = 'InputFile_name.txt';
fileID = fopen(fileName);
radiationRecorded = textscan(fileID,'%f %f %f %f %f %f',…
                             …'Delimiter','\t');
fclose(fileID);
radiationRecorded = cell2mat(radiationRecorded);
```

The .txt file is converted as a .mat, (matrix in MATLAB)

```
Energy = radiationRecorded(:,1);
Time = radiationRecorded(:,2);
Detector = radiationRecorded(:,3);
X = radiationRecorded(:,4);
Y = radiationRecorded(:,5);
Z = radiationRecorded(:,6);
```

The matrix is separated into vectors reporting:

1) Energy
2) Time
3) Detector
4) X
5) Y
6) Z

```
X_data_tori = {};
Y_data_tori = {};
Z_data_tori = {};

NCouples = 0;
C = 30;
minorRadius = 0.3;
```

Minor radius of the torus

```
for i=1:(length(Energy)-1)
   if Detector(i)~=Detector(i+1)

      if (Energy(i)<=2.823 && Energy(i)>=2.659 && …
          Energy(i+1)<=6.321 && Energy(i+1)>=5.946) ||…
         (Energy(i+1)<=2.823 && Energy(i+1)>=2.659 && …
          Energy(i)<=6.321 && Energy(i)>=5.946)
```

A *couple* of γ-rays is selected: two γ-rays in the *couple* are recorded one after each other, in two different detectors, and have energy centred in 2.741 and 6.128 MeV, irrespective of order

```
          NCouples = NCouples + 1;

          r_hit1 = Length(i)*c;
          x_hit1 = X(i);
          y_hit1 = Y(i);
          z_hit1 = Z(i);

          r_hit2 = Length(i+1)*c;
          x_hit2 = X(i+1);
          y_hit2 = Y(i+1);
          z_hit2 = Z(i+1);
```

For each γ-ray in the *couple* the time and the X, Y, Z coordinates recorded by the spectrometer are saved

The time is multiplied by c = 30 cm/ns and converted in length.

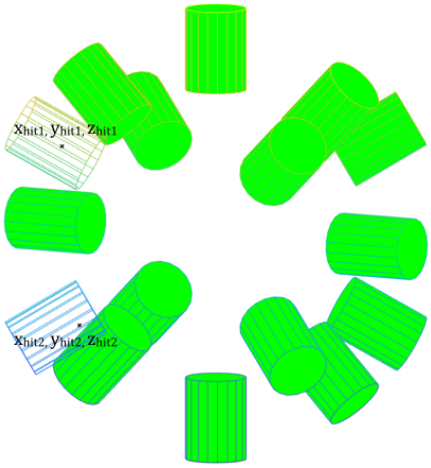

```
[cIntCirc, RIntCirc, vIntCirc] = sphereIntersection(…
                    x_hit1, y_hit1, z_hit1, x_hit2,…
                    y_hit2, z_hit2, r_hit1, r_hit2)
```

sphereIntersection.m

Input: centres (*xc1, yc1, zc1*) & (*xc2, yc2, zc2*) and radii *r1 & r2* of the two spheres
Output:

- *cIntCirc* = centre of the intersection circle
- *RIntCirc* = radius of the intersection circle
- *vIntCirc* = versor from *cIntCirc* to (*xc1, yc1, zc1*)

```
function [cIntCirc, RIntCirc, vIntCirc] = sphereIntersection(x_hit1, y_hit1, z_hit1, r2, x_hit2, y_hit2, r_hit1, r_hit2)

% The equations of the two spheres can be expressed as:
% (x-x_hit1)^2+(y-y_hit1)^2+(z-z_hit1)^2 = r1^2 sphere 1   (S1)
% (x-x_hit2)^2+(y-y_hit2)^2+(z-z_hit2)^2 = r_hit2 ^2 sphere 2;  (S2)

% S1 - S2 = linear equation satisfied by the plane containing the intersection circle.
% (x-x_hit1)^2+(y-y_hit1)^2+(z-z_hit1)^2-(x-x_hit2)^2-(y-y_hit2)^2-(z-z_hit2)^2 = r_hit1^2-r_hit2 ^2 (A);

% The line defined by (x_hit1, y_hit1, z_hit1), (x_hit2, y_hit2, z_hit1) is expressed by:
% x = t*x_hit1 + (1-t)*x_hit2   (B);
% y = t*y_hit1 + (1-t)*y_hit2  (C);
% z = t*z_hit1 + (1-t)*z_hit2  (D);
% (A), (B), (C),(D) are 4 equations with 4 variables and can be solved for cIntCirc.

syms x y z t
eqns = [(x-x_hit1)^2+(y-y_hit1)^2+(z-z_hit1)^2-(x-x_hit2)^2-(y-y_hit2)^2-(z-z_hit2)^2 ==…
        r_hit1^2 - r_hit2^2;   x == t*x_hit1 + (1-t)*x_hit2; y == t*y_hit1 + (1-t)*y_hit2;…
        z == t*z_hit1 + (1-t)*z_hit2]; vars = [x y z t];
[solx, soly, solz, ~] = solve(eqns, vars);
cIntCirc_x=double(solx);
cIntCirc_y=double(soly);
cIntCirc_x=double(solz);

cIntCirc=[cIntCirc_x cIntCirc_y cIntCirc_z];
```

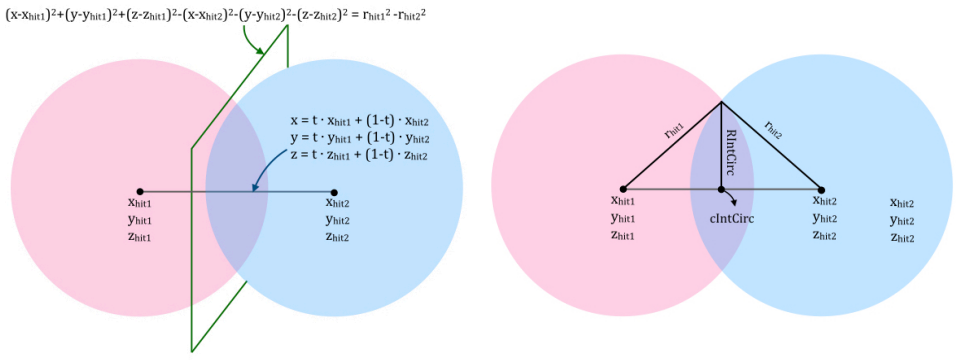


```
% For the Pythagoras theorem RIntCirc^2 = is the square of one of the two spheres' radii (r_hit1^2 for example)
% minus the square of the distance from the hit position ((x_hit1, y_hit1, z_hit1) for example) to cIntCirc.

Distance=sqrt((cIntCirc_x-x_hit1)^2+(cIntCirc_y-y_hit1)^2+(cIntCirc_z-z_hit1)^2);

  if r1 >= Distance
    RIntCirc=double(sqrt(r_hit1^2-Distance^2));
    else RIntCirc=double(sqrt(Distance^2-r_hit1^2));
  end

% Vec: cIntCirc_x—>(x_hit1, y_hit1, z_hit1)
vectIntCirc=[cIntCirc_x-x_hit1, cIntCirc_y-y_hit1, cIntCirc_z-z_hit1];
% Ver: cIntCirc_x—>(x_hit1, y_hit1, z_hit1)
vIntCirc=vectIntCirc/(norm(vectIntCirc));
```

```
V_Z=[0, 0, cIntCirc(3:3)-10-cIntCirc(3:3)];
vZ = vZ/norm(V_Z);
```

vZ = versor from *cIntCirc* parallel to Z axis

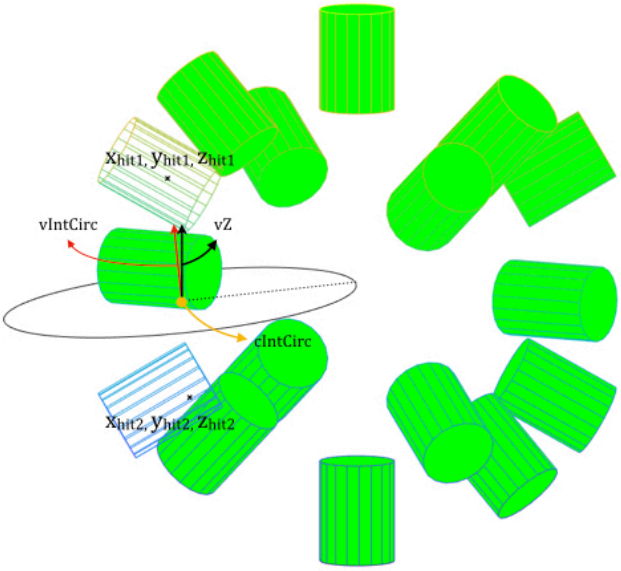


```
[xt, yt, zt] = torusCalculation(minorRadius,RIntCirc);
```

torusCalculation.m

Input: Minor radius of the torus (*minorRadius*) and radius of the intersection circle (*RIntCirc*)
Output:

- *xt, yt, zt* = coordinates of a torus centred in (0,0,0) with major radius *RIntCirc* and minor radius *minorRadius*

```
function [xt, yt, zt] = torusCalculation(minorRadius, RIntCirc)

n = 50
alpha = pi*(0:2:2*n)/n;
beta = 2*pi*(0:2:n)'/n;
xt=(RIntCirc+minorRadius*cos(beta))*cos(alpha);
yt=(RIntCirc+minorRadius*cos(beta))*sin(alpha);
zt=minorRadius*sin(beta)*ones(size(alpha));
```

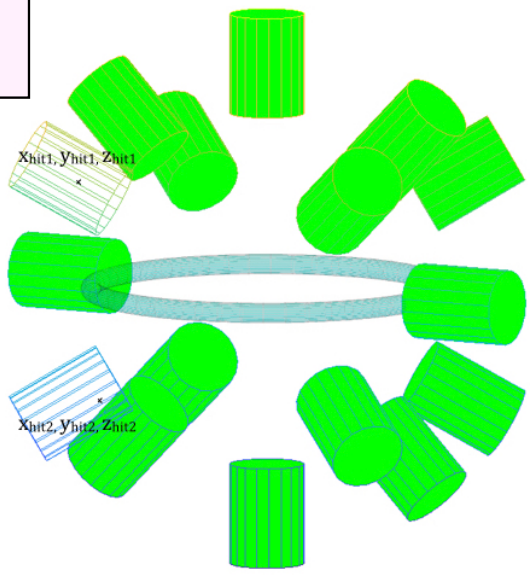

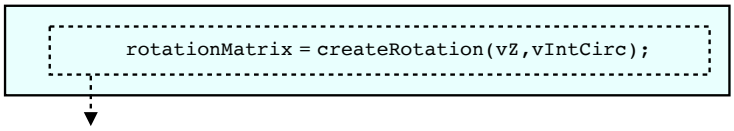

createRotation.m

Input: versor from *cIntCirc* parallel to Z axis (*vZ*) and versor from *cIntCirc* to (xc1, yc1, zc1) (*vIntCirc*)
Output:

- *RotationMatrix* = rotation matrix to rotate the vector *V1* to *vIntCirc*. The chosen rotation is around XYZ axes ("Tait-Bryan convention").

```
function rotationMatrix = createRotation(vZ,vIntCirc)

% Angle-axis representation
axis=cross (vIntCirc,vZ)/norm(cross(vIntCirc,vZ));
angle=acos(dot(vIntCirc,vZ));

% Angle-axis to quaternion conversion
q1  = axis(1)*sin(angle/2); % X
q2  = axis(2)*sin(angle/2); % Y
q3  = axis(3)*sin(angle/2); % Z
q4  = cos(angle/2); % angle rad

% Euler angles  XYZ in "the Tait-Bryan convention"
sine=(2*(q4*q2 - q3*q1));
if (sine ~= 1) && (sine ~= -1)

  phi = atan2(2*(q4*q1 + q2*q3),1-2*(q1^2 + q2^2));

    if (abs(sine) < 1)
      theta = asin(sine);

    elseif sine > 1
        theta = asin(1);

    elseif sine < -1
        theta = asin(-1);
    end

  psi = atan2(2*(q4*q3 - q1*q2),1-2*(q2^2 + q3^2));

elseif sine == 1

  phi = atan2(q3,q4);
  psi = 0;
  theta = asin(sine);

elseif sine == -1

  phi = -atan2(q3,q4);
  psi = 0;
  theta = asin(sine);

end

% Create first transformation around X axis
co_phi = cos(phi);
si_phi = sin(phi);
Rot1_X = [1 0 0 0;...
      0 co_phi si_phi 0;...
      0 -si_phi co_phi 0;...
      0 0 0 1];

% Create second transformation around Y axis
co_theta = cos(theta);
si_theta = sin(theta);
Rot2_Y = [co_theta  0  -si_theta  0;...
      0    1    0  0;...
      si_theta 0  co_theta  0;...
      0    0    0  1];

% Create third transformation around Z axis
co_psi = cos(psi);
si_psi = sin(psi);
Rot3_Z = [co_psi si_psi 0 0;...
     -si_psi co_psi 0 0;...
      0 0 1 0;...
      0 0 0 1];

RotationMatrix=Rot1_X*Rot2_Y*Rot3_Z;
```

```
translationMatrix = createTranslation(cIntCirc);
```

createTranslation.m

Input: centre of the intersection circle (*cIntCirc*)
Output:

- *TranslationMatrix* = translation matrix from (0,0,0) to *cIntCirc*

```
function translationMatrix = createTranslation3D(cIntCirc)

dx = var(1);
dy = var(2);
dz = var(3);
% create the translation matrix
trans = [1 0 0 dx ; 0 1 0 dy ; 0 0 1 dz; 0 0 0 1];
```

```
transformation = translationMatrix*rotationMatrix;
```

The final transformation matrix is obtained (rotation + translation)

```
[x_Torus, y_Torus, z_Torus] = transformPoint(x_t,y_t,z_t, transformation);
```

transformPoint.m

Input: coordinates of a torus centred in (0,0,0) (*xt, yt, zt*) and transformation
Output:

- *x_Torus, y_Torus, z_Torus* = coordinates of a torus centred in *xIntCirc* with major radius *RIntCirc* and minor radius *minorRadius*

```
function [x_Torus, y_Torus, z_Torus] = transformPoint(x_t,y_t,z_t, trans)

% Eventually add null translation
if size(trans, 2) == 3
   trans = [trans zeros(size(trans, 1), 1)];
end
% Eventually add normalisation
if size(trans, 1) == 3
   trans = [trans; 0 0 0 1];
end
% convert coordinates
NP  = numel(x_t);
try
   res = [x_t(:) y_t(:) z_t(:) ones(NP,1,class(x))] * trans';

   % Back-fill x,y,z with new result
   x_Torus(:) = res(:,1);
   y_Torus(:) = res(:,2);
   z_Torus(:) = res(:,3);
end
```

```
      X_data_tori = [X_data_tori {x_Torus}];
      Y_data_tori = [Y_data_tori {y_Torus}];
      Z_data_tori = [Z_data_tori {z_Torus}];

      end
   end
end
```

The coordinates of the torus (*x_Torus, y_Torus, z_Torus*) are stored

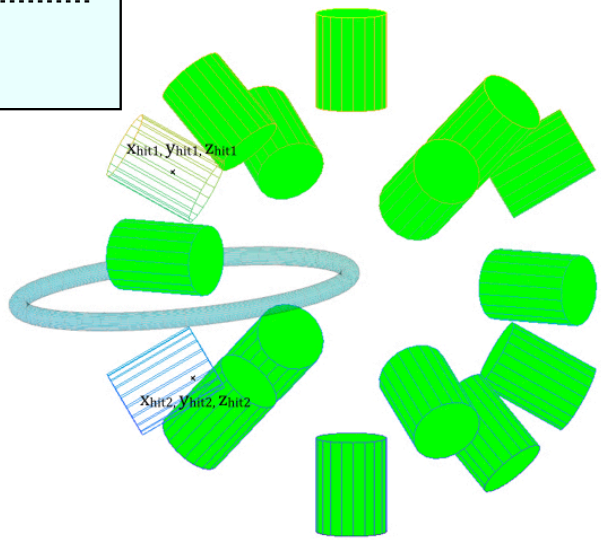

```
coordSource = torInt(NCouples, X_data_tori,…
Y_data_tori, Z_data_tori);
```

torInt.m

Input: total number of couples NCouples and coordinates of all tori (*x_Torus, y_Torus, z_Torus*)

Output:

- *CcoordSource* = intersection between two subsequent tori is calculated and the centre of intersection is stored

surf2solid.m

https://uk.mathworks.com/matlabcentral/fileexchange/30709-surf2solid

```
function coordSource = torInt1(NCouples,X_data_tori,Y_data_tori,Z_data_tori)

n = 0;
for i=1:(NCouples - 1)
      n=n+1;
   Surface1=surf2solid(X_data_tori{1, i},Y_data_tori{1, i},Z_data_tori{1, i}, 'thickness',0.01,'triangulation','f');
   Surface2=surf2solid(X_data_tori{1, i+1},Y_data_tori{1, i+1},Z_data_tori{1, i+1},'thickness',0.01,'triangulation','f');
   [~, SurfInt] = surfaceIntersection(Surface1, Surface2);
      if isempty(SurfInt.vertices)
         X_coord = NaN;
         Y_coord = NaN;
         Z_coord = NaN;
      else
         X_coord=(max(SurfInt.vertices(:,1))+ min(SurfInt.vertices(:,1)))/2;
         Y_coord=(max(SurfInt.vertices(:,2))+ min(SurfInt.vertices(:,2)))/2;
         Z_coord=(max(SurfInt.vertices(:,3))+ min(SurfInt.vertices(:,3)))/2;
      end
         coordSource(n,:) = [i i+1 X_coord Y_coord Z_coord];
End

coordSource( ~any(coordSource(:,3),2), : ) = [];
```

surfaceIntersection

https://uk.mathworks.com/matlabcentral/fileexchange/48613-surface-intersection

```
Projection = [];
reconstructedEmittingPos(:,1)=Coord_Source(:,3);
reconstructedEmittingPos(:,2)=Coord_Source(:,4);
reconstructedEmittingPos(:,3)=Coord_Source(:,5);
```

The coordinates of the intersection points are saved as reconstructed-emitting positions

Chapter 14

Appendix 3

In this Section is reported the full MATLAB 2018b code for Algorithm 2. Algorithm 2 is the position reconstruction algorithm illustrated in Panaino *et al* [274].

Algorithm 2 - Hyperboloids

Panaino, C.M., *et al*, 2020. *Computer Physics Communications*, *252*, p.107131.

```
cd('/Users/…/InputFile');
```

Folder where the .txt file from Geant4 is saved

```
fileName = 'InputFile_name.txt';
fileID = fopen(fileName);
radiationRecorded = textscan(fileID,'%f %f %f %f %f %f',…
                             …'Delimiter','\t');
fclose(fileID);
radiationRecorded = cell2mat(radiationRecorded);
```

The .txt file is converted as a .mat, (matrix in MATLAB)

```
Energy = radiationRecorded(:,1);
Time = radiationRecorded(:,2);
Detector = radiationRecorded(:,3);
```

The matrix is separated into vectors reporting:
1) Energy
2) Time
3) Detector

```
for i=1:(length(Energy)-1)
    if Detector(i)~=Detector(i+1)
       if (Energy(i)<=1.2081 && Energy(i)>=1.1379 && …
           Energy(i+1)<=1.1847 && Energy(i+1)>=1.1613) ||…
          (Energy(i+1)<=1.2081 && Energy(i+1)>=1.1379 && …
           Energy(i)<=1.1847 && Energy(i)>=1.1613)

            coupleDet(i,:)=[Detector(i),Detector(i+1)];

         end
      end
end

indices = find(coupleDet(:,1) == 0);
coupleDet(indices,:) = [];
```

A *couple* of γ-rays is selected: the two γ-rays in the *couple* are recorded one after each other, in two different detectors, and have energy centred at 1.173 and 1.332 MeV, irrespective of order

The detector n^0, in which two γ-rays from a *couple* have been detected, are stored in *coupleDet*

```
coupleNumDet(:,1)=(1:16)';
for i=1:16
    % Nxdet
    coupleNumDet(i,2)=sum(coupleDet(:) == i);
    % SQRT(Nxdet)
    coupleNumDet(i,3)=round(sqrt(sum(coupleDet(:)==i)));
    coupleNumDet(i,4)=coupleNumDet(i,2)+coupleNumDet(i,3);
    coupleNumDet(i,5)=coupleNumDet(i,2)-coupleNumDet(i,3);
end
```

For each detector is estimated:
1) *Nγdet* = the n^0 of γ-rays, belonging to *couples,* recorded in the detector
2) *SQRT(Nγdet)* = The sqrt of this n^0
3) *Nγdet + SQRT(Nγdet)*
4) *Nγdet - SQRT(Nγdet)*

```
cubeSize= 4;
```

Size of the virtual voxelised cube

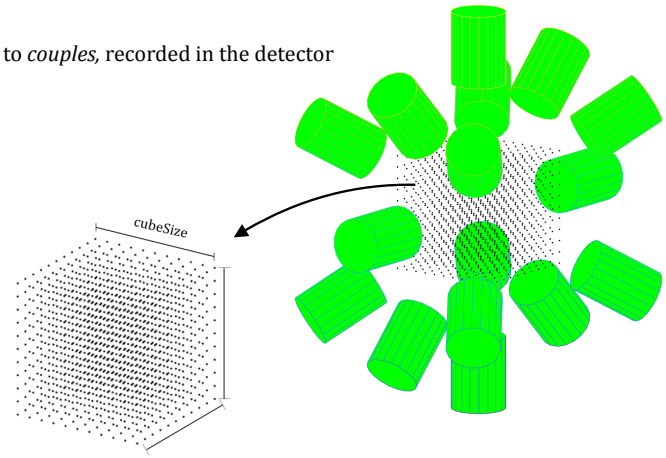

```
[X_neg,X_pos] = XmeshgridCalculation(coupleNumDet,cubeSize);
```

XmeshgridCalculation.m

Input: *Nγdet ± SQRT(Nγdet)* from *coupleNumDet* and the size of the virtual voxellised cube (*cubeSize*)
Output:

- X_neg, X_pos

```
function [X_neg,X_pos] = XmeshgridCalculation(coupleNumDet,cubeSize)

for i=[10 16 11 14]
     for j=[9 15 12 13]
         if coupleNumDet(j,5) < coupleNumDet(i,4)
            X_neg = 0;  X_pos = cubeSize;
% Source closer to detectors (10,16,11,14) then (9, 15,12,13).
         elseif coupleNumDet(j,4) > coupleNumDet(i,5)
            X_neg = cubeSize;  X_pos = 0;
% The source is closer to detectors (9,15,12,13) then (10,16,11,14).
         else
            X_neg = cubeSize;  X_pos = cubeSize;
         end
     end
end
```

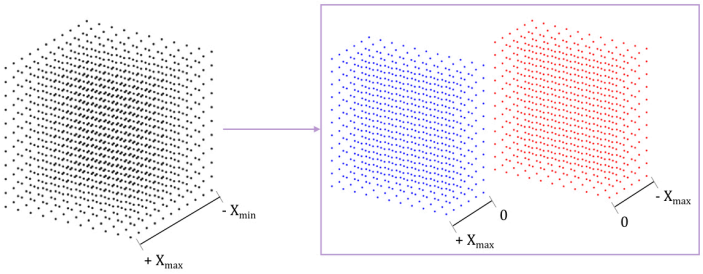


```
[Y_neg,Y_pos] = YmeshgridCalculation(coupleNumDet,cubeSize);
```

YmeshgridCalculation.m

Input: *Nγdet ± SQRT(Nγdet)* from *coupleNumDet* and the size of the virtual voxellised cube (*cubeSize*)
Output:

- Y_neg, Y_pos

```
function [y_neg,y_pos] = YmeshgridCalculation(coupleNumDet,cubeSize)

for i=11:14
     for j=[9 10 15 16]
         if coupleNumDet(j,5) < coupleNumDet(i,4)
            Y_neg = 0;  Y_pos = cubeSize;
% Source is closer to detectors (9,19,15,16) then 11-14.
         elseif coupleNumDet(j,4) > coupleNumDet(i,5)
            Y_neg = cubeSize;  Y_pos = 0;
% Source is closer to detectors 11-14 then detectors (9,19,15,16).
         else
            Y_neg = cubeSize;  Y_pos = cubeSize;
         end
     end
end
```

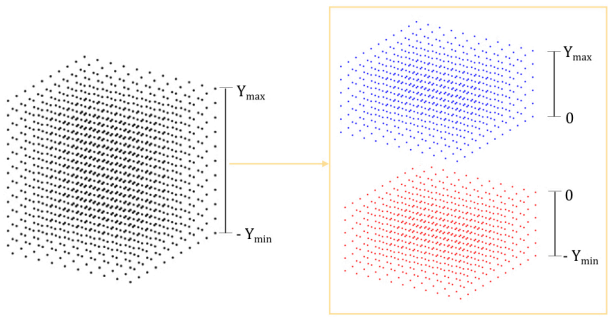

```
[Z_neg,Z_pos] = ZmeshgridCalculation(coupleNumDet,cubeSize);
```

ZmeshgridCalculation.m

Input: *Nydet ± SQRT(Nydet)* from *coupleNumDet* and the size of the virtual voxellised cube (*cubeSize*)

Output:

- Z_neg, Z_pos

```
function [Z_neg,Z_pos] =
ZmeshgridCalculation(coupleNumDet,cubeSize)

for i=9:12
     for j=13:16
         if coupleNumDet(j,5) < coupleNumDet(i,4)
            Z_neg = 0;  Z_pos = cubeSize;
% Source closer to detectors 13-16 then 9-12.
         elseif coupleNumDet(j,4) > coupleNumDet(i,5)
            Z_neg = cubeSize;  Z_pos = 0;
% Source closer to detectors 9-12 then 13-16.
         else
            Z_neg = cubeSize;  Z_pos = cubeSize;
         end
     end
end
```

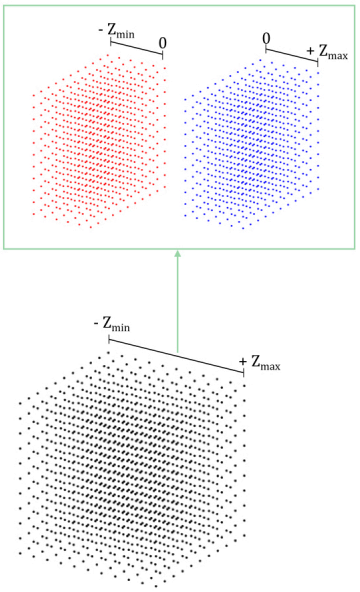


```
cubeSize_small= cubseSize/2;

if X_neg == cubeSize && X_pos == cubeSize &&…
   Y_neg == cubeSize && Y_pos == cubeSize &&…
   Z_neg == cubeSize && Z_pos == cubeSize

   X_neg = cubeSize_small;
   X_pos = cubeSize_small;
   Y_neg = cubeSize_small;
   Y_pos = cubeSize_small;
   Z_neg = cubeSize_small;
   Z_pos = cubeSize_small;
end
```

Halving option

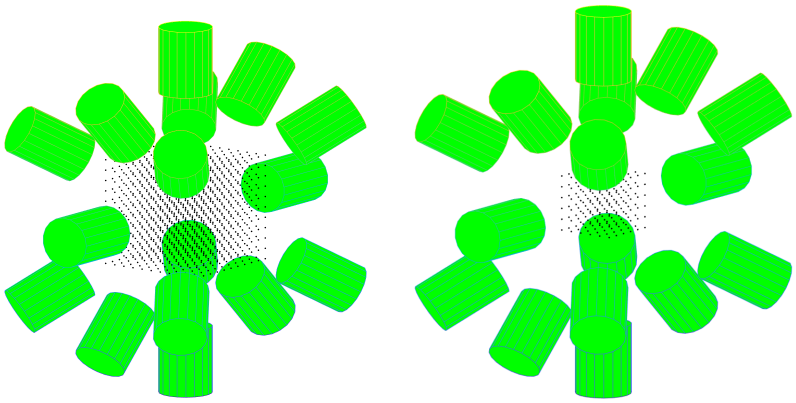

```
NCouples = 0;

for i=1:(length(Energy)-1)

    if Detector (i)~=Detector(i+1)

        if (Energy(i)<=1.2081 && Energy(i)>=1.1379 && …
            Energy(i+1)<=1.1847 && Energy(i+1)>=1.1613) ||…
           (Energy(i+1)<=1.2081 && Energy(i+1)>=1.1379 && …
            Energy(i)<=1.1847 && Energy(i)>=1.1613)

        NCouples=NCouples+1;

        Det1 = Detector(i);
        Det2 = Detector(i+1);

        [x_hit1,y_hit1,z_hit1] = HitPosFinder16(Det1);
        [x_hit2,y_hit2,z_hit2] = HitPosFinder16(Det2);
```

A *couple* of γ-rays is selected: the two γ-rays in the *couple* are recorded one after each other, in two different detectors, and have energy centred at 1.173 and 1.332 MeV, irrespective of order

For each γ-ray in the *couple* the detector is saved

HitPosFinder16.m

Input: detector in which the γ-ray, from a *couple*, is recorded (*Det*)

Output:

- *x_hit, y_hit, z_hit* = random hit position in the detector (obtained by loading the PDFs - one per axis - and sampling it with the acceptance-rejection method)

```
function [x_hit,y_hit,z_hit] = HitPosFinder16(Det)

switch Detector
    case 1
        load('Position_Distributions_16det.mat',…
             'Hit_pos_det1');
        x_hit = RejectionMethod_x(Hit_pos_det1);
        y_hit = RejectionMethod_y(Hit_pos_det1);
        z_hit = RejectionMethod_z(Hit_pos_det1);

    case 2
        load('Position_Distributions_16det.mat',…
             'Hit_pos_det2');
        x_hit = RejectionMethod_x(Hit_pos_det2);
        y_hit = RejectionMethod_y(Hit_pos_det2);
        z_hit = RejectionMethod_z(Hit_pos_det2);

    case 3
        load('Position_Distributions_16det.mat',…
             'Hit_pos_det3');
        x_hit = RejectionMethod_x(Hit_pos_det3);
        y_hit = RejectionMethod_y(Hit_pos_det3);
        z_hit = RejectionMethod_z(Hit_pos_det3);
          .
          .
          .
        case 16
        load('Position_Distributions_16det.mat',…
             'Hit_pos_det16');

        x_hit = RejectionMethod_x(Hit_pos_det16);
        y_hit = RejectionMethod_y(Hit_pos_det16);
        z_hit = RejectionMethod_z(Hit_pos_det16);
end
```

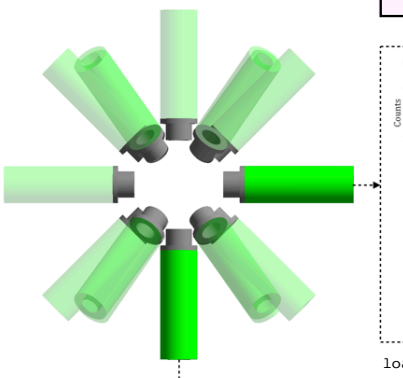

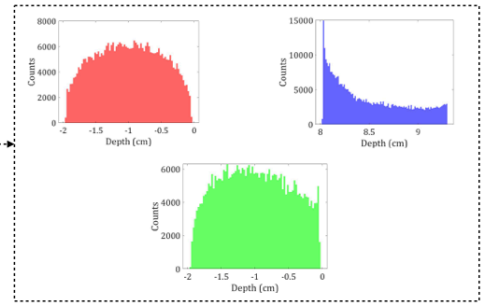

load('Position_Distributions_16det.mat','Hit_pos_det1');

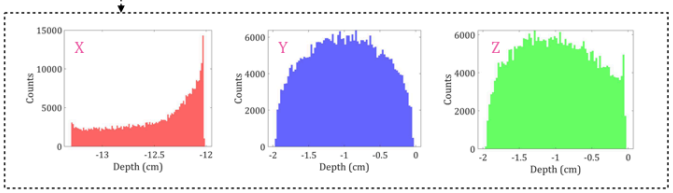

load('Position_Distributions_16det.mat','Hit_pos_det3');

```
t1 = Time(i);
t2 = Time(i+1);

K=(abs(t1-t2))*c;
```

For each γ-ray in the *couple* the time, from the start of the acquisition to the detection, is saved

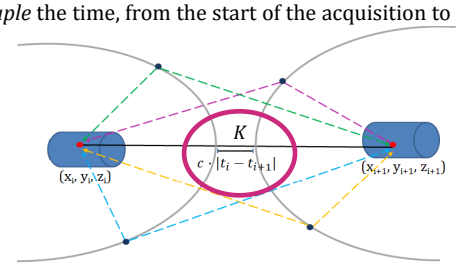

From the time difference between the two events, and c = 30 cm/ns, the parameter *K* of the hyperboloid is calculated

```
TotEvent_Det1 = totEvent_Det(Det1,Total_events);
TotEvent_Det2 = totEvent_Det(Det2,Total_events);
```

totEventDet.m

Input: detector in which the γ-ray is recorded (*Det*) and the total number of γ-ray, belonging to *couples*, recorded in all detectors (*coupleNumDet(:,2)*)

Output:

- total number of γ-rays, from *couples*, recorded in *Det*

```
function totEventDet = totEventDet(Det,coupleNumDet)

switch Det
    case 1
        totEventDet = coupleNumDet(1,2);
    case 2
        totEventDet = coupleNumDet(2,2);
    case 3
        totEventDet = coupleNumDet(3,2);
    case 4
        totEventDet = coupleNumDet(4,2);
    case 5
        totEventDet = coupleNumDet(5,2);
    case 6
        totEventDet = coupleNumDet(6,2);
    case 7
        totEventDet = coupleNumDet(7,2);
    case 8
        totEventDet = coupleNumDet(8,2);
    case 9
        totEventDet = coupleNumDet(9,2);
    case 10
        totEventDet = coupleNumDet(10,2);
    case 11
        totEventDet = coupleNumDet(11,2);
    case 12
        totEventDet = coupleNumDet(12,2);
    case 13
        totEventDet = coupleNumDet(13,2);
    case 14
        totEventDet = coupleNumDet(14,2);
    case 15
        totEventDet = coupleNumDet(15,2);
    case 16
        totEventDet = coupleNumDet(16,2);
end
```

```
Couples(i,:) = [x_hit1,y_hit1,z_hit1,x_hit2,y_hit2,z_hit,K, …
                TotEvent_Det1,TotEvent_Det2];

    end
  end
end

indices = find(Couples(:,1)==0);
Couples(indices,:) = [];
```

For each γ-rays *couple* are saved:

1) *(x_hit1,y_hit1,z_hit1) & (x_hit2,y_hit2,z_hit2)* = the hits coordinates sampled from the PDFs;
2) *K* = parameter of the hyperboloid;
3) *TotEvent_Det1 & TotEvent_Det2* = total number of γ-rays, from *couples*, recorded in the two detectors (*Det1 & Det2*)

```
n=0;
v_dim=0.05;
```

Voxel size of the virtual voxelised cube

```
X_coord_src = {};
Y_coord_src = {};
Z_coord_src = {};
Length = [];

for n1 = 1:NCouples-1
    n2 = n1+1;

    % Hyperboloid 1

    if Couples(n1,8) > Couples(n1,9)
       % NumEvents Det1 > NumEvents Det2 --> source closer to Det1 -> t1 < t2

       % Hyperboloid 1 - sheet(+)
       hyp1 = Hyperboloid_sheetPlus(Couples(n1,1),Couples(n1,2),…
                                    Couples(n1,3),Couples(n1,4),…
                                    Couples(n1,5),Couples(n1,6),…
                                    Couples(n1,7),v_dim,X_neg,X_pos,…
                                    Y_neg,Y_pos,Z_neg,Z_pos);
       if isempty(hyp1.vertices)
          SurfInt = [];
       else

          % Hyperboloid 2

          if Couples(n2,8) > Couples(n2,9)

              % Hyperboloid 2 - sheet(+)
              hyp2 = Hyperboloid_sheetPlus(Couples(n2,1),Couples(n2,2), …
                                           Couples(n2,3),Couples(n2,4), …
                                           Couples(n2,5),Couples(n2,6), …
                                           Couples(n2,7),v_dim,X_neg,X_pos, …
                                            Y_neg,Y_pos,Z_neg,Z_pos);
              if isempty(hyp2.vertices)
                 SurfInt = [];
              else
                 % Hyperboloids Intersection
                 SurfInt = surfacesIntersect(hyp1.vertices,hyp1.faces, …
                                             hyp2.vertices,hyp2.faces);
              end

          elseif Couples(n2,8) < Couples(n2,9)

                 % Hyperboloid 2 - sheet(-)
                 hyp2 = Hyperboloid_sheetMinus(Couples(n2,1),Couples(n2,2), …
                                               Couples(n2,3),Couples(n2,4), …
                                               Couples(n2,5),Couples(n2,6), …
                                               Couples(n2,7),v_dim,X_neg,X_pos, ...
                                               Y_neg,Y_pos,Z_neg,Z_pos);
                 if isempty(hyp2.vertices)
                    SurfInt  [];
                 else
                    % Hyperboloids Intersection
                    SurfInt = surfacesIntersect(hyp1.vertices,hyp1.faces, …
                                                hyp2.vertices,hyp2.faces);
                 end

          elseif Couples(n2,8) == Couples(n2,9)

                 % Hyperboloid 2 - sheet(+)
                 hyp2_plus = Hyperboloid_sheetPlus(Couples(n2,1),Couples(n2,2), …
                                                   Couples(n2,3),Couples(n2,4), …
                                                   Couples(n2,5),Couples(n2,6), …
                                                   Couples(n2,7),v_dim,X_neg,X_pos, …
                                                   Y_neg,Y_pos,Z_neg,Z_pos);

                 % Hyperboloid 2 - sheet(-)
                 hyp2_minus = Hyperboloid_sheetMinus(Couples(n2,1),Couples(n2,2), …
                                                     Couples(n2,3),Couples(n2,4), …
                                                     Couples(n2,5),Couples(n2,6), …
                                                     Couples(n2,7),w_dim,X_neg,X_pos, …
                                                     Y_neg,Y_pos,Z_neg,Z_pos);

                 hyp2.vertices = [hyp2_plus.vertices; hyp2_minus.vertices];
                 hyp2.faces = [hyp2_plus.faces; hyp2_minus.faces];
```

```
            if isempty(hyp2.vertices)
               SurfInt = [];
            else
               % Hyperboloids Intersection
               SurfInt = surfacesIntersect(hyp1.vertices,hyp1.faces, …
                                           hyp2.vertices,hyp2.faces);
            end

      end
   end

% Hyperbolod 1

elseif Couples(n1,8) < Couples(n1,9)
       % NumEvents Det1 < NumEvents Det2 --> source closer to Det2 --> t1 > t2

       % Hyperboloid 1 - sheet(-)
       hyp1 = Hyperboloid_sheetMinus(Couples(n1,1),Couples(n1,2), …
                                     Couples(n1,3),Couples(n1,4), …
                                     Couples(n1,5),Couples(n1,6), …
                                     Couples(n1,7),v_dim,X_neg,X_pos, …
                                     Y_neg,Y_pos,Z_neg,Z_pos);
       if isempty(hyp1.vertices)
          SurfInt = [];
       else

          % Hyperbolod 2

          if Couples(n2,8) > Couples(n2,9)

             % Hyperboloid 2 - sheet(+)
             hyp2 = Hyperboloid_sheetPlus(Couples(n2,1),Couples(n2,2), …
                                          Couples(n2,3),Couples(n2,4), …
                                          Couples(n2,5),Couples(n2,6), …
                                          Couples(n2,7),v_dim,X_neg,X_pos, …
                                          Y_neg,Y_pos,Z_neg,Z_pos);
             if isempty(hyp2.vertices)
                SurfInt = [];
             else
                % Hyperboloids intersection
                SurfInt = surfacesIntersect(hyp1.vertices,hyp1.faces, …
                                            hyp2.vertices,hyp2.faces);
             end

             elseif Couples(n2,8) < Couples(n2,9)

                    % Hyperboloid 2 - sheet(-)
                    hyp2 = Hyperboloid_sheetMinus(Couples(n2,1),Couples(n2,2), …
                                                  Couples(n2,3),Couples(n2,4), …
                                                  Couples(n2,5),Couples(n2,6), …
                                                  Couples(n2,7),v_dim,X_neg,X_pos, …
                                                  Y_neg,Y_pos,Z_neg,Z_pos);
                    if isempty(hyp2.vertices)
                       SurfInt = [];
                    else
                       % Hyperboloids Intersection
                       SurfInt = surfacesIntersect(hyp1.vertices,hyp1.faces, …
                                                   hyp2.vertices,hyp2.faces);
                    end

             elseif Couples(n2,8) == Couples(n2,9)

                    % Hyperboloid 2 - sheet(+)
                    hyp2_plus = Hyperboloid_sheetPlus(Couples(n2,1), …
                                                      Couples(n2,2), …
                                                      Couples(n2,3), …
                                                      Couples(n2,4), …
                                                      Couples(n2,5), …
                                                      Couples(n2,6), …
                                                      Couples(n2,7),v_dim,X_neg, …
                                                      Y_neg,Y_pos,Z_neg,Z_pos);
```

```
                    % Hyperboloid 2 - sheet(-)
                    hyp2_minus = Hyperboloid_sheetMinus(Couples(n2,1),
                                                        Couples(n2,2), …
                                                        Couples(n2,3), …
                                                        Couples(n2,4), …
                                                        Couples(n2,5), …
                                                        Couples(n2,6), …
                                                        Couples(n2,7),v_dim,X_neg, …
                                                        X_pos,Y_neg,Y_pos,Z_neg,Z_pos);

                    hyp2.vertices = [hyp2_plus.vertices; hyp2_minus.vertices];
                    hyp2.faces = [hyp2_plus.faces; hyp2_minus.faces];

                    if isempty(hyp2.vertices)
                       SurfInt = [];
                    else
                       % Hyperboloids Intesection
                       SurfInt = surfacesIntersect(hyp1.vertices,hyp1.faces,…
                                                   hyp2.vertices,hyp2.faces);
                    end
                end
               end

    elseif Couples(n1,8) == Couples(n1,9)
           % NumEvents Det1 = NumEvents Det2 -> source at the same distance to Det1 & Det2

           % Hyperboloid 1 - sheet(+)
           hyp1_plus = Hyperboloid_sheetPlus(Couples(n1,1),Couples(n1,2), …
                                             Couples(n1,3),Couples(n1,4), …
                                             Couples(n1,5),Couples(n1,6), …
                                             Couples(n1,7),v_dim,X_neg,X_pos, …
                                             Y_neg,Y_pos,Z_neg,Z_pos);

           % Hyperboloid 1 - sheet(-)
           hyp1_minus = Hyperboloid_sheetMinus(Couples(n1,1),Couples(n1,2), …
                                               Couples(n1,3),Couples(n1,4), …
                                               Couples(n1,5),Couples(n1,6), …
                                               Couples(n1,7),v_dim,X_neg,X_pos, …
                                               Y_neg,Y_pos,Z_neg,Z_pos);

           hyp1.vertices = [hyp1_plus.vertices; hyp1_minus.vertices];
           hyp1.faces = [hyp1_plus.faces; hyp1_minus.faces];

           if isempty(hyp1.vertices)
              SurfInt = [];

          elseif Couples(n2,8) > Couples(n2,9)
                  % Hyperboloid 2 - sheet(+)
                  hyp2 = Hyperboloid_sheetPlus(Couples(n2,1),Couples(n2,2), …
                                               Couples(n2,3),Couples(n2,4), …
                                               Couples(n2,5),Couples(n2,6), …
                                               Couples(n2,7),v_dim,X_neg,X_pos, …
                                               Y_neg,Y_pos,Z_neg,Z_pos);
                  if isempty(hyp2.vertices)
                       SurfInt = [];
                  else
                       % Hyperboloids Intersection
                       SurfInt = surfacesIntersect(hyp1.vertices,hyp1.faces, …
                                                   hyp2.vertices,hyp2.faces);
                  end

           elseif Couples(n2,8) < Couples(n2,9)

                  % Hyperboloid 2 - sheet(-)
                  hyp2 = Hyperboloid_sheetMinus(Couples(n2,1),Couples(n2,2), …
                                                Couples(n2,3),Couples(n2,4), …
                                                Couples(n2,5),Couples(n2,6), …
                                                Couples(n2,7),v_dim,X_neg,X_pos, …
                                                Y_neg,Y_pos,Z_neg,Z_pos);
                  if isempty(hyp2.vertices)
                     SurfInt = [];
                  else
                     % Hyperboloids Intersection
                     SurfInt = surfacesIntersect(hyp1.vertices,hyp1.faces, …
                                                 hyp2.vertices,hyp2.faces);
                  end
```

```
elseif Couples(n2,8) == Couples(n2,9)

        % Hyperboloid 2 - sheet(+)
        hyp2_plus = Hyperboloid_sheetPlus(Couples(n2,1),
                                          Couples(n2,2), …
                                          Couples(n2,3),
                                          Couples(n2,4), …
                                          Couples(n2,5),
                                          Couples(n2,6), …
                                          Couples(n2,7),v_dim,X_neg, …
                                          X_pos,Y_neg,Y_pos,Z_neg,Z_pos);

        % Hyperboloid 2 - sheet(-)
        hyp2_minus = Hyperboloid_sheetMinus(Couples(n2,1), …
                                            Couples(n2,2), …
                                            Couples(n2,3), …
                                            Couples(n2,4), …
                                            Couples(n2,5), …
                                            Couples(n2,6), …
                                            Couples(n2,7),m,X_neg,…
                                            X_pos,Y_neg,Y_pos,Z_neg,Z_pos);
```

Hyperboloid_sheetPlus.m

Input: the hits coordinates form the two events in a *couple*, the parameter *K* of the hyperboloid, the voxel size *v_dim*, and the values *X_neg, X_pos, Y_neg, Y_pos, Z_neg, Z_pos*

Output:

- *hyp2_plus* = Triangulated surface of the half-hyperboloid (expressed in vertices and faces)

Hyperboloid_sheetMinus.m

Input: the hits coordinates form the two events in a *couple*, the parameter *K* of the hyperboloid, the voxel size *v_dim*, and the values *X_neg, X_pos, Y_neg, Y_pos, Z_neg, Z_pos*

Output:

- *hyp2_minus* = Triangulated surface of the half-hyperboloid (expressed in vertices and faces)

```
function hyp =
Hyperboloid_sheetPlus(x_hit1,y_hit1, …
                      z_hit1,x_hit2, …
                      y_hit2,z_hit2, …
                      K,m,X_neg, …
                      X_pos,Y_neg, …
                      Y_pos,Z_neg,Z_pos)

[x,y,z]=meshgrid(-X_neg:m:X_pos, …
                 -Y_neg:m:Y_pos, …
                 -Z_neg:m:Z_pos);

hyp_sheet = (sqrt((x-xc1).^2 + (y-yc1).^2 +
            (z-zc1).^2) - sqrt((x-xc2).^2 +
            (y-yc2).^2 + (z-zc2).^2) + K);

hyp = isosurface(x, y, z, hyp_sheet, 0);

end
```

```
function hyp =
Hyperboloid_sheetPlus(x_hit1,y_hit1, …
                      z_hit1,x_hit2, …
                      y_hit2,z_hit2, …
                      K,m,X_neg, …
                      X_pos,Y_neg, …
                      Y_pos,Z_neg,Z_pos)

[x,y,z]=meshgrid(-X_neg:m:X_pos, …
                 -Y_neg:m:Y_pos, …
                 -Z_neg:m:Z_pos);

hyp_sheet = (sqrt((x-xc1).^2 + (y-yc1).^2 +
            (z-zc1).^2) - sqrt((x-xc2).^2 +
            (y-yc2).^2 + (z-zc2).^2) - K);

hyp = isosurface(x, y, z, hyp_sheet, 0);

end
```

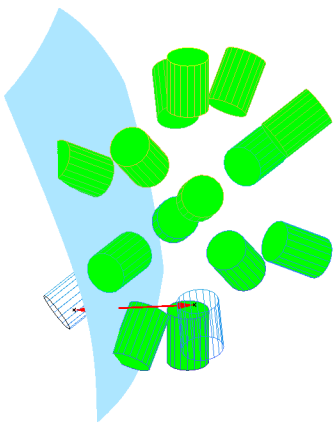

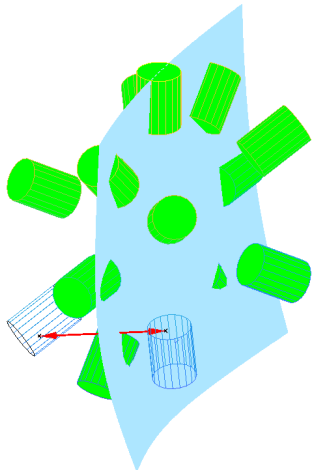

```
                    hyp2.vertices = [hyp2_plus.vertices; hyp2_minus.vertices];
                    hyp2.faces = [hyp2_plus.faces; hyp2_minus.faces];

                    if isempty(hyp2.vertices)
                       SurfInt = [];
                    else
                       % Hyperboloids Intersection
                       SurfInt = surfacesIntersect(hyp1.vertices,hyp1.faces, …
                                                   hyp2.vertices,hyp2.faces);
                    end
                end
            end
        end
```

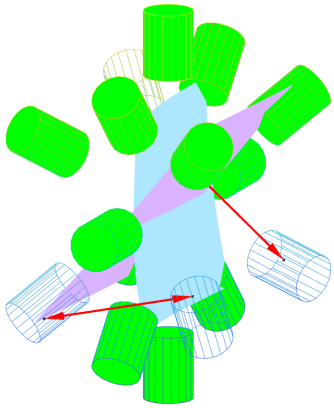

surfacesIntersect.m

Input: faces and vertices of two subsequent triangulated half-hyperboloid (*hyp1.vertices, hyp1.faces, hyp2.vertices, hyp2.faces*)
Output:

- SurfInt = 3D intersection points between two half-hyperboloids

https://uk.mathworks.com/matlabcentral/fileexchange/55803-surfaces-intersect

```
    Length(n,:) = length(SurfInt);

    end

    if isempty(SurfInt)
       X_coord = NaN;
       Y_coord = NaN;
       Z_coord = NaN;
    else
       X_coord=SurfInt(:,3);
       Y_coord=SurfInt(:,4);
       Z_coord=SurfInt(:,5);
    end

       X_coord_src = [X_coord_src {X_coord}];
       Y_coord_src = [Y_coord_src {Y_coord}];
       Z_coord_src = [Z_coord_src {Z_coord}];

       SurfInt=[];
end

Data_intersection(:,1)=cell2mat(X_coord_src');
Data_intersection(:,2)=cell2mat(Y_coord_src');
Data_intersection(:,3)=cell2mat(Z_coord_src');
Data_intersection(~any(~isnan(Data_intersection),2),:)=[]
```

The n of all 3D intersection points between two half-hyperboloids is saved

The 3D intersection points between two half-hyperboloids is saved (and cancelled if null)

The 3D intersection points between two half-hyperboloids are all merged together

```
% Remove null intersections
Length( ~any(Length,2), : ) = [];
% Add a 0 at the beginning of Length
Length = [0;Length];
% Create a cell array
Intersection = cell(1,length(Length)-1);
sum = 0;

% In each cell insert one intersection
% between two one-sheet hyperboloids
for i = 1:(length(Length)-1)
    temp = Data_intersection((sum + 1):(sum + …
           Length(i+1)),:);
    Intersection(i) = {temp};
    sum = sum + Length(i+1);
end
```

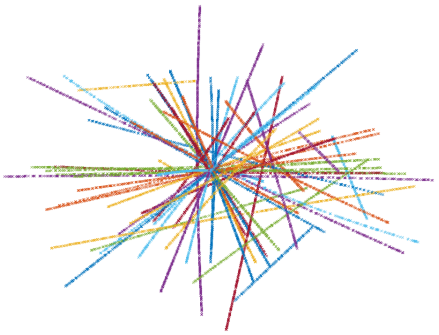

A cell array is created, each cell contains one 3D intersection

```
% Create a cell array
Intersection_Fit = cell(1,length(Length)-1);

for i = 1:(length(Length)-1)
    % Read the size of an intersection matrix
    Size = size(Intersection{1,i},1);
    % Crete an arbitrary parameter S
    S=((0:Size-1)/(Size-1))';

    % Fit all the coordinates with a polynomial
    % function of the 3d order.
    fitX = fit(S,Intersection{1,i}(:,1),'poly3');
    fitY = fit(S,Intersection{1,i}(:,2),'poly3');
    fitZ = fit(S,Intersection{1,i}(:,3),'poly3');

    % Define the interval where the curve is considered
    temp = -0.2:0.001:1;
    % Evaluate the curve
    Curve = [feval(fitX,temp), feval(fitY,temp), …
             feval(fitZ,temp)];
    % In each cell insert the fit of one intersection
    Intersection_Fit(i) = {Curve};
end
```

All 3D intersections are fitted with a 3rd order polynomial fit and the points of the fitted curves are stored in a cell array

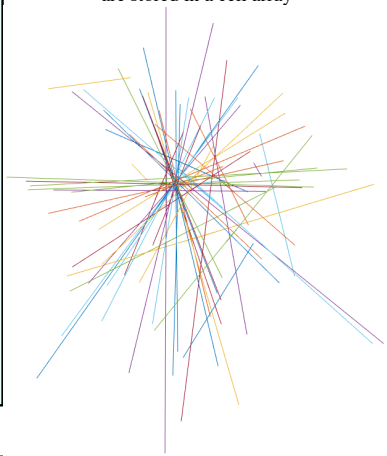

```
X_int = [];
Y_int = [];
Z_int = [];

% create a matrix that contains the fit of two intersection
for i = 2:(length(Length)-2)

    for j = (i+1):(length(Length)-2)

        Mat(:,1) = (Intersection_Fit{:,i}(:,1));
        Mat(:,2) = (Intersection_Fit{:,i}(:,2));
        Mat(:,3) = (Intersection_Fit{:,i}(:,3));
        Mat(:,4) = (Intersection_Fit{:,j}(:,1));
        Mat(:,5) = (Intersection_Fit{:,j}(:,2));
        Mat(:,6) = (Intersection_Fit{:,j}(:,3));
        % calculate the euclidean distance between any two
        % points belonging to the two different fits
        Mat(:,7) = sqrt ( ( Mat(:,1)-Mat(:,4) ).^2 + ...
                          ( Mat(:,2)-Mat(:,5) ).^2 + ...
                          ( Mat(:,3)-Mat(:,6) ).^2 );

        % calculate the minimum euclidean distance
        Min_Dist = min(Mat(:,7));

        % calculate the average value between the two
        % points with distance Min_Dist
        for k = 1: length(temp)
            if Mat(k,7) == Min_Dist
               % Mean X of the two values
               X_int = [X_int; (Mat(k,1)+ Mat(k,4))/2];
               % Mean Y of the two values
               Y_int = [Y_int;(Mat(k,2)+ Mat(k,5))/2];
               % Mean Z of the two values
               Z_int = [Z_int; (Mat(k,3)+ Mat(k,6))/2];
            else
            end
        end

    Mat = [];
    Min_Dist = [];
    end
end

reconstructedEmittingPos(:,1) = X_int;
reconstructedEmittingPos(:,2) = Y_int;
reconstructedEmittingPos(:,3) = Z_int;
```

For every two subsequent fits the euclidean distance between any couple of points - one from one fit, one from the other - is calculated

The minimum euclidean distance is found

The coordinates of the average between the two points with minimum euclidean distance

The coordinates of the average points are saved as reconstructed-emitting positions

Chapter 15

Appendix 4

The Geant4 script for an isotropic point source emitting, with equal probability, at 2.741 and 6.128 MeV, is reported. The source is at (0,0,0).

```
# Particle 1
/gps/particle gamma
# Energy 1
/gps/ene/type Mono
/gps/ene/mono 2.7415 MeV
# Position 1
/gps/pos/type Point
/gps/pos/centre 0.0 0.0 0.0 cm
# Angular distribution 1
/gps/ang/type iso
/gps/ang/minphi 0. deg
/gps/ang/maxphi 360. deg
/gps/ang/mintheta 0. deg
/gps/ang/maxtheta 180. deg

# Particle 2
/gps/source/add 1
/gps/particle gamma
# Energy 2
/gps/ene/type Mono
/gps/ene/mono 6.12863 MeV
# Position 2
/gps/pos/type Point
/gps/pos/centre 0.0 0.0 0.0 cm
# Angular distribution 2
/gps/ang/type iso
/gps/ang/minphi 0. deg
/gps/ang/maxphi 360. deg
/gps/ang/mintheta 0. deg
/gps/ang/maxtheta 180. deg
```

Bibliography

[1] E. Lawrence and N. Edlefsen, "On the production of high speed protons," *Science*, vol. 72, p. 376, 1930.

[2] R. Wilson, "Radiological use of fast protons," *Radiology*, vol. 47.

[3] J. Lawrence, "Proton irradiation of the pituitary," *Cancer*, vol. 10, pp. 795–798, 1957.

[4] C. Tobias *et al.*, "Pituitary irradiation with high-energy proton beams a preliminary report," *Cancer Res*, vol. 18, pp. 121–134, 1958.

[5] L. Leksell *et al.*, "Lesions in the depth of the brain produced by a beam of high energy protons," *Acta Radiol*, vol. 54, pp. 251–264, 1960.

[6] B. Larsson, L. Leksell, and B. Rexed, "The use of high energy protons for cerebral surgery in man," *Acta Chir Scand*, vol. 125, 1963.

[7] R. Kjellberg, W. Sweet, W. Preston, and A. Koehler, "The Bragg peak of a proton beam in intracranial therapy of tumors," *Trans Am Neurol Assoc*, vol. 87, 1962.

[8] R. Kjellberg and B. Kliman, "Proton-beam therapy of pituitary disease: Bragg peak proton treatment for pituitary-related conditions," 1974.

[9] E. S. Gragoudas *et al.*, "Proton irradiation of small choroidal malignant melanomas," *Am J Ophthalmol*, vol. 83, pp. 665–673, 1977.

[10] I. Chuvilo *et al.*, "ITEP synchrotron proton beam in radiotherapy," *Int J Radiat Oncol Biol Phys*, vol. 10, pp. 185–195, 1984.

[11] T. Kanai *et al.*, "Spot scanning system for proton radiotherapy," *Med Phys*, vol. 7, pp. 365–369, 1980.

[12] D. Kurihara, S. Suwa, A. Tachikawa, Y. Takada, and K. Takikawa, "A 300-MeV proton beam line with energy degrader for medical science," *Jpn J Appl Phys*, vol. 22, p. 1599, 1983.

[13] J. Slater *et al.*, "The proton treatment center at loma linda university medical center: rationale for and description of its development," *Int J Radiat Oncol Biol Phys*, vol. 22, pp. 383–389, 1992.

[14] PTCOG, "Particle therapy facilities in clinical operation (last update: February 2020)," 2020.

[15] PTCOG, "Particle therapy facilities under construCTion (update December 2019)," 2020.

[16] PTCOG, "Particle therapy facilities in a planning stage (update December 2019)," 2020.

[17] PTCOG, "Statistics of patients treated in particle therapy facilities worldwide," 2020.

[18] The Clatterbridge Cancer Centre NHS Foundation Trust, "Our eye proton therapy service," 2020.

[19] The Christie Charitable Found, "The Christie Charity," 2020.

[20] University College London NHS Foundation Trust, "A new clinical facility - proton beam therapy, blood disorders and surgery," 2020.

[21] NHS, "Proton beam therapy (last update: February 2020)," 2020.

[22] M. Limb, "How NHS investment in proton beam therapy is coming to fruition," *Br Med J*, vol. 364, 2019.

[23] Rutherford Health PLC Proton Beam Therapy, "Rutherford health plc is at the vanguard of advancing cancer care.," 2020.

[24] Y. Lievens and M. Pijls-Johannesma, "Health economic controversy and cost-effeCTiveness of proton therapy," vol. 23, pp. 134–141, 2013.

[25] D. Jones and j. v. p. y. d. others, title=A systematic review of health economic evaluations of proton beam therapy for adult cancer: Appraising methodology and quality

[26] Y. Lievens and K. Nagels, "Economic data for particle therapy: Dealing with different needs in a heterogeneous landscape," *Radiother Oncol*, vol. 128, no. 1, 2018.

[27] M. Goitein and M. Jermann, "The relative costs of proton and X-ray radiation therapy," *J Clin Oncol*, vol. 15, pp. S37–S50, 2003.

[28] A. Peeters *et al.*, "How costly is particle therapy? Cost analysis of external beam radiotherapy with carbon-ions, protons and photons," *Radiother Oncol*, vol. 95, pp. 45–53, 2010.

[29] A. B. de Gonzalez *et al.*, "A clarion call for large-scale collaborative studies of pediatric proton therapy," *Int J Radiat Oncol Biol Phys*, vol. 98, pp. 980–981, 2017.

[30] M. Goitein and J. Cox, "Should randomized clinical trials be required for proton radiotherapy?," *J Clin Oncol*, vol. 26, pp. 175–176, 2008.

[31] M. Goitein, "Trials and tribulations in charged particle radiotherapy," *Radiother Oncol*, vol. 95, pp. 23–31, 2010.

[32] T. Bortfeld, "IMRT: a review and preview," *Phys Med Biol*, vol. 51, p. R363, 2006.

[33] N. Lukens, A. Lin, and S. Hahn, "Proton therapy for head and neck cancer," *Curr Opin Oncol*, vol. 27, pp. 165–171, 2015.

[34] J. K. Kim *et al.*, "Proton therapy for head and neck cancer," *Curr Treat Option On*, vol. 19, p. 28, 2018.

[35] C. Cancer Research UK, "Medulloblastoma," 2020.

[36] M. Schwab, *Encyclopedia of cancer*. Springer Science & Business Media, 2008.

[37] T. Yock *et al.*, "Long-term toxic effects of proton radiotherapy for paediatric medulloblastoma: a phase 2 single-arm study," *Lancet Oncol*, vol. 17, pp. 287–298, 2016.

[38] H. Bethe, "Zur Theorie des Durchgangs schneller Krpuskularstrahlen durch Materie," *Annalen der Physik*, vol. 397, pp. 325–400, 1930.

[39] F. Bloch, "Zur Bremsung rasch bewegter Teilchen beim Durchgang durch Materie," *Annalen der Physik*, vol. 408, pp. 285–320, 1933.

[40] D. Thwaites, "Bragg's rule of stopping power additivity: A compilation and summary of results," *Radiat Res*, vol. 95, pp. 495–518, 1983.

[41] W. Bragg and R. Kleeman, "On the α particles of radium, and their loss of range in passing through various atoms and molecules," *The London, Edinburgh, and Dublin Philosophical Magazine and Journal of Science*, vol. 10, pp. 318–340, 1905.

[42] T. Bortfeld, "An analytical approximation of the Bragg curve for therapeutic proton beams," *Med Phys*, vol. 24, pp. 2024–2033, 1997.

[43] J. Janni, "Proton range-energy tables, 1 KeV - 10GeV, 1KeV - 10 GeV. Atomic data and nuclear data table, 27 parts 1 (compounds) and 2 (mixture)," 1982.

[44] H. Paganetti, "Nuclear interactions in proton therapy: dose and relative biological effect distributions originating from primary and secondary particles," *Phys Med Biol*, vol. 47, p. 747, 2002.

[45] International Commission on Radiation Units (ICRU), *Nuclear data for neutron and proton radiotherapy and for radiation protection*, vol. 63. ICRU Report 63, 2000.

[46] R. Carlson *et al.*, "Proton total reaction cross sections for the doubly magic nuclei ^{16}O, ^{40}Ca, and ^{208}Pb in the energy range 20-50 MeV," *Phys Rev C*, vol. 12, p. 1167, 1975.

[47] P. Renberg *et al.*, "Reaction cross sections for protons in the energy range 220–570 MeV," *Nucl Phys A*, vol. 183, pp. 81–104, 1972.

[48] R. Chapman and A. Macleod, "Proton nuclear reaction cross sections in oxygen and neon at 13 MeV," *Nucl Phys A*, vol. 94, pp. 313–323, 1967.

[49] B. Kozlovsky, R. Murphy, and R. Ramaty, "Nuclear deexcitation gamma-ray lines from accelerated particle interactions," *Astrophys J Suppl S*, vol. 141, p. 523, 2002.

[50] P. Dyer, D. Bodansky, A. Seamster, E. Norman, and D. Maxson, "Cross sections relevant to gamma-ray astronomy: Proton induced reactions," *Phys Rev C*, vol. 23, p. 1865, 1981.

[51] F. Lang, C. Werntz, C. Crannell, J. I. Trombka, and C. Chang, "Cross sections for production of the 15.10-MeV and other astrophysically significant gamma-ray lines through excitation and spallation of ^{12}C and ^{16}O with protons," *Phys Rev C*, vol. 35, 1987.

[52] J. Narayanaswamy, P. Dyer, S. Faber, and S. Austin, "Production of 6.13-MeV gamma rays from the ^{16}O(p, p$'\gamma$)^{16}O reaction at 23.7 and 44.6 MeV," *Phys Rev C*, vol. 24, p. 2727, 1981.

[53] K. Lesko *et al.*, "Measurements of cross sections relevant to γ-ray line astronomy," *Phys Rev C*, vol. 37, p. 1808, 1988.

[54] V. Tatischeff *et al.*, "Gamma-ray lines of carbon and oxygen from orion," *Astrophys J*, vol. 472, p. 205, 1996.

[55] W. Zobel, F. Maienschein, J. Todd, and G. Chapman, "Gamma rays from bombardment of light and intermediate weight nuclei by 16- to 160-MeV protons and 59-MeV alpha particles," *Nucl Sci Eng*, vol. 32, pp. 392–406, 1968.

[56] J. Kiener *et al.*, "γ-ray production by inelastic proton scattering on ^{16}O, ^{12}C," *Phys Rev C*, vol. 58, p. 2174, 1998.

[57] K. Foley, A. Clegg, and G. Salmon, "Gamma-radiation from the medium energy proton bombardment of sodium, magnesium, aluminium, silicon phosphorus and sulphur," *Nucl Phys*, vol. 37, pp. 23–44, 1962.

[58] S. Agosteo, C. Birattari, M. Caravaggio, M. Silari, and G. Tosi, "Secondary neutron and photon dose in proton therapy," *Radiother Oncol*, vol. 48, pp. 293–305, 1998.

[59] J. Valentin *et al.*, *The 2007 recommendations of the international commission on radiological protection*, vol. 37. Elsevier Oxford, 2007.

[60] W. Newhauser and M. Durante, "Assessing the risk of second malignancies after modern radiotherapy," *Nat. Rev. Cancer*, vol. 11, pp. 438–448, 2011.

[61] U. Amaldi *et al.*, "Accelerators for hadrontherapy: from Lawrence cyclotrons to linacs," *Nucl Instrum Methods Phys Res A*, vol. 620, pp. 563–577, 2010.

[62] J. Flanz, "Accelerators for charged particle therapy," *Mod Phys Lett A*, vol. 30, p. 1540020, 2015.

[63] J. Schippers, "Cyclotrons for particle therapy," *arXiv preprint arXiv:1804.08541*, 2018.

[64] A. Schreuder *et al.*, "The non-orthogonal fixed beam arrangement for the second proton therapy facility at the National Accelerator Center," *AIP Conf Proc*, vol. 475, pp. 963–966, 1999.

[65] S. Yan, H. Lu, J. Flanz, J. Adams, A. Trofimov, and T. Bortfeld, "Reassessment of the necessity of the proton gantry: analysis of beam orientations from 4332 treatments at the massachusetts general hospital proton center over the past 10 years," *Int J Radiat Oncol Biol Phys*, vol. 95, pp. 224–233, 2016.

[66] M. Engelsman, H. Lu, D. Herrup, M. Bussiere, and H. Kooy, "Commissioning a passive-scattering proton therapy nozzle for accurate SOBP delivery," *Med Phys*, vol. 36, pp. 2172–2180, 2009.

[67] E. Pedroni, D. Meer, C. Bula, S. Safai, and S. Zenklusen, "Pencil beam characteristics of the next-generation proton scanning gantry of PSI: design issues and initial commissioning results," *Eur Phys J Plus*, vol. 126, p. 66, 2011.

[68] T. Pugh *et al.*, "Quality of life and toxicity from passively scattered and spot-scanning proton beam therapy for localized prostate cancer," *Int J Radiat Oncol Biol Phys*, vol. 87, pp. 946–953, 2013.

[69] M. Moteabbed, T. Yock, and H. Paganetti, "The risk of radiation-induced second cancers in the high to medium dose region: a comparison between passive and scanned proton therapy, IMRT and VMAT for paediatric patients with brain tumors," *Phys Med Biol*, vol. 59, p. 2883, 2014.

[70] M. Chuong *et al.*, "Pencil beam scanning versus passively scattered proton therapy for unresectable pancreatic cancer," *World J Gastrointest Oncol*, vol. 9, p. 687, 2018.

[71] S. James, C. Grassberger, and H. Lu, "Considerations when treating lung cancer with passive scatter or active scanning proton therapy," *Transl Lung Cancer Res*, vol. 7, p. 210, 2018.

[72] B. Arjomandy, N. Sahoo, J. Cox, A. Lee, and M. Gillin, "Comparison of surface doses from spot scanning and passively scattered proton therapy beams," *Phys Med Biol*, vol. 54, p. N295, 2009.

[73] D. J. Brenner and E. J. Hall, "Secondary neutrons in clinical proton radiotherapy: a charged issue," *Radiother Oncol*, vol. 86, pp. 165–170, 2008.

[74] A. Knopf and A. Lomax, "In vivo proton range verification: a review," *Phys Med Biol*, vol. 58, p. R131, 2013.

[75] A. Trofimov *et al.*, "Radiotherapy treatment of early-stage prostate cancer with IMRT and protons: a treatment planning comparison," *Int J Radiat Oncol Biol Phys*, vol. 69, pp. 444–453, 2007.

[76] J. M. Verburg, "Reducing range uncertainty in proton therapy," 2015.

[77] A. Carabe, M. Moteabbed, N. Depauw, J. Schuemann, and H. Paganetti, "Range uncertainty in proton therapy due to variable biological effectiveness," *Phys Med Biol*, vol. 57, p. 1159, 2012.

[78] C. Grassberger, A. Trofimov, A. Lomax, and H. Paganetti, "Variations in linear energy transfer within clinical proton therapy fields and the potential for biological treatment planning," *Int J Radiat Oncol Biol Phys*, vol. 80, pp. 1559–1566, 2011.

[79] A. Chvetsov and S. Paige, "The influence of CT image noise on proton range calculation in radiotherapy planning," *Phys Med Biol*, vol. 55, p. N141, 2010.

[80] B. Schaffner and E. Pedroni, "The precision of proton range calculations in proton radiotherapy treatment planning: experimental verification of the relation between CT-HU and proton stopping power," *Phys Med Biol*, vol. 43, p. 1579, 1998.

[81] W. Newhauser *et al.*, "Can megavoltage computed tomography reduce proton range uncertainties in treatment plans for patients with large metal implants?," *Phys Med Biol*, vol. 53, p. 2327, 2008.

[82] S. España and H. Paganetti, "The impact of uncertainties in the CT conversion algorithm when predicting proton beam ranges in patients from dose and PET-activity distributions," *Phys Med Biol*, vol. 55, p. 7557, 2010.

[83] N. Hünemohr, H. Paganetti, S. Greilich, O. Jäkel, and J. Seco, "Tissue decomposition from dual energy CT data for MC based dose calculation in particle therapy," *Med Phys*, vol. 41, p. 061714, 2014.

[84] T. Li *et al.*, "Reconstruction for proton computed tomography by tracing proton trajectories: A Monte Carlo study," *Med Phys*, vol. 33, pp. 699–706, 2006.

[85] M. Berger *et al.*, "Report 49," *J ICRU*, 1993.

[86] Y. Kumazaki *et al.*, "Determination of the mean excitation energy of water from proton beam ranges," *Radiat Meas*, vol. 42, pp. 1683–1691, 2007.

[87] H. Bischel and T. Hiraoka, "Energy loss of 70 MeV protons in elements," *Nucl Instrum Methods Phys Res B*, vol. 66, pp. 345–351, 1992.

[88] M. Dingfelder, D. Hantke, M. Inokuti, and H. Paretzke, "Electron inelastic-scattering cross sections in liquid water," *Radiat Phys Chem*, vol. 53, pp. 1–18, 1998.

[89] P. Andreo, "On the clinical spatial resolution achievable with protons and heavier charged particle radiotherapy beams," *Phys Med Biol*, vol. 54, p. N205, 2009.

[90] A. Besemer, H. Paganetti, and B. Bednarz, "The clinical impact of uncertainties in the mean excitation energy of human tissues during proton therapy," *Phys Med Biol*, vol. 58, p. 887, 2013.

[91] M. Urie, M. Goitein, W. Holley, and G. T. Chen, "Degradation of the Bragg peak due to inhomogeneities," *Phys Med Biol*, vol. 31, p. 1, 1986.

[92] G. Sawakuchi, U. Titt, D. Mirkovic, and R. Mohan, "Density heterogeneities and the influence of multiple coulomb and nuclear scatterings on the Bragg peak distal edge of proton therapy beams," *Phys Med Biol*, vol. 53, p. 4605, 2008.

[93] B. Bednarz, J. Daartz, and H. Paganetti, "Dosimetric accuracy of planning and delivering small proton therapy fields," *Phys Med Biol*, vol. 55, p. 7425, 2010.

[94] H. Paganetti, H. Jiang, K. Parodi, R. Slopsema, and M. Engelsman, "Clinical implementation of full Monte Carlo dose calculation in proton beam therapy," *Phys Med Biol*, vol. 53, no. 17, p. 4825, 2008.

[95] H. Paganetti, "Range uncertainties in proton therapy and the role of Monte Carlo simulations," *Phys Med Biol*, vol. 57, p. R99, 2012.

[96] K. Langen and D. Jones, "Organ motion and its management," *Int J Radiat Oncol Biol Phys*, vol. 50, pp. 265–278, 2001.

[97] F. Albertini *et al.*, "Sensitivity of intensity modulated proton therapy plans to changes in patient weight," *Radiother Oncol*, vol. 86, pp. 187–194, 2008.

[98] J. Booth and S. Zavgorodni, "Set-up effort & organ motion uncertainty: A review," *Australas Phys Eng S*, vol. 22, 1999.

[99] A. Lomax, "Intensity modulated proton therapy and its sensitivity to treatment uncertainties 2: the potential effects of inter-fraction and inter-field motions," *Phys Med Biol*, vol. 53, p. 1043, 2008.

[100] C. Grassberger *et al.*, "Motion interplay as a function of patient parameters and spot size in spot scanning proton therapy for lung cancer," *Int J Radiat Oncol Biol Phys*, vol. 86, pp. 380–386, 2013.

[101] C. Grassberger, S. Dowdell, G. Sharp, and H. Paganetti, "Motion mitigation for lung cancer patients treated with active scanning proton therapy," *Med Phys*, vol. 42, pp. 2462–2469, 2015.

[102] S. J. Thomas, "Margins for treatment planning of proton therapy," *Phys Med Biol*, vol. 51, p. 1491, 2006.

[103] F. Albertini, E. Hug, and A. Lomax, "Is it necessary to plan with safety margins for actively scanned proton therapy?," *Phys Med Biol*, vol. 56, p. 4399, 2011.

[104] J. Unkelbach *et al.*, "Robust radiotherapy planning," *Phys Med Biol*, vol. 63, p. 22TR02, 2018.

[105] K. Parodi and J. Polf, "In vivo range verification in particle therapy," *Med Phys*, vol. 45, pp. e1036–e1050, 2018.

[106] B. Gottschalk *et al.*, "Water equivalent path length measurement in proton radiotherapy using time resolved diode dosimetry," *Med Phys*, vol. 38, no. 4, 2011.

[107] M. Gensheimer *et al.*, "In vivo proton beam range verification using spine MRI changes," *Int J Radiat Oncol Biol Phys*, vol. 78, pp. 268–275, 2010.

[108] K. Jones *et al.*, "Acoustic-based proton range verification in heterogeneous tissue: simulation studies," *Phys Med Biol*, vol. 63, p. 025018, 2018.

[109] F. Hueso-González, M. Rabe, T. Ruggieri, T. Bortfeld, and J. Verburg, "A full-scale clinical prototype for proton range verification using prompt gamma-ray spectroscopy," *Phys Med Biol*, vol. 63, p. 185019, 2018.

[110] A. Knopf *et al.*, "Accuracy of proton beam range verification using post-treatment positron emission tomography/computed tomography as function of treatment site," *Int J Radiat Oncol Biol Phys*, vol. 79, pp. 297–304, 2011.

[111] H. Lu, "A potential method for in vivo range verification in proton therapy treatment," *Phys Med Biol*, vol. 53, p. 1413, 2008.

[112] H. Lu, "A point dose method for in vivo range verification in proton therapy," *Phys Med Biol*, vol. 53, p. N415, 2008.

[113] Y. Yuan *et al.*, "Feasibility study of in vivo MRI based dosimetric verification of proton end-of-range for liver cancer patients," *Radiother Oncol*, vol. 106, pp. 378–382, 2013.

[114] V. Blomlie *et al.*, "Female pelvic bone marrow: serial MR imaging before, during, and after radiation therapy.," *Radiology*, vol. 194, pp. 537–543, 1995.

[115] L. Sulak *et al.*, "Experimental studies of the acoustic signature of proton beams traversing fluid media," *Nucl Instrum Meth*, vol. 161, pp. 203–217, 1979.

[116] W. Assmann *et al.*, "Ionoacoustic characterization of the proton Bragg peak with submillimeter accuracy," *Med Phys*.

[117] M. Ahmad, L. Xiang, S. Yousefi, and L. Xing, "Theoretical detection threshold of the proton-acoustic range verification technique," *Med Phys*, vol. 42, pp. 5735–5744.

[118] E. Kipergil, H. Erkol, S. Kaya, G. Gulsen, and M. Unlu, "An analysis of beam parameters on proton-acoustic waves through an analytic approach," *Phys Med Biol*, vol. 62, p. 4694, 2017.

[119] D. Litzenberg *et al.*, "On-line monitoring and PET imaging of proton radiotherapy beams," in *IEEE Nucl Sci Symp MIC*, pp. 954–956, IEEE, 1992.

[120] S. Vynckier *et al.*, "Is it possible to verify directly a proton-treatment plan using positron emission tomography?," *Radiother Oncol*, vol. 26, pp. 275–277, 1993.

[121] C. Ammar *et al.*, "Comparing the biological washout of β^+-activity induced in mice brain after ^{12}c-ion and proton irradiation," *Phys Med Biol*, vol. 59, p. 7229, 2014.

[122] G. Shakirin and v. p. y. d. others, journal=Phys Med Biol, "Implementation and workflow for PET monitoring of therapeutic ion irradiation: a comparison of in-beam, in-room, and off-line techniques,"

[123] A. Knopf, K. Parodi, T. Bortfeld, H. Shih, and H. Paganetti, "Systematic analysis of biological and physical limitations of proton beam range verification with offline PET/CT scans," *Phys Med Biol*, vol. 54, p. 4477, 2009.

[124] V. Ferrero *et al.*, "Online proton therapy monitoring: clinical test of a Silicon-photodetector-based in-beam PET," *Sci Rep*, vol. 8, pp. 1–8, 2018.

[125] P. Crespo, G. Shakirin, and W. Enghardt, "On the detector arrangement for in-beam PET for hadron therapy monitoring," *Phys Med Biol*, vol. 51, p. 2143, 2006.

[126] K. Parodi, Ponisch, and W. Enghardt, "Experimental study on the feasibility of in-beam PET for accurate monitoring of proton therapy," *IEEE Trans Nucl Sci*, vol. 52, pp. 778–786, 2005.

[127] X. Zhu *et al.*, "Monitoring proton radiation therapy with in-room PET imaging," *Phys Med Biol*, vol. 56, p. 4041, 2011.

[128] H. Tashima *et al.*, "Development of a small single-ring OpenPET prototype with a novel transformable architecture," *Phys Med Biol*, vol. 61, p. 1795, 2016.

[129] A. Miyatake *et al.*, "Measurement and verification of positron emitter nuclei generated at each treatment site by target nuclear fragment reactions in proton therapy," *Med Phys*, vol. 37, pp. 4445–4455, 2010.

[130] K. Parodi *et al.*, "Patient study of in vivo verification of beam delivery and range, using positron emission tomography and computed tomography imaging after proton therapy," *Int J Radiat Oncol Biol Phys*, vol. 68, pp. 920–934, 2007.

[131] K. Parodi *et al.*, "PET/CT imaging for treatment verification after proton therapy: a study with plastic phantoms and metallic implants," *Med Phys*, vol. 34, pp. 419–435, 2007.

[132] M. Moteabbed, S. España, and H. Paganetti, "Monte Carlo patient study on the comparison of prompt gamma and PET imaging for range verification in proton therapy," *Phys Med Biol*, vol. 56, p. 1063, 2011.

[133] R. Murphy, B. Kozlovsky, J. Kiener, and G. Share, "Nuclear gamma-ray de-excitation lines and continuum from accelerated-particle interactions in solar flares," *Astrophys J Suppl S*, vol. 183, p. 142, 2009.

[134] H. Benhabiles-Mezhoud *et al.*, "Measurements of nuclear γ-ray line emission in interactions of protons and α particles with N, O, Ne, and Si," *Phys Rev C*, vol. 83, p. 024603, 2011.

[135] A. Belhout *et al.*, "γ-ray production by proton and α-particle induced reactions on ^{12}C, ^{16}O, ^{24}Mg, and Fe," *Phys Rev C*, vol. 76, p. 034607, 2007.

[136] C. Min, C. H. Kim, M. Youn, and J. Kim, "Prompt gamma measurements for locating the dose falloff region in the proton therapy," *Appl Phys Lett*, vol. 89, no. 18, p. 183517, 2006.

[137] J. Verburg, H. Shih, and J. Seco, "Simulation of prompt gamma-ray emission during proton radiotherapy," *Phys Med Biol*, vol. 57, p. 5459, 2012.

[138] F. Ajenberg-Selove, "Energy levels of light nuclei A = 12," *Nucl Phys A*, vol. 336, pp. 1–154, 1980.

[139] D. Tilley, H. Weller, and C. Cheves, "Energy levels of light nuclei A = 16," *Nucl Phys A*, vol. 564, no. 1, pp. 1–183, 1993 (Revised 2017).

[140] F. Ajenberg-Selove, "Energy levels of light nuclei A = 14," *Nucl Phys A*, vol. 360, pp. 1–186, 1981.

[141] J. Verburg, K. Riley, T. Bortfeld, and J. Seco, "Energy- and time-resolved detection of prompt gamma-rays for proton range verification," *Phys Med Biol*, vol. 58, p. L37, 2013.

[142] G. Pausch *et al.*, "Detection systems for range monitoring in proton therapy: Needs and challenges," *Nucl Instrum Methods Phys Res A*, vol. 954, p. 161227, 2020.

[143] J. Polf and other, "Measurement of characteristic prompt gamma rays emitted from oxygen and carbon in tissue-equivalent samples during proton beam irradiation," *Phys Med Biol*, vol. 58, p. 5821, 2013.

[144] J. Polf, S. Peterson, G. Ciangaru, M. Gillin, and S. Beddar, "Prompt gamma-ray emission from biological tissues during proton irradiation: a preliminary study," *Phys Med Biol*, vol. 54, p. 731, 2009.

[145] J. Polf *et al.*, "Measurement and calculation of characteristic prompt gamma ray spectra emitted during proton irradiation," *Phys Med Biol*, vol. 54, p. N519.

[146] L. Kelleter, , *et al.*, "Spectroscopic study of prompt-gamma emission for range verification in proton therapy," *Phys Medica*, vol. 34, pp. 7–17, 2017.

[147] E. Lee *et al.*, "Study of the angular dependence of a prompt gamma detector response during proton radiation therapy," *Int J Part Ther*, vol. 1, pp. 731–744, 2014.

[148] M. Zarifi *et al.*, "Characterization of prompt gamma-ray emission with respect to the Bragg peak for proton beam range verification: A Monte Carlo study," *Phys Medica*, vol. 33, pp. 197–206, 2017.

[149] C. Golnik *et al.*, "Range assessment in particle therapy based on prompt γ-ray timing measurements," *Phys Med Biol*, vol. 59, p. 5399, 2014.

[150] M. Zarifi *et al.*, "Characterization of prompt gamma ray emission for in vivo range verification in particle therapy: A simulation study," *Phys Medica*, vol. 62, pp. 20–32, 2019.

[151] J. Krimmer, D. Dauvergne, J. Létang, and É. Testa, "Prompt-gamma monitoring in hadrontherapy: A review," *Nucl Instrum Methods Phys Res A*, vol. 878, pp. 58–73, 2018.

[152] C. Kim, C. Min, K. Seo, and J. Kim, "Simulation studies on the correlation of distal dose falloff of a 70-MeV proton beam with a prompt gamma distribution," *J Korean Phys Soc*, vol. 50, p. 1510, 2007.

[153] C. Min, J. Kim, M. Youn, and C. Kim, "Determination of distal dose edge location by measuring right-angled prompt-gamma rays from a 38 MeV proton beam," *Nucl Instrum Methods Phys Res A*, vol. 580, pp. 562–565, 2007.

[154] F. Roellinghoff *et al.*, "Real-time proton beam range monitoring by means of prompt-gamma detection with a collimated camera," *Phys Med Biol*, vol. 59, p. 1327, 2014.

[155] M. Pinto *et al.*, "Design optimisation of a TOF-based collimated camera prototype for online hadrontherapy monitoring," *Phys Med Biol*, vol. 59, p. 7653, 2014.

[156] P. C. Lopes *et al.*, "Simulation of proton range monitoring in an anthropomorphic phantom using multi-slat collimators and time-of-flight detection of prompt-gamma quanta," *Phys Medica*, vol. 54, pp. 1–14, 2018.

[157] C. Min, H. Lee, C. Kim, and S. Lee, "Development of array-type prompt gamma measurement system for in vivo range verification in proton therapy," *Med Phys*, vol. 39, pp. 2100–2107, 2012.

[158] H. Lee, J. Park, C. Kim, and C. Min, "Design optimization of a 2D prompt-gamma measurement system for proton dose verification," *J. Korean Phys Soc.*, vol. 61, pp. 239–242, 2012.

[159] J. Park *et al.*, "Multi-slit prompt-gamma camera for locating of distal dose falloff in proton therapy," *Nucl Eng Technol*, vol. 51, pp. 1406–1416, 2019.

[160] H. Zhang *et al.*, "Design and performance evaluation of a BGO + SiPM detector for high-energy prompt gamma imaging in proton therapy monitoring," *IEEE TRPMS*, vol. 4, pp. 184–193, 2020.

[161] J. Kim, "Pinhole camera measurements of prompt gamma-rays for detection of beam range variation in proton therapy," *J Korean Phys Soc*, vol. 55, pp. 1673–1676, 2009.

[162] V. Bom, L. Joulaeizadeh, and F. Beekman, "Real-time prompt gamma monitoring in spot-scanning proton therapy using imaging through a knife-edge-shaped slit," *Phys Med Biol*, vol. 57, p. 297, 2011.

[163] J. Smeets *et al.*, "Prompt gamma imaging with a slit camera for real-time range control in proton therapy," *Phys Med Biol*, vol. 57, p. 3371, 2012.

[164] I. Perali *et al.*, "Prompt gamma imaging of proton pencil beams at clinical dose rate," *Phys Med Biol*, vol. 59, p. 5849, 2014.

[165] P. C. Lopes *et al.*, "Time-resolved imaging of prompt-gamma rays for proton range verification using a knife-edge slit camera based on digital photon counters," *Phys Med Biol*, vol. 60, p. 6063, 2015.

[166] M. Priegnitz *et al.*, "Measurement of prompt gamma profiles in inhomogeneous targets with a knife-edge slit camera during proton irradiation," *Phys Med Biol*, vol. 60, p. 4849, 2015.

[167] M. Priegnitz *et al.*, "detection of mixed-range proton pencil beams with a prompt gamma slit camera," *Phys Med Biol*, vol. 61, p. 855, 2016.

[168] M. Priegnitz *et al.*, "Towards clinical application: prompt gamma imaging of passively scattered proton fields with a knife-edge slit camera," *Phys Med Biol*, vol. 61, p. 7881, 2016.

[169] C. Richter *et al.*, "First clinical application of a prompt gamma based in vivo proton range verification system," *Radiother Oncol*, vol. 118, no. 2, pp. 232–237, 2016.

[170] Y. Xie *et al.*, "Prompt gamma imaging for in vivo range verification of pencil beam scanning proton therapy," *Int J Radiat Oncol Biol Phys*, vol. 99, pp. 210–218, 2017.

[171] L. Nenoff *et al.*, "Sensitivity of a prompt-gamma slit-camera to detect range shifts for proton treatment verification," *Radiother Oncol*, vol. 125, pp. 534–540, 2017.

[172] F. Roellinghoff *et al.*, "Design of a Compton camera for 3D prompt-γ imaging during ion beam therapy," *Nucl Instrum Methods Phys Res A*, vol. 648, pp. S20–S23, 2011.

[173] G. Llosá *et al.*, "Detector characterization and first coincidence tests of a Compton telescope based on $LaBr_3$ crystals and SiPMs," *Nucl Instrum Methods Phys Res A*, vol. 695, pp. 105–108, 2012.

[174] G. Llosá *et al.*, "First Compton telescope prototype based on continuous $LaBr_3$-SiPM detectors," *Nucl Instrum Methods Phys Res A*, vol. 718, pp. 130–133, 2013.

[175] P. Solevi *et al.*, "Performance of MACACO Compton telescope for ion-beam therapy monitoring: first test with proton beams,"

[176] J. Gillam *et al.*, "Hodoscope coincidence imaging for hadron therapy using a Compton camera," pp. 3508–3513, 2011.

[177] P. Ortega *et al.*, "Noise evaluation of Compton camera imaging for proton therapy," *Phys Med Biol*, vol. 60, p. 1845, 2015.

[178] G. Llosá *et al.*, "First images of a three-layer Compton telescope prototype for treatment monitoring in hadron therapy," *Front Oncol*, vol. 6, p. 14, 2016.

[179] E. Muñoz *et al.*, "Performance evaluation of MACACO: a multilayer Compton camera,"

[180] E. Muñoz *et al.*, "Tests of MACACO Compton telescope with 4.44 MeV gamma rays," *J Instrum*, vol. 13, p. P05007, 2018.

[181] E. Muñoz *et al.*, "Study and comparison of different sensitivity models for a two-plane Compton camera," *Phys Med Biol*, vol. 63, p. 135004, 2018.

[182] J. Barrio *et al.*, "Performance improvement tests of MACACO: A Compton telescope based on continuous crystals and SiPMs," *Nucl Instrum Methods Phys Res A*, vol. 912, pp. 48–52, 2018.

[183] F. Hueso-González, G. Pausch, J. Petzoldt, K. Römer, and W. Enghardt, "Prompt gamma rays detected with a BGO block Compton camera reveal range deviations of therapeutic proton beams," *IEEE TRPMS*, vol. 1, pp. 76–86, 2016.

[184] M. Jan, M. Lee, and H. Huang, "PSF reconstruction for Compton-based prompt gamma imaging," *Phys Med Biol*, vol. 63, p. 035015, 2018.

[185] A. Kishimoto, J. Kataoka, T. Nishiyama, T. Taya, and S. Kabuki, "Demonstration of three-dimensional imaging based on handheld Compton camera," *J Instrum*, vol. 10, p. P11001, 2015.

[186] T. Taya *et al.*, "First demonstration of real-time gamma imaging by using a handheld Compton camera for particle therapy," *Nucl Instrum Methods Phys Res A*, vol. 831, pp. 355–361, 2016.

[187] H. Seo *et al.*, "Development of double-scattering-type Compton camera with double-sided silicon strip detectors and NaI(Tl) scintillation detector," *Nucl Instrum Methods Phys Res A*, vol. 615, pp. 333–339, 2010.

[188] M. Richard *et al.*, "Design study of the absorber detector of a Compton camera for on-line control in ion beam therapy," *IEEE Trans Nucl Sci*, vol. 59, pp. 1850–1855, 2012.

[189] M. Frandes, A. Zoglauer, V. Maxim, and R. Prost, "A tracking Compton-scattering imaging system for hadron therapy monitoring," *IEEE Trans Nucl Sci*, vol. 57, pp. 144–150, 2010.

[190] P. Thirolf *et al.*, "Development of a Compton camera for online range monitoring of laser-accelerated proton beams via prompt-gamma detection," vol. 66, p. 11036, 2014.

[191] P. Thirolf *et al.*, "A Compton camera prototype for prompt gamma medical imaging," vol. 117, p. 05005, 2016.

[192] S. Aldawood *et al.*, "Development of a Compton camera for prompt-gamma medical imaging," *Radiat Phys Chem*, vol. 140, pp. 190–197, 2017.

[193] T. Kormoll *et al.*, "A Compton imager for in-vivo dosimetry of proton beams - A design study," *Nucl Instrum Methods Phys Res A*, vol. 626, pp. 114–119, 2011.

[194] F. Hueso-González *et al.*, "Test of Compton camera components for prompt gamma imaging at the ELBE bremsstrahlung beam," *J Instrum*, vol. 9, p. P05002, 2014.

[195] F. Hueso-González *et al.*, "Comparison of LSO and BGO block detectors for prompt gamma imaging in ion beam therapy," *J Instrum*, vol. 10, p. P09015, 2015.

[196] C. Golnik *et al.*, "Tests of a Compton imaging prototype in a monoenergetic 4.44 MeV photon field - A benchmark setup for prompt gamma-ray imaging devices," *J Instrum*, vol. 11, p. P06009, 2016.

[197] H. Rohling *et al.*, "Requirements for a Compton camera for in vivo range verification of proton therapy," *Phys Med Biol*, vol. 62, p. 2795, 2017.

[198] C. Hyeong Kim, J. Hyung, H. Seo, and H. Rim, "Gamma electron vertex imaging and application to beam range verification in proton therapy," *Med Phys*, vol. 39, pp. 1001–1005, 2012.

[199] H. Lee *et al.*, "Prototype system for proton beam range measurement based on gamma electron vertex imaging," *Nucl Instrum Methods Phys Res A*, vol. 857, pp. 82–97, 2017.

[200] S. Peterson, D. Robertson, and J. Polf, "Optimizing a three-stage Compton camera for measuring prompt gamma rays emitted during proton radiotherapy," *Phys Med Biol*, vol. 55, p. 6841, 2010.

[201] D. Robertson, J. Polf, S. Peterson, M. Gillin, and S. Beddar, "Material efficiency studies for a Compton camera designed to measure characteristic prompt gamma rays emitted during proton beam radiotherapy," *Phys Med Biol*, vol. 56, p. 3047, 2011.

[202] D. Mackin, J. Polf, S. Peterson, and S. Beddar, "The effects of Doppler broadening and detector resolution on the performance of three-stage Compton cameras," *Med Phys*, vol. 40, p. 012402, 2013.

[203] M. McCleskey *et al.*, "Evaluation of a multistage CdZnTe Compton camera for prompt γ imaging for proton therapy," *Nucl Instrum Methods Phys Res A*, vol. 785, pp. 163–169, 2015.

[204] J. Polf, S. Avery, D. Mackin, and S. Beddar, "Imaging of prompt gamma rays emitted during delivery of clinical proton beams with a Compton camera: feasibility studies for range verification," *Phys Med Biol*, vol. 60, p. 7085, 2015.

[205] E. Draeger *et al.*, "Feasibility studies of a new event selection method to improve spatial resolution of Compton imaging for medical applications," *IEEE TRPMS*, vol. 1, pp. 358–367, 2017.

[206] E. Draeger *et al.*, "3D prompt gamma imaging for proton beam range verification," *Phys Med Biol*, vol. 63, p. 035019, 2018.

[207] Z. Yao, Y. Xiao, Z. Chen, B. Wang, and Q. Hou, "Compton-based prompt gamma imaging using ordered origin ensemble algorithm with resolution recovery in proton therapy," *Sci Rep*, vol. 9, pp. 1–15, 2019.

[208] A. Gutierrez *et al.*, "Progress towards a semiconductor Compton camera for prompt gamma imaging during proton beam therapy for range and dose verification," *J Instrum*, vol. 13, 2018.

[209] T. Tanimori *et al.*, "Time projection chamber based on micro-pattern detector for neutron time-resolved imaging," *Nucl Instrum Methods Phys Res A*, vol. 529, pp. 373–377, 2004.

[210] A. Takada *et al.*, "Observation of diffuse cosmic and atmospheric gamma rays at balloon altitudes with an electron-tracking Compton camera," *Astrophys J*, vol. 733, p. 13, 2011.

[211] S. Kabuki *et al.*, "Development of electron tracking Compton camera using micro pixel gas chamber for medical imaging," *Nucl Instrum Methods Phys Res A*, vol. 580, pp. 1031–1035, 2007.

[212] S. Kurosawa *et al.*, "Prompt gamma detection for range verification in proton therapy," *Curr Appl Physs*, vol. 12, pp. 364–368, 2012.

[213] M. Takahashi *et al.*, "Development of an electron-tracking Compton camera using CF4 gas at high pressure for improved detection efficiency," *Nucl Instrum Methods Phys Res A*, vol. 628, pp. 150–153, 2011.

[214] F. Hueso-González *et al.*, "First test of the prompt gamma ray timing method with heterogeneous targets at a clinical proton therapy facility," *Phys Med Biol*, vol. 60, p. 6247, 2015.

[215] J. Petzoldt *et al.*, "Characterization of the microbunch time structure of proton pencil beams at a clinical treatment facility," *Phys Med Biol*, vol. 61, p. 2432, 2016.

[216] T. Werner *et al.*, "Processing of prompt gamma-ray timing data for proton range measurements at a clinical beam delivery," *Phys Med Biol*, vol. 64, p. 105023, 2019.

[217] J. Krimmer *et al.*, "A cost-effective monitoring technique in particle therapy via uncollimated prompt gamma peak integration," *Appl Phys Lett*, vol. 110, p. 154102, 2017.

[218] J. Verburg and J. Seco, "Proton range verification through prompt gamma-ray spectroscopy," *Phys Med Biol*, vol. 59, p. 7089, 2014.

[219] P. Martins Magalhaes *et al.*, "Prompt gamma spectroscopy for range control with CeBr3," *Curr Dir Biomed Eng*, vol. 3, pp. 113–117, 2017.

[220] M. Testa *et al.*, "Range verification of passively scattered proton beams based on prompt gamma time patterns," *Phys Med Biol*, vol. 59, p. 4181, 2014.

[221] J. Verburg, M. Testa, and J. Seco, "Range verification of passively scattered proton beams using prompt gamma-ray detection," *Phys Med Biol*, vol. 60, p. 1019, 2015.

[222] F. Hueso-González and T. Bortfeld, "Compact method for proton range verification based on coaxial prompt gamma-ray monitoring: a theoretical study," *IEEE TRPMS*, vol. 4, pp. 170–183, 2019.

[223] J. Smeets *et al.*, "experimental comparison of knife-edge and multi-parallel slit collimators for prompt gamma imaging of proton pencil beams," *Front Oncol*, vol. 6, p. 156, 2016.

[224] H. Lin, H. Chang, T. Chao, and K. Chuang, "A comparison of two prompt gamma imaging techniques with collimator-based cameras for range verification in proton therapy," *Radiat Phys Chem*, vol. 137, pp. 144–150, 2017.

[225] J. o. Park, "Comparison of knife-edge and multi-slit camera for proton beam range verification by Monte Carlo simulation," *Nucl Eng Technol*, vol. 51, pp. 533–538, 2019.

[226] Hueso-González *et al.*, "Compton camera and prompt gamma ray timing: two methods for in vivo range assessment in proton therapy," *Front Oncol*, vol. 6, p. 80, 2016.

[227] L. Parra, "reconstruction of cone-beam projections from Compton scattered data," *IEEE Trans Nucl Sci*, vol. 47, pp. 1543–1550, 2000.

[228] T. Tomitani and M. Hirasawa, "Image reconstruction from limited angle Compton camera data," *Phys Med Biol*, vol. 47, p. 2129, 2002.

[229] M. Hirasawa and T. Tomitani, "An analytical image reconstruction algorithm to compensate for scattering angle broadening in Compton cameras," *Phys Med Biol*, vol. 48, p. 1009, 2003.

[230] R. Basko, G. Zeng, and G. Gullberg, "Application of spherical harmonics to image reconstruction for the Compton camera," *Phys Med Biol*, vol. 43, p. 887, 1998.

[231] M. Cree and P. Bones, "Towards direct reconstruction from a gamma camera based on Compton scattering," *IEEE Trans Med Imaging*, vol. 13, pp. 398–407, 1994.

[232] V. Maxim, M. Frandeş, and R. Prost, "Analytical inversion of the Compton transform using the full set of available projections," *Inverse Problems*, vol. 25, p. 095001, 2009.

[233] X. Lojacono *et al.*, "Low statistics reconstruction of the Compton camera point spread funCTion in 3D prompt-gamma imaging of ion beam therapy," *IEEE Trans Nucl Sci*, vol. 60, pp. 3355–3363, 2013.

[234] V. Maxim, "Filtered backprojection reconstruction and redundancy in Compton camera imaging," *IEEE T Image Process*, vol. 23, pp. 332–341, 2013.

[235] S. Wilderman, N. Clinthorne, J. Fessler, and W. Rogers, "List-mode maximum likelihood reconstruction of Compton scatter camera images in nuclear medicine," vol. 3, pp. 1716–1720, 1998.

[236] S. Tornga, M. R. Sullivan, and J. Sullivan, "Three-dimensional Compton imaging using list-mode maximum likelihood expectation maximization," *IEEE Trans Nucl Sci*, vol. 56, pp. 1372–1376, 2009.

[237] V. Maxim *et al.*, "Probabilistic models and numerical calculation of system matrix and sensitivity in list-mode MLEM 3D reconstruction of Compton camera images," *Phys Med Biol*, vol. 61, p. 243, 2015.

[238] S. Schoene *et al.*, "An image reconstruction framework and camera prototype aimed for Compton imaging for in-vivo dosimetry of therapeutic ion beams," *IEEE TRPMS*, vol. 1, pp. 96–107, 2016.

[239] S. M. Kim *et al.*, "Fully three-dimensional OSEM-based image reconstruction for Compton imaging using optimized ordering schemes," *Phys Med Biol*, vol. 55, p. 5007, 2010.

[240] M. Lee, S. Lee, V. Nguyen, S. M. Kim, and J. S. Lee, "3D maximum likelihood reconstruction of Compton camera images using a row-action method," *J Nucl Med*, vol. 49, p. 400P, 2008.

[241] J. Gillam *et al.*, "A Compton imaging algorithm for on-line monitoring in hadron therapy," vol. 7961, p. 79611O, 2011.

[242] V. Nguyen, S. Lee, and M. N. Lee, "GPU-accelerated 3D bayesian image reconstruction from Compton scattered data," *Phys Med Biol*, vol. 56, p. 2817, 2011.

[243] N. Metropolis *et al.*

[244] K. Hastings, "Monte Carlo sampling methods using Markov chains and their applications," 1970.

[245] A. Sitek, "Representation of photon limited data in emission tomography using origin ensembles," *Phys Med Biol*, vol. 53, p. 3201, 2008.

[246] A. Andreyev, A. Sitek, and A. Celler, "Fast image reconstruction for Compton camera using stochastic origin ensemble approach," *Med Phys*, vol. 38, pp. 429–438, 2011.

[247] D. Mackin, S. Peterson, S. Beddar, and J. Polf, "Evaluation of a stochastic reconstruction algorithm for use in Compton camera imaging and beam range verification from secondary gamma emission during proton therapy," *Phys Med Biol*, vol. 57, p. 3537, 2012.

[248] M. Hamel, J. Polack, A. Poitrasson-Rivière, S. Clarke, and S. Pozzi, "Localization and spectral isolation of special nuclear material using stochastic image reconstruction," *Nucl Instrum Methods Phys Res A*, vol. 841, pp. 24–33, 2017.

[249] A. Andreyev, A. Celler, I. Ozsahin, and A. Sitek, "Resolution recovery for Compton camera using origin ensemble algorithm," *Med Phys*, vol. 43, pp. 4866–4876, 2016.

[250] D. Raeside, "Monte Carlo principles and applications," *Phys Med Biol*, vol. 21, p. 181, 1976.

[251] D. Rogers, "Fifty years of Monte Carlo simulations for medical physics," *Phys Med Biol*, vol. 51, p. R287, 2006.

[252] P. Andreo, "Monte Carlo simulations in radiotherapy dosimetry," *Radiat Oncol*, vol. 13, p. 121, 2018.

[253] L. Sihver *et al.*, "A comparison of total reaction cross section models used in particle and heavy ion transport codes," *Adv Space Res*, vol. 49, pp. 812–819, 2012.

[254] C. Robert *et al.*, "Distributions of secondary particles in proton and carbon-ion therapy: a comparison between gate/GEANT4 and FLUKA Monte Carlo codes," *Phys Med Biol*, vol. 58, p. 2879, 2013.

[255] ENDF, "Evaluated nuclear data file (ENDF)," 2020.

[256] M. Chadwick *et al.*, "ENDF/B-VII. 1 nuclear data for science and technology: cross sections, covariances, fission product yields and decay data," *Nucl Data Sheets*, vol. 112, pp. 2887–2996, 2011.

[257] M. Chadwick, "ENDF nuclear data in the physical, biological, and medical sciences," *Int J Radiat Biol*, vol. 88, pp. 10–14, 2012.

[258] EXFOR, "Experimental nuclear reaction data (EXFOR)," 2020.

[259] S. Agostinelli *et al.*, "GEANT4 - A simulation toolkit," *Nucl Instrum Methods Phys Res A*, vol. 506, pp. 250–303, 2003.

[260] J. Briesemeister, "MCNP-A generalized Monte Carlo code for neutron and photon transport, version 3A," *LA-7396-M, Rev. 2, Los Alamos National Laboratory (September 1986)*, 1986.

[261] G. Battistoni *et al.*, "The FLUKA code: Description and benchmarking," *AIP Conf Proc*, vol. 896, pp. 31–49, 2007.

[262] C. Jarlskog and H. Paganetti, "Physics settings for using the GEANT4 toolkit in proton therapy," *IEEE Trans Nucl Sci*, vol. 55, pp. 1018–1025, 2008.

[263] T. G. Collaboration, "GEANT4: A simulation toolkit (last update: February 2020)," 2020.

[264] J. Jeyasugiththan and S. Peterson, "Evaluation of proton inelastic reaction models in GEANT4 for prompt gamma production during proton radiotherapy," *Phys Med Biol*, vol. 60, p. 7617, 2015.

[265] G. Dedes *et al.*, "Assessment and improvements of GEANT4 hadronic models in the context of prompt-gamma hadrontherapy monitoring," *Phys Med Biol*, vol. 59, p. 1747, 2014.

[266] M. Pinto *et al.*, "Assessment of GEANT4 prompt-gamma emission yields in the context of proton therapy monitoring," *Front Oncol*, vol. 6, p. 10, 2016.

[267] C. Panaino, R. Mackay, K. Kirkby, and M. Taylor, "A new method to reconstruct in 3D the emission position of the prompt gamma rays following proton beam irradiation," *Sci Rep*, vol. 9, pp. 1–12, 2019.

[268] G. F. Knoll, *Radiation detection and measurement*. John Wiley & Sons, 2010.

[269] National Institute of Standards and Technology, "X-ray mass attenuation coefficients," 2004.

[270] B. Löher *et al.*, "High count rate γ-ray spectroscopy with $LaBr_3$:Ce scintillation detectors," *Nucl Instrum Methods Phys Res A*, vol. 686, pp. 1–6, 2012.

[271] M. Vencelj, K. Bučar, R. Novak, and H. Wörtche, "Event by event pile-up compensation in digital timestamped calorimetry," *Nucl Instrum Methods Phys Res A*, vol. 607, pp. 581–586, 2009.

[272] A. Drescher *et al.*, "Gamma-gamma coincidence performance of $LaBr_3$:Ce scintillation detectors vs HPGe detectors in high count-rate scenarios," *Appl Radiat Isot*, vol. 122, pp. 116–120, 2017.

[273] S. Aldawood *et al.*, "Comparative characterization study of a $LaBr_3$(Ce) scintillation crystal in two surface wrapping scenarios: Absorptive and reflective," *Front Oncol*, vol. 5, p. 270, 2015.

[274] C. Panaino, R. Mackay, M. Sotiropoulos, K. Kirkby, and M. Taylor, "Full 3D position reconstruction of a radioactive source based on a novel hyperbolic geometrical algorithm," *Comput Phys Commun*, vol. 252, p. 107131, 2020.

[275] MathWorks, "MATLAB - profile your code to improve performance," 2020.

[276] M. Durante and H. Paganetti, "Nuclear physics in particle therapy: a review," *Rep. Prog. Phys.*, vol. 79, p. 096702, 2016.

[277] AAPM Meetings, "https://www.aapm.org/meetings/ (last update: August 2020)," 2020.

[278] U. Schneider, E. Pedroni, and A. Lomax, "The calibration of CT Hounsfield units for radiotherapy treatment planning," *Phys Med Biol*, vol. 41, p. 111, 1996.

[279] R. Nicolini *et al.*, "Investigation of the properties of a 1" × 1" $LaBr_3$:Ce scintillator," *Nucl Instr Meth Phys Res A*, vol. 582, pp. 554–561, 2007.

[280] R. Shearman *et al.*, "Commissioning of the UK NAtional nuclear array," *Radiat Phys Chem*, vol. 140, pp. 475–479, 2017.

[281] S. Collins, R. Shearman, J. Keightley, and P. Regan, "Investigation of γ-γ coincidence counting using the National Nuclear Array (NANA) as a primary standard," *Appl Radiat Isot*, vol. 134, pp. 290–296, 2018.

[282] CERN, "DICOM extended example," 2019.

[283] V. Giacometti *et al.*, "Development of a high resolution voxelised head phantom for medical physics applications," *Phys Medica*, vol. 33, pp. 182–188, 2017.

[284] CIRS, "CIRS Tissue Simulation & Phantom Technology," 2020.

[285] N. Burnet *et al.*, "Proton beam therapy: perspectives on the National Health Service England clinical service and research programme," *Brit J Radiol*, vol. 93, p. 20190873, 2020.

[286] The Christie NHS Foundation Trust, "Proton beam therapy," 2020.

[287] Hepco Motion, "System Solutions and Motion Control," 2020.

[288] Bollin Dale, "Bollin Dale Engineering," 2020.